



The
University
Of
Sheffield.

Regulation of the Hippo pathway via the multi-PDZ domain MAGI proteins in epithelial cells

By:

Claire Murzeau

A thesis submitted in partial fulfilment of the requirements for the degree of

Doctor of Philosophy

The University of Sheffield

Faculty of Science

Department of Biomedical Science

Declaration

I hereby declare that my thesis entitled "**Regulation of the Hippo pathway via the multi-PDZ domain MAGI proteins in epithelial cells**" has been entirely composed by myself and is the sole result of my work, unless otherwise stated by reference or acknowledgment. I confirm that this work has not been submitted, in whole or in parts, in any previous application for a degree.

December 10th, 2019

Date


Claire MURZEAU

Signature

Abstract

The Hippo pathway is known to regulate organ size by controlling essential cellular functions such as proliferation and survival. Dysregulation of this signalling cascade leads to hyper-activation of the key downstream effectors YAP and TAZ, associated with several types of cancers. The current paradigm for the regulation of YAP in response to cell density focuses on Ser127 phosphorylation-dependent nucleocytoplasmic shuttling by an intricate network of upstream regulators. However, the mechanisms at play in the signal transduction from upstream mediators, such as tight junctions, to the core Hippo cascade remain largely elusive.

In the present study, we investigated the contribution of the multi-PDZ domain MAGI family of proteins, which play a role in tight junction maintenance and integrity. This essential feature of epithelial tissues is often disrupted in cancer and gives way to metastasis. MAGI-1 was recently implicated in the regulation YAP subcellular localization in a cell density-dependent manner. However, the mechanism at play remains unclear. Here, we further establish MAGI-1 as a regulator of the Hippo pathway. We show that MAGI-1 and MAGI-3 form a complex with key regulators of the Hippo pathway such as the LATS1/2 kinases, the protein tyrosine phosphatase PTPN14 and YAP itself. In addition, we found that MAGI-1 can recruit LATS1/2 and PTPN14 to tight junctions. MAGI-1 and MAGI-3 single and double DLD-1 knockout cells still displayed nuclear YAP at high cell density. Interestingly, YAP Ser127 phosphorylation status was lower at medium cell density but normal in dense knockout cells. We therefore suggest that MAGI-1 is involved in YAP regulation through two a two-step mechanism: (1) Recruitment of LATS1/2 kinases and PTPN14 at tight junctions for activation of the kinase cascade at medium density and (2) Sequestration of YAP pSer127 in the cytosol in dense cells. Our data further underline the importance of tight junctions in the regulation of the Hippo pathway.

Acknowledgments

First, I would like to express my sincere gratitude to my supervisor, Dr. Kai Erdmann, for giving me the opportunity to undertake this PhD in biomedical science, a tremendous challenge for me coming from an engineering school. His continuous support, patience and guidance were invaluable and made the transition smoother. Thank you for believing in me and pushing me to believe in myself.

I would like to warmly thank my advisors Prof. Elizabeth Smythe and Prof. Peter Andrews whose support and constructive criticism were precious throughout my PhD. I thank Dr. Matthieu Piel, Institut Curie and Dr. Henriette Lanz, MIMETAS, as well as their team members, for welcoming me into their labs and teaching me state of the art techniques. I would like to thank as well the whole ITN-BIOPOL network for the stimulating and captivating scientific discussions during the annual meetings, and Agnieszka for successfully organising them.

I would like to thank all past and current Erdmann lab members with whom I shared part of the journey. This lab gave me room to grow as a scientist by receiving precious advice, engaging in scientific discussions during lab meetings and all together providing a supporting environment to complete this PhD. I also would like to acknowledge all the people from the Biomedical science department of the University of Sheffield who advised me on technical issues, provided reagents and were generally always happy to help.

A special thanks to Agnieszka for teaching me all the techniques when I first started and for her patience and encouragements. A huge thank you to my amazing lab mates, fellow PhD students and friends, Agnieszka, Shruti, Toni, Sindhu, Kinga, Andrew, Lily, Wirda, Judit and Keith for your emotional and moral support, for simply going through PhD life with me in good and bad times and for sharing so many entertaining lunches.

Finally, this work would not have been possible without the unwavering support and trust of my family over the years. I am truly thankful to my mom, my dad and my brother for bringing the best in me and for their constant love and belief in my abilities to pursue this research degree. A heartfelt thank you to my grandparents who always encouraged me, specially my late grandfather who would have been so proud of me.

Abbreviations

3D: Three dimensions

A5+6: MAGI1/MAGI3 double knockout bulk or clone derived from MAGI-1 knockout clone G1 8 (A)

Ad9: Adenovirus type 9

AIP4: Atrophin-1-interacting protein 4 (E3 ubiquitin ligase, also known as ITCH)

AJs: Adherens junctions

AMOT: Angiomotin

AMOTL1/2: Angiomotin-like-1/2

AmpR: Ampicilin resistant

ANOVA: ANalysis Of VAriance

aPKC: atypical protein kinase C

APS: Ammonium persulfate

ATCC: American Type Culture Collection

B5+6: MAGI1/MAGI3 double knockout bulk or clone derived from MAGI-1 knockout clone G2 14 (B)

BD: Binding domain

BI: Barrier integrity

BioID: Proximity-dependent biotin identification

Bp: base pair

BSA: Bovine serum albumin

Caco-2: Human colon colorectal adenocarcinoma epithelial cell line

Cas9: CRISPR-associated protein-9

CC: Coiled-coil domain

CIP (methods section): Calf intestinal alkaline phosphatase

CIP (other): Contact inhibition of proliferation

CK1: Casein kinase 1

CK2: Casein kinase 2

CNTN5: Contactin-5

Co-ip: Co-immunoprecipitation

Col-I: Collagen-I

Crb3: Crumbs 3 protein

CRC: Colorectal cancer

CRISPR: Clustered regularly interspaced short palindromic repeats

CRL2: Cytokine receptor-like factor 2

Da: Dalton (kDa: kilo Dalton)

DAPI: 4',6-diamidino-2-phenylindole

DC assay: Detergent compatible protein assay

DLD-1: Human colon adenocarcinoma cell line
Dlg1: Drosophila disc large tumor suppressor
DMEM: Dulbecco's Modified Eagle Medium
DMSO: Dimethyl sulfoxide
DNA: Deoxyribonucleic acid
dNTPs: Deoxynucleotide triphosphates
DSB: Double stranded break
E. coli: Escherichia coli
ECACC: European Collection of Authenticated Cell Cultures
ECM: Extracellular matrix
EDTA: Ethylenediaminetetraacetic acid
EdU: (5-ethynyl-2'-deoxyuridine)
EMT: Epithelial to mesenchymal transition
Erk: Extracellular signal-regulated kinase
EtOH: Ethanol
FBS: Foetal bovine serum
FERM: Four-point-one, ezrin, radixin, moesin
Fiji: Fiji Is Just ImageJ
FITC: fluorescein isothiocyanate
FL: Full length
FWD: Forward
G1 8 (A): MAGI-1 knockout clone
G2 14 (B): MAGI-1 knockout clone
G5+6 bulk or clone 28: MAGI-3 knockout bulk population or clone
gDNA: genomic DNA
GFP: Green fluorescent protein
GPCRs: GG protein-coupled receptors
GuK: Guanylate kinase
g α r: goat anti-rabbit
HBSS: Hanks' Balanced Salt Solution
HDR: Homology Directed Repair
HEK293: human embryonic kidney cell line
HEPES: (4-(2hydroxyethyl)-1piperazineethanesulfonic acid
HER2: Tyrosine kinase-type cell surface receptor (also known as ERBB2)
HF: High fidelity
Hpo: Drosophila homologue of MST1/2 kinases
HPV: Human papilloma virus
IBD: Inflammatory bowel disease

IF: Immunofluorescence
IN: Inlet (OrganoPlate®)
Indel: insertion/deletion
JAMs: Junctional adhesion molecules
KanaR: Kanamycin resistant
Kb: kilo base pair
KIBRA: Kidney and brain protein
KO: Knockout
LATS1/2: Large tumor suppressor homolog 1/2 (Drosophila homologue: Warts)
LB: Luria-Bertani
Lgl: Lethal giant larvae
LKB1: Liver kinase B1
LPA: Lysophosphatidic acid
LPA₂: Lysophosphatidic acid receptor 2
LRR1: Leucine-rich repeat protein
MAGI-1: Membrane-associated guanylate kinase inverted 1
MAGI-2: Membrane-associated guanylate kinase inverted 2
MAGI-3: Membrane-associated guanylate kinase inverted 3
MAGUK: Membrane-associated guanylate kinases
mcs: multiple cloning site
MDCK: Madin-Darby canine kidney cell line
MDCKts-src: MDCK cells with a temperature-sensitive v-SRC gene
MEM: Minimum Essential Medium
MeOH: Methanol
mM: mmol/L
MOB1A: Mps one binder kinase activator-like 1A
MolDev: Molecular Devices
MPDZ: Multi-PDZ
MST1/2: Mammalian sterile 20-like 1/2 (Drosophila homologue: Hpo)
MW: Molecular weight
NEAA: Non-essential amino acids
NEDD4: Neural precursor cell expressed developmentally down-regulated protein 4
NeoR: Neomycin resistant
NES: Nuclear exclusion signal
NETN: NaCl, EDTA, Tris, NP-40
Nf2: Neurofibromin-2 (gene coding for Merlin protein)
NF-κB: Nuclear factor kappa-light-chain-enhancer of activated B cells
NHEJ: Non-homologous end joining repair

NHERF2: Na⁺/H⁺ exchanger regulatory factor
NLS: Nuclear localisation signal
NP-40: 4-Nonylphenyl-polyethylene glycol, Nonidet PTM 40
Oligos: Oligonucleotides
ORF: Open reading frame
OUT: Outlet (OrganoPlate®)
PAC - puromycin-N-acetyltransferase
PAK-1: Serine/threonine-protein kinase 1
PALS1: Protein Associated with Lin-Seven 1
PAM: Protospacer adjacent motif
Par-1: Proteinase-activated receptor 1
PAR3: Partitioning defective-3 protein (mammalian homologue of Bazooka)
PAR6: Partitioning defective-6 protein
PATJ: PALS1 associated Tight Junction Protein
PBS: Phosphate buffered saline
PBST: Phosphate buffered saline with Tween20
PCI: Protease cocktail inhibitor
PCR: Polymerase chain reaction
PDZ: PSD95/Dlg1/ZO-1
PEG: Polyethylene-glycol
Pen/Strep or P/S: Penicillin/Streptomycin
PFA: Paraformaldehyde
PI3K: Phosphoinositide 3-kinase
PLL: Poly-L-Lysine
pPa: Prematurely polyadenylated
PPXY: Proline/proline/any amino acid/tyrosine
PSD-95: Postsynaptic density protein 95
PTEN: phosphatase and tensin homolog
PTP: Phosphatase domain
PTPN14: Receptor-type tyrosine-protein phosphatase zeta
Ptprz: Receptor-type tyrosine-protein phosphatase zeta
PuroR: Puromycin resistant
PY motif: Proline-tyrosine motif
RE: Restriction enzyme
REV: Reverse
RhoA: Ras homolog gene family member A
RIPA: Radioimmunoprecipitation assa
RNA: Ribonucleic acid

rpm: round per minutes

RPMI: Roswell Park Memorial Institute

RT: Room temperature

S.E.M.: Standard error to the mean

SAVI: Salvador

SCF B-TrCP: Skp, Cullin, F-box containing E3 ubiquitin ligase and its adaptor beta-transducin repeat containing protein

Scr siRNA: Scrambled siRNA

Scrib: Scribble protei

SDS-PAGE: Sodium dodecyl sulphate polyacrylamide gel electrophoresis

Ser: Serine

sgRNA: single guide RNA

SH3: Src homology 3 domain

SIP1: Signal-induced proliferation-associated protein 1

siRNA: small interfering RNA

SNPs: Single nucleotide polymorphism

S-SCAM: Synaptic scaffolding molecule

STXBP4: syntaxin binding protein

Su(dx): Suppressor of Deltex (Drosophila homologue of WWP1)

T7: Endonuclease

TAD: Trans-activation domain

TAE: tris-acetate buffer

TAZ: Transcriptional co-activator with PDZ binding motif

TBE: Tris-Borate-EDTA

TBS: Tris buffered saline

TBST: Tris buffered saline with Tween20

TEADs: Transcriptional enhancer factor domains

TEER: Trans-epithelial and endothelial electrical resistance

TEMED: Tetramethylethylenediamine

TJs: Tight junctions

Tm: Melting temperature

TRIP6: Thyroid receptor interacting protein 6

TRITC: Tetramethyl Rhodamine Iso-Thiocyanate

UV: Ultra violet

VPAC1: Vasoactive intestinal peptide type I receptor variant

WB: Western blot

WST-8: water-soluble tetrazolium salt 8

WT: Wild Type

WW: Domain with two conserved tryptophan residues

WWC1: WW domain-containing protein 1 (also known as Kibra)

WWP1: WW domain-containing protein 1 (E3 ubiquitin ligase, mammalian homologue of Su(dx))

YAP: Yes-associated protein

ZO: Zonula Occludens

Table of Contents

Declaration	3
Abstract	5
Acknowledgments	7
Abbreviations	9
Table of Contents	15
List of figures	18
List of tables	22
1 Introduction	25
1.1 <i>Contact inhibition of proliferation</i>	25
1.2 <i>The Hippo signalling pathway</i>	25
1.2.1 Canonical Hippo pathway	25
1.2.2 Complex layers of YAP regulation	28
1.2.3 Regulation of the Hippo pathway players by post-translational modifications.....	37
1.2.4 Role of YAP/TAZ in tissue homeostasis and cancer.....	39
1.2.5 Towards a better understanding of signal transduction from upstream regulators to the activation of the Hippo core kinase cascade.....	40
1.3 <i>MAGI family, multi-PDZ domain and tight junction proteins</i>	40
1.3.1 A unique structure	40
1.3.2 Splicing variants, subcellular localisation and tissue distribution	42
1.3.3 MAGIs, scaffolding proteins, involved in tight junction integrity	44
1.3.4 MAGIs in cancer signalling.....	46
1.4 <i>AIM: Investigate the molecular mechanism by which MAGI proteins negatively regulate YAP activity in response to cell density cues</i>	49
2 Chapter 2: Materials and Methods	51
2.1 <i>Materials</i>	51
2.1.1 Devices	51
2.1.2 Reagents	52
2.2 <i>Methods</i>	61

2.2.1	Cell culture methods.....	61
2.2.2	Ribonucleic acid methods.....	64
2.2.3	Molecular cloning and plasmid preparation.....	66
2.2.4	CRISPR/Cas9 and stable knockout cell lines.....	76
2.2.5	Protein assays and Western Blot.....	97
2.2.6	Immunofluorescence imaging.....	107
2.2.7	Statistical analysis.....	111
2.2.8	OrganoPlate® methods.....	112
3	Chapter 3: MAGI-1 and MAGI-3 regulate the Hippo-YAP pathway's response to cell density and YAP cytoplasmic retention	121
3.1	<i>Introduction</i>	121
3.2	<i>Aims</i>	121
3.3	<i>Results</i>	122
3.3.1	MAGI proteins play a role in YAP nuclear exclusion at high cell density.....	122
3.3.6	MAGI-1/MAGI-3 double depletion reduces LATS1/2-mediated phosphorylation of YAP Ser127 at high cell density.....	141
3.3.7	MAGI knockout DLD-1 cells form 3D leak-tight tubules in OrganoPlate®	144
3.4	<i>Discussion</i>	149
3.4.1	Redundancy among the MAGI family of proteins.....	149
3.4.2	Lack of both MAGI-1 and MAGI-3 impairs Hippo-YAP response to cell density cue in 2D cultures.....	150
3.4.3	YAP localisation in 3D tubules under bilateral fluid flow.....	152
3.4.4	Single MAGI knockout does not affect epithelial barrier integrity in the tubules.....	153
4	Chapter 4: MAGI-1 and MAGI-3 form a complex with essential players of the Hippo cascade at tight junctions.....	155
4.1	<i>Introduction</i>	155
4.2	<i>Aims</i>	156
4.3	<i>Results</i>	156
4.3.1	MAGI-1 interacts with PTPN14, a well-established negative regulator of YAP	156
4.3.2	YAP is in MAGI-1 protein complex.	167
4.3.3	MAGI-1 interacts with LATS1/2, key players of the Hippo pathway.....	170
4.3.4	PTPN14, LATS1/2, AMOT and YAP are co-precipitated by MAGI-1.....	177
4.3.5	MAGI-1 colocalises with its binding partners at tight junctions.....	182
4.4	<i>Discussion</i>	188
4.4.1	MAGI-1 interacts with key players of the Hippo pathway.....	188

4.4.2	MAGI-1 and MAGI-3 share the same Hippo pathway interactors.....	193
4.4.3	The MAGIs, scaffolding proteins, assembling part of the Hippo signal transduction machinery.....	195
5	Discussion and future perspectives	201
5.1	<i>WW domains at the centre of Hippo signal transduction.....</i>	<i>201</i>
5.2	<i>Regulation of the Hippo pathway by the MAGI proteins in response to cell density</i>	<i>202</i>
5.2.1	Role of MAGI proteins in the early phase activation of the Hippo cascade upon cell density cue	203
5.2.2	MAGI proteins implicated in YAP cytoplasmic retention	204
5.2.3	Shape change, additional density trigger ^p	205
5.2.4	Our model.....	207
5.2.5	MAGIs in colorectal cancer	208
5.3	<i>Concluding remarks and future perspectives.....</i>	<i>209</i>
	ANNEX 1: Generation of hMAGI-1Cβ1 cDNA using overlapping PCR.....	211
	ANNEX 2: Supplement to Figure 3.1 and Figure 3.4	215
	ANNEX 3: Generation of MAGI2 single and MAGI1/MAGI2 double knockout in DLD-1 cells.....	216
	ANNEX 4: Proliferation and immunostaining in the OrganoPlate[®].....	223
	ANNEX 5: Spatial confinement of single cells induces cytoplasmic YAP past a certain threshold	231
	ANNEX 6: Is MAGI-1 stabilising PTPN14^p	234
	ANNEX 7: Optimisation of pulldown experiments for MAGI1/LATS interaction	238
	References	241

List of figures

Figure 1.1 Conservation of the core Hippo pathway across species.....	26
Figure 1.2 Domain structures of YAP and TAZ, downstream effectors of the Hippo pathway.	27
Figure 1.3 LATS-mediated phosphorylation of YAP induces cytoplasmic retention and degradation.....	28
Figure 1.4 Four types of epithelial intercellular junctions.....	31
Figure 1.5 Mechanical cues affect YAP subcellular localisation and activity.....	37
Figure 1.6 YAP/TAZ output functions are hallmarks of cancer.....	39
Figure 1.7 MAGI proteins have an inverted domain organisation compared to other prototypical MAGUKs.....	41
Figure 1.8 Alternatively spliced regions of MAGI-1.....	42
Figure 1.9 Alternative START codons give rise to three MAGI-2 isoforms.....	43
Figure 1.10 MAGI-3 has two alternatively spliced regions.....	44
Figure 2.1 CRISPR/Cas9 gene editing and repair mechanisms.....	77
Figure 2.2 BbsI cloning site in pSpCas9(BB) vectors.....	81
Figure 2.3 Molecular cloning of G1 and G2 into PX458-Cas9-GFP vector.....	82
Figure 2.4 Excitation and emission spectra of EGFP and TO-PRO-3 viability dye.....	86
Figure 2.5 Excitation and emission spectra of Propidium Iodide.....	88
Figure 2.6 T7 assay workflow.....	92
Figure 2.7 Example of manual reading of sequencing results from a heterozygous CRISPR clone, G2 14.....	95
Figure 2.8 Protein migration and ion fronts in a denaturing discontinuous system.....	102
Figure 2.9 Western blot quantification using Image Studio™ Lite software.....	105
Figure 2.10 OrganoPlate® 3-lane design.....	112
Figure 2.11 Phase contrast images of a 3-lane design from the observation window (Top view).....	113
Figure 2.12 Example of quantification of the barrier integrity assay in OrganoPlate®.....	115
Figure 2.13 Edu incorporation in DNA and easy detection via click reaction.....	116
Figure 2.14 Confocal imaging of gut tubules in a 3-lane OrganoPlate®.....	120
Figure 3.1 YAP subcellular localisation is cell density dependent in epithelial cells.....	123
Figure 3.2 MAGI-1 transient knockdown in HEK293, Caco-2 and DLD-1 cells.....	124

Figure 3.3 MAGI-1 transient knockdown induces nuclear localisation of YAP at high cell density.....	125
Figure 3.4 MAGI-1 overexpression does not induce exclusion of YAP from the nucleus in sparse cells.....	127
Figure 3.5 MAGI-1 colocalises with ZO-1 at tight junctions.....	128
Figure 3.6 Design of two sgRNAs targeting MAGI-1 Exon1.....	129
Figure 3.7 Validation of MAGI-1 knockout clones G1 8 (A) and G2 14 (B).....	131
Figure 3.8 MAGI-1 knockout mildly affects YAP subcellular localisation at high cell density.	132
Figure 3.9 MAGI-2 expression in Caco-2, DLD-1 and HEK293 cell lines.	133
Figure 3.10 MAGI-3 expression in Caco-2, DLD-1 and HEK293 cell lines.....	134
Figure 3.11 MAGI-3 protein levels are not upregulated upon MAGI-1 knockout.	135
Figure 3.12 Two sgRNAs targeting Exon1 and all isoforms of MAGI-3.....	135
Figure 3.13 Validation of MAGI-3 single and MAGI1/MAGI3 double knockout at the protein level.	137
Figure 3.14 Mutations of MAGI-3 single and MAGI1/MAGI3 double knockout clones.....	138
Figure 3.15 MAGI1/MAGI3 double knockout enhances YAP defect at high cell density.....	139
Figure 3.16 MAGIs single and double knockout appear to push back to threshold for high cell density sensing.....	140
Figure 3.17 Validation of antibodies.	141
Figure 3.18 MAGIs knockout reduces YAP Ser127 phosphorylation at medium density.....	143
Figure 3.19 Formation of tubules in 3-lane OrganoPlate®.....	145
Figure 3.20 MAGI1 and MAGI3 single knockouts do not affect barrier integrity of the tubules.	147
Figure 3.21 YAP cytoplasmic localisation in DLD-1 tubules cultured under flow in OrganoPlate®.....	148
Figure 3.22 Canonical view of the core mammalian Hippo pathway.....	150
Figure 4.1 MAGI-1 interacts with PTPN14.....	157
Figure 4.2 MAGI-1 WW1 domain interacts with PTPN14.....	158
Figure 4.3 PTPN14 PPxY motifs are necessary for the binding of MAGI-1 WW domains.....	160
Figure 4.4 Potential second binding site between mMAGI-1 and PTPN14.....	161
Figure 4.5 PTPN14 interaction is conserved with the human isoform: hMAGI-1Cβ1.....	163
Figure 4.6 MAGI-1 appears to enhance PTPN14 plasma membrane localisation.	165
Figure 4.7 MAGI-3 interacts with PTPN14.	166
Figure 4.8 YAP interacts with MAGI-1 C-terminal PDZ domains.....	168

Figure 4.9 MAGI-1 and YAP are both localised at cell-cell contacts.	169
Figure 4.10 MAGI-1 is in a protein complex with either of the LATS kinases.	170
Figure 4.11 MAGI-1 WW domains are sufficient to bind to the LATS kinases.	173
Figure 4.12 LATS1/2 interaction is conserved with the human isoform: hMAGI-1C β 1.	173
Figure 4.13 MAGI-1 and the LATS kinases are localised at the cell-cell contacts.	175
Figure 4.14 MAGI-3 interacts with the LATS kinases.....	176
Figure 4.15 PTPN14 competes with LATS1/2 for the binding of mMAGI-1B WW domains. ...	177
Figure 4.16 AMOT family of proteins.....	179
Figure 4.17 AMOT proteins are part of mMAGI-1B complex, alongside LATS1/2, PTPN14 and YAP.	180
Figure 4.18 AMOT was not detected in pulldown complexes in the presence of MAGI-3....	182
Figure 4.19 PTPN14 is recruited to tight junctions by MAGI-1.....	183
Figure 4.20 YAP is enriched at the tight junctions regardless of MAGI-1 expression..	185
Figure 4.21 LATS1/2 kinases are recruited to tight junctions by MAGI-1.	186
Figure 4.22 AMOT is not expressed in DLD-1 cells.....	187
Figure 4.23 MAGI-1 interacts with PTPN14.	189
Figure 4.24 MAGI-1 interacts with both LATS kinases.....	189
Figure 4.25 hMAGI-1 WW domains are farther apart than in the mouse protein.....	190
Figure 4.26 MAGI-1 interacts with AMOT p130.....	191
Figure 4.27 MAGI-1 interacts with YAP.....	192
Figure 4.28 Kibra (WWC1) shares many binding partners with MAGI-1 due to their tandem WW domains but have, otherwise, very different structures.....	193
Figure 4.29 MAGI-3 interacts with key players of the Hippo pathway.....	195
Figure 4.30 Hippo multi-protein complex assembled around MAGI-1.	197
Figure 4.31 Hippo multi-protein complex assembled around MAGI-3.....	198
Figure 4.32 MAGI proteins assemble part of the Hippo signal transduction machinery at the plasma membrane.....	200
Figure 5.1 Alignments of WW-tandems of the Hippo pathway.....	201
Figure 5.2 Hypothetical view of MAGI-1 role in the regulation of the Hippo-YAP pathway .	207

Figure A. 1 Synthesis of hMAGI-1C β 1 using overlapping PCR.	211
Figure A. 2 Specificity of the YAP antibody for immunofluorescence.....	215
Figure A. 3 Potential MAGI-2 alternative START codons and three isoforms.	216
Figure A. 4 Two sgRNAs targeting MAGI-2 Exon5.....	217

Figure A. 5 Sense and anti-sense strand targeting and sgRNA oligo design.....	218
Figure A. 6 Assessment of MAGI2 and MAGI1/MAGI2 bulk populations.	219
Figure A. 7 Screening of MAGI-2 single and MAGI1/MAGI2 double knockout clones.	221
Figure A. 8 MAGI-2 overexpression and antibody specificity.....	222
Figure A. 9 EdU signal in DLD-1 WT tubules at early and late stage in 3-lane OrganoPlate®.	224
Figure A. 10 Growth arrest of cells in OrganoPlate® between Day4 and Day10.	225
Figure A. 11 MAGI knockouts do not affect cell viability.....	226
Figure A. 12 E-cadherin and Occludin staining in DLD-1 tubules in the 3-lane OrganoPlate®.	227
Figure A. 13 Immunostaining of a DLD-1 WT tubule.	228
Figure A. 14 DLD-1 tubules in the OrganoPlate® show proper F-actin and ZO-1 polarisation.	229
Figure A. 15 Effects of 2D spatial confinement on YAP subcellular localisation in HEK293 cells.	232
Figure A. 16 PTPN14 is targeted for degradation by two E3 ubiquitin ligases.	234
Figure A. 17 MAGI-1 could be the protein rescuing PTPN14 from WWP1-mediated degradation in human.....	235
Figure A. 18 Modular structure of the NEDD4 family of E3 ubiquitin ligases.....	236
Figure A. 19 Autoinhibition mechanisms of E3 ligases of the NEDD4 family.	236
Figure A. 20 Potential rescue mechanism of PTPN14's WWP1-mediated degradation by MAGI- 1.....	237
Figure A. 21 MAGI-1 interacts with both LATS1 and LATS2 kinases.	239

List of tables

Table 1.1 YAP is upregulated in several types of cancers.....	39
Table 1.2 Tissue distribution of MAGI-1 alternatively spliced regions.....	42
Table 2.1 List of devices.....	51
Table 2.2 List of kits and chemicals.....	52
Table 2.3 List of primary antibodies	53
Table 2.4 List of secondary antibodies.....	53
Table 2.5 List of cloning primers	54
Table 2.6 List of mutagenesis primers	55
Table 2.7 List of sequencing primers.....	55
Table 2.8 List of siRNAs.....	56
Table 2.9 List of sgRNAs.....	56
Table 2.10 List of expression constructs.....	57
Table 2.11 List of mammalian cell lines	59
Table 2.12 List of reagents used for cell culture.....	60
Table 2.13 List of bacteria strain and reagents used for bacteria culture.....	60
Table 2.14 Summary of mammalian cell lines and culture conditions	61
Table 2.15 Subculture procedure for mammalian cell lines	61
Table 2.16 Mammalian cells seeding densities	62
Table 2.17 Transfection protocols for mammalian cell lines	63
Table 2.18 DNase I treatment.....	64
Table 2.19 Reverse transcription.....	65
Table 2.20 Phusion [®] High-Fidelity PCR reaction mix.....	67
Table 2.21 GoTaq [®] PCR reaction mix.....	68
Table 2.22 Restriction enzyme digestion	69
Table 2.23 Ligation reaction.....	73
Table 2.24 MAGI-1 sgRNAs targeting Exon1.....	77
Table 2.25 MAGI-2 sgRNAs targeting Exon5	78
Table 2.26 MAGI-3 sgRNAs targeting Exon1.....	79
Table 2.27 T4 Polynucleotide Kinase reaction mix.....	80
Table 2.28 BbsI restriction enzyme digestion of pSpCas9(BB) vectors	81
Table 2.29 Ligation reaction of sgRNAs into pSpCas9(BB) vectors.....	81

Table 2.30 Transfection combinations for the generation of MAGI single and double knockouts	84
Table 2.31 Primer pairs to amplify CRISPR/Cas9 targeted region.....	89
Table 2.32 GoTaq [®] amplification of gDNA	90
Table 2.33 GoTaq [®] master mixes.....	90
Table 2.34 Summary of isogenic clones from MAGI knockouts and associated mutations .	95
Table 2.35 Volumes for extraction of total protein in CRISPR populations.....	96
Table 2.36 Buffer composition for protein assays and western blotting technique	97
Table 2.37 Volume of lysis buffer used depending on the application	98
Table 2.38 Co-immunoprecipitation conditions for the interactions investigated	99
Table 2.39 Composition of stacking and resolving gels for SDS-PAGE	103
Table 2.40 List of antibodies used for Western blot and associated buffers	104
Table 2.41 Phosphatase treatment after transfer.....	106
Table 2.42 Seeding densities for density assay in wild-type cell lines	108
Table 2.43 Seeding densities for 24hrs density assay in MAGI knockout cell lines	108
Table 2.44 Buffer composition for immunostaining procedure.....	109
Table 2.45 Cell lines cultured in the 3-lane OrganoPlate [®]	114
Table 2.46 Click-iT [®] Plus reaction cocktail.	117
Table 2.47 Parameters used in the MIMETAS plugin to process EdU assay.....	118
Table 2.48 Primary antibodies used for immunostaining in the OrganoPlate [®]	118
Table 2.49 Fluorescent antibodies used for immunostaining in the OrganoPlate [®]	119
Table 3.1 MAGI-1 sgRNAs targeting Exon1	129
Table 3.2 MAGI-3 sgRNAs targeting Exon1	136

Table A. 1 Reaction mix for Phusion [®] overlapping PCR.....	212
Table A. 2 Reaction mix for mutagenesis.....	213
Table A. 3 MAGI-2 sgRNAs targeting Exon5.....	217

1 Introduction

1.1 Contact inhibition of proliferation

Epithelial tissues, once reaching their adult size, are able to maintain homeostasis by adapting to their environment through a dynamic and fine equilibrium of cell proliferation and cell death. The question of how a sum of individual cells functions as a tissue is particularly interesting as most human solid tumours occur in epithelia. Contact inhibition, discovered over 60 years ago, shed some light on that particular mechanism. Contact inhibition of proliferation occurs when cells establish contacts with one another to form a monolayer, resulting in a substantial decrease in proliferation rate (1,2). Nowadays, it is believed that growth arrest occurs upon reaching a threshold of cell density that may depend on number cell-cell and cell-matrix contacts as well as a reduced cell area (3). If crowding continues due to cell division, it may lead to fewer cell-matrix contacts than neighbours and promote cell extrusion (4,5). Loss of this paramount contact inhibition is often found in cancers.

One of the signalling pathways that have been reported to be involved in the control of organ size and cell proliferation in response to cell density is the Hippo cascade (6-8).

1.2 The Hippo signalling pathway

1.2.1 Canonical Hippo pathway

*1.2.1.1 Discovery of the pathway in *Drosophila**

The Hippo pathway was first identified in *Drosophila melanogaster* as a signal transduction pathway regulating organ size (6,7). A kinase cascade composed of Hippo (9-13) and Warts (6,7) together with the Sav (14,15) and Mob (16) adaptor proteins regulate the inhibition of the downstream effector Yorkie (**Figure 1.1**) (17). Unphosphorylated Yorkie accumulates in the nucleus where it associates with Scalloped transcription factor to promote cell proliferation and survival (18,19). Upon activation of the kinase cascade by upstream regulators, Warts phosphorylates Yorkie which is subsequently retained in the cytosol and can no longer activate transcriptional programmes (20).

1.2.1.2 The core Hippo pathway is conserved in mammals

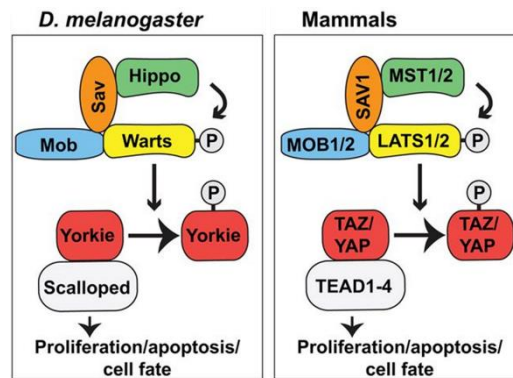


Figure 1.1 | Conservation of the core Hippo pathway across species.

The core kinase cascade and the downstream effectors are highly conserved between *D. melanogaster* and mammals. Adapted from Figure 1 of (21).

The core cascade and downstream effectors are highly conserved in mammals (**Figure 1.1**) (20). However, the pathway became more complex with evolution. Indeed, many players in *Drosophila* have two or more homologues in mammals (22). In mammals, the kinase cascade involves mammalian STE20-like kinase 1/2 (MST1/2) and large tumour suppressor 1/2 (LATS1/2) (23). Upon activation by upstream regulators, MST1/2 phosphorylate the scaffolding proteins SAV1 and MOB1 (24,25) to help recruiting and phosphorylating LATS1/2 (26). Interestingly, key players of the Hippo pathway have been reported to be activated upon membrane targeting: LATS1 (26,27) and MST1 (28). The plasma membrane was therefore suggested to be a critical subcellular compartment for signal transduction via the Hippo pathway. The physiological outcome of this cascade is the inhibition of the two key downstream effectors, Yes-associated protein (YAP) (29) and transcriptional coactivator with PDZ-binding motif (TAZ) (30), by LATS-mediated phosphorylation and subsequent cytoplasmic retention (31). When in the nucleus, YAP/TAZ bind to transcription factors such as TEADs (32). Phosphorylation of YAP Ser127 (or TAZ Ser89) by the LATS kinases uncovers a 14-3-3 binding site resulting in their cytoplasmic sequestration (8,20,30,33).

1.2.1.3 YAP/TAZ, transcriptional co-activators

YAP and TAZ are the downstream effectors of the Hippo signalling pathway. Active YAP/TAZ translocate and accumulate in the nucleus to fulfil their role of transcriptional coactivators. As they do not possess DNA-binding domains (**Figure 1.2**) they need to associate with transcription factors to regulate gene expression. TEAD1-4 play a major role in mediating the biological output of the Hippo-YAP pathway (18,19,32,34-36) by inducing expression of

many genes involved in cell proliferation, growth and survival (20,32,37-39). Dysregulation of TEADs has been linked to tumorigenesis (40). Elevated expression of TEADs is often found in cancers (41,42). The transforming potential of the TEAD transcription factors depends on their ability to bind to YAP (43).

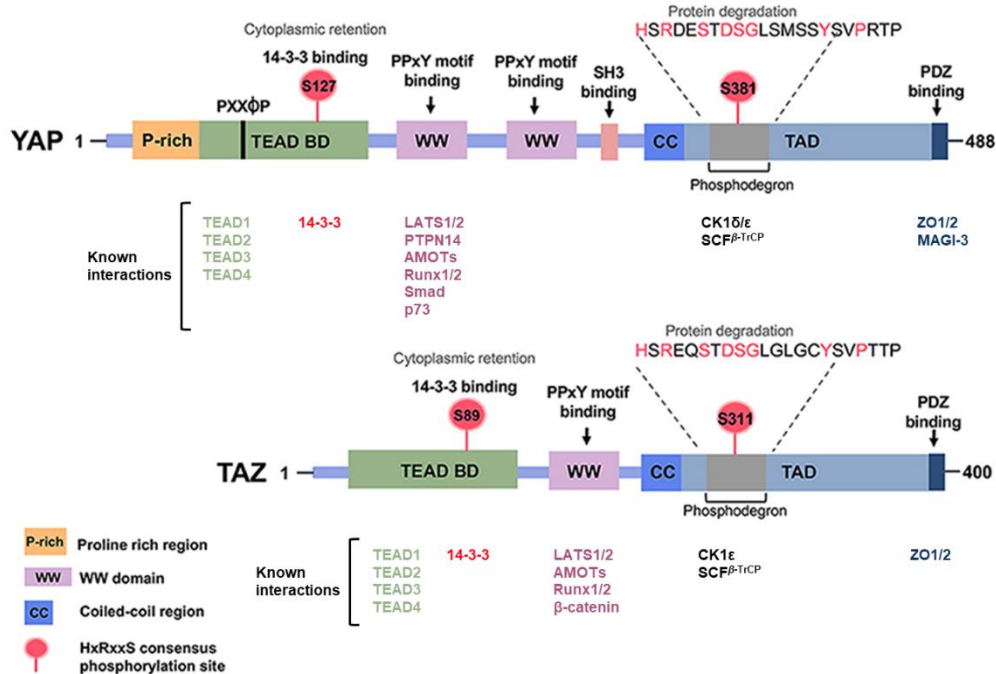


Figure 1.2 | Domain structures of YAP and TAZ, downstream effectors of the Hippo pathway.

Both paralogues possess similar domain structures with a TEAD binding domain (BD), WW-domain(s), an SH3 binding site, a coiled-coil domain (C-C), a transcriptional activation domain (TAD) and a PDZ-binding motif. Some of the known binding partners are indicated below each domain. YAP and TAZ possess five and four HxRxxS consensus sequences for LATS phosphorylation respectively. Only the main two, linked to their inhibition, are represented. Ser127 (Ser89 in TAZ) phosphorylation status regulates binding to either TEAD transcription factors or the 14-3-3 cytoplasmic anchor. Additional phosphorylation of YAP/TAZ on Ser381 (Ser311 in TAZ) in the phosphodegron induces subsequent ubiquitination and degradation by the SCF^{β-TrCP} ubiquitin ligase. Adapted from Figure 3 of (44,45).

YAP and TAZ have also been shown to activate other transcription factors such as p73 (46), Runx2 (47,48) and SMADs (46,49-51) in specific cellular contexts. Interaction of YAP/TAZ with these transcription factors is mediated via the WW domains and are not disrupted by LATS-mediated phosphorylation of YAP Ser127 residue (Ser89 in TAZ).

1.2.1.4 YAP WW domains tandem and cognate motifs

One of YAP interaction modules is a WW domains tandem (**Figure 1.2**). A WW domain contains approximately 40 amino acids with two signature tryptophan (W) residues. These domains have a high affinity for proline-rich regions and are sorted into different classes

depending on their cognate motifs (52,53). YAP and TAZ possess two and one WW domains respectively, which belong to Class I associated with [L/P]PxY ligands (where x is any amino acid) (54,55). WW domains represent a versatile platform to a vast repertoire of putative interactors harbouring proline-rich motifs (56). WW-[L/P]PxY are particularly recurrent interactions within the Hippo pathway and contribute to signal transduction. Indeed, these modules link YAP to transcription factors, as mentioned in the previous section, as well as to upstream regulators of the pathway. For instance, the LATS kinases possess PPxY motifs and interact with YAP via its WW domains (31,57-59) to exert their negative regulation through phosphorylation of YAP Ser127 residue (8,20,31).

1.2.2 Complex layers of YAP regulation

YAP and TAZ control critical transcriptional programmes which, if executed at the wrong time and place, can lead to the formation of cancer. It is therefore paramount that their activity be tightly regulated by an intricate network of proteins that transduce external cues to the Hippo cascade. Among the upstream regulators of the pathway are found junctional and polarity proteins, mechanotransduction through the actin cytoskeleton as well as extracellular signalling. Furthermore, other signalling pathways, such as Wnt and GPCRs, have been shown to crosstalk with the Hippo pathway and impinge on YAP/TAZ regulation (60,61).

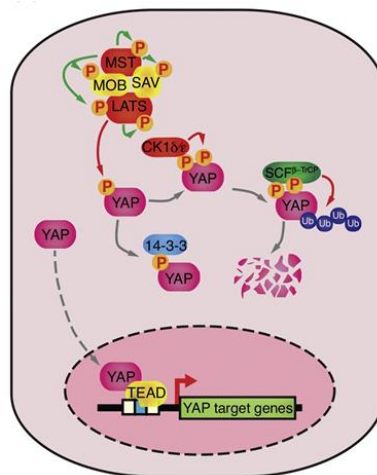


Figure 1.3 | LATS-mediated phosphorylation of YAP induces cytoplasmic retention and degradation.

YAP accumulates in the nucleus to promote transcription of target genes through binding to the TEAD transcription factors. Upon activation of the core Hippo cascade, MST1/2 phosphorylate the Sav1 and MOB1 adaptor proteins to help activate the LATS1/2 kinases. LATS in turn phosphorylate YAP on Ser127 which promote cytoplasmic sequestration by the 14-3-3 protein. Additional phosphorylation by the CK1δ/ε kinase induces YAP degradation via the SCF^{β-TrCP} ubiquitin ligase. Figure 1b of (45,62).

Many upstream signals converge at the activation of the LATS1/2 kinases and subsequent YAP/TAZ Serine phosphorylation. As mentioned previously, phosphorylation on YAP Ser127 (Ser89 in TAZ) creates the consensus binding sequence of the 14-3-3 protein (8,20,30,33) which results in their cytosolic retention (**Figure 1.3**). LATS-mediated phosphorylation of an additional serine, YAP Ser381 (Ser311 in TAZ), induces additional phosphorylation by the CK1 kinase thereby creating a “phosphodegron” recognised by the β -TrCP adaptor protein of SCF E3 ubiquitin ligase (**Figure 1.3**) (63,64). Endogenous YAP is relatively stable contrary to TAZ which half-life is less than 2hrs (64), indicating that the aforementioned degradation route may play an important role in TAZ’s inhibition.

In recent years, the Hippo signalling pathway has become more complex than the initially reported canonical and binary model (**Figure 3.22**) where phosphorylated YAP Ser127 triggers its cytoplasmic exclusion by binding of the 14-3-3 protein (8). The picture depicted nowadays is that of a more dynamic and constant nucleocytoplasmic shuttling of YAP/TAZ. Up until recently, YAP/TAZ were not known to bear any nuclear localisation or export signals (NLS and NES respectively) and were reported to need other proteins, such as ZO-2 (65) or Nf2 (66) for nuclear/cytoplasmic translocation. Kofler and co-workers identified non-canonical NLS and NES in TAZ that are conserved in YAP (67). They propose an updated model where YAP/TAZ subcellular translocation and localisation are regulated by nuclear import and export rates. Phosphorylation of YAP Ser127 still conserves its important role in the regulation of the protein. Indeed, Ser127 is located in the TEAD-binding domain which upon phosphorylation uncovers the 14-3-3 binding site (8,30,33). In parallel, many studies have reported cytoplasmic anchors that bound to YAP independently of its Ser127 phosphorylation status, for example mediated by its PDZ-binding domain or WW-tandem (68-79).

YAP and TAZ have largely overlapping functions but also exhibit specificities in their binding partners and activity (80,81). This work will mainly focus on YAP regulation and function.

In the past two decades, extensive research has been carried out to understand the mechanisms of YAP regulation. One of the outstanding questions of the field is whether the upstream events occur in parallel or are interdependent. Here, we describe those related to cell density sensing and contact inhibition.

1.2.2.1 Regulation of YAP/TAZ by junctional complexes

1.2.2.1.1 Epithelial barrier and cell-cell junctions

Epithelial cells assemble into polarised sheets with a basal side attached to a basal lamina, which provides an interface with the underlying tissue, and an apical surface that usually faces an extracellular fluid. Epithelial tissues constitute a highly selective physical barrier against pathogens, toxins and unwanted molecules. On one hand, most substances that go through the epithelial layer enter the cells by active transport or diffusion. On the other hand, paracellular transport allows some small molecules and ions to go through the epithelial layer by passing in between cells. The extent of the paracellular transport is tissue-specific and depends on the composition of tight junctions; its measurement provides information on the barrier integrity of an epithelium which is often compromised in diseases such as cancer.

Adjacent epithelial cells are attached to their neighbours through several junctions, namely tight junctions, adherens junctions, desmosomes and gap junctions (**Figure 1.4**). This ensures continuity of the cell monolayer and barrier function in epithelial tissues while allowing cells to communicate with one another.

Adherens and tight junctions allow apical-basal polarisation which consists in an asymmetrical distribution of proteins and lipids along the plasma membrane. The apical surface faces the lumen and controls the exchange of biological molecules whereas the basolateral membrane allows cell-cell and cell-matrix interactions. Both tight and adherens junctions are linked to the actin cytoskeleton (82) and signalling cascades. Tight junctions' main components are the Claudins, Occludin and JAMs (junctional adhesion molecules) transmembrane proteins which associate with many MAGUKs such as the Zonula Occludens (ZO-1/2/3) membrane associated proteins, in a PDZ (PSD-95/Dlg/ZO-1)-dependent manner (82-86). Together, they ensure proper function and selectivity of the epithelial barrier (87,88). Adherens junctions involve cadherin-catenin and nectin complexes. Establishment of tight junctions depends on adherens junctions and *vice versa* (89). In adherens junctions, E-cadherin molecules form intercellular homophilic bonds, linking neighbouring cells. E-cadherin interacts with β -catenin which binds to α -catenin, an actin-binding protein (90,91). Nectins provide another link to the actin cytoskeleton through binding of afadin (92).

Gap junctions connect the cytoplasm of adjacent cells to allow regulated exchange of ions and molecules. Desmosomes associate adhesion complexes to intermediate filaments.

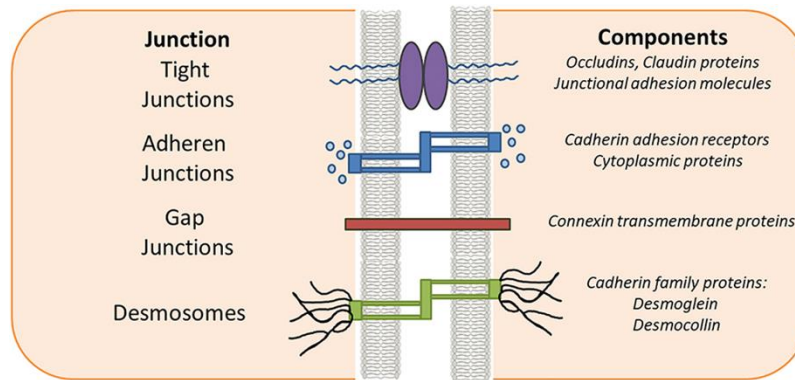


Figure 1.4 | Four types of epithelial intercellular junctions.

Figure 1 of (45,93).

1.2.2.1.2 Cadherin-catenin complex affects YAP localisation

Adherens junctions and in particular the cadherin-catenin complex have been shown to activate the Hippo cascade and be involved in contact inhibition of proliferation (80,94-97). Formation of the intercellular E-cadherin homophilic bonds promotes LATS-mediated phosphorylation of YAP and subsequent cytoplasmic retention (97). This role in the activation of the Hippo-LATS activation is dependent on the interaction of E-cadherin with α - and β -catenins (97,98). However, the link between the cadherin-catenin complex and the Hippo signalling is not fully understood. E-cadherin ligation is required for the establishment of tight junctions in epithelial cells (99-103). Moreover, α -catenin provides a link to the cytoskeleton (90). E-cadherin's role in activating the Hippo cascade might therefore be indirect via tight junctions associated proteins, such as Merlin or Kibra (97) and/or via the actin cytoskeleton which are known to play a role in the Hippo pathway regulation (described below).

1.2.2.1.3 PTPN14, negative regulator of YAP

The non-receptor tyrosine phosphatase PTPN14 has been shown by many groups to regulate, both directly and indirectly, YAP subcellular localisation (71-75). PTPN14 is involved in maintaining adherens junctions by stabilising, via dephosphorylation, β -catenin (104,105). It is also necessary for the formation of tight junctions in epithelial cells (104). PTPN14 involvement in the regulation of the Hippo pathway is complex. First, in a phosphatase-independent manner, PTPN14 was found to associate with YAP WW domains and inhibit its nuclear localisation at high cell density (71-75). Second, PTPN14 has also been shown to stabilise and activate LATS1, independently of the MST upstream kinases, and thereby promote YAP phosphorylation (72,75). Moreover, activation of LATS1 by PTPN14 can occur cooperatively

with Kibra. Indeed, Wilson et al. suggest that PTPN14, Kibra and LATS1 form a tripartite complex to efficiently activate LATS1 and promote subsequent YAP phosphorylation (75).

PTPN14 role in the Hippo-YAP pathway is thought to be cell density-dependent (71,72,74). However, the mechanism activating PTPN14 remains unclear. Wang and co-workers showed, in MCF10A breast cancer cells, that PTPN14 is kept at low abundance at low cell density by the CRL2_{LRR1} E3 ligase complex. Interestingly, they found that the protein levels of the LRR1 adaptor necessary to specifically target PTPN14 for degradation, were decreasing with cell density (74). This mechanism of regulation may be tissue specific as Furukawa and collaborators found similar PTPN14 levels in sparse and dense MDCK cultures (66).

1.2.2.1.4 Kibra activates the Hippo cascade

Kibra is a WW-containing protein. It was linked to the Hippo pathway in *Drosophila* where it was shown to form a complex with the Merlin and Expanded proteins at the apical surface to activate the pathway via Hpo (MST1/2 homologues) and Warts (LATS1/2 homologues) kinases (106-108). In mammals, Xiao and co-workers found Kibra to interact with the LATS1/2 kinases through its WW domains and promote their autophosphorylation and activation, independently of the MST1/2 upstream kinases. This resulted in YAP Ser127 subsequent phosphorylation by LATS (109). Wilson's team corroborated the role of Kibra in the activation of the LATS cascade and showed that it can act cooperatively with PTPN14, as described above (75). Kibra was also found to shield LATS2 from ubiquitination. To add another layer of regulation, Kibra is a transcriptional target of YAP (109).

1.2.2.1.5 Nf2/Merlin translocates YAP from nucleus to cytoplasm

Nf2 gene encoding the Merlin protein localises at and stabilises adherens junctions where it interacts with E-cadherin and F-actin (110-112). Merlin acts as a tumour-suppressor, upstream of the Hippo cascade to regulate contact inhibition of proliferation (113,114). Merlin can activate directly the MST1/2 kinases (106,115,116) or recruit LATS1/2 to the plasma membrane for activation by MST1/2 (27). Up until recently, the mechanism activating Merlin role in the Hippo pathway remained unknown. Two studies shed some lights on potential mechanisms of regulation of Merlin activation.

Li and collaborators found that Merlin is in an auto-inhibitory conformation that masks the LATS-binding site located in its FERM domain. The AMOT protein binds to Merlin C-terminal domain and thereby releases its dormant conformation, allowing subsequent

interaction with the LATS kinases. Phosphorylation of Ser518 on the C-terminal tail of Merlin, partially due to PAK-1 kinase, weakens AMOT binding. They suggest that AMOT acts upstream and activates the Merlin route via a Ser518 phosphorylation-dependent mechanism to relay cell-cell contact cues (117).

Furukawa and co-workers identified another mechanism of Merlin regulation. Several groups reported Merlin to shuttle between nucleus and cytoplasm and to have functions in the nucleus (118-120). Furukawa and collaborators show that Merlin's exit from the nucleus is involved in suppressing YAP nuclear localisation by direct interaction. They propose that, at high cell density, contraction of the actin circumferential belt provokes a remodelling of the adherens junctions and results in Merlin being released from its E-cadherin interaction. Then, Merlin enters the nucleus where it binds to YAP and the complex exits the nucleus (66).

1.2.2.1.6 The AMOT family, dual regulators of YAP

The AMOT family of proteins is composed of angiomin's (AMOT) two isoforms p80 (80kDa) and p130 (130kDa) as well as angiomin-like-1 (AMOTL1) and angiomin-like-2 (AMOTL2). All members have tissue and cell-specific expression patterns. AMOT proteins localise at tight junctions (76,121-124), bind to F-actin (78,125-128) and have been found in the nucleus (129-132). Literature agrees that AMOT proteins are upstream regulators of the Hippo-YAP pathway. However, despite extensive research, discrepancies arise on their positive or negative regulation of YAP. Consequently, it is not clear whether AMOTs act as oncogenes (130,133) or tumour-suppressors (134-136).

Negative regulators of YAP: Several mass spectrometry studies have shown the interaction of AMOTs with both LATS1/2 and YAP (76,77,95,137-139). AMOT p130, AMOTL1 and AMOTL2 were reported to act as scaffolds to promote LATS activation and subsequent phosphorylation of YAP Ser127 (140,141). The AMOT family members are substrates of the LATS kinases and phosphorylation has been shown to disrupt their binding to F-actin (78,96,126,142). Li and al. suggest that LATS-mediated phosphorylation of AMOT and subsequent release from the cytoskeleton is the trigger for Merlin binding and activation (as discussed above) (117). Another study showed that upon phosphorylation, AMOT formed a complex with the AIP4 ubiquitin ligase leading to the degradation of YAP (126,142-144). AMOT is also reported to directly sequester YAP to the cytoplasm and specific cellular compartments such as tight junctions (76) and cytoskeleton (76-79). However, the AMOT-mediated cytoplasmic retention can occur independently of YAP Ser127 phosphorylation suggesting that AMOT and the Hippo pathway may have both overlapping and separate roles in YAP inhibition (76,77,138).

Positive regulators of YAP: Others describe AMOT and AMOTL1 as YAP cofactors which facilitate its nuclear entry and promote cell proliferation in certain tissues (78,96,131,142,145-147). In addition, AMOT interaction with YAP antagonises the LATS-YAP interaction and thereby prevent its inhibitory phosphorylation (131,133).

Several studies highlighted the importance of Ser175 of AMOT p130, residue phosphorylated by the LATS1/2 kinases, as modulating its function towards YAP (78,96,126,140,143,145). Moleirinho and collaborators depict phosphorylation of the Ser175 residue of AMOT p130 as a key event controlling its positive or negative role on YAP by regulating AMOT subcellular localisation (145). Overall, the interplay between AMOT p130, LATS1/2, YAP and potentially other proteins such as Merlin is complex and convoluted. Further studies are required to sort the various functions of the Motin family in the regulation of the Hippo-YAP pathway.

Interestingly, it was shown recently that YAP uses a negative feedback loop to activate the Hippo pathway. YAP-TEAD complex directly binds to LATS2 and AMOTL2 promoters and induces their transcription to normalize YAP activity (148-150). Negative feedback loops are common in signal transduction as they partially ensure low noise and prevent signal fluctuation.

1.2.2.1.7 ZO-2 exerts both positive and negative roles on YAP in a density-dependent manner

Zonula occludens 2 is a scaffolding protein localised at tight junctions which contains three PDZ domains. ZO-2 possesses several nuclear localisation and export signals (NLS and NES respectively) indicating a role in the nucleus (151,152). Indeed, ZO-2 was found to associate with, in a PDZ-dependent manner, and promote nuclear localisation of YAP (65). ZO-2 localisation was found to be cell-density dependent: ZO-2 is nuclear in subconfluent, proliferating cells and TJ-associated in confluent monolayers (153-156). This nuclear-cytoplasmic translocation relies on a number of post-translational modifications. A recent study, published in BioRxiv, suggests a role of ZO-2 in YAP nuclear exclusion in response to cell density cues. They show that ZO-2 recruits LATS1/2 to tight junctions in dense cells and acts as a scaffold to bring together angiominin, Merlin and YAP to activate the LATS1/2 kinases which results in YAP inhibition (69).

1.2.2.2 Regulation of YAP/TAZ by apical-basal polarity

Proper apical-basal polarisation of epithelial cells has been reported to be important for suppression of YAP activity upon high cell density conditions. Three complexes involved in the maintenance of apical-basal polarity are organised around the proteins SCRIB (Scribble), CRB (Crumbs) and PAR (Partitioning defective).

1.2.2.2.1 The SCRIB lateral complex activates the Hippo cascade

The SCRIB complex is composed of Scribble, Discs large (Dlg) and lethal giant larvae (Lgl) and is localised along the basolateral membrane (157,158). The membrane-localised Scribble protein serves as a scaffold to assemble MST1/2, LATS1/2 and TAZ and activate the kinase cascade (159). It was later found that LBK1 stabilises this complex at the plasma membrane via its substrate Par-1 (160). Inactivation or mislocalisation of Scribble is often found in cancer (161-164).

1.2.2.2.2 The CRB apical complex recruits Hippo players for activation of the kinase cascade

The CRB complex features the transmembrane protein Crumbs-3 (165-167) as well as two cytoplasmic proteins PALS1 and PATJ (168) and is localised at the apical membrane and tight junctions of polarised epithelial cells. CRB had been shown to integrate and relay density cues by interacting with YAP/TAZ and promoting their inhibition through LATS-mediated phosphorylation and cytosolic retention (95). Recently, Mao and colleagues reported that CRB complex functions upstream of the Hippo cascade by recruiting other players such as Kibra (169).

1.2.2.2.3 The PAR apical complex activates YAP at low cell density

The PAR complex is composed of PAR3, PAR6 proteins and atypical protein kinase C (aPKC) and is localised at tight junctions (170). PAR3 was recently reported to have a dual effect on YAP. At low cell density, PAR3 co-localised with YAP in the nucleus where it assembles LATS1 and protein phosphatase subunit A (PP1A), promoting inactivation of LATS and resulting in activation of YAP. At high cell density, the PAR3-YAP complex was predominantly localised at the plasma membrane. These studies suggest that PAR3 is an upstream regulator of the Hippo pathway primarily implicated in YAP/TAZ activation in sparse culture (171,172).

1.2.2.3 Regulation of YAP/TAZ by mechanical forces

In epithelial tissues, cells are subjected to constant mechanical stimuli from neighbouring cells such as pulling forces and pressure. Cells adapt and remodel their cytoskeleton to balance external forces (173-175). It has now become clear that cells are able to translate their physical environment, i.e. external mechanical cues and cytoskeleton status, into biochemical signals via mechanotransduction pathways to make crucial decisions regarding proliferation, survival, differentiation (176-179). Interestingly, mechanical stimuli constitute a fundamental input on YAP/TAZ regulation. YAP/TAZ have therefore emerged as mechanotransducers (180,181), integrating mechanical cues such as cell shape, extracellular matrix stiffness, cell adhesion..., all of which influence remodelling of the actin cytoskeleton architecture (182-184). The actin cytoskeleton is a key regulator of YAP, yet whether through Hippo-dependent (185-187) or –independent routes (180,188) is still subjected to debate. It is important to note that YAP/TAZ subcellular localisation and therefore transcriptional activity require an intact and structured actin cytoskeleton irrespectively of the upstream inputs: Hippo, Wnt, GPCR signalling (189).

The mechanisms at play during CIP appear complex and in some contexts do not require the Hippo upstream kinases (70,190). Several studies underlined the significance of cells physical properties such as cell spreading and extracellular matrix (ECM) stiffness to regulate YAP/TAZ activity (180,186,188). Even though the activity of the core Hippo pathway is sensitive to mechanical cues, it is overridden by cytoskeleton signalling to regulate YAP/TAZ in some physiological contexts (**Figure 1.5**). For example, stretching of a confluent monolayer forces YAP back into the nucleus instead of its usual cytoplasmic inactive state (**Figure 1.5f**) (8,188). Another example is the cytoplasmic localisation of YAP in single cells cultured on small adhesive areas or on soft extracellular matrices (**Figure 1.5b and c**) (180,188). However, the mechanism by which F-actin cytoskeleton modulates YAP and TAZ activity remains elusive. It was postulated that mechanical cues are actually tuning the cells' response to Hippo, Wnt and GPCR signalling. Aragona et al. proposed an alternative model for contact inhibition of proliferation: as cells start establishing contacts with one another, junctional proteins trigger LATS activation and as a consequence YAP Ser127 phosphorylation. They estimated that this phenomenon only accounts for about 30% of growth inhibition and YAP/TAZ cytoplasmic translocation. A second, mechanical, input is required: as proliferation slowly goes on, cells eventually get boxed into smaller areas which induces remodelling of the actin cytoskeleton and fully triggers growth arrest (188).

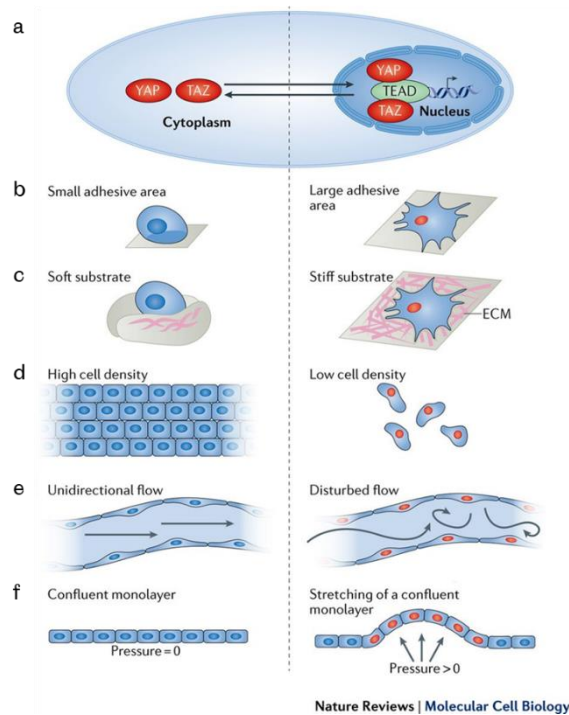


Figure 1.5 | Mechanical cues affect YAP subcellular localisation and activity.

Schematic representation of mechanical stimuli inducing (Left) cytoplasmic localisation and inhibition or (Right) nuclear localisation and activation (Red) of YAP. Adapted from Figure 1 of (191). b, (180,188). c, (180,188,192-199). d, (8,188). e, (200-204). f, (98,188).

1.2.3 Regulation of the Hippo pathway players by post-translational modifications

In recent years, researchers have been showing that posttranslational modifications are essential to regulate the Hippo signalling pathway (205). In particular, ubiquitination and subsequent degradation have emerged as a crucial regulatory mechanism for the players of the Hippo pathway. In this section, we focus on the stability regulation of a few key components of the Hippo pathway.

1.2.3.1 *PTPN14*

PTPN14 has been reported to have a negative effect on YAP activity, either by direct interaction (72,74) or through stabilisation and activation of the LATS1 kinase (75). However, the mechanism activating PTPN14 remained unclear. Wang et al. showed that PTPN14 protein level is regulated by an E3 ligase complex: CRL2^{LRR1} (74). Interestingly, they found that the abundance of the adaptor protein, LRR1, necessary to specifically target PTPN14 for degradation, was changing with cell density. Indeed, the study shows that in sparse cultures, LRR1 is stable and promotes PTPN14 CRL2^{LRR1}-mediated degradation. However, in confluent

cells, LRR1 levels are significantly reduced while PTPN14 stability is increased. They therefore provided a model by which PTPN14 is regulated by cell density and activates the Hippo pathway accordingly.

In *Drosophila*, the homologue of PTPN14, Pez, was reported to be degraded by Suppressor of Deltex (Su(dx)), a member of NEDD4 (neural precursor cell-expressed developmentally downregulated gene 4) E3 ligase family (206). Their study shows that PTPN14 can be rescued from Su(dx)-mediated degradation via interaction with Kibra, another upstream regulator of the Hippo pathway. This phenomenon was reported to rely on WW domain-PPxY motifs interaction which suggests an interesting model of regulation of protein stability driven by WW-PPxY binding. In the mammalian system, this mechanism is partly conserved. PTPN14 stability was shown to be regulated by WWP1 (WW domain containing E3 ubiquitin protein ligase 1), a NEDD4-like E3 ligase and human homologue of Su(dx). However, WWP1-mediated degradation of PTPN14 could not be rescued by WWC1 (WW containing protein 1), Kibra human homologue (206), although interaction between the two latter proteins is conserved in human (75). This opens the possibility for another WW-domain containing protein to fulfil this role in mammalian cells.

1.2.3.2 LATS1/2 kinases

NEDD4 E3 ligase family was reported to play an important role in the regulation of several key players of the Hippo pathway and for its activation at high cell density (207). In sparse cells, NEDD4 mediates LATS kinases degradation which ensures inhibition of the pathway. However, in confluent cells, NEDD4 becomes deactivated, promoting LATS stabilisation and subsequent activation of the Hippo pathway. They demonstrated that activation of the Hippo pathway in response to cell density relies on the changes in NEDD4 E3 ligase activity itself. The reasons for the activation/deactivation of NEDD4 are not fully understood yet. It was suggested that the protein is auto-inhibited by intramolecular interaction between domains, dependent on calcium levels (208). Another potential explanation is that NEDD4 stability is governed by another E3 ligase, namely SCF ^{β -TRCP} (209). Interestingly, this ubiquitin ligase is also the one responsible for YAP degradation following activation of the Hippo pathway (63,64).

Overall, these studies suggest a tight regulation of the key players of the Hippo pathway governed by a degradation/stabilisation competing mechanism. However, the phenomena

shifting the outcome toward activation or inhibition of the Hippo pathway remain to be elucidated.

1.2.4 Role of YAP/TAZ in tissue homeostasis and cancer

YAP/TAZ induce essential cell processes involved in tissue homeostasis: cell proliferation, epithelial to mesenchymal transition (EMT) (48,210,211), cell survival (59,137,212) and stem cell maintenance (213,214). The Hippo-YAP pathway tightly regulates these crucial processes during development, morphogenesis and wound healing. However, these functions also represent hallmarks of cancer in which contact inhibition of proliferation is usually lost. YAP has therefore emerged as a powerful oncogene over the years while most players of the Hippo pathway appear as tumour suppressors. Indeed, many studies linked human cancerous behaviour and neoplasia to dysregulation of the Hippo pathway or hyperactivation of YAP/TAZ (20,37,215-217). In various human cancers, YAP nuclear levels are elevated (**Table 1.1**).

Table 1.1 | YAP is upregulated in several types of cancers. Table from (218).

Cancers	Cases (n)	Upregulated (%)	References
Colorectal cancer	168	72.6	(Wang et al., 2013)
Lung cancer	40	70	(Su et al., 2012)
Breast cancer	69	75.4	(Wang et al., 2012)
Gastric cancer	78	69.23	(Zhang et al., 2012)
Ovarian cancer	68	94	(Steinhardt et al., 2008)
Hepatocellular carcinoma	177	62	(Xu et al., 2009)

The exact mechanisms leading to the transformation of normal cells to malignant tumour cells by dysregulated YAP/TAZ are not yet fully understood. However, the transformation is likely to implicate enhanced cell growth and survival together with the acquisition of additional cancer cell features which are all YAP/TAZ-promoted processes (**Figure 1.6**).

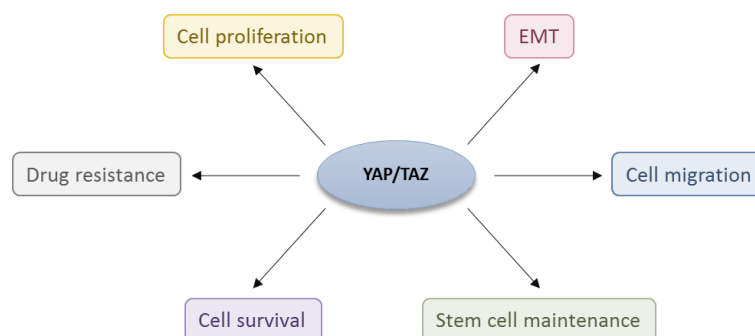


Figure 1.6 | YAP/TAZ output functions are hallmarks of cancer.

The Hippo-YAP pathway has been extensively studied over the past decade as it holds the key to understanding malignant transformation and cancer. Components of the Hippo pathway and regulators of YAP/TAZ have emerged as potential therapeutic targets (218,219), especially kinases which are the most popular and studied class of targets for small-molecule anti-cancer treatment (220).

1.2.5 Towards a better understanding of signal transduction from upstream regulators to the activation of the Hippo core kinase cascade

Despite extensive research on the Hippo-YAP pathway to unravel the mechanisms of regulation, many questions remain unanswered and require additional investigation. The body of evidence gathered until today depicts a highly complex and convoluted pathway with many intricate layers of regulation. One of the outstanding questions of the field regards the mechanisms at play in the signal transduction from upstream regulators, such as tight junctions, to the activation of the core kinase cascade which remains largely elusive.

Mohseni and colleagues identified several proteins of the Hippo pathway kinome, including MAGI-1, a tight junction and multi-PDZ domain scaffolding protein (160), that affected YAP subcellular localisation in a cell density-dependent manner. Using a HEK293T cell line stably expressing an mCherry reporter for Hippo-YAP activity (containing several repeats of the TEAD DNA-binding sequence), they performed a primary siRNA screen of the human kinome. FACS analysis of the mean fluorescence intensity of cells led to the pre-selection of candidate kinases impinging on YAP. A second siRNA screen confirmed that individual knockdown of 16 kinases, including MAGI-1, enhanced YAP activity.

Interestingly, MAGI-1 has been suggested to interact with PTPN14 and LATS1/2 kinases by two large scale proteomics screens (221,222). MAGI-1 is also reported to interact with the Motin family of proteins (223,224). However, the mechanism of MAGI-1 regulation of YAP in a cell density-dependent manner remains to be elucidated.

1.3 MAGI family, multi-PDZ domain and tight junction proteins

1.3.1 A unique structure

Membrane-associated guanylate kinase inverted 1 (MAGI-1) was identified as a new member of the membrane-associated guanylate kinase (MAGUK) family (225). MAGUKs are known to be scaffolding molecules for protein complexes at cell-cell contacts. MAGI-1 presents

an inverted and unique organization of protein-protein interaction domains compared to other typical MAGUKs (**Figure 1.7**): a PDZ-like domain, the GuK domain, a WW-tandem followed by five PDZ domains. Later two other MAGI proteins were identified with a similar domain structure, namely MAGI-2 (also known as S-SCAM - synaptic scaffolding molecule) and MAGI-3 (226,227).

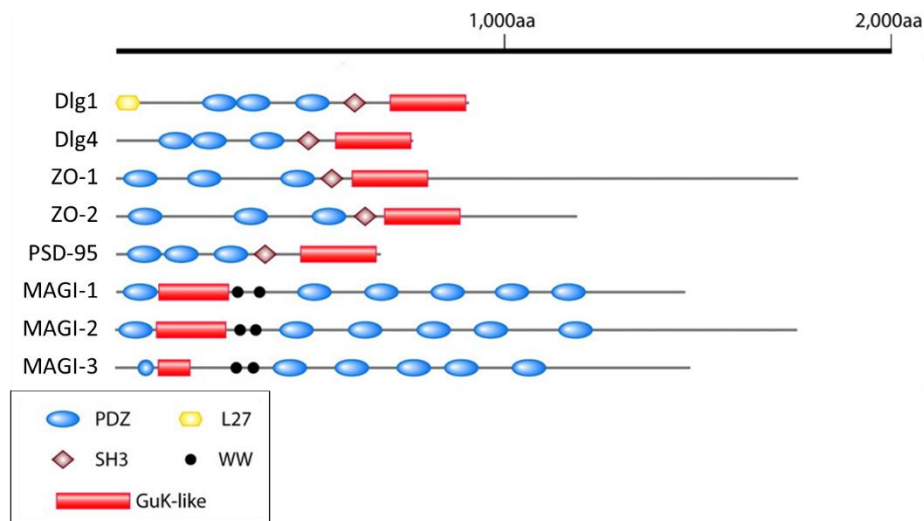


Figure 1.7 | MAGI proteins have an inverted domain organisation compared to other prototypical MAGUKs

Prototypical MAGUK proteins such as Dlg, Zonula occludens (ZO) and PSD-95 possess amino-terminal (multi-) PDZ domains followed by an SH3 domain and a C-terminal Guanylate kinase-like domain (GuK-like). MAGI proteins are MAGUK-inverted which refers to the inverted organisation of their protein domains: the GuK-like domain is located towards the N-terminal, the SH3 domain is replaced by a WW domain-tandem and the C-terminal tail contains multiple PDZ domains. PDZ: repeat of 80-100 amino acids found in PSD-95, DLG and ZO-1. SH3: SRC Homology 3 Domain, WW: short domain with conserved tryptophan residues spaced of 20 amino acids. Adapted from Figure 1 of (45,228).

PDZ domains are named after a repeat of 80-100 amino acids found in three prototypical members of the MAGUK family: PSD-95, DLG and ZO-1. WW domains are named after two characteristic tryptophan residues and were first identified in mouse YAP65 (29). Both WW and SH3 domain functions are similar and have been reported to bind to proline-rich regions (229). The GuK domain is not known to be catalytically active in MAGUK proteins but may rather be a site for protein-protein interactions (230,231) and even a phospho-peptide-binding modules (232).

1.3.2 Splicing variants, subcellular localisation and tissue distribution

1.3.2.1 MAGI-1

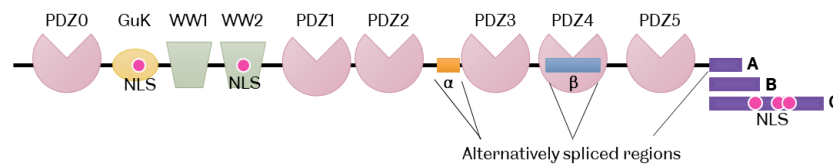


Figure 1.8 | Alternatively spliced regions of MAGI-1.

The C-terminal region of MAGI-1 can be 16, 48 or 251 amino-acids long in isoform A, B and C respectively. The α -region consisting of 29 residues is located between PDZ2 and PDZ3 domains. The β -region corresponds to most of PDZ4 domain. Adapted from (233). NLS: Nuclear localisation signal.

MAGI-1 possesses three splice variants of its C-terminal region leading to isoforms A, B or C (**Figure 1.8**) (225). Two additional alternatively spliced regions were identified: the α and β regions (233). MAGI-1 alternative splicing appears to be tissue specific (**Table 1.2**) (233). MAGI-1C β is the endogenous form present in HEK293, Caco-2 and MDCK cell lines and more generally in epithelial tissues (233,234).

Table 1.2 | Tissue distribution of MAGI-1 alternatively spliced regions. MAGI-1A is highly abundant in the brain and pancreas while MAGI-1B is mostly expressed in epithelial-poor tissues such as brain and heart. Conversely, MAGI-1C was reported to be strongly present in epithelial tissues. Regarding the alternatively spliced regions, α appears to be brain-specific whereas β is ubiquitously expressed. Adapted from (233).

Spliced domains	Colon	Brain	Kidney	Lung	Skeletal muscle	Liver	Pancreas	Heart
A	-	+++	++	-	-	+	+++	+
B	-	+++	-	-	+	-	-	++
C	+++	+	+++	+++	+	+++	+++	+
α	+/-	+++	-	-	-	-	-	-
β	+++	+++	+++	+++	+++	+++	+++	+++

MAGI-1C was then shown to co-localise with ZO-1 at tight junctions in fully polarised cells (233). MAGI-1 interacts with JAM4, junctional adhesion molecule 4, in a PDZ-dependent manner. JAM4 was shown to recruit MAGI-1 to tight junctions in L, enteroendocrine cells (235). MAGI-1 was also identified as part of a tripartite complex with β -catenin and E-cadherin at adherens junctions. Several studies showed that MAGI-1 PDZ5 domain was critical for membrane localisation (233,236,237).

Two nuclear localisation signals (NLS), predicted by PSORTII (234,238), are found in the GuK and WW2 domains respectively and the C isoform C-terminus carries three bipartite NLS (233,239). MAGI-1 mutant expression constructs with either of these domains alone was found

in the nucleus (233,234). However, full length MAGI-1 was only observed in the nucleus in a specific context: abolition of E6 oncoprotein in HPV-positive cells which restored MAGI-1 expression at the plasma membrane as well as in the nucleus (See section 1.3.3.2) (240). No study explaining the potential function of MAGI-1 in the nucleus is available. This suggests that, in most cellular contexts, the signal targeting MAGI-1 to cell-cell junctions (PDZ domains) is likely to dominate over the nuclear localisation signals in the full-length protein.

1.3.2.2 MAGI-2

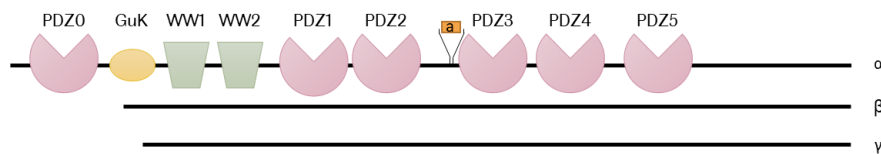


Figure 1.9 | Alternative START codons give rise to three MAGI-2 isoforms.

Two alternative START codons were identified by Hirao and co-workers generating three MAGI-2 isoforms that they named α, β and γ (241). Similar to MAGI-1, MAGI-2 possesses a very short, alternatively spliced, region between its PDZ2 and PDZ3 domains (233).

MAGI-2 protein is predominantly expressed in the brain and kidney. It was first identified in neuronal tissues and called S-SCAM, for synaptic scaffolding molecule, due to its scaffolding role at synaptic junctions (226). The protein counts three isoforms, α, β and γ, arising from two alternative START codons (**Figure 1.9**) (241). Laura and colleagues found an additional alternatively spliced region between PDZ2 and PDZ3 domains, similar to MAGI-1 α region (233). The tissue distribution and function of the two shorter β and γ isoforms is unknown. MAGI-2 is known to localise to tight junctions in epithelial cells such as MDCK. Nuclear staining of MAGI-2 was also observed in some cells but its role has not been investigated (227).

1.3.2.3 MAGI-3

MAGI-3 is ubiquitously expressed and possesses two alternatively spliced regions (**Figure 1.10**). The long C-terminal tail corresponds to isoform a while the shorter one was named b. Interestingly, the other alternatively spliced region, referred to as “*” in this thesis, disrupts the WW domain tandem. The tissue distribution and function of each of the isoforms remains to be elucidated. MAGI-3 has also been reported to localise at tight junctions, at the apical surface and in the nucleus of epithelial cells such as Caco-2 (242).

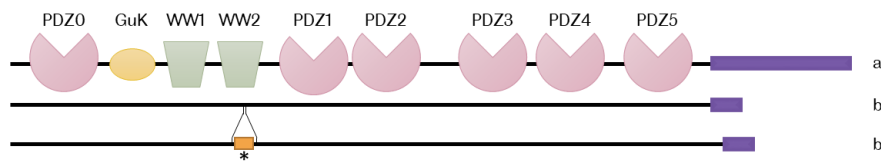


Figure 1.10 | MAGI-3 has two alternatively spliced regions.

The alternatively spliced C-terminal region is either long, a, or short, b. An additional alternatively spliced region, *, disrupts the second WW domain.

1.3.3 MAGIs, scaffolding proteins, involved in tight junction integrity

MAGI proteins display nine protein-protein interaction domains including six PDZ domains. They are believed to be scaffolding proteins assembling junctional complexes, similarly to other multi-PDZ domain proteins (233,243,244).

Drosophila counts one Magi protein, sole homologue of the mammalian MAGI-1/2/3 proteins. Zaessinger and co-workers found that Magi is involved in adherens junctions' remodelling in the late eye development by recruiting Bazooka (Baz, PAR3 homologue) (245). In addition, Barmchi and colleagues showed that Magi and Baz are localised at adherens junctions and antagonise each other for proper localisation of the PAR polarity complex (246). The association of any of the mammalian MAGI proteins with the PAR complex has not yet been investigated. In *C. elegans*, MAGI-1 is required for proper segregation and stabilisation of junctional complexes (247,248).

All three mammalian MAGI proteins have been shown to interact with β -catenin (225,249-251). Gujral and collaborators' data suggest that the interaction of β -catenin with several tight junction proteins, including MAGI-1, contributes to cell-cell contact integrity, favours cell adhesion and prevents cell proliferation and migration (250). Moreover, MAGI-1 overexpression is associated with stabilisation of adherens junctions through E-cadherin and β -catenin recruitment as well as suppression of invasiveness. In contrast, transient knockdown of MAGI-1 resulted in decreased adhesion and a propensity towards migration (252,253).

An important function of the MAGI proteins is the stabilisation of cell-cell contacts, making them prime targets during apoptosis as well as viral infection.

1.3.3.1 *MAGI-1 in apoptosis*

MAGI-1 was found to interact via its PDZ2-PDZ3 domains with RASSF6, a tumour suppressor that induces apoptosis via both caspase-dependent and -independent pathways (254). RASSF6 had been previously shown to inhibit MST1/2 kinases and crosstalk with the Hippo pathway to induce apoptosis (255).

During apoptosis, MAGI-1 is the target of caspase-3 and -7 cleavage (256,257). It was later found that, in MDCK cells, the N-terminal cleavage product translocates to the cytoplasm while the C-terminal part accumulates in the nucleus (257). However, only minor pro-apoptotic activity was shown by MAGI-1 caspase cleavage products suggesting a passive role in apoptosis. MAGI-1 cleavage, most likely disrupting many MAGI-1-mediated interactions, appeared to be a crucial step in dismantling cell-cell junctions in early onset apoptosis (256).

1.3.3.2 *MAGI proteins targeted by viral oncoproteins*

Two adenoviruses oncoproteins, namely adenovirus type 9 (Ad9) E4-ORF1 and high-risk human papillomavirus (HPV) E6, display tumorigenic potential (258-260) and have been shown to interact with MAGI-1 in a PDZ-dependent manner (261). The adenovirus E4-ORF1 has been found to aberrantly sequester MAGI-1 in the cytoplasm (261). High-risk human papillomavirus (HPV) types 16 and 18 target MAGI-1 and induce its proteasome-mediated degradation which leads to the disruption of tight junctions (240,261,262). Knockdown of E6 or overexpression of a MAGI-1 mutant inhibiting its interaction with E6 in HeLa cells (HPV-positive cervical cancer cell line) drives tight junctions reassembly and induces growth arrest and apoptosis (240,263).

MAGI-2 and MAGI-3 proteins were also reported to be targeted by the E6 oncoprotein for degradation (264).

1.3.3.3 *MAGIs role in epithelial barrier integrity*

It was reported that knockdown of MAGI-1 induced a slight but significant decrease of trans-epithelial electrical resistance (TEER), used to assess the leak-tightness of a monolayer (265). In addition, patients suffering from Microscopic colitis (266) or inflammatory bowel disease (267) have been shown to have lower MAGI-1 and MAGI-3 expression levels respectively. In both diseases, the epithelial paracellular permeability is increased.

Single-nucleotide polymorphisms (SNPs) in MAGI-2 introns have been found to correlate with inflammatory bowel disease (IBD) (268-270), especially rs2160322 in intron6.

One of the characteristics of this disease is a compromised intestinal epithelial barrier. The same SNP, namely rs2160322 in MAGI-2 intron6, has been found to correlate with Graves' disease susceptibility (271). Graves' disease is an autoimmune disorder that induces hyperthyroidism. Jia and collaborators suggest that abnormal expression of MAGI-2 may cause dysfunction in the epithelial barrier function (271). Increased permeability of the gut is thought to be a common factor in the development of several autoimmune and inflammatory conditions (272,273).

Together these reports point at an important role of the MAGI proteins in the maintenance of tight junction and barrier integrity.

1.3.4 MAGIs in cancer signalling

MAGI proteins have emerged as tumour suppressors (274). Here we review key roles of these multi-PDZ domain proteins in suppressing malignancy.

1.3.4.1 *MAGIs suppress Akt signalling through interaction with the PTEN tumour suppressor*

MAGI-1 was identified as an adaptor molecule between the PTEN tumour suppressor and β -catenin in E-cadherin junctional complexes (253). MAGI-1 recruits PTEN to adherens junctions which reduces PI3K/Akt signalling and was shown to revert invasiveness in MDCKts-src cells. TRIP6, thyroid receptor interacting protein 6 was later identified as a novel binding partner of the MAGI-1/PTEN signalosome. Depending on the physiological context, TRIP6 may compete with β -catenin to bind the MAGI-1/PTEN signalosome, via MAGI-1 PDZ5 domain, resulting in the destabilisation of E-cadherin junctional complexes and cell invasiveness through activation of Akt/NF- κ B signalling pathways (275).

MAGI-2 has been reported to stabilise PTEN through maintaining its interaction with β -catenin (276,277). Similar to MAGI-1, MAGI-2 binds to PTEN (278) promoting suppression of Akt signalling (227), cell proliferation and migration in human hepatocarcinoma cells (279). Interestingly, Vazquez and collaborators found that phosphorylation of PTEN tail caused a conformational change, masking its PDZ-binding motif and therefore inhibiting its interaction with MAGI-2, and probably other PDZ-containing proteins (280). The kinase responsible for the phosphorylation of PTEN tail has been shown to be CK2, casein kinase 2 (281). CK2 has been reported to be activated by Wnt signalling (282).

MAGI-3 has also been shown to interact with PTEN and indirectly downregulate Akt signalling. It was proposed that MAGI-3 brings PTEN to specific subcellular locations where Akt

is activated (283). In glioma cells, MAGI-3 is downregulated compared to normal brain tissue and its expression levels are positively correlated with that of PTEN. Overexpression of MAGI-3 leads to the inactivation of the PI3K/Akt pathway, through PTEN, and subsequent suppression of proliferation (284). Interestingly, MAGI-3, in glioma cells, is also associated with negative regulation of Wnt signalling via sequestration of β -catenin out of the nucleus, thereby inhibiting its transcriptional activity (251).

1.3.4.2 MAGI-1 is downregulated in colorectal cancer

MAGI-1 is often found downregulated in rectal cancers and colorectal adenocarcinomas and is correlated with metastasis (252,265).

Cyclooxygenase enzyme 2 (COX-2, also known as PTGS2) was found elevated in about 50% of colorectal adenomas and 85% of adenocarcinomas (285-287). Zaric et al. reported that MAGI-1 is downstream of and downregulated by COX-2, and consequently found low levels of MAGI-1 in colorectal cancer (CRC) cells (252). Overexpression of MAGI-1 in CRC cells induces epithelial-like morphology by stabilising cell-cell junctions, promoting actin stress fibres and adhesion (252). As MAGI-1 stabilises β -catenin at cell-cell contacts and thereby reduce the level of free β -catenin, MAGI-1 may act as a negative regulator of the Wnt pathway, known to initiate most of human colorectal cancers (288).

Dr. Khanzada thesis work also reported an increased potential for invasion and migration in two colorectal cancer cell lines, HT-115 and RKO, upon MAGI-1 knockdown (265). MAGI-1 thereby displays a tumour-suppressive and anti-metastatic activity in CRC cells.

1.3.4.3 MAGI-3 is downregulated in colorectal cancer

MAGI-3 expression has been reported to be downregulated in colon adenocarcinomas while NHERF2 expression showed a reverse trend. Lee and colleagues demonstrated that MAGI-3 and NHERF2 reciprocally regulate the signalling of LPA₂ (289), a G protein-coupled receptor that binds to lysophosphatidic acid (LPA). LPA is known to have tumorigenic potential through activation of LPA₂ which is upregulated in various types of cancer, such as CRC (290-292). LPA₂ together with NHERF2 activate Akt and Erk1/2 signalling (291), as well as induce cell proliferation, expression of COX-2 and anti-apoptotic behaviour in colon cancer cells (291,293,294). MAGI-3 is thought to oppose NHERF2 in binding LPA₂ and thereby negatively regulating LPA signalling and inhibiting migration and invasion (289). MAGI-3 together with LPA₂ activate RhoA signalling (295,296).

1.3.4.4 *MAGI-3 is recurrently mutated in breast cancer*

MAGI-3 expression was found downregulated in breast cancer cells (297), yet this gene is not frequently subjected to nonsynonymous mutations or loss of copy number (298,299).

A recurrent gene rearrangement, 5'- MAGI3-Akt3 -3' fusion mutation, was reported by Banerji and co-workers in triple negative (oestrogen receptors, progesterone receptors and HER2-negative) breast cancers. The resulting fusion protein possesses MAGI-3 N-terminal region until after the WW-domains followed by Akt3 with a disrupted PH domain but an intact kinase domain. The fusion protein lacks all MAGI-3 C-terminal PDZ domains including PDZ2, known to interact with PTEN and suppress PI3K/Akt signalling (283). MAGI3-AKT3 was found to be constitutively phosphorylated (active), leading to loss of contact inhibition when overexpressed in rat fibroblasts (300).

Ni and collaborators recently identified MAGI-3 as a novel driver of breast cancer tumorigenesis. MAGI-3 was recurrently mutated at the mRNA level. Indeed, they demonstrated that MAGI-3 was prematurely poly-adenylated (pPA) and truncated, ending within intron10 (MAGI-3^{pPA}). The resulting truncated protein retains part of the PDZ2 domain but lacks all following PDZ domains. The authors found that truncation of MAGI-3, whether arising from pPA or other genetic alterations (300), induced YAP-dependent mammary transformation. Interestingly, they showed that MAGI-3 PDZ5 domain interacts with YAP PDZ-binding motif. They showed that the MAGI-3^{pPA}, unable to bind to YAP, dimerises with its full length self, impeding association with YAP and thereby acting as a dominant negative. Their results suggest MAGI-3 as a novel component of the Hippo pathway (301).

1.4 AIM: Investigate the molecular mechanism by which MAGI proteins negatively regulate YAP activity in response to cell density cues

MAGI proteins have emerged as tumour suppressors, limiting cell proliferation and invasive behaviour. MAGI-1 was suggested as a novel negative regulator of YAP, potentially interacting with components of the Hippo pathway (160,221,222) but the mechanism at play remains to be elucidated. In addition, MAGI-3 has recently been shown to negatively control YAP oncogenic protein in breast cancer cells (301). As MAGI proteins are involved in tight junctions' maintenance and integrity, they could provide an additional link between cell-cell contacts and the regulation of the Hippo-YAP pathway. Indeed, despite intensive research, the signal transduction mechanism from upstream regulators, such as tight junctions, to the Hippo cascade remains largely elusive.

In this study, we aim at:

- ~ Further establishing MAGI-1 as an upstream regulator of the Hippo pathway,
And,
- ~ Unravelling the molecular mechanism at play to provide a molecular link between tight junctions and YAP inhibition in response to cell density cues.

To do so, we tackled the question from two different angles:

- ~ Investigation of MAGI proteins loss of function with respect to YAP Ser127 phosphorylation and subcellular localisation using CRISPR/Cas9 gene editing technique.
- ~ Investigation and dissection of molecular interactions of MAGI proteins with key players of the Hippo pathway to identify critical protein-protein interaction domains.

Members of the MAGI family, namely MAGI-1 and MAGI-3, have been reported to be downregulated in colorectal cancers (252,289). We therefore decided to carry out this study in the human colorectal adenocarcinoma cell line DLD-1.

2 Chapter 2: Materials and Methods

2.1 Materials

2.1.1 Devices

Table 2.1 | List of devices

	Device	Company
Cell culture	Class II Biological Safety Cabinet	ESCO
	Galaxy 170S CO2 Incubator	New Brunswick Scientific
	NEW INCUBATOR	Panasonic
	Neubauer-improved counting chamber	Labor Optik
	Universal 320 centrifuge	Hettich Centrifuge
Buffers preparation	Entris® Analytical Balance	Sartorius
	PGW 753M Precision Balance	Adam Equipment Ltd
	Jenway 3510 Bench pH/mV meter	JENWAY
Total protein extraction, samples preparation and western blot	Sigma 1-14K Refrigerated Microfuge	SIGMA
	PerfectSpin mini	Peqlab
	PerfectSpin 24 Plus	Peqlab
	NeoLab-Rotator with Vortex RM-2M	NeoLab
	Dry block heating system QBD2	Grant Instruments
	FluoSTAR OPTIMA Microplate Reader	BMG LabTech
	Mini-PROTEAN Tetra Cell	Bio-Rad Laboratories
	Mini Trans-Blot electrophoretic transfer cell	Bio-Rad Laboratories
	3D gyratory rocker SSM3	Stuart Equipments
	Analogue tube rollers SRT6	Stuart Equipments
	Odyssey Sa® Infrared Imaging System	LI-COR
PCR and Agarose gel	peqSTAR Dual 48-Well PCR Thermal Cycler	Peqlab
	PerfectBlue™ Gel System Mini M	Peqlab
	BLUE LED illuminator	Nippon Genetics Europe
	Gel Doc™ EZ System	Bio-Rad Laboratories
Microscopy	ZOETM Fluorescent Cell Imager	BioRad
	Epifluorescence microscope	Olympus
	LSM880 Airyscan Confocal	ZEISS
Bacteria culture	Rotina 46 R centrifuge	Hettich Centrifuge
	Innova® 44 incubator shaker series	New Brunswick Scientific
	Incubator (Heratherm)	Thermo Fisher Scientific

2.1.2 Reagents

2.1.2.1 Kits and chemicals

Table 2.2 | List of kits and chemicals

	Kit / Chemical	Catalogue #	Company
Protein techniques	cOmplete™, EDTA-free Protease Inhibitor Cocktail	11873580001	Roche
	PhosSTOP EASYpack	04906845001	Roche
	Protein A agarose	P2545	Sigma Aldrich (Merk)
	GFP-Trap®_A	gta-20	ChromoTek
	Myc-Trap®_A	yta-20	ChromoTek
	Binding Control Agarose	bab-20	ChromoTek
	DC Protein Assay Reagent A Reagent B Reagent S	500-0113 500-0114 500-0115	Bio-rad Laboratories
	PageRuler™ Prestained Protein Ladder	26616	Thermo Scientific™
	Amersham™ Protran™ 0.2 µm NC	10600004	GE Healthcare Life Sciences
	Whatman™ chromatography paper, 3 mm	3030-672	GE Healthcare Life Sciences
	Bovine Serum Albumin Fraction V (protease free)	5479	Sigma Aldrich (Merk)
	DNA techniques	Phenol solution	bp1751
Proteinase K		P8107S	Roche
RNeasy® Mini Kit		74104	Qiagen
Deoxyribonuclease I, Amplification Grade		18068-015	Invitrogen™
SuperScript II RT		18064-014	Invitrogen™
dNTPs Mix (10mM)		R0191	Thermo Scientific™
GoTaq Taq Hot Start Polymerase		M5005	Promega
Phusion High Fidelity DNA Polymerase		F530S	Thermo Scientific™
Quick change XL Mutagenesis kit		200521-5	Agilent technologies
T4 ligase		EL0011	Thermo Scientific™
T4 kinase		18004-010	Invitrogen™
Lambda protein phosphatase		P0753S	New England BioLabs
Alkaline Phosphatase, Calf Intestinal (CIP)		M0290S	New England BioLabs
Restriction enzymes		Various	New England BioLabs
T7 endonuclease I		M0302S	New England BioLabs
NucleoSpin Gel and PCR Clean-up		740609250	Macherey Nagel
SYBR™ Safe DNA Gel Stain		S33102	Invitrogen™
Gel Loading Dye Purple (6X)		B7024S	New England BioLabs
Quick-Load Purple 100bp DNA Ladder		N0551	New England BioLabs
Quick-Load Purple 1kb DNA Ladder	N0468	New England BioLabs	

	Quick-Load Purple 2-Log DNA Ladder	N0469	New England BioLabs
	GeneJET Plasmid Miniprep Kit	k0503	Thermo Scientific™
	NucleoBond® Xtra Midi	740410.50	Macherey-Nagel
Microscopy	Hoechst 33342	H3570	Invitrogen™
	Prolong Gold mounting medium	p36930	Invitrogen™

2.1.2.2 Antibodies

2.1.2.2.1 Primary antibodies

Table 2.3 | List of primary antibodies

IF: immunofluorescence; WB: Western Blot.

Antibody	Host species	Clonality	Applications & dilutions	Supplier
Anti-AMOT	Rabbit	Monoclonal	WB (1:1000)	Cell Signaling Technology (D204H #433130)
Anti- β -tubulin	Mouse	Polyclonal	WB (1:5000)	Sigma-Aldrich (M8064)
Anti-Flag	Mouse	Monoclonal	IF (1:1000) IP (1:500) WB (1:500)	Sigma-Aldrich (F1804)
Anti-GFP	Rabbit	Polyclonal	WB (1:2000)	Gift from Andrew Peden (custom made)
Anti-GFP	Rabbit	Polyclonal	WB (1:2000)	Invitrogen™ (A-11122)
Anti-MAGI-1	Rabbit	Polyclonal	IF (1:250) WB (1:500)	Sigma-Aldrich (M5691)
Anti-MAGI-2	Mouse	Polyclonal	WB (1:200)	Santa Cruz Biotechnology (sc-517008)
Anti-MAGI-3	Mouse	Polyclonal	WB (1:200)	Santa Cruz Biotechnology (sc-136471)
Anti-Myc (9E10)	Mouse	Monoclonal	WB (1:1000)	Acro Biosystems (MYC-MMYCc)
Anti-Myc (A-14)	Rabbit	Polyclonal	IF (1:40)	Santa Cruz Biotechnologies (SC-789)
Anti-PhosphoYAP Ser127	Rabbit	Polyclonal	WB (1:1000)	Cell Signaling Technology (#4911)
Anti-PTPN14	Rabbit	Monoclonal	WB (1:500)	Cell Signaling Technology (D5T6Y #13808)
Anti-YAP	Rabbit	Polyclonal	IF (1:250) WB (1:1000)	Cell Signaling Technology (#4912)
Anti-YAP/TAZ	Mouse	Monoclonal	IF (1:200) WB (1:200)	Santa Cruz Biotechnology (sc-101199)
Anti-ZO-1 (1A12)	Mouse	Monoclonal	IF (1:100)	Invitrogen™ (33-9100)

2.1.2.2.2 Secondary antibodies

Table 2.4 | List of secondary antibodies

IF: immunofluorescence; WB: Western Blot.

Antibody	Applications & dilutions	Supplier
Donkey anti-rabbit IgG (H+L) Alexa Fluor® 488	IF (1:500)	ThermoFisher Scientific (A-11034)
Goat anti-mouse IgG (H+L) Alexa Fluor® 488	IF (1:500)	ThermoFisher Scientific (A-11001)
Donkey anti-rabbit IgG (H+L) Alexa Fluor® 568	IF (1:500)	ThermoFisher Scientific (A-11011)
Donkey anti-mouse IgG (H+L) Alexa Fluor® 568	IF (1:500)	ThermoFisher Scientific (A-11004)
Donkey anti-rabbit IgG (H+L) Alexa Fluor® 594	IF (1:500)	ThermoFisher Scientific (A-11012)
Donkey anti-mouse IgG (H+L) Alexa Fluor® 594	IF (1:500)	ThermoFisher Scientific (A-11005)
Goat anti-mouse IgG (H+L) Alexa Fluor® 647	IF (1:500)	ThermoFisher Scientific (A-21235)
Donkey anti-rabbit IgG (H+L) Alexa Fluor® 680	WB (1:10 000)	ThermoFisher Scientific (A-21109)
DyLight™ 800 4X PEG conjugate anti-mouse IgG (H + L)	WB (1:10000)	ThermoFisher Scientific (SA5-35521)

2.1.2.3 Primers

All primers were purchased from Sigma-Aldrich.

2.1.2.3.1 Cloning

All primers were designed by myself as described in Section 2.2.3.1.

Table 2.5 | List of cloning primers

Tm: Melting temperature of the entire primer as predicted by the Multiple Primer Analyzer webtool from ThermoFisher Scientific.

No	Primer name	Sequence 5'-3'	Length (bp)	Tm (°C)
1	mMAGI-1B Δ(N-ter-Guk) NotI FWD	ATATATAGCGGCCGCTGGCATAGTCCACCCGGAGAATGAG	40	83.9
2	mMAGI-1B Δ(N-ter-Guk) XbaI REV	GCGCGTCTAGATTCACCTCCGGAACACCTTGTGCAC	36	83.2
3	mMAGI-1B WW1-WW2 NotI FWD	ATATAGCGGCCGCTGGCATAGTCCACCCGGAGAATGAG	38	84.8
4	mMAGI-1B WW1-WW2 XbaI REV	GCGGCGTCTAGATTCACACAACAGATGCATGATCCTC	37	82.1
5	mMAGI-1B WW1 NotI FWD	ATGCTAAGCGGCCGCTTACCTACCTCTTCTGCAGAG	37	80.5
6	mMAGI-1B WW2 NotI FWD	ATATAAAGCGGCCGCTCAGCAGAAGCCTCTGGAAGAA	37	81.9
7	mMAGI-1B WW1 XbaI REV	GGGGGCTCTAGATTCATTCTCCAGAGGCTTCTGCTG	37	80.9
8	mMAGI-1B WW2 XbaI REV	GGGCGGGTCTAGATTCACCTGTTCAAGCTGTTCTTCCG	38	82
9	mMAGI-1B FL BamHI FWD	GCAGGATCCTCGAAAGTGATCCAGAAGAAG	30	74.8
10	mMAGI-1B FL EcoRI REV	GCAGAATTCCTCACTCCGGAACACCTTGT	30	76.3
11	mMAGI-1B WW1-2 5'P FWD	[Phos]AAGAAACAGCTTGAACAGCAG	21	61.2
12	mMAGI-1B WW1-2 5'P REV	[Phos]GTACTGAGGGAACCTTCTGAGA	21	57.5
13	mMAGI-1B WW1 5'P FWD	[Phos]CAGAAGCCTCTGGAAGAATGT	21	62.3
14	mMAGI-1B WW2 5'P REV	[Phos]ACATTCTCCAGAGGCTTCTG	21	62.3
15	mMAGI-1B WW1 EcoRI REV	GCAGAATTCCTGAGTACTGAGGGAACCTTCTGAGA	34	74.5

16	mMAGI-1B WW2 BamHI FWD	GCAGGATCCAAGAAACAGCTTGAACAGCAG	30	76.2
17	mMAGI-1B PDZ2 BamHI FWD	GCAGGATCCCCACTGGAGAGGAAAGACAGC	30	79.3
18	PX459 Puro PacI FWD	CGCTTAATTAAGTGATGACCGAGTACAAGCCCAC	34	75.5
19	PX459 Puro BstBI REV	GCATTGAAAATTCTCAGGCACCGGGC	27	79.1
20	pcDNA3.1(+) ΔNeoR BstBI FWD	GCATTGAAATGACCGACCAAGC	23	72.3
21	pcDNA3.1(+) ΔNeoR PacI REV	GCATTAATTAACGATCCTCATCCTGTCTCTT	32	70.2
22	hMAGI-1αβ1 Δα 5'P FWD	[Phos]CTACCAGATTACCAGGAACAGG	22	61.3
23	hMAGI-1αβ1 Δα 5'P REV	[Phos]TCGGTTTTTCATACATGCTC	19	58.7
24	hMAGI-1αβ1 overlap FWD_A	TCCAAAGTGATCCAGAAGAAGAACC	25	67.3
25	hMAGI-1αβ1 overlap FWD_A KpnI	GCGGGTACCTCCAAAGTGATCCAGAAGAAGAACC	34	78.6
26	hMAGI-1αβ1 overlap REV_B	CCACCATTCTTAATCAGTTCTATAGCTCG	29	67.1
27	hMAGI-1Cβ1 overlap FWD_C	CGAGCTATAGAACTGATTAAGAATGGTGG	29	67.1
28	hMAGI-1Cβ1 overlap REV_D	TCAGATACTGAGGTCGGTGCTAC	23	64.3
29	hMAGI-1Cβ1 overlap REV_D EcoRI	GCAGAATTCATCAGATACTGAGGTCGGTGCTAC	33	74.6
30	GFP-hMAGI-1Cβ1 HindIII FWD	ATGAAGCTTTCGCCACCATGG	21	70.2
31	GFP-hMAGI-1Cβ1 EcoRI REV	ATGGAATTCATCAGATACTGAGGTCGGT	28	69.9
32	hPTPN14 FL EcoRI FWD	GGAGAATTCTGCCTTTTGGTCTGAAGCTC	29	73.2
33	hPTPN14 FL NotI REV	GCAGCGGCCGCTAAATGAGTCTGGAGTTTTG	32	80.1

2.1.2.3.2 Mutagenesis

Mutagenesis primers were designed using the web-based QuikChange Primer Design Program (www.agilent.com/genomics/qcpd).

Table 2.6 | List of mutagenesis primers

No	Primer name	Sequence 5'-3'	Length (bp)	T _m (°C)
1	hMAGI-1Cβ Mini4 muta FWD	ACGGCTCAGTACCAGAATATGACCCCAGCAG	31	77.3
2	hMAGI-1Cβ Mini4 muta REV	CTGCTGGGGTCATATTCTGGTACTGAGCCGT	31	77.3

2.1.2.3.3 Sequencing

Sequencing primers were designed by myself unless otherwise stated.

Table 2.7 | List of sequencing primers

(*) Primers from the Erdmann library. (-) Primers from the Core Genomic Facility of the University of Sheffield.

No	Primer name	Sequence 5'-3'	Length (bp)
1	mMAGI-1B SEQ1	GTCCACCCGGAGAATGAGGAGG	22
2	mMAGI-1B SEQ2	GATGGTCTGCCGCACTGGATG	22
3	mMAGI-1B SEQ3	GCCTGCACACTGCGTCCCCG	20

4	mMAGI-1B SEQ4	GGGGAGAACGAGGGCTTTGGG	21
5	mMAGI-1B SEQ5	CTTGGAGTCCAGTTACCCACC	21
6	mMAGI-1B SEQ6	GTAGCACCGACCTCAGCATC	20
7	hMAGI-1C β 1 SEQ1	CTTTACAGCAGCCGATTCTGG	21
8	hMAGI-1C β 1 SEQ2	TCCTGCTGCATTGGATGGCA	20
9	hMAGI-1C β 1 SEQ3	ACAGCACACAGGTGCTCCCCG	21
10	hMAGI-1C β 1 SEQ4	CTGACCGCTGTGGCAAGCTG	20
11	hMAGI-1C β 1 SEQ5	AACTGATTAAGAATGGTGGC	20
12	hPTPN14 SEQ1	GCATTTTCTTTATGGGGATTTTC	23
13	hPTPN14 SEQ2	GTACAGCCAACCGGAGATGCG	21
14	hPTPN14 SEQ3	GTACAGTGCCAGCTGCAGGCG	22
15	EGFP 5' FWD (*)	GTCCGCCCTGAGCAAAGACCC	21
16	CMV primer FWD (*)	CGCAAATGGGCGGTAGGCGT	20
17	T7 FWD (-)	TAATACGACTCACTATAGGG	20
18	bGH REV (-)	TAGAAGGCACAGTCGAGG	18
19	hMAGI-1 Exon1 CRISPR FWD1-2	TGTTTCTCCCATGAACAAGCG	21
20	hMAGI-1 Exon1 CRISPR REV1-2	GGAGGGAAGCAGGAAATCGAG	21
21	hMAGI-2 Exon5 CRISPR FWD4-9	GACGAGTGAAGGAGAGCTCA	21
22	hMAGI-2 Exon5 CRISPR REV4-9	CGCCCTTCTCTGTATAGGCC	20
23	hMAGI-3 Exon1 CRISPR FWD5-6	AGACGCTGAAGAAGAAGAAGCA	22
24	hMAGI-3 Exon1 CRISPR REV5-6	GTCTTGAGACGGATGGGCTC	20
25	U6 primer FWD (*)	GACTATCATATGCTTACCGT	20

2.1.2.4 siRNAs

Table 2.8 | List of siRNAs

No	siRNA target [name in thesis]	Sequence 5'-3' or catalogue number	Source
1	Silencer® Negative Control #1 siRNA Ambion [Scr siRNA]	AM4611	Applied Biosystems
2	hMAGI-1C β [siMAGI-1]	CCCAAGCAACACAGGAGCAAGATTT	(302)

2.1.2.5 sgRNAs

Table 2.9 | List of sgRNAs

No	sgRNA name	Sequence 5'-3'	Length (bp)
1	hMAGI-1 Exon1 G1 Bbsl Top	CACCGGGAGTTTCCGTACGTCGGAG	25
2	hMAGI-1 Exon1 G1 Bbsl Bottom	AAACCTCCGACGTACGGAAACTCCC	25
3	hMAGI-1 Exon1 G2 Bbsl Top	CACCGTTGCCCGCTATGACGTGCT	25

4	hMAGI-1 Exon1 G2 Bbsl Bottom	AAACAGCACGTCATAGCGGGGCAAC	25
5	hMAGI-2 Exon5 G9 Bbsl Top	CACCGGCTGACTGTACACTGGTGC	24
6	hMAGI-2 Exon5 G9 Bbsl Bottom	AAACGCACCAGTGTACAGTCAGCC	24
7	hMAGI-2 Exon5 G4 Bbsl Top	CACCGCAGACCCATTGCCTGATAAC	25
8	hMAGI-2 Exon5 G4 Bbsl Bottom	AAACGTTATCAGGCAATGGGTCTGC	25
9	hMAGI-3 Exon1 G5 Bbsl Top	CACCGGACTTCGGCGCGGAGATCCG	25
10	hMAGI-3 Exon1 G5 Bbsl Bottom	AAACCGGATCTCCGCGCCGAAGTCC	25
11	hMAGI-3 Exon1 G6 Bbsl Top	CACCGGTAAACGGGACGCCTGTCAG	25
12	hMAGI-3 Exon1 G6 Bbsl Bottom	AAACCTGACAGCGTCCCGTTTACC	25

2.1.2.6 Expression vectors

Table 2.10 | List of expression constructs

GOI: Gene of interest.

No	Plasmid name	Source and description	Vector size (bp)	GOI Segment (bp)
1	pcDNA3.1(+) EGFP	pcDNA3.1(+) plasmid with EGFP tag inserted between HindIII & KpnI sites From the library of the Erdmann Lab	6167	
2	pcDNA3.1(+) 3xFlag	pcDNA3.1(+) plasmid with 3xFlag tag inserted between EcoRI & NotI sites From the library of the Erdmann Lab	5496	
3	pcDNA3.1(+) myc	pcDNA3.1(+) plasmid with myc tag inserted between HindIII & KpnI sites From the library of the Erdmann Lab	5491	
4	pFN21A HaloTag- hMAGI-1A $\alpha\beta$	Purchased from Promega	8479	(1-3774)
5	pcDNA3 2xFlag- mMAGI-1B	1432 pcDNA3 flag MAGI1c construct purchased from Addgene (Addgene plasmid # 10714 ; http://n2t.net/addgene:10714 ; RRID:Addgene_10714) (280) Mouse MAGI1 fused to an N-ter 2xFlag tag Advertised as Flag-mMAGI-1C but after reception of the plasmid, sequencing data showed that it was actually mMAGI-1B followed by 3' UTR	9836	(4-3516)
6	pcDNA3.1(+) 3xFlag mMAGI-1B Δ N-ter & Δ C-ter	Cloning of mMAGI-1B middle part (691-3252) into pcDNA3.1(+) 3xFlag without the N-ter part (4-690) or the C-ter part (3253-3516) using primers #1 & #2 from Table 2.5	8037	(691-3252)
7	pcDNA3.1(+) 3xFlag mMAGI-1B WW1-WW2	Cloning of mMAGI-1B WW1 & WW2 domains (691-1239) into pcDNA3.1(+) 3xFlag using primers #3 & #4 from Table 2.5	6038	(691-1239)
8	pcDNA3.1(+) EGFP-mMAGI-1B WW1-2	Cloning of mMAGI-1B WW1 & WW2 domains (868-1170) into pcDNA3.1(+) EGFP using primers #5 & #6 from Table 2.5	6464	868-1170
9	pcDNA3.1(+) EGFP-mMAGI-1B WW1	Cloning of mMAGI-1B WW1 domain (868-1031) into pcDNA3.1(+) EGFP using primers #5 & #7 from Table 2.5	6323	868-1031

10	pcDNA3.1(+) EGFP-mMAGI-1B WW2	Cloning of mMAGI-1B WW2 domain (1009-1170) into pcDNA3.1(+) EGFP using primers #6 & #8 from Table 2.5	6323	1009-1170
11	pcDNA3.1(+) EGFP-mMAGI-1B	mMAGI-1B FL (4-3516) recloned in pcDNA3.1(+) EGFP using primers #9 & #10 from Table 2.5	9656	(4-3564)
12	pcDNA3.1(+) EGFP-mMAGI-1B Δ WW1	Deletion of WW1 domain (Δ 871-1011) from pcDNA3.1(+) EGFP-mMAGI-1B construct using primers #13 & #12 from Table 2.5	9515	Δ (871-1011)
13	pcDNA3.1(+) EGFP-mMAGI-1B Δ WW2	Deletion of WW2 domain (Δ 1033-1152) from pcDNA3.1(+) EGFP-mMAGI-1B construct using primers #11 & #14 from Table 2.5	9536	Δ (1033-1152)
14	pcDNA3.1(+) EGFP-mMAGI-1B Δ WW1-2	Deletion of WW1 domain (Δ 871-1152) from pcDNA3.1(+) EGFP-mMAGI-1B construct using primers #11 & #12 from Table 2.5	9374	Δ (871-1152)
15	pcDNA3.1(+) EGFP-mMAGI-1B N1	Cloning of mMAGI-1B N-ter-GuK (4-870) into pcDNA3.1(+) EGFP using primers #9 & #15 from Table 2.5	7013	4-870
16	pcDNA3.1(+) EGFP-mMAGI-1B C2	Cloning of mMAGI-1B PDZ1-5 domains (1153-3516) into pcDNA3.1(+) EGFP using primers #16 & #10 from Table 2.5	8507	1153-3516
17	pcDNA3.1(+) EGFP-mMAGI-1B C3	Cloning of mMAGI-1B PDZ3-5 domains (2140-3516) into pcDNA3.1(+) EGFP using primers #17 & #10 from Table 2.5	7520	2140-3516
18	pcDNA3.1(+) myc PuroR	PuroR gene cloned from PX459 vector using primers #18 & #19 (from Table 2.5) and pcDNA3.1(+) Myc Δ NeoR cloned using primers #20 & #21 (from Table 2.5) were ligated together to generate pcDNA3.1(+) Myc PuroR vector	5287	
19	pcDNA3.1(+) EGFP-hMAGI-1C β 1 NeoR	pcDNA3.1(+) vector containing the hMAGI-1C β 1 isoform found in epithelial tissues. The cloning steps are listed below and described in Annex 1: <u>STEP1:</u> Deletion of the α region (2422-2508) from pFN21A HaloTag-hMAGI-1A α β 1 and replacing it with a Leu (CTA) using primers #22 & #23 from Table 2.5 <u>STEP2:</u> Amplification of hMAGI-1 β 1 (excluding the C-ter isoform A) 4- Δ (2422-2508)-3674 using primers #24 & #26 (Product AB) from Table 2.5 <u>STEP3:</u> Amplification of endogenous hMAGI-1C β C-ter (3562-4398) from DLD-1 WT cDNA using primers #27 & #28 (Product CD \Leftrightarrow hMAGI-1C β 1) from Table 2.5 <u>STEP4:</u> Overlapping PCR to join the AB & CD fragments to obtain AD using primers #25 & #29 from Table 2.5 <u>STEP5:</u> Ligate hMAGI-1C β 1 into pcDNA3.1(+) EGFP	10526	(4-4398)
20	pcDNA3.1(+) EGFP-hMAGI-1C β 1 PuroR	Recloning of EGFP-hMAGI-1 into pcDNA3.1(+) PuroR (pcDNA3.1(+) myc PuroR digested to exclude myc-tag) using primers #30 & #31 from Table 2.5	10333	(4-4398)
21	pcDNA3 V5-hPTPN14 WT	pcDNA3-V5-PTPN14-wild type purchased from Addgene (Addgene plasmid # 61003 ; http://n2t.net/addgene:61003 ; RRID:Addgene_61003) (75) Human PTPN14 fused with a N-terminal V5 tag	9035	(1-3564)
22	pcDNA3 V5-hPTPN14 PPxY mutant	pcDNA3-V5-PTPN14-PPxY purchased from Addgene (Addgene plasmid # 61006 ; http://n2t.net/addgene:61006 ; RRID:Addgene_61006) (75) V5-PTPN14 where the PPPY (567-570) & PPEY (749-752) proline-rich motifs are mutated to alanines (AAAA)	9035	(1-3564)

23	pcDNA3.1(+) myc-hPTPN14 WT	hPTPN14 WT (4-3564) recloned in pcDNA3.1(+) Myc using primers #32 & #33 from Table 2.5	9034	(4-3564)
24	pcDNA3.1(+) myc-hPTPN14 PPxY mutant	hPTPN14 WT (4-3564) recloned in pcDNA3.1(+) Myc using primers #32 & #33 from Table 2.5	9034	(4-3564)
25	pSpCas9(BB)- 2A-GFP (PX458)	pSpCas9(BB)-2A-GFP (PX458) purchased from Addgene (Addgene plasmid # 48138 ; http://n2t.net/addgene:48138 ; RRID:Addgene_48138) (303) Human codon-optimized Cas9 fused to a nuclear localisation sequence to ensure its targeting to the nucleus and an EGFP sequence separated by a T2A sequence that will be cleaved during translation to generate two separate polypeptides. sgRNA cloning site delimited by two BbsI sites ahead of the gRNA scaffold sequence.	9288	
26	pSpCas9(BB)- 2A-Puro (PX459)	Gift from Andrew Peden Same as for pSpCas9(BB)-2A-GFP (PX458) but the selection marker is a puromycin resistance gene.	9175	
27	PX458-sgRNA1 (hMAGI-1 Exon1)	sgRNA1 (G1) targeting hMAGI-1 Exon1 (#1 & #2 from Table 2.9) cloned into PX458 Cas9-GFP vector using BbsI enzyme (see Section 2.2.4.2 for protocol)	9291	
28	PX458-sgRNA2 (hMAGI-1 Exon1)	sgRNA2 (G2) targeting hMAGI-1 Exon1 (#3 & #4 from Table 2.9) cloned into PX458 Cas9-GFP vector using BbsI enzyme (see Section 2.2.4.2 for protocol)	9291	
29	PX459-sgRNA9 (hMAGI-2 Exon5)	sgRNA9 (G9) targeting hMAGI-2 Exon5 (#5 & #6 from Table 2.9) cloned into PX459 Cas9-PuroR vector using BbsI enzyme (see Section 2.2.4.2 for protocol)	9178	
30	PX459-sgRNA4 (hMAGI-2 Exon5)	sgRNA4 (G4) targeting hMAGI-2 Exon5 (#7 & #8 from Table 2.9) cloned into PX459 Cas9-PuroR vector using BbsI enzyme (see Section 2.2.4.2 for protocol)	9178	
31	PX459-sgRNA5 (hMAGI-3 Exon1)	sgRNA5 (G5) targeting hMAGI-3 Exon1 (#9 & #10 from Table 2.9) cloned into PX459 Cas9-PuroR vector using BbsI enzyme (see Section 2.2.4.2 for protocol)	9178	
32	PX459-sgRNA6 (hMAGI-3 Exon1)	sgRNA6 (G6) targeting hMAGI-3 Exon1 (#11 & #12 from Table 2.9) cloned into PX459 Cas9-PuroR vector using BbsI enzyme (see Section 2.2.4.2 for protocol)	9178	

2.1.2.7 Mammalian cell lines

Table 2.11 | List of mammalian cell lines

Name	Description
HEK293	H uman e mbrionic k idney cell line (304,305) Supplier: ECACC (ECACC 85120602)
Caco-2	Human c olorectal adenocarcinoma epithelial cell line (306) Supplier: ATCC (Caco2 [Caco2] (ATCC® HTB37™))
DLD-1	Human colon, Dukes' type C, colorectal adenocarcinoma epithelial cell line DLD-1 is one of the two cell lines isolated by Daniel L. Dexter (307,308) Supplier: ATCC (DLD1 (ATCC® CCL221™))
MDCKII	M adin- D arby C anine K idney epithelial cell line Supplier: ECACC (ECACC 00062107)

Details about cell culture can be found in Section 2.2.1.

Table 2.12 | List of reagents used for cell culture

DMEM	DMEM (1X) + GlutaMAX™-I - Dulbecco's Modified Eagle Medium [+] 4.5g/L D-glucose [+] Pyruvate Supplier: Gibco®, Life Technologies™ (10569010)
MEM	MEM (1X) - Minimum Essential Medium [+] Earle's Salts [+] L-Glutamine Supplier: Gibco®, Life Technologies™ (11095080)
RPMI	RPMI-1640 Medium (1X) [+] L-Glutamine [+] NaHCO ₃ Supplier: Sigma-Aldrich® (R8758-500ML)
OPTI-MEM	Opti-MEM™ I (1X) - Reduced Serum Medium [+] L-Glutamine [+] HEPES [-] Phenol Red Supplier: Gibco®, Life Technologies™ (11058021)
FBS	Fetal Bovine Serum, qualified, heat inactivated, E.U.-approved, South America Origin Supplier: Gibco®, Life Technologies™ (10500064)
Pen/Strep	Penicillin-Streptomycin (5,000U/mL) (100X) 5000units/mL of penicillin 5000µg/mL of streptomycin Supplier: Gibco®, Life Technologies™ (15070063)
Trypsin	Trypsin-EDTA (0.05%), Phenol red (1X) Supplier: Gibco®, Life Technologies™ (25300062)
Lipofectamine™ 2000	Lipofectamine™ 2000 Transfection Reagent Supplier: Invitrogen™, Fisher Scientific (11668019)
Poly-L-lysine	Poly-L-Lysine solution (0.1% (w/v) in H ₂ O) Supplier: Sigma-Aldrich® (P8920)
Puromycin	Supplier: Santa Cruz Biotechnologies (sc-108071)

2.1.2.8 Bacteria

Table 2.13 | List of bacteria strain and reagents used for bacteria culture

Strain	Description
<i>E.coli</i> NovaBlue (XL1)	K-12 strain of competent cells used for DNA cloning applications Genotype: <i>recA1 endA1 gyrA96 thi-1 hsdR17 supE44 relA1 lac</i> [<i>F' proAB lacI^qZΔM15 Tn10 (Tet^r)</i>] Supplier: Stratagene GmbH, Heidelberg, Germany
Reagents	Description / Recipe
LB medium	10g/L Peptone 5g/L Yeast extract 10g/L NaCl up to 1L ddH ₂ O
LB agar plates	15g/L agar in LB medium Supplemented with: 100µg/mL Ampicillin

2.2 Methods

2.2.1 Cell culture methods

2.2.1.1 Cell lines and culture conditions

Table 2.14 | Summary of mammalian cell lines and culture conditions

Cell line	Organism	Tissue	Morphology	Complete growth medium
HEK293	Human	Embryonic kidney	Epithelial Adherent	DMEM-GlutaMAX + 10% FBS + 1% P/S
MDCKII	Dog	Kidney	Epithelial Adherent	
Caco-2	Human	Colon	Epithelial Adherent	MEM + 10% FBS + 1% P/S + 1x NEAA
DLD-1	Human	Colon	Epithelial Adherent	RPMI-1840 + 10% FBS + 1% P/S

2.2.1.2 Subculture procedure

Table 2.15 | Subculture procedure for mammalian cell lines

Cell line	PBS 1X	Trypsin 1X	Incubation at 37°C	Complete medium	Centrifugation	Passaging ratios
HEK293	7mL	1mL	1min	9mL	320xg for 3min	1:10
MDCKII	7mL	2mL	5min	8mL	320xg for 3min	1:10
Caco-2	7mL	2mL	5min	8mL	320xg for 3min	1:4-1:8
DLD-1	7mL	2mL	5min	5-8mL	130xg for 5min	1:10

Cells were cultured in 10cm dishes (DLD-1 cells) or T-75 flasks (HEK293, Caco-2 and MDCK cells) in an incubator at 37°C with 5% CO₂. Once cells reached 70-90% confluency, they were passaged as follow. First, medium was discarded and cells were washed once with PBS 1X to remove traces of serum that could inhibit the action of the trypsin. Trypsin was added to the cells and the dish was placed back in the incubator to allow cells to detach. Dispersion of the cell layer was checked after a few minutes under an inverted microscope. Once cells were detached, complete medium was added to stop the action of trypsin and cells were resuspended by gently pipetting up and down. The suspension was centrifuged at the speed indicated in **Table 2.15** to pellet cells. Supernatant was gently discarded and cells were then resuspended in 1mL of complete medium. The appropriate ratio of cells was pipetted into the new culture vessel (See **Table 2.15**) in 10mL of complete growth medium. The cell suspension inside the new vessel was gently homogenize to favour uniform growth.

2.2.1.3 Cryopreservation

2.2.1.3.1 Freezing

Cells were treated as for subculturing. After the centrifugation step, the cell pellet was resuspended in cold freezing medium (90% complete medium + 10% DMSO; 90% FBS + 10% DMSO for DLD-1 cells). Cells cultured in 10cm dishes or in T-75 flasks were aliquoted in two cryovials. To ensure a slow freezing process, vials were first kept at -20°C for 2hrs and were then transferred to -80°C for at least 24hrs. For long-term storage, vials were kept in liquid nitrogen.

2.2.1.3.2 Thawing

Vials of cells were retrieved from liquid nitrogen and transported in dry ice. Vials were placed in a water bath at 37°C for 3-5min to thaw. Cells were resuspended in 9mL of pre-warmed complete medium and centrifuged (See **Table 2.15**). The supernatant was carefully discarded and cells were resuspended in 10mL of complete medium and transferred to the vessel of choice (10cm dish or T-75). Cells were allowed to attach overnight in the incubator at 37°C, 5% CO₂. The next day (or after 48hrs for Caco-2), fresh medium was applied to the cells to remove all traces of DMSO and dead cells.

2.2.1.4 Cell counting and seeding

Cells were treated as for subculturing. After the centrifugation step, the cell pellet was resuspended in 10mL of complete medium. Cells were counted using the Neubauer counting chamber (Hemocytometer) under an inverted microscope. Depending on the cell line and on the application, cells were seeded as indicated in **Table 2.16**.

Table 2.16 | Mammalian cells seeding densities

Cell line	6-well plate	12-well plate	Density assay
HEK293	2.5x10 ⁵ cells/well	1x10 ⁵ cells/well	See Section 2.2.6.2
Caco-2	/	1.5x10 ⁵ cells/well	
DLD-1	3x10 ⁵ cells/well	1.5x10 ⁵ cells/well	

2.2.1.5 Transfection protocol

One day prior to transfection (two days for Caco-2 cells as they require more time to attach properly), cells were seeded at the densities described previously (**Table 2.16**). Cells were allowed to attach to the dish for at least 24hrs and were then transfected using

Lipofectamine™ 2000 following manufacturer's instructions. The amounts of reagents used are recapitulated in **Table 2.17**.

Table 2.17 | Transfection protocols for mammalian cell lines

The amount of DNA (Example for HEK293 cells: 1µg) indicated represent the total amount; if co-transfection of two plasmids: 1:1 mass ratio; if co-transfection of three plasmids: 1:1:1 mass ratio. P/S: Penicillin/Streptomycin

DNA transfection		
HEK293	2.5x10 ⁵ cells/well in 6-well plate	{150µL of OPTIMEM + 2.5µL of Lipofectamine {150µL of OPTIMEM + 1µg of DNA In growth medium without P/S Medium changed for complete medium after 24hrs Protein expression was assessed after 48hrs
DLD-1	3x10 ⁵ cells/well in 6-well plate	{150µL of OPTIMEM + 5µL of Lipofectamine {150µL of OPTIMEM + 2µg of DNA In growth medium without P/S Medium changed for complete medium after 24hrs Protein expression was assessed after 48hrs
siRNA transfection		
HEK293	1x10 ⁵ cells/well in 12-well plate	{125µL of OPTIMEM + 2.5µL of Lipofectamine {125µL of OPTIMEM + 50pmoles of siRNA In growth medium without P/S Medium changed for complete medium after 24hrs Knockdown efficiency was assessed after 72hrs
Caco-2	1.5x10 ⁵ cells/well in 12-well plate	<u>Day1:</u> {125µL of OPTIMEM + 2.5µL of Lipofectamine {125µL of OPTIMEM + 50pmoles of siRNA In growth medium without P/S <u>Day2:</u> Changed for complete medium <u>Day3:</u> {125µL of OPTIMEM + 2.5µL of Lipofectamine {125µL of OPTIMEM + 50pmoles of siRNA In growth medium without P/S <u>Day4:</u> Changed for complete medium <u>Day5:</u> Knockdown efficiency was assessed after 96hrs
DLD-1	1.5x10 ⁵ cells/well in 12-well plate	<u>Day1:</u> {125µL of OPTIMEM + 2.5µL of Lipofectamine {125µL of OPTIMEM + 50pmoles of siRNA In growth medium without P/S <u>Day2:</u> Changed for complete medium <u>Day3:</u> {125µL of OPTIMEM + 2.5µL of Lipofectamine {125µL of OPTIMEM + 50pmoles of siRNA In growth medium without P/S <u>Day4:</u> Changed for complete medium <u>Day5:</u> Knockdown efficiency was assessed after 96hrs

2.2.2 Ribonucleic acid methods

Total RNA was extracted from DLD-1 WT cells and used as a template for reverse transcription. The corresponding cDNA was then used to amplify the endogenous MAGI-1 C-terminus to generate the EGFP-hMAGI-1C β 1 expression construct (Annex 1).

2.2.2.1 RNA extraction and purification

2.2.2.1.1 Initial preparation of mammalian cells

DLD-1 cells were cultured in a 35mm dish until confluency (**Table 2.16**). At this point, cells were collected as described in steps 1-6 of Section 2.2.1.2. The cell pellet was washed once in PBS 1x. Cells were once again pelleted at 130xg. Total RNA extraction was performed as described below.

2.2.2.1.2 Total RNA extraction

Prior to working with RNA, bench, pipettes, tubes and gloves were treated with RNAZap[®]. Filtered tips were used as well as freshly autoclaved microcentrifuge and PCR tubes.

Total RNA was extracted and purified using the Qiagen RNeasy[®] Mini Kit according to manufacturer's instructions.

2.2.2.2 DNase I treatment

RNA purification was completed by DNase I treatment aiming at removing any potential gDNA contamination. RNA samples were prepared in duplicates for the reverse transcriptase positive and negative controls.

RNA concentration and purity were assessed by NanoDrop.

Table 2.18 | DNase I treatment

Components	Amount
RNA	1 μ g
10X DNase I Reaction Buffer	1 μ L
DNase I, Amp Grade (1U/ μ L)	1 μ L
RNase-free water	Up to 10 μ L

The reaction described in **Table 2.18** was prepared in duplicate. Samples were incubated for 15min at room temperature. Special care was taken not to exceed 15min of

incubation on the indicated temperature as it could result in hydrolysis of the RNA. Then, 1 μ L of EDTA 25mM was added to the reaction. Finally, samples were incubated for 10min at 65°C to heat-inactivate the DNase I.

2.2.2.3 Reverse transcription – cDNA synthesis

Bench, pipettes, tubes and gloves were treated with RNAZap[®]. Filtered tips were used as well as freshly autoclaved microcentrifuge and PCR tubes.

First-strand cDNA library from DLD-1 cells total RNA was synthesised with the Super-Script™ Reverse Transcriptase using random hexamers (5'-NNNNNN-3'). Random hexamers are a mixture of every possible combination of six bases.

All steps were performed in a thermocycler. For each sample, a duplicate was prepared that was incubated with RNase-free water instead of the reverse transcriptase (-RT).

Table 2.19 | Reverse transcription

a. STEP1. b. STEP2.

a		STEP1		+RT	-RT
Random hexamers (100 μ M)		1 μ L	1 μ L		
DNase I treated total RNA		11 μ L	11 μ L		
dNTPs mix (10mM)		1 μ L	1 μ L		

b		STEP2		+RT	-RT
5X First-strand Buffer		4 μ L	4 μ L		
0.1M DTT		2 μ L	2 μ L		

First, reactions as described in **Table 2.19a** were prepared. The mixtures were incubated at 65°C for 5min, then, chilled on ice for 2min and spun to collect liquid at the bottom of the tube. Afterwards, the components indicated in **Table 2.19b** were added, solutions were mixed gently and tubes were incubated at 25°C for 2min. 1 μ L (200 units) Super-Script™ Reverse Transcriptase was added to the +RT tube while 1 μ L of RNase-free water was added to the -RT tube. Solutions were mixed by gently pipetting up and down and incubated at 25°C for 10min, then for 1hr at 42°C. The reactions were heat-inactivated by incubating at 70°C for 15min. The resulting cDNA was aliquoted to avoid degradation through repeated freeze-thaw cycles and stored at -20°C.

Synthesized cDNA was subsequently used to clone hMAGI-1C β C-terminus (See Annex 1).

2.2.3 Molecular cloning and plasmid preparation

Molecular cloning was performed by PCR amplification of the region of the gene of interest and ligation in the recipient vector using restriction sites.

2.2.3.1 *Primer design*

Restriction enzymes selection:

Restriction sites were selected based on the following criteria:

- Do not cut the gene or region of the gene being cloned. This was checked using the web tool NEBcutter (<http://nc2.neb.com/NEBcutter2/>), and
- Are located in the multiple cloning site of the recipient plasmid (and do not cut anywhere else).

Whenever possible, two different restriction sites were used to ensure correct orientation of the insert in the recipient vector.

Primer design:

Primers were designed to contain:

- 18-21 nucleotides annealing to the template DNA,
- Optional: Start codon (forward primer) and/or Stop codon (reverse primer) if needed,
- Optional: Extra nucleotides to ensure conservation of the open reading frame in the recipient plasmid when creating fusion proteins,
- Specific restriction sites flanked on the 5' end by extra 3-6 base pairs allowing the restriction enzymes (RE) to bind more comfortably and cleave efficiently.

Overall, the part of the primer that annealed to the template (therefore excluding START/STOP codons, RE sites and extra nucleotides) had a 40-60% GC content and a melting temperature (T_m) between 50°C and 70°C within 5°C of each other (forward and reverse).

Secondary structure or primer-dimer formation was checked using ThermoFisher Multiple Primer Analyser web tool.

Primers were purchased lyophilized from Sigma-Aldrich[®], reconstituted in ddH₂O to a concentration of 100µM. For PCR, primers were further diluted in ddH₂O to a working concentration of 10µM.

2.2.3.2 Polymerase Chain Reaction

2.2.3.2.1 Standard PCR

2.2.3.2.1.1 Phusion® High-Fidelity Polymerase

DNA fragments required for molecular cloning were amplified by PCR using the Phusion® High-Fidelity Polymerase. The high-fidelity feature is obtained by fusion of the DNA-binding domain of the polymerase to a *Pyrococcus-like* proofreading polymerase. Phusion® polymerase possesses both 5'→3' DNA polymerase activity and 3'→5' exonuclease proofreading activity, generating blunt-ended products with very high accuracy.

Reactions were prepared as shown in **Table 2.20**. During the optimisation phase, 20µL reactions were used; afterwards 50µL reactions were preferred to yield higher amounts of amplicon and be able to proceed with subsequent steps. DMSO was added in particular cases such as for amplification of large templates (~10kb).

Table 2.20 | Phusion® High-Fidelity PCR reaction mix

Components	20µL reaction	50µL reaction
5X Phusion Green HF Buffer (contains 7.5mM MgCl ₂ and two dyes, yellow and blue, for easy monitoring of gel electrophoresis)	4µL	10µL
dNTPs (10mM)	0.4µL	1µL
Forward primer (10µM)	1µL	2.5µL
Reverse primer (10µM)	1µL	2.5µL
Template DNA (plasmid DNA)	5-10ng	20-40ng
DMSO (Optional)	0.6µL	1.5µL
Phusion® High-Fidelity Polymerase (2U/µL) * Added last	0.2µL	0.5µL
ddH ₂ O	Up to 20µL	Up to 50µL

Annealing temperature of a given primer-pair was determined using the ThermoFisher T_m Calculator web tool.

Amplification of the DNA fragments was carried out in a thermocycler as follow:

1. Heat lid to 110°C
2. Temp. 98.0°C for 30s – initial denaturation
3. Start cycle, 35x
 - a. Temp. 98°C for 10s – denaturation step
 - b. Temp. x°C for 30s – annealing step
 - c. Temp. 72°C for 30s/kb – extension step
4. Close cycle
5. Temp. 72°C for 10min – final extension
6. Hold at 4°C

Following PCR amplification, DNA was purified (See Section 2.2.3.4) before proceeding with restriction digestion.

2.2.3.2.1.2 GoTaq[®] Polymerase

GoTaq[®] polymerase was used to amplify small fragments of DNA (< 1kb). Indeed, as a Taq DNA polymerase, GoTaq[®] lacks the 3'→5' exonuclease proofreading activity and can introduce errors if amplifying long fragments. GoTaq[®] generates DNA amplicons with 3'-end A overhangs.

Reactions were prepared as shown in **Table 2.21**.

Table 2.21 | GoTaq[®] PCR reaction mix

gDNA: genomic DNA. * cDNA synthesis reaction mixture from 1µg of total RNA (Should be ≤ 10% of reaction total volume).

Components	20µL reaction	50µL reaction
5X Green GoTaq [®] Flexi Buffer (Contains two dyes, yellow and blue, for easy monitoring of gel electrophoresis)	4µL	10µL
MgCl ₂ (25mM)	3.2µL	8µL
dNTPs (10mM)	0.4µL	1µL
Forward primer (10µM)	1µL	2.5µL
Reverse primer (10µM)	1µL	2.5µL
Template DNA: a. gDNA or b. cDNA	100ng of gDNA 2µL of cDNA*	250ng of gDNA 5µL of cDNA*
GoTaq [®] DNA Polymerase (5U/µL) * Added last	0.1µL	0.25µL
ddH ₂ O	Up to 20µL	Up to 50µL

Melting temperature of each primer was determined using the Promega Tm Calculator web tool (www.promega.com/biomath). For a specific primer-pair, the annealing temperature was chosen, as a rule of thumb, 3°C below the lowest melting temperature.

Amplification of the DNA fragments was performed in a thermocycler as follow:

1. Heat lid to 110°C
2. Temp. 95.0°C for 3min – initial denaturation
3. Start cycle, 35x
 - a. Temp. 95°C for 45s – denaturation step
 - b. Temp. x°C for 30s – annealing step
 - c. Temp. 72°C for 1min/kb – extension step
4. Close cycle
5. Temp. 72°C for 10min – final extension

6. Hold at 4°C

The number of cycles were increased to 40x for cDNA amplification.

GoTaq® polymerase was used to amplify the genomic region targeted by the sgRNAs. Subsequently, samples were either sent for sequencing (See Section 2.2.4.3.8.1) or PCR purified to proceed with T7 assay (See Sections 2.2.3.4.2 and 2.2.4.3.6).

2.2.3.3 Restriction enzyme digestion

Double restriction enzyme (RE) digestions were used in the cloning procedure to cut both recipient plasmid and DNA insert fragment. RE were selected to be cutting within the multiple cloning site (mcs) of the recipient plasmid but not within the insert sequence. Whenever possible the high-fidelity version of the RE was used in Cutsmart Buffer.

Optimal conditions (reaction buffer, duration, denaturation conditions...) for the digestion were determined using the NEB double digest web tool. Then, the reaction described in **Table 2.22** was prepared and incubated at 37°C from 1hr, for classic digestions, to overnight when digesting large amounts of DNA.

Recipient vectors were treated with CIP (Calf intestinal alkaline phosphatase) by adding 1µL directly to the digestion reaction to dephosphorylate the 5'-ends of the DNA and prevent re-circularisation of the vector. The solution was incubated for another 30min at 37°C.

Digested vectors were purified on agarose gel while digested DNA inserts were purified by column purification to reduce DNA loss

Table 2.22 | Restriction enzyme digestion

The definition states that 1 unit of enzyme is enough to digest 1µg of λ DNA in 1 hour when incubated at 37°C. However, to accommodate variability of DNA, it is recommended to increase the enzyme:DNA ratio 5-10 folds. As most enzymes from New England Biolabs Inc. have a 20 units/µL concentration, 1µL/µg of DNA to be digested was used as a rule of thumb. In any restriction digestion, the amount of glycerol, component of the enzyme storage buffer, has to be less than 10% of the total volume to avoid star activity (being <5µL in a 50µL reaction).

Components	Amounts
10X Reaction Buffer	5µL
DNA (vector or PCR product)	500ng-4µg
Restriction enzyme I * Added last	1µL per µg of DNA to digest
Restriction enzyme II * Added last	1µL per µg of DNA to digest
ddH ₂ O	Up to 50µL

Restriction digestions were also performed as diagnostic digests to verify that an insert was successfully cloned into the recipient vector (500ng of plasmid). Resulting fragments were analysed by gel electrophoresis before resorting to sequencing of the plasmid.

2.2.3.4 DNA purification

2.2.3.4.1 Agarose gel extraction

Agarose gel electrophoresis is commonly used to separate DNA fragments by their length in base pairs. DNA is negatively charged and will move toward the positive electrode when subjected to an electrical current.

The typical percentage of agarose gels used here was 1% and allowed a good separation of DNA fragments ranging from 100bp to 10kb.

After PCR amplification, PCR products were run on agarose gel for separation and isolation of the desired product. To that end, an agarose solution was prepared by adding the appropriate amount of agarose powder to TAE buffer 1X (40 mM Tris, 20 mM acetic acid, 1 mM EDTA). The solution was then microwaved in 30s increments. During those intervals, the flask was swirled to allow homogenisation of the melting. The total microwaving time varied from 1min to 3min depending on the volume of solution. Once the agarose was completely dissolved and the solution was as clear as water, it was allowed to cool down to approximately 50°C. SYBR[®] Safe DNA gel stain was then added to the agarose solution (1:10 000 dilution) to later be able to visualize DNA with a UV light. The agarose was poured into the gel tray containing a comb, and left to solidify at room temperature for 20-30min. The agarose gel was then placed into the electrophoresis kit, submerged with TAE 1X buffer and the comb was delicately removed. Next, 6X Purple gel loading dye was added to the DNA samples (except for PCR reactions which already have dyes from the buffer). Samples were carefully loaded into every other lanes of the agarose gel when purifying DNA to avoid contamination from adjacent samples. An appropriate DNA ladder, 100bp, 1kb or 2-log, was added to the gel to be able, later on, to assess the size of the DNA fragments. The gel was run at 80-100V until the lower dye line is approximately 75-80% through the gel. DNA fragments were visualised using a *Blue LED Illuminator* (GeneFlow, Nippon Genetics Europe, Taiwan). The gel was exposed for as little time as possible to minimize DNA damage. The band(s) of interest were excised from the gel using a sterile scalpel and the agarose was trimmed as close to the band as possible. Finally, DNA was extracted using the NucleoSpin[®] Gel and PCR clean-up kit (Macherey-Nagel) according to manufacturer's instructions.

Agarose gel electrophoresis was also used simply to assess size of DNA fragments without subsequent extraction and purification. In that case, gels were imaged using a *Gel Doc™ EZ System (BioRad)*.

2.2.3.4.2 Column purification

To purify DNA from proteins (enzymes), nucleotides, primers, dyes and buffer salts, column clean-up was performed using the NucleoSpin® Gel and PCR clean-up kit (Macherey-Nagel) according to manufacturer's instructions. These columns are made to purify up to 15µg of DNA (ranging from 50bp to 20kb) with a recovery of 60-90%.

This method was preferred after a PCR reaction when there was a clean single product (verified by running a small amount of the reaction on an agarose gel).

2.2.3.4.3 Phenol-chloroform DNA purification

Phenol-chloroform extraction of DNA relies on liquid-liquid phase separation between an aqueous phase, containing the DNA, and an organic phase, composed of phenol-chloroform. Phenol has a higher density (1.07g/cm³) than water (1g/cm³) and will therefore constitute the lower phase. To accentuate the phase separation and reduce cross-contamination of the aqueous phase, phenol is mixed with chloroform (1.47g/cm³). Isoamyl alcohol is added to prevent foaming. In this mixture, DNA and RNA will be soluble in the aqueous phase while proteins and polymers will precipitate at the interface between phenol and water; Lipids will dissolve in the organic phase. The pH of the phenol determines the separation of DNA and RNA. Neutral or slightly alkaline pH (pH 7-8) results in both DNA and RNA being soluble in the aqueous phase. However, acidic pH, while retaining RNA in the aqueous phase, shifts DNA to the phenol phase.

This method was used to purify either a large quantity of plasmid, and thereby decrease the loss of DNA inherent to other purification methods, or to extract genomic DNA from cells. The latter will be described in more details in Section 2.2.4.3.4, as extra steps are required.

First, an equal volume of Phenol:Chloroform:Isoamyl alcohol pH 8.0 (Lower phase of the bottle) was added to the aqueous solution (containing the plasmid) and the tube was inverted to mix. Phase separation was achieved by centrifugation for 2min at top speed in a benchtop centrifuge. The top phase (aqueous phase, containing the DNA) was transferred into a new 1.5mL tube. Centrifugation and extraction of the aqueous phase into a new tube were repeated as described. Then, 1:10 volume of 3M Sodium acetate pH 5.2 was added to the aqueous phase.

Proper homogenisation of the salts around the DNA molecules was ensured by inverting the tube a few times. Next, DNA precipitation was performed by adding a 1:1 volume (as aqueous phase) of room temperature isopropanol followed by thorough vortexing and, the tube was incubated for 1-2hrs at -80°C or overnight at -20°C. DNA was collected at the bottom of the tube by centrifugation for 30min at 13000xg, 4°C, after which, the supernatant was carefully discarded. The DNA pellet was washed with 1mL of 70% EtOH. DNA was once again collected at the bottom of the tube by centrifugation for 5min at top speed. The supernatant was carefully discarded and the DNA pellet was allowed to dry for a few minutes (until transparent) before being resuspended in ddH₂O (the volume has to be adjusted to the size of the pellet – typically 30-50µL). DNA concentration and purity were measured with a NanoDrop and the purified DNA was stored at -20°C.

2.2.3.5 Nucleic acid quantification and purity

Nucleic acid concentration and purity were determined with a NanoDrop Lite spectrophotometer from Thermo Scientific. First, a blank measurement was performed with the reference solution (dH₂O or elution buffer). Absorbance of 1µL of the sample at 260nm was then measured and normalised to the reference spectrum (blank). The concentration of the sample is calculated by the machine using a modified equation of the Beer-Lambert equation:

$$\text{Concentration (ng/}\mu\text{L)} = \frac{(A * \epsilon)}{b}$$

Where A is the absorbance of the sample at 260nm, ϵ is the wavelength-dependent extinction coefficient (double-stranded DNA: 50ng.cm/µL, single-stranded DNA: 33ng.cm/µL, RNA: 40ng.cm/µL) and b is the length travelled by light (in cm – 1cm in that case).

Purity of DNA samples was assessed with the A260/280 ratio: between 1.8-2.0 is considered “pure” DNA (~2.0 for RNA).

2.2.3.6 Ligation

DNA ligation was performed using a T4 DNA ligase (#EL0011 – ThermoFisher) to achieve the construction of a recombinant plasmid between a backbone and an insert.

In most cases, ligation reactions involved DNA fragments with overhangs, generated by restriction enzyme digestion. The T4 ligase was then creating covalent bonds to permanently join the phosphate backbone of compatible cohesive ends. Beforehand, backbones were

dephosphorylated using CIP (Calf intestinal alkaline phosphatase) treatment to decrease the likelihood of re-circularisation. Proper DNA ligation requires at least one phosphorylated 5'-end, provided by the RE digested inserts, to create an intact phosphodiester bond and thereby "repair the double-stranded break"

For some of the plasmids generated in this work such as the deletion constructs, ligation was performed to re-circularise a blunt-ended vector. In that case, PCR was performed using phosphorylated 5'-end primers.

Control reactions, containing the digested backbone but not the insert, were carried out in parallel to check for unwanted re-circularisation of the vector in spite of 5'-end dephosphorylation.

Amounts and backbone:insert ratios were calculated using the following equation that gives a 1:1 molar ratio:

$$ng\ of\ insert = ng\ of\ backbone * \frac{length\ of\ insert\ (bp)}{length\ of\ backbone\ (bp)}$$

Usually, 50ng of backbone and a backbone:insert ratio of 1:5 were used in a 20µL reaction.

First, the reaction described in **Table 2.23** was prepared and the T4 DNA ligase was left to catalyse the reaction overnight at room temperature. The complete plasmid was then ready for bacterial transformation.

Table 2.23 | Ligation reaction

Components	Amounts
10X T4 DNA Ligase buffer (400 mM Tris-HCl, 100 mM MgCl ₂ , 100 mM DTT, 5 mM ATP, pH 7.8 at 25°C)	2µL
Backbone	50ng
Insert	1:5 molar ratio (see above)
T4 DNA Ligase (5 Weiss U/µL) * Added last	1µL
ddH ₂ O	Up to 20µL

2.2.3.7 Bacterial transformation

Bacteria transformation was performed using the heat shock procedure. Steps were carried out in a sterile environment (Bunsen burner).

First, a 50µL aliquot of competent cells (E. coli NovaBlue) was thawed on ice for 10min. In the meantime, LB agar plates supplemented with the appropriate antibiotics were pre-warmed at

37°C. Then, a sterile environment was created and the DNA solution to transform was pipetted into the bacteria. The bottom of the tube was gently flicked a few times to ensure homogenous repartition of the DNA. The quantity of DNA used depended on the source:

- a. 500ng of a validated plasmid
- b. 5µL of a 10µL ligation reaction (CRISPR)
- c. 7µL of a 20µL ligation reaction

The tube was incubated on ice for 15min followed by a heat shock of 1min at 42°C. During this step, the abrupt increase in temperature alters the bacteria membrane integrity by creating holes thereby allowing the plasmid to enter cells. The tube was then placed back on ice for 2min. The subsequent chilling on ice restores the membrane integrity and traps the plasmid inside the cells. 500µL of LB medium were added to the bacteria and the tube was incubated for 30-45min (Amp^R plasmids) or 1h15min (Kana^R plasmids) at 37°C under constant shaking (230rpm). During this incubation, cells develop resistance to the antibiotics provided by the plasmid which allows them to later grow on Amp⁺ or Kana⁺ agar plates. This step is critical for Kanamycin resistance. Following the incubation, an aliquot of bacteria culture was plated on an LB agar plate containing the appropriate antibiotics: A drop of bacteria culture was pipetted at the centre of the agar plate and the liquid was distributed evenly by moving a sterile spreader back and forth while rotating the plate until the liquid was absorbed by the agar. The amount of bacteria plated depended on the type DNA being transformed:

- a. Validated plasmid: Plate 10% (50µL) of the culture.
- b. Ligation reaction: Plate 100% of the culture by following these extra steps:
Bacteria were centrifuged for 2min at 3615xg, 400µL of supernatant were discarded and the bacteria pellet was resuspended in the remaining 100µL which were plated onto the agar plate.

The plates were then incubated upside down overnight at 37°C. The next morning, the plates were inspected for single colonies. Finally, plates were sealed with Parafilm[®] and stored at 4°C until inoculation and up to 4-6 weeks.

2.2.3.8 *Plasmid isolation and purification*

2.2.3.8.1 [MiniPrep](#)

Following bacteria transformation with a ligation product, a 5mL culture was first inoculated. This scale was allowing the screening of several colonies and was sufficient to run the validation steps before further propagation of the correct plasmid.

First, a sterile environment was created and 5mL of LB medium supplemented with the appropriate antibiotics were prepared in a 10mL bacteria tube. A single colony from the agar plate was picked using a sterile loop and inoculated into the culture. The culture was loosely covered with the provided cap so as not to be air-tight. The tube was then incubated with a ~45° angle overnight (~16hrs) at 37°C under constant shaking (230rpm). The next morning, the culture was checked for growth. To facilitate future propagation of the plasmid, a glycerol stock was prepared: 500µL of 60% glycerol/ddH₂O were thoroughly mixed with 500µL of the bacterial culture into a 1mL screw-top tube and stored at -80°C. The remaining of the culture was centrifuged for 15min at 1000xg ≤RT to pellet bacteria before proceeding with plasmid isolation.

Plasmids were isolated and purified using the GeneJET Plasmid Miniprep Kit according to manufacturer's instructions (typical yield 10-15µg). DNA was eluted in ddH₂O (typically 30-50µL) and the concentration and purity were assessed with a NanoDrop (See Section 2.2.3.5). A diagnostic digest was performed to verify the presence and the size of the insert. Finally, the plasmid was validated with sequencing.

2.2.3.8.2 [MidiPrep](#)

For validated plasmid propagation, the scale was increased to a 100mL culture. A sterile environment was created and 100mL of LB medium supplemented with the appropriate antibiotics were prepared in a 250mL conical flask. Bacteria were inoculated from either:

- a. A single colony from an agar plate (pre-warmed) using a sterile loop.
or
- b. Glycerol stock. The desired glycerol stock was removed from -80°C and placed on dry ice to prevent complete thawing. The surface of the frozen stock was scraped with a sterile 200µL pipette tip to harvest some bacteria which was dropped in the LB medium.

The culture was loosely covered with aluminium foil and the flask was incubated overnight (~16hrs) at 37°C under constant shaking (230rpm). The next morning, the culture was checked for growth. If needed, a glycerol stock was made: 500µL of 60% glycerol/ddH₂O to 500µL were thoroughly mixed with 500µL of culture into a 1mL screw-top tube and stored at -80°C. The remaining of the culture was centrifuged for 15min at 1000xg ≤RT to pellet bacteria before proceeding with plasmid isolation.

Plasmids were isolated and purified using the Nucleo Bond[®] Xtra Midi kit according to manufacturer's instructions (typical yield 500-750µg). DNA was resuspended in ddH₂O (typically 200-300µL to begin with) and the concentration and purity were assessed with a NanoDrop (See Section 2.2.3.5).

2.2.3.9 DNA sequencing

DNA sequencing was used to verify constructs or assess indels generated by CRISPR/Cas9 after PCR amplification of the region of interest from gDNA.

Sequencing was performed at the University of Sheffield Core Genomic Facility where they used the Applied Biosystems' 3730 DNA Analyser and the BigDye™ Terminator v3.1 Cycle Sequencing Kit.

Usually, clean reads of 800-900 base-pairs were achieved, however, to be on the safe side, an average of about 700bp was considered and primers were designed accordingly.

Electropherogram data were analysed using SnapGene Viewer. When "Ns" were found in the results, it meant the sequencing analysis programme could not confidently assign a single nucleotide to that particular position. Depending on the template being analysed, a "N" may indicate a high signal-to-noise ratio or the occurrence of two nucleotides at that one position in the case of a CRISPR heterozygote for example. Often, by manually looking at the chromatogram, one was able to "determine" the nucleotide(s) for that particular position. The sequences were then compared to the original one using a NCBI nucleotide blast

2.2.4 CRISPR/Cas9 and stable knockout cell lines

CRISPR (clustered regularly interspaced short palindromic repeats) was discovered as an immune memory and defence mechanism against bacteriophage infection (309-311) and is now used as a powerful gene editing technique. By introducing Cas9 protein into the desired organism, along with a single guide-RNA, one can target any locus in the genome. The desired target site needs to be close to a PAM (Protospacer adjacent motif) sequence that the Cas9 will bind to induce a DNA double stranded break (DSB) a few nucleotides upstream of this motif. Two pathways can then occur to repair the DSB: non-homologous end-joining (NHEJ) repair or homology-directed repair (HDR) (**Figure 2.1**). The first pathway, NHEJ, is very error-prone and nucleotide insertions or deletion occur when cells try to repair their DNA at the targeted site, potentially inducing a frameshift, leading to a premature stop codon and

eventually gene knockout. The HDR pathway, on the other hand, uses exogenous repair templates to precisely modify the gene. In this thesis, the NHEJ route was used to generate complete knockout cell lines.

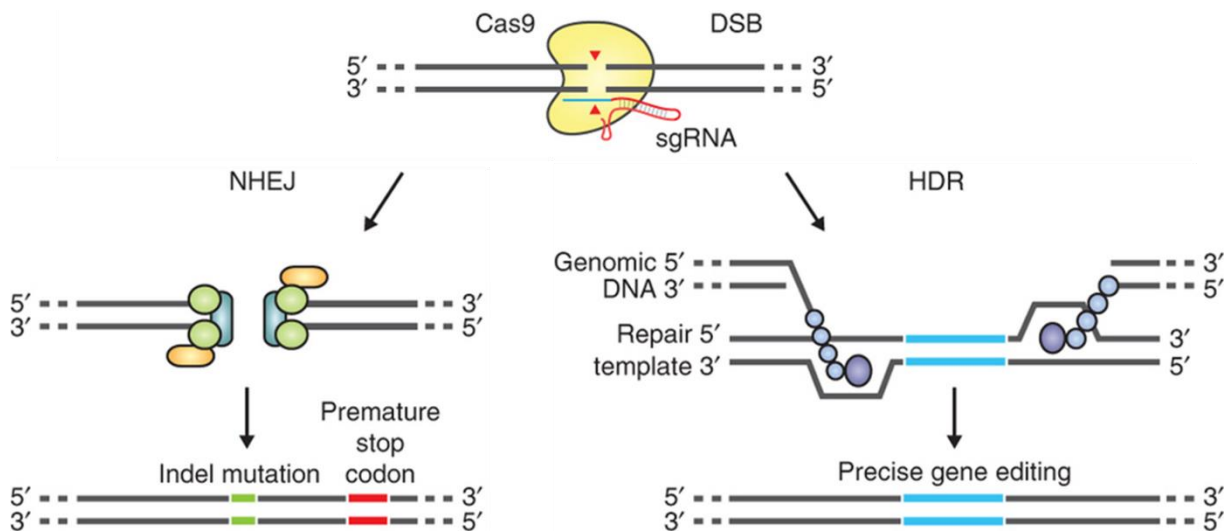


Figure 2.1 | CRISPR/Cas9 gene editing and repair mechanisms.

The Cas9 directed to the desired locus via the single guide-RNA (sgRNA), induces a DNA double stranded break (DSB) which can be repaired in two ways. The Non-Homologous End Joining (NHEJ) repair will, in most cases, introduce some insertion/deletion mutations and the appearance of a premature stop codon causing a gene knockout. The Homology Directed Repair (HDR) uses an exogenously provided template that lead to a precise editing of the gene. Figure 2 from (303).

2.2.4.1 sgRNA design

2.2.4.1.1 Human MAGI-1 knockout

We aimed at generating a complete MAGI-1 knockout in DLD-1 cells, using the CRISPR NHEJ repair mechanism. hMAGI-1 single guide RNAs targeting Exon1 were designed using the CRISPR MIT design tool (<http://crispr.mit.edu/>), developed by the Zhang Lab (303).

Table 2.24 | MAGI-1 sgRNAs targeting Exon1

Table recapitulating the two single guide RNAs selected to induce MAGI-1 knockout. BbsI site. Oligonucleotide numbers (#) refer to **Table 2.9**.

Single guide RNA	Targeted Sequence_PAM	Exonic off-targets
sgRNA1 (G1) (#1 and #2)	GGAGTTTCCGTACGTCGGAG_CGG Top: 5' - CACCGGGAGTTTCCGTACGTCGGAG - 3' Bottom: 5' - AAACCTCCGACGTACGAAACTCC - 3' Duplex: 5' - CACCGGGAGTTTCCGTACGTCGGAG - 3' 3' - CCTCAAAGGCATGCAGCCTCAAA - 5'	None

sgRNA2 (G2) (#3 and #4)	TTGCCCCGCTATGACGTGCT_GGG Top: 5' - CACCGTTGCCCCGCTATGACGTGCT - 3' Bottom: 5' - AACAGCACGTTCATAGCGGGGCAAC - 3' Duplex: 5' - CACCGTTGCCCCGCTATGACGTGCT - 3' 3' - CAACGGGGCGATACTGCACGACAAA - 5'	SIPA1 (NM_006747) TTTGCCCACTATGACGTGCAAAG CNTN5 (NM_001243270) TTGCTTAGCTATGAAGTGCTAAG
----------------------------	--	---

Two sgRNAs were selected amongst the highest scores with an extra criterion of fewest exonic off-targets (**Table 2.24**). Plus, the two guides were not too close to each other so as to increase the chances of efficiency.

2.2.4.1.2 Human MAGI-2

Table 2.25 | MAGI-2 sgRNAs targeting Exon5

Table recapitulating the two single guide RNAs selected to induce MAGI-2 knockout. BbsI site. Oligonucleotide numbers (#) refer to **Table 2.9**. (\Rev) indicates that the single guide RNA targets the reverse strand (See Annex 2).

Single guide RNA	Targeted Sequence_PAM	Exonic off-targets
sgRNA9 (G9) (#5 and #6)	GGCTGACTGTACTGGTGC_AGG (\Rev) Top: 5' - CACCGGGCTGACTGTACTGGTGC - 3' Bottom: 5' - AACGCACCAGTGTACAGTCAGCC - 3' Duplex: 5' - CACCGGGCTGACTGTACTGGTGC - 3' 3' - CCGACTGACATGTGACCACGACAAA - 5'	DEPDC5 (NM_014662.5) CCTGCACCAGTATGAAGTCAGCA KCNN4 (NM_002250.3) CCAGCACCAGTCCCAGCCGGCC SGSM2 (NM_014853.3) CCTGCACCAGTCTGCAGAGAGCC PER1 (NM_002616.3) GGCTGACTGTTCACTGCTGCGGG EPHA10 (NM_001099439.2) CCTTGCCAGTGTCCAGTCAGCC FOXO3 (NM_001455.4) CCAGCAGCAGTCTCCTGTCAGCC KIF13B (NM_015254.4) GGCTGACTGCACCATGATGCGGG SMTNL1 (NM_001105565.2) GGCTGACTGTGCTCAGCTGCTGG ARHGEF38 (NM_001242729.2) GGCTTACTCCACACTTGTGCCGG
sgRNA4 (G4) (#7 and #8)	CAGACCCATTGCCTGATAAC_TGG Top: 5' - CACCGCAGACCCATTGCCTGATAAC - 3' Bottom: 5' - AACGTTATCAGGCAATGGGTCTGC - 3' Duplex: 5' - CACCGCAGACCCATTGCCTGATAAC - 3' 3' - CGTCTGGGTAACGGACTATTGACAAA - 5'	/

We aimed at generating a complete MAGI-2 knockout in DLD-1 cells, using the CRISPR NHEJ repair mechanism. Ensembl lists only two isoforms of the protein with an alternatively spliced Exon13. However, Hirao and co-workers reported two alternative START codons yielding three isoforms that they denominated α , β and γ (241). As even the shortest isoform, γ , still possesses the WW domains and PDZ domains, it is highly probable that it would conserve most of MAGI-2 full length interactions and function. We decided to design sgRNAs targeting Exon5 of the gene, after all potential alternative START codons. As the MIT webtool was no longer operating, we used the CRISPOR webtool (312) (<http://crispor.tefor.net/>) to design two sgRNAs targeting MAGI-2 Exon5 (**Table 2.25**). The same criteria were used to select guides: compromise between high specificity score and low predicted exonic off-targets.

2.2.4.1.3 Human MAGI-3

Table 2.26 | MAGI-3 sgRNAs targeting Exon1

Table recapitulating the two single guide RNAs selected to induce MAGI-3 knockout. BbsI site. Oligonucleotide numbers (#) refer to **Table 2.9**. lncRNA: Long non-coding RNA.

Single guide RNA	Targeted Sequence_PAM	Exonic off-targets
sgRNA5 (G5) (#9 and #10)	GACTTCGGCGCGGAGATCCG_CGG Top: 5' - CACCGGACTTCGGCGCGGAGATCCG - 3' Bottom: 5' - AAACCGGATCTCCGCGCCGAAGTCC - 3' Duplex: 5' - CACCGGACTTCGGCGCGGAGATCCG - 3' 3' - CCTGAAGCCGCGCCTCTAGGCCAAA - 5'	GON4L (NM_032292.5) CCTCGGAGCGCCGCGCCGAGTG LINC00543 (NR_135254.1) lncRNA CCCCGCACCTCCGCGCCGTAGTT RP1-118J21.25 (No protein) GGCCTCGGCGCAGAGATCCTAGG RP11-401P9.7 (No protein) CCTCAGGTCTCCGCACTGAAGTC
sgRNA6 (G6) (#11 and #12)	GTAAACGGGACGCCTGTCAG_CGG Top: 5' - CACCGGTAAACGGGACGCCTGTCAG - 3' Bottom: 5' - AAACCTGACAGGCGTCCCCTTTAC - 3' Duplex: 5' - CACCGGTAAACGGGACGCCTGTCAG - 3' 3' - CCATTTGCCCTGCGGACAGTCCAAA - 5'	PLCL1 (NM_006226.4) CCGCTGCCGGGCGTCCCCTTTTC CPA1 (NM_001868.4) CCTATGAAGGCGTCCCATTAC LINC01134 (NR_024455.1) lncRNA CCCCTGAGAGGCTTACCGTTTCC

We aimed at generating a complete MAGI-3 knockout in DLD-1 cells, using the CRISPR NHEJ repair mechanism. Ensembl lists four transcripts: MAGI3-201, 202, 203 and 204, leading to three isoforms of the protein. CRISPOR webtool (312) (<http://crispor.tefor.net/>) was used

to design two sgRNAs targeting Exon1 (**Table 2.26**). The criteria of selection were the same as previously for MAGI-1 and MAGI-2. G5 is targeting the beginning of Exon1 and has four predicted exonic off-targets. G6, on the other hand, targets the end of Exon1 and was predicted to have three exonic off-targets.

2.2.4.2 Cloning of sgRNA in Cas9 vectors

The cloning protocol was adapted from the Zhang Lab (303).

2.2.4.2.1 Phosphorylation and annealing of oligonucleotides

The partially complementary oligonucleotides were phosphorylated at their 5'-ends and then annealed to allow cloning into the pSpCas9(BB) vectors. The mixture described in **Table 2.27** was prepared and the solution was first incubated at 37°C for 30min to allow phosphorylation of the oligos 5' ends by the polynucleotide kinase (PNK). Then, complete denaturation of the mixture was achieved by a 5min incubation at 98°C in a heat block. Finally, the block containing the tube was extracted from the machine and allowed to cool down very slowly overnight on the bench. This step ensured annealing of the complementary oligonucleotides.

Table 2.27 | T4 Polynucleotide Kinase reaction mix

Components	Amount (μL)
sgRNA TOP (100μM)	1
sgRNA BOTTOM (100μM)	1
T4 DNA ligase Buffer 10x (400mM Tris-HCl, 100mM MgCl ₂ , 100mM DTT, 5mM ATP, pH 7.8 at 25°C)	1
T4 Polynucleotide Kinase (PNK)	1
ddH ₂ O	6
Total	20

2.2.4.2.2 Digestion of the Cas9 vector

PX458 Cas9-GFP and PX459 Cas9-PuroR vectors were digested using the restriction enzyme BbsI (GAAGACNN↓N>NNN↑), where N is any of the four bases. These vectors contain two different BbsI sites that allow cloning of the sgRNA between the U6 promoter and the gRNA scaffold (**Figure 2.2**).

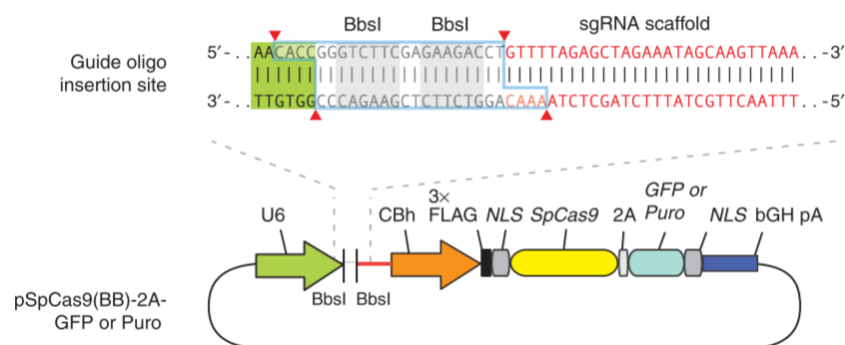


Figure 2.2 | BbsI cloning site in pSpCas9(BB) vectors

Taken from (303).

First, pSpCas9(BB) vectors were digested as indicated in **Table 2.28** for 1hr at 37°C. The digested backbone 5'-ends were then, dephosphorylated by adding 1µL of CIP (Alkaline Phosphatase, Calf Intestinal) to the reaction for another 30min at 37°C. This step prevented re-circularisation of the vector. Finally, the digested vector was purified on agarose gel. See Section 2.2.3.4.1 for detailed protocol.

Table 2.28 | BbsI restriction enzyme digestion of pSpCas9(BB) vectors

Components	Amount (µL)
pSpCas9(BB) vector (2µg)	x
Cutsmart Buffer 10X	5
BbsI-HF enzyme	1
ddH2O	Up to 50
Total	50

2.2.4.2.3 Ligation of the sgRNAs into a Cas9 vector

Table 2.29 | Ligation reaction of sgRNAs into pSpCas9(BB) vectors

*: Added last.

Components	Amount (µL)
pSpCas9(BB) digested vector (100ng)	x
Diluted oligo duplex	1
T4 DNA ligase Buffer 10x (400mM Tris-HCl, 100mM MgCl ₂ , 100mM DTT, 5mM ATP, pH 7.8 at 25°C)	1
T4 ligase *	0.5
ddH2O	Up to 10
Total	10

The annealed sgRNAs were ligated into the BbsI digested pSpCas9(BB) vectors. A no-insert ligation negative control containing only the pSpCas9(BB) digested vector was carried out in parallel. Prior to the ligation step, annealed sgRNAs were diluted 1:200 by adding 1µL of oligo to 199µL of room temperature ddH₂O. The ligation reaction was then set up for each guide as indicated in **Table 2.29** and the mixture was incubated at room temperature for 1-2hrs.

2.2.4.2.4 Validation and amplification of the pSpCas9(sgRNA) vectors

2.2.4.2.4.1 Validation of the pSpCas9(sgRNA) vectors

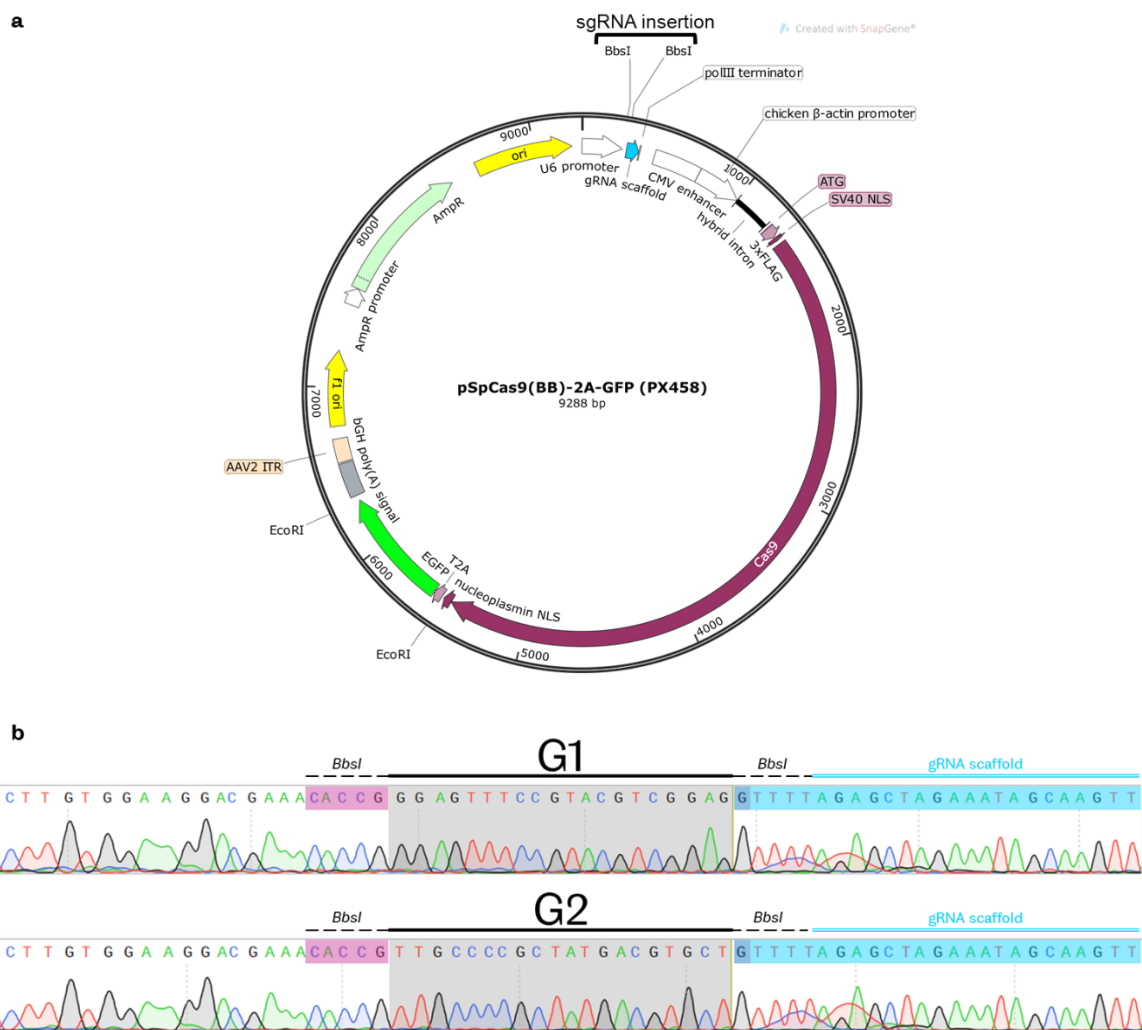


Figure 2.3 | Molecular cloning of G1 and G2 into PX458-Cas9-GFP vector.

a. SnapGene map of the pSpCas9(BB)-2A-GFP vector, also called PX458, used as backbone to insert the sgRNAs (303). The sgRNA insertion site, lined on both sides by BbsI sites, is followed by a gRNA scaffold for the *Streptococcus pyogenes* CRISPR/Cas9 system. Within the same vector is found the sequence coding for the Cas9 endonuclease from the *Streptococcus pyogenes* Type II CRISPR/Cas system. Nuclear localisation signals (NLS) are found upstream and downstream of the Cas9 protein to target it to the nucleus where it will inflict DNA double

stranded breaks at the site indicated by the sgRNA. To allow easy identification and sorting of successfully transfected cells, a EGFP tag has been added after the Cas9 sequence. The presence of a 2A peptide from *Thosea asigna* virus capsid protein (T2A) ensures that the Cas9 protein will be separate from the fluorescent marker (Addgene #48138). **b.** Sequencing results of the successfully clones sgRNA1 (G1) and sgRNA2 (G2) within the PX458 vector using the U6 primer (#25 in **Table 2.7**).

First, 5µL of the ligation reaction were transformed into *E. coli Nova blue* competent cells with using the heat-shock protocol (See Section 2.2.3.7 for detailed protocol). The bacteria were plated onto an LB plate containing 100µg/mL ampicillin and incubated overnight at 37°C. The next morning, plates were inspected for colonies. The no-insert negative control plate should have very few to no colonies while the pSpCas9(sgRNA) should contain tens to hundreds of colonies. 2-3 colonies were picked to check for successful insertion of the sgRNA. Using a sterile loop, a single colony was inoculated into 5mL of LB medium supplemented with 100µg/mL ampicillin. The culture was incubated at 37°C overnight under constant shaking. The next day, a glycerol stock of each culture was prepared to facilitate future amplification of the plasmid: 500µL of 60% glycerol/ddH₂O were thoroughly mixed with 500µL of the bacterial culture into a 1mL screw-top tube and stored at -80°C. The pSpCas9(sgRNA) plasmid was isolated from each culture using a GeneJET Plasmid Miniprep Kit according to manufacturer's instructions. Finally, correct insertion of the sgRNA into the Cas9 vector was verified by DNA sequencing (**Figure 2.3**) using the U6 FWD primer (#25 in **Table 2.7**).

2.2.4.2.4.2 Amplification of the pSpCas9(sgRNA) vectors

To amplify the validated pSpCas9(sgRNA) vector, a 100mL culture of LB medium supplemented with 100µg/mL ampicillin was inoculated using the corresponding glycerol stock. The culture was then incubated at 37°C overnight under constant shaking. The pSpCas9(sgRNA) was isolated from each culture using a NucleoBond[®] Xtra Midi kit according to manufacturer's instructions. Once again the presence of the sgRNA was checked by sequencing using the U6 FWD primer (#25 in **Table 2.7**).

2.2.4.3 Generation and screening of stable knockout cell lines

DLD-1 cells were selected to generate CRISPR knockouts.

First, hMAGI-1 knockout clones were generated using the pSpCas9(sgRNA)-2A-GFP plasmid (#25 of **Table 2.10**) containing either G1 or G2 and FACS sorting GFP positive cells into single cells.

Subsequent hMAGI-2 or hMAGI-3 knockouts were performed by transfecting validated hMAGI-1 KO clones, G1 8 (A) and G2 14 (B), with PuroR-Cas9 vector (#26 of **Table 2.10**) containing sgRNAs. In parallel, single MAGI-2 and MAGI-3 knockouts were generated from DLD-1 WT cells. To increase the efficiency of gene editing, G9 & G4 were used simultaneously for MAGI-2 and G5 & G6 for MAGI-3. Here, first a bulk population was generated by puromycin selection. Then, single clones were isolated by FACS sorting of live cells.

From that moment on, extra care was given to not cross-contaminate samples and clones.

2.2.4.3.1 Transfection of sgRNA

Table 2.30 | Transfection combinations for the generation of MAGI single and double knockouts

Numbers (#) refer to the expression constructs in **Table 2.10**.

Gene targeted	Vector(s) transfected	Cell line transfected
hMAGI-1	pSpCas9(sgRNA1)-2A-GFP (#27) (G1)	DLD-1 WT
	pSpCas9(sgRNA2)-2A-GFP (#28) (G2)	DLD-1 WT
hMAGI-2	pSpCas9(sgRNA9)-2A-Puro (#29) + (G9+G4)	DLD-1 WT DLD-1 G1 8 (A) hMAGI-1 KO DLD-1 G2 14 (B) hMAGI-1 KO
	pSpCas9(sgRNA4)-2A-Puro (#30)	
hMAGI-3	pSpCas9(sgRNA5)-2A-Puro (#31) + (G5+G6)	DLD-1 WT DLD-1 G1 8 (A) hMAGI-1 KO DLD-1 G2 14 (B) hMAGI-1 KO
	pSpCas9(sgRNA6)-2A-Puro (#32)	

One day prior to transfection, cells were seeded at 2.5×10^5 cells/well in 6-well plates (2 wells/sgRNA). Cells were then transfected with Lipofectamine2000 as follow in antibiotics-free medium:

$$\begin{cases} 150\mu\text{L of OPTIMEM} + 5\mu\text{L of Lipofectamine2000} \\ 150\mu\text{L of OPTIMEM} + 2\mu\text{g of pSpCas9(sgRNA)} \end{cases}$$

Medium was changed to complete medium (with antibiotics) after 24hrs and transfection efficiency was monitored with a fluorescence microscope. **Table 2.30** lists the transfections carried out in DLD-1 for the generation of knockout clones. 48hrs post-transfection, transfected cells were split 1:1 and either sorted by FACS into GFP positive single cells (hMAGI-1) or selected using puromycin (hMAGI-2 and hMAGI-3).

2.2.4.3.2 Puromycin selection of DLD-1 cells

2.2.4.3.2.1 Determination of the minimum effective dose

Puromycin is an antibiotic widely used for mammalian cells selection. It interferes with protein synthesis by mimicking aminoacyl-tRNA and binding to ribosomes. Puromycin can be inactivated by an enzyme produced by *Streptomyces alboniger* called puromycin-N-acetyltransferase or PAC which acetylates puromycin and thereby prevents its binding to ribosomes. Puromycin-N-acetyltransferase is commonly referred to as puromycin resistance gene (PuroR) and used to provide a selective advantage to transfected mammalian cells and generate stable cell lines.

To determine the minimum effective concentration to kill non-resistant DLD-1 WT cells, a kill-curve was performed. Eight puromycin concentrations were tested on duplicate wells: [0; 0.5; 1; 1.5; 2; 2.5; 5; 7 μ g/mL]. First, DLD-1 WT cells were seeded at 1.5×10^5 cells/well in 16 well of a 24-well plate. 24hrs later, puromycin diluted in complete RPMI medium was added at the desired concentrations to the cells. Cell death was monitored daily while refreshing medium every two days. The minimum effective concentration, corresponding to the one able to kill all non-resistant cells within 5 days was selected: 2 μ g/mL.

2.2.4.3.2.2 Generation of stable cell lines

Puromycin selection was carried out to generate bulk populations of MAGI-2 and MAGI-3 single, hMAGI-1/hMAGI-2 and hMAGI-1/hMAGI-3 double KO. In parallel to the pSpCas9(sgRNA)-2A-Puro transfected cells, a dish of non-transfected cells was kept to monitor selection efficiency.

Puromycin selection was started 48hrs after transfection with complete RPMI medium supplemented with 2 μ g/mL of puromycin. Medium was refreshed every two days. The selective pressure was alleviated once all the non-transfected control cells were dead. The bulk populations were then cultured in complete RPMI medium.

2.2.4.3.3 Isolation of single clones by FACS

Cells were sorted with a FACSAria™ Ilu cell sorter with technical support at the Flow cytometry facility of the University of Sheffield Medical School.

96-well plates were prepared beforehand with 200 μ L of complete RPMI medium per well for the sorting. Each population was sorted into 2x 96-well plates to ensure a sufficient number of clones.

Preparation of cells for FACS (see **Table 2.15** for specific volumes):

First, cells were washed with PBS 1X. Dissociation was achieved by adding Trypsin to the cells and placing the dish back in the incubator for 5min. Cells were resuspended with complete RPMI medium and centrifuged for 5min at 130xg to pellet the cells. The supernatant was discarded and cells were resuspended in an appropriate volume of complete medium to allow counting of the cells. Cells were counted and 1×10^6 cells were aliquoted into a new 15mL tube. Cells were centrifuged for 5min at 130xg and resuspended in 500 μ L of OPTIMEM (fluorescent sorting requires clear medium). Proper dissociation of the population into single cells was ensured by filtering the suspension into the cell strainer tube through its mesh cap. The cells were kept on ice until sorting.

2.2.4.3.3.1 Sorting of GFP positive cells

Cells were transfected and prepared as described above. The following samples were prepared:

DLD-1 WT untransfected cells
DLD-1 pSpCas9(sgRNA1)-2A-GFP
DLD-1 pSpCas9(sgRNA2)-2A-GFP

Directly before sorting, the viability dye, TO-PRO[®]-3, was added to the cells to a final concentration of 50nM. **Figure 2.4** shows the EGFP and TO-PRO-3 spectra. TO-PRO-3 dye only stains nucleic acids of the cells when the membrane integrity has been compromised and is therefore used to label dead cells.

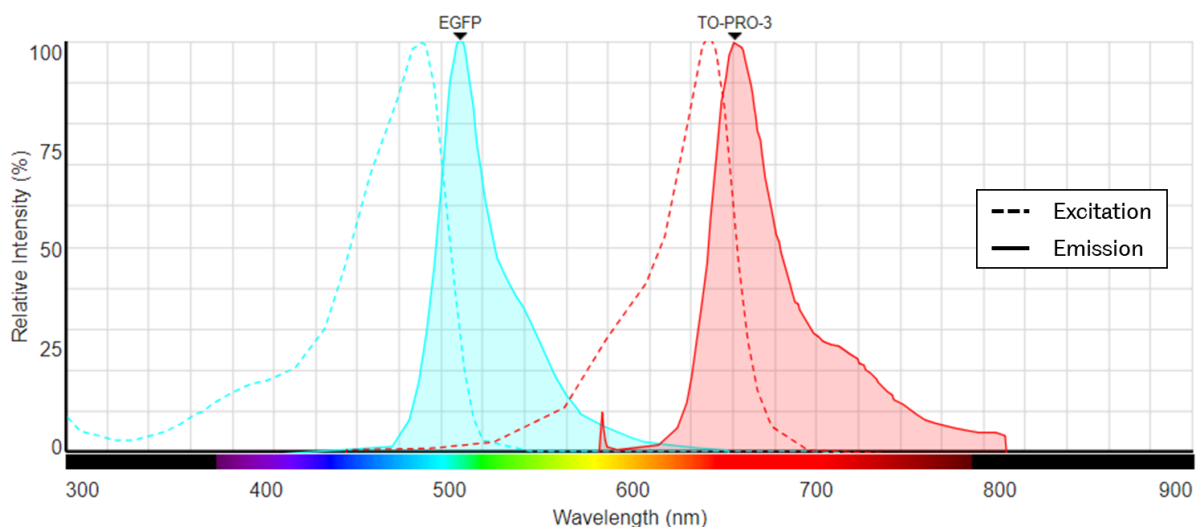


Figure 2.4 | Excitation and emission spectra of EGFP and TO-PRO-3 viability dye.

Graph generated by ThermoFisher Fluorescence SpectraViewer.

The FACSria cell sorter was first calibrated and the sorting parameters (BD FACSDiva 8.0.1 software) adjusted with the DLD-1 WT non-transfected cells. A doublet-discrimination parameter was applied to consider single cells only. The TO-PRO-3 dye was used to exclude dead cells. The brightest 2% of GFP-positive single live cells of each sample were sorted into single cells (2x 96-well plates/sample). The rest of the cells was sorted into bulk GFP-positive (brightest 2%) and GFP-negative populations to later determine the overall efficiency of the guides (See Section 2.2.4.3.6 for T7-assay protocol).

2.2.4.3.3.2 Sorting of live cells

After generation of hMAGI-2 and hMAGI-3 single KO as well as hMAGI-1/hMAGI-2 and hMAGI-1/hMAGI-3 double KO bulk populations by puromycin selection, live cells were sorted to obtain single clones.

The following samples were prepared:

hMAGI-2	DLD-1 G9+G4 bulk
hMAGI-1/hMAGI-2	DLD-1 G1 8 G9+G4 bulk
	DLD-1 G2 14 G9+G4 bulk
hMAGI-3	DLD-1 G5+G6 bulk
hMAGI-1/hMAGI-3	DLD-1 G1 8 G5+G6 bulk
	DLD-1 G2 14 G5+G6 bulk

To be calibrated with:

WT	DLD-1 WT
hMAGI-1	DLD-1 G1 8 (A) MAGI-1 KO clone
	DLD-1 G2 14 (B) MAGI-1 KO clone

Directly before sorting, the viability dye, Propidium Iodide, was added to the cells to a final concentration of 0.25µg/mL. **Figure 2.5** shows the Propidium iodide spectrum. Similar to TO-PRO-3, Propidium iodide is used to label dead cells.

The FACSria cell sorter was first calibrated and the sorting parameters (BD FACSDiva 8.0.1 software) adjusted with either DLD-1 WT, G1 8 or G2 14 cells as appropriate. A doublet-discrimination parameter was applied to consider single cells only. The Propidium Iodide was used to exclude dead cells. Each sample was sorted into single live cells into 96-well plates (2x 96-well plates/sample).

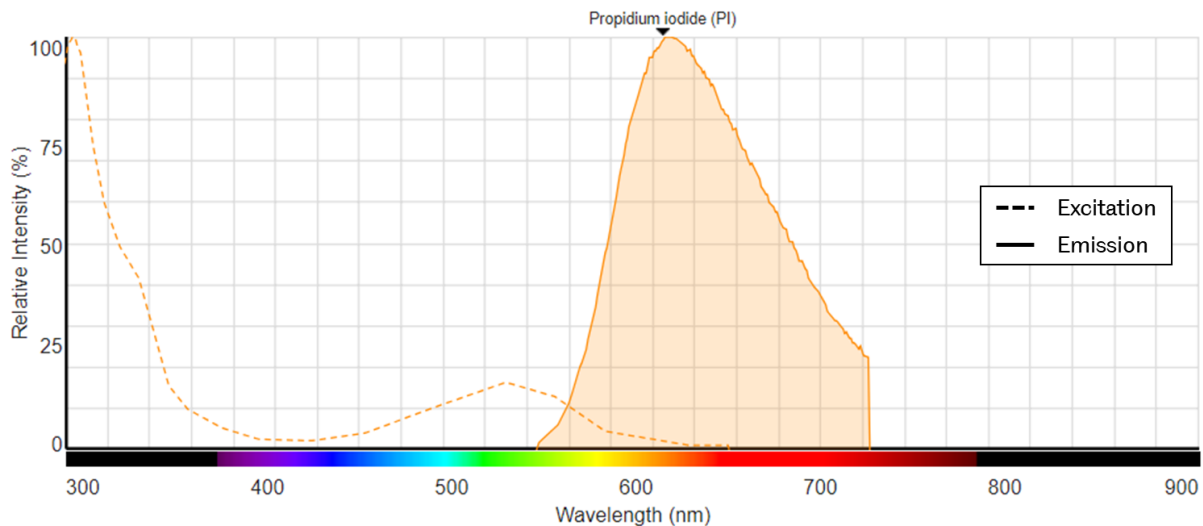


Figure 2.5 | Excitation and emission spectra of Propidium iodide.

Graph generated by ThermoFisher Fluorescence SpectraViewer.

2.2.4.3.4 gDNA extraction

Genomic DNA (gDNA) was extracted for each individual clone to check the mutations introduced by the NHEJ repair process. As gDNA was being extracted from cells, extra steps were needed compared to the phenol-chloroform DNA purification presented in Section 2.2.4.3.4. To facilitate the separation between nucleic acids and amino acids, the sample was treated, prior to phenol-chloroform purification, with Proteinase K. Proteinase K is a broad spectrum serine protease that was used to break down proteins into smaller peptides such as histones, freeing the DNA, or nucleases that could degrade the DNA, leaving it whole and undamaged. The digestion buffer contains Triton-X 100 to denature proteins and expose more hydrophobic residues, targeted by the Proteinase K, that would otherwise rather be unreachable at the core of proteins.

Cells preparation for gDNA extraction:

First, the cell suspension was transferred (typically the equivalent of either 3x 96-well wells, 1x 12-well well or 1:10 from a 10cm dish) into a 1.5mL tube. Cells were pelleted by a 5min-centrifugation at 130xg and the pellet was washed once with PBS 1X. Cells were pelleted once again by a 5min-centrifugation at 130xg. Cells pellets were stored at -20°C if the following steps of the gDNA extraction protocol (described below) were not performed right away.

gDNA extraction procedure:

The following lysis buffer was prepared in advance:

20mM EDTA
10mM Tris-HCl pH 8.0
200mM NaCl
0.2% Triton X-100

The lysis buffer could be stored at room temperature for several weeks.

At the time of gDNA extraction, Proteinase K was added to an aliquot of lysis buffer to a final concentration of 100µg/ml. The volume of lysis buffer needed to be adjusted to the quantity of cells to be lysed. As an indication, 500µL/sample were used for cells collected from a 12-well well. The cell pellet was resuspended in lysis buffer and incubated for 1hr at 37°C. Then, Proteinase K was heat inactivated at 95°C for 5min. The tube was centrifuged for 5min at 13000xg at room temperature and the supernatant was transferred to a new 1.5mL tube. Phenol-chloroform extraction of the gDNA contained in the sample was performed as described in Section 2.2.4.3.4 (steps 2-12). The DNA pellet was resuspended in ddH₂O (typically 50µL). DNA concentration was measured with the NanoDrop and the gDNA was stored at -20°C unless proceeding directly with PCR amplification.

2.2.4.3.5 PCR amplification of the targeted region

PCR amplification of the targeted region was performed using GoTaq[®] polymerase. Primers used are listed in **Table 2.31**.

Table 2.31 | Primer pairs to amplify CRISPR/Cas9 targeted region

The annealing temperature was determined by using the Promega T_m calculator webtool and following the rule of thumb of 3°C below the lowest melting temperature.

Primer name (# from Table 2.7)	Sequence 5'-3'	Guides	Annealing T°C
FWD1-2 (#19)	TGTTTCTCCCATGAACAAGCG	G1 & G2	64°C
REV1-2 (#20)	GGAGGGAAGCAGGAAATCGAG		
FWD4-9 (#21)	GACGAGTGAAGGAGAGCTCA	G9 & G4	62°C
REV4-9 (#22)	CGCCCTTCTCTGTATAGGCC		
FWD5-6 (#23)	AGACGCTGAAGAAGAAGAAGCA	G5 & G6	62°C
REV5-6 (#24)	GTCTTGAGACGGATGGGCTC		

For each sample, the mixture described in **Table 2.32** was prepared. The volume of the reaction depended on the amount of gDNA available – 50µL was preferred whenever possible.

If simultaneous amplification of several samples was carried out, PCR reactions were prepared using a master mix combination described in **Table 2.33**.

Table 2.32 | GoTaq® amplification of gDNA

*: Added last.

Components	20µL reaction	50µL reaction
5x Green Buffer	4µL	10µL
MgCl ₂ (25mM)	3.2µL	8µL
dNTPs (10mM each)	0.4µL	1µL
FWD primer (10µM stock solution)	1µL	2.5µL
REV primer (10µM stock solution)	1µL	2.5µL
Template gDNA	100ng	250ng
GoTaq polymerase (5U/µL) *	0.1µL	0.25µL
ddH ₂ O	Up to 20µL	Up to 50µL

Samples were incubated in a thermocycler using the following programme:

- a. Heat lid to 110°C
- b. 95°C for 3min
- c. Start cycle, 35x:
 - i. 95°C for 45s – denaturation
 - ii. Annealing T°C for 30s (See **Table 2.31**) – annealing step
 - iii. 72°C for 1min – extension step
- d. Close cycle
- e. 72°C for 10min – final extension step
- f. Hold at 4°C

Table 2.33 | GoTaq® master mixes

*: Added last.

Master Mix 1
5x Green Buffer
GoTaq polymerase *

Master Mix 2
ddH ₂ O
MgCl ₂
dNTPs
FWD primer (10µM stock solution)
REV primer (10µM stock solution)
gDNA template

Proper amplification of the amplified fragments was verified by loading 5µL of the PCR reaction in a 1% agarose gel in TAE 1X Buffer along with the 100bp DNA ladder.

- a. For single clone characterisation, the remaining volume of the PCR reaction was sent for clean-up and sequencing to the Core Genomic Facility of the University of Sheffield with the forward primer used for PCR amplification (Final concentration 1µM).
- b. For bulk population characterisation, the remaining PCR reaction was purified using Macherey-Nagel NucleoSpin PCR Clean-up kit according to the manufacturers' instructions.

2.2.4.3.6 T7-assay

The efficiency of a single guide RNA was assessed using a T7-endonuclease assay on the PCR-amplified targeted region of a bulk population (GFP-positives sorted cells or puromycin selected cells). T7-endonuclease I recognizes and cleaves mismatched DNA, therefore the more indels generated by NHEJ, the more intense will be the cleaved fragments on an agarose gel.

First, gDNA was extracted from bulk populations, including all appropriate controls (WT cells and GFP-negative population when applicable). The target region was amplified by PCR using GoTaq polymerase (50µL reaction). See Section 2.2.4.3.5 for complete protocol. Then, the following mixture was prepared in duplicates for each sample:

200ng-500ng of PCR amplified DNA fragment in 17µL of ddH ₂ O + 2µL of 10X NEBuffer 2
--

DNA fragments were hybridized to form hetero-duplexes in a thermocycler using the following programme:

- a. Heat lid to 110.0°C
- b. Temp. 95°C for 5min – denaturation
- c. 95-85°C with a ramp of -2°C/s – annealing
- d. 85-25°C with a ramp of -0.1°C/s – annealing
- e. Hold at 4°C

Next, 1µL of T7-endonuclease I was added to one of the duplicates (+T7 sample) while 1µL of ddH₂O was added to the other duplicate (-T7 sample). The reaction was incubated for 1hr at 37°C and was then stopped by adding 0.75µL of 0.5M EDTA and mixing thoroughly. 4µL of 6X Purple Loading dye, containing SDS, were added to the samples which were run on a 2% agarose gel in TBE 1X Buffer (90mM Tris, 90mM Boric acid, 2mM EDTA pH 8.0) to allow good

separation and detection of the cleaved DNA fragments. The workflow is summarised in **Figure 2.6**.

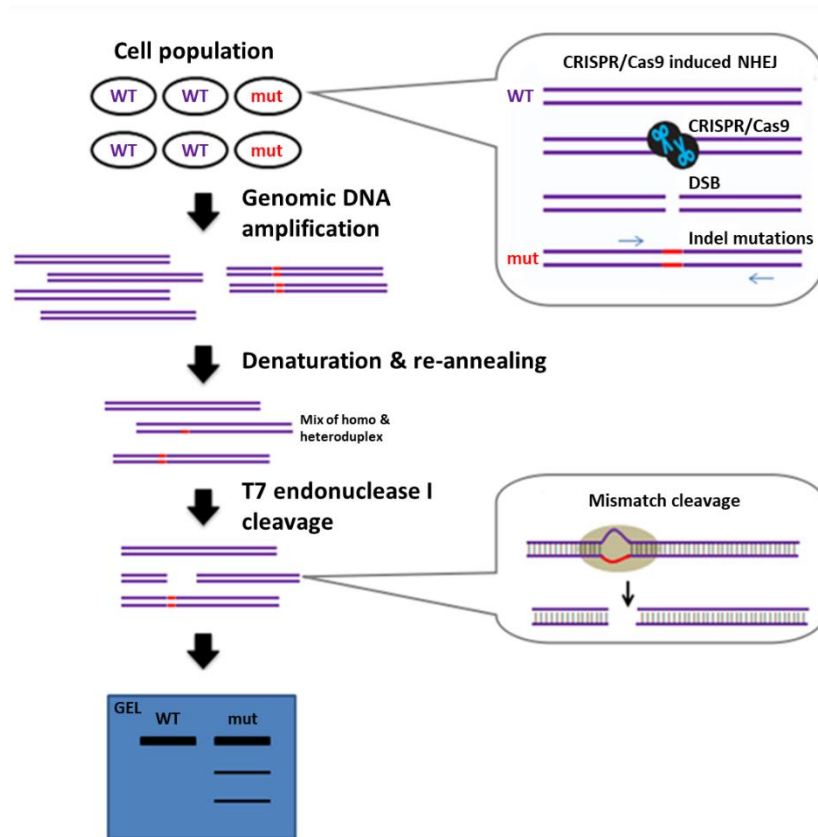


Figure 2.6 | T7 assay workflow.

Workflow diagram of a T7 endonuclease I assay. Within a cell population subjected to CRISPR/Cas9 gene editing, the PCR-amplified targeted region will result in a mix of WT and mutant products. The DNA fragments are then denatured and re-annealed to form hetero-duplexes that will be the target of the T7 endonuclease I digestion. Cleaved and uncleaved DNA fragments are then resolved on an agarose gel. Adapted from:

<https://www.genecopoeia.com/product/t7-endonuclease-i-assay-kit/>

2.2.4.3.7 Clones expansion

After FACS sorting, the 96-well plates were placed in the cell culture incubator. From day5 after sorting, plates were screened under an inverted microscope (4x objective) to identify wells containing single colonies. Empty wells or wells containing more than one colony were crossed out. Medium was refreshed 7 days after sorting: 150µL of medium out of 200µL were taken out then replenished using a multichannel pipette to minimize cell loss.

When cells were more than 60% confluent well, they were split. Medium was discarded and cells were washed once with 100µL of PBS 1X. Then, 30µL of trypsin were added to the well and the 96-well plate was put back in the incubator at 37°C for 5min. Cell dissociation

progress was checked under the inverted microscope and the plate was incubated longer if necessary. Once cells appeared rounded and loose, 170µL of complete medium were added to stop the action of trypsin and cells were resuspended thoroughly. Complete cell dissociation was verified under inverted microscope. Next, 100µL of the cell suspension (1:2) was transferred into a new 96-well plate (1x well) for freezing (Plate A) while 5x 20µL of the cell suspension (5x 1:10) were pipetted into 5 wells of another 96-well plate for propagation of the clonal lines (Plate B). Volume was topped-up to 200µL in each wells.

Plate A (96-well plate containing very early passage number of each clone) was frozen once cells reached 80-100% confluency of the wells. The same steps as for splitting, described in the paragraph above, were carried out. Following trypsinisation of the cells in 30µL, 70µL of complete RPMI medium were added and cells were resuspended thoroughly. Complete cell dissociation was verified under inverted microscope. The cell suspension for each clone was transferred to a new 96-well plate already containing 100µL of freezing medium (90% FBS + 10% DMSO) in each well and pipetted up and down thoroughly. The plate was sealed with Parafilm® and placed into a Styrofoam box for slower freezing and stored at -80°C.

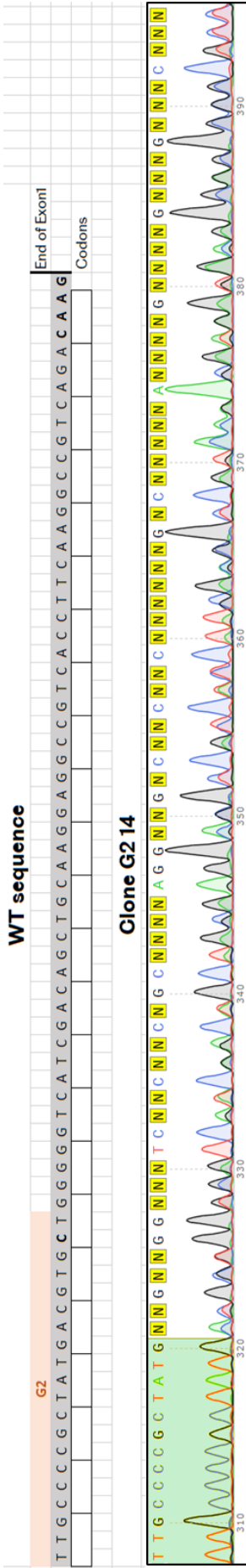
Clones from Plate B (5x 96-well well for each clone) were subcultured and prepared for gDNA extraction. First, cells were collected and resuspended in 170µL of complete medium, as described above. The cell suspension of 3x wells (out of 5) were transferred into a 1.5mL tube (600µL in total) for gDNA extraction and genotyping (See Sections 2.2.4.3.4 and 2.2.4.3.8.1). The cell suspension from one of the remaining wells was transferred into a 35mm dish to propagate for future protein extraction. Finally, the cell suspension from the last well was transferred into a 60mm dish for expansion of the clone. If the clone is validated as a KO by genomic analysis and western blotting, the population was expanded to 10cm dishes. Stocks were then prepared for liquid nitrogen cryopreservation (See Section 2.2.1.3.1).

2.2.4.3.8 Clones screening

To characterise single clones, the following steps were undertaken.

2.2.4.3.8.1 Genomic analysis

The PCR-amplified region of interest (See Section 2.2.4.3.5) was sent for sequencing to the Core Genomic Facility of the University of Sheffield with the forward primer used for PCR amplification (Final concentration 1µM).



STEP 1 Identify the last few bp of the Exon1

T T G C C C C G C T A T G A C G C T G G G G T C A T C G A C A G C T G C A A G G A G G C C G T C A C C T T C A A G G C C G T C A G A C A A G

T T G C C C C G C T A T G A C G C T G G G G T C A T C G A C A G C T G C A A G G A G G C C G T C A C C T T C A A G G C C G T C A G A C A A G

T T G C C C C G C T A T G C T G G G G T C A T C G A C A G C A G C A G A G G C C G T C A C C A C C A A G A A C G T C A G C A C A C C C C C T T T

STEP 2 Attribute Alleles

T T G C C C C G C T A T G A C G C T G G G G T C A T C G A C A G C T G C T G C G A G G A G G C C G T C T T C T T C G C G G C C G T T A A A C G A G C T G A G G G G G G G C G C C

T T G C C C C G C T A T G C T G G G G T C A T C G A C A G C A G C A G A A G G C C G T C A C C A C C A A G A A C G T C A G C C A A G G T A G A C A A G

STEP 3 Retrace each Allele sequence backwards

T T G C C C C G C T A T G A C G T G C T G G G G T C A T C G A C A G C T G C A A G G A G G C C G T C A C C T T C A A G G C C G T C A G A C A A G

T T G C C C C G C T A T G A C G C T G G G G T C A T C G A C A G C T G C G A G G A G G C C G T C A C C T T C G C G C C G T A A G A C A A G

T T G C C C C G C T A T G C T G G G G T C A T C G A C A G C A G C A G A G G C C G T C A C C A C C A A G A A C G T C A G C C A A G

T T G C C C C G C T A T G A C G T G C T G G G G T C A T C G A C A G C T G C A A G G A G G C C G T C A C C T T C A A G G C C G T C A G A C A A G

T T G C C C C G C T A T G A C G C T G G G G T C A T C G A C A G C A G C A G A A G G C C G T C T T C T T C G C G C C G T A A G A C A A G

T T G C C C C G C T A T G C T G G G G T C A T C G A C A G C A G C A G A A G G C C G T C A C C A C C A A G A A C G T C A G C C A A G

STEP 4 Re-arrange sequences to reveal indels

T T G C C C C G C T A T G A C G T G C T G G G G T C A T C G A C A G C T G C A A G G A G G C C G T C A C C T T C A A G G C C G T C A G A C A A G

T T G C C C C G C T A T G A C G C T G G G G T C A T C G A C A G C T G C A A G G A G G C C G T C A C C T T C A A G G C C G T C A G A C A A G

T T G C C C C G C T A T G C T G G G G T C A T C G A C A G C T G C A A G G A G G C C G T C A C C T T C A A G G C C G T C A G A C A A G

T T G C C C C G C T A T G A C G T G C T G G G G T C A T C G A C A G C T G C A A G G A G G C C G T C A C C T T C A A G G C C G T C A G A C A A G

T T G C C C C G C T A T G A C G C T G G G G T C A T C G A C A G C T G C A A G G A G G C C G T C A C C T T C A A G G C C G T C A G A C A A G

T T G C C C C G C T A T G C T G G G G T C A T C G A C A G C T G C A A G G A G G C C G T C A C C T T C A A G G C C G T C A G A C A A G

Figure 2.7 | Example of manual reading of sequencing results from a heterozygous CRISPR clone, G2 14

Excel sheet recapitulating the steps of manual reading of the sequencing results of an heterozygous CRISPR clone: G2 14 (B). The top part shows the WT sequence from G2 until the end of Exon1. The boxes below indicate the ORF. G2 14 chromatogram is displayed (colour code: A T C G). The part highlighted in green represents the clear sequence of both alleles before the Cas9 cleavage site; what follows is different for each allele as indicated by the double peaks and many undetermined nucleotides (N). STEP1: The last few base pairs (bp) of the Exon1 (CAAG) were identified for each allele. STEP2: Allele A and B were randomly assigned. STEP3: The sequence of each allele was retraced backwards to the site of mutation, indicated by the bold red line |. STEP4: Sequences were rearranged to reveal the mutations; in the case of G2 14: a 2bp deletion for Allele A and a 5bp deletion for Allele B.

DLD-1 cells are near-diploid with 46 chromosomes occurring in 86% of the cells, according to ATCC which means that in most cases, there are two alleles to mutate. This also means that each allele can be mutated in a different way:

- Clean sequencing chromatogram (single peaks) were analysed against the WT sequence using NCBI nucleotide blast to check for homozygous mutations of the two alleles.
- Chromatograms displaying two peaks from the site targeted by the guide onwards indicated heterozygous mutations. In that case, the sequence of each individual allele was determined manually. The two potential nucleotides per position were entered in an excel file from the targeted site until the end of the exon or amplicon, as illustrated in **Figure 2.7**. Starting from the end of the sequence, each possible nucleotide was assigned to either AlleleA or AlleleB before proceeding backwards until reaching the site of mutation.

The mutated sequence was then translated to protein to identify potential premature STOP codons. Genomic knockout was considered when the premature STOP codon appeared before any domain of the protein with a known function.

The generated knockout clones, validated by genomic analysis, are listed in **Table 2.34**.

Table 2.34 | Summary of isogenic clones from MAGI knockouts and associated mutations

The mutation nomenclature follows (313).

CRISPR target	Clone name	Genomic mutation		STOP codon
hMAGI-1	G1 8 (A)	MAGI-1 Exon1		aa85
		132_133insG		
	G2 14 (B)	MAGI-1 Exon1		Allele A: aa125 Allele B: aa124
		Allele A: 257_258del	Allele B: 254_259del	
hMAGI-2	G9+4 clone3	MAGI-2 Exon5		Allele A: aa283 Allele B: aa275
		Allele A: 824delC	Allele B: 823_917del	

hMAGI-1/hMAGI-2	A9+4 clone9	MAGI-2 Exon5		aa281
		822_823insG		
	B9+4 clone10	MAGI-2 Exon5		Allele A: aa280 Allele B: aa281
		Allele A: 823_829del	Allele B: 818C>T 819_825del 830_832del	
hMAGI-3	G5+6 clone28	MAGI-3 Exon1		aa64
		99_235del		
hMAGI-1/hMAGI-3	A5+6 clone7	MAGI-3 Exon1		aa53
		83_234del 236T>A		
	B5+6 clone2	MAGI-3 Exon1		aa109
		99_100del		

2.2.4.3.8.2 Western Blot

Clones were also tested at the protein level by Western blotting. Refer to Section 2.2.5 for complete protocols.

First, cells were cultured in 35mm or 60mm dishes until 90-100% confluent. Cell lysate was collected for each clone using RIPA buffer supplemented with 1X protease cocktail inhibitor. Lysis buffer volumes are listed in **Table 2.35**. Complete protocol in Section 2.2.5.1.

Table 2.35 | Volumes for extraction of total protein in CRISPR populations

Dish	Volume of Lysis buffer
35mm	100µL
60mm	200µL

Protein concentration was measured using DC assay (Section 2.2.5.3) and samples were prepared to contain equal amount of proteins (40-60µg). Samples were denatured by addition of 4x Laemmli buffer, 5min boiling at 98°C and run on an 8% polyacrylamide gel (Section 2.2.5.4). Proteins were then transferred on a nitrocellulose membrane (0.2µm pores) for 90min at 250mA (Section 2.2.5.5). Membranes were subjected to western blotting (Section 2.2.5.6) with all the steps being performed under gentle agitation. Membranes were cut (at ~70kDa) to allow blotting of the top part (high molecular weights) with hMAGI-1, hMAGI-2 or hMAGI-3 antibody while the bottom part (lower molecular weights) was blotted with β-tubulin antibody (loading control). Blocking of the membrane was performed 1hr in 5% Milk/PBST 1X at room temperature after which membranes were incubated overnight with primary antibody (MAGI-1, MAGI-2 or MAGI-3) in 1-3mL of 5% Milk/PBST 1X at 4°C (See **Table 2.40** for antibody dilutions). Excess antibody was removed by three washes of 10min in PBST 1X. Next,

membranes were incubated for 1hr with the secondary antibody in 5mL of 5% Milk/PBST 1X at room temperature. For this step, tubes were covered with aluminium foil to limit light exposure of the membranes. Excess antibody was removed by three washes of 10min in PBST 1X. Then, membranes were allowed to dry for a few minutes in a dark environment. Finally, proteins were detected using the Odyssey Sa[®] Infrared Imaging System from LI-COR.

2.2.4.3.8.3 Immunofluorescence

hMAGI-1 knockouts were assessed by immunofluorescence. Refer to Section 2.2.6 for complete protocol.

First, cells were seeded at 3×10^5 cells/well on coverslips in 12-well plates (clones alongside WT cells). Immunostaining (Section 2.2.6.4) was carried out 48hrs after seeding using anti-hMAGI-1 rabbit antibody (1:250 dilution) and gar 488 secondary antibody (1:500 dilution) and cells were imaged using a ZEISS Airyscan Confocal microscope (Section 2.2.6.5.2).

2.2.5 Protein assays and Western Blot

The list of buffers used in this section can be found in **Table 2.36**.

Table 2.36 | Buffer composition for protein assays and western blotting technique

*: added at the last moment.

Name	Composition
PBS 1X	137mM NaCl, 2.7mM KCl, 10mM Na ₂ PO ₄ , 1.8mM KH ₂ PO ₄ , pH 7.4
HEPES Lysis Buffer 1% Triton	50mM HEPES pH 7.5, 150mM NaCl, 1.5mM MgCl ₂ , 1mM EDTA, 10% glycerol, 1% Triton X-100, *1x protease cocktail inhibitor
HEPES Lysis Buffer 0.5% Triton	50mM HEPES pH 7.5, 150mM NaCl, 1.5mM MgCl ₂ , 1mM EDTA, 10% glycerol, 0.5% Triton X-100, *1x protease cocktail inhibitor
HEPES Wash Buffer 0.1% Triton	50mM HEPES pH 7.5, 150mM NaCl, 1.5mM MgCl ₂ , 1mM EDTA, 10% glycerol, 0.1% Triton X-100, *1x protease cocktail inhibitor
NETN Lysis Buffer 0.5% NP-40	100mM NaCl, 20mM Tris-HCl pH 8.0, 0.5mM EDTA, 0.5% (v/v) Nonidet P-40 (NP-40, # 2111-100 BioVision), *1x protease cocktail inhibitor
NETN Wash Buffer 0.1% NP-40	100mM NaCl, 20mM Tris-HCl pH 8.0, 0.5mM EDTA, 0.1% (v/v) Nonidet P-40 (NP-40, # 2111-100 BioVision), *1x protease cocktail inhibitor
RIPA Buffer	50mM Tris pH 7.5, 150mM NaCl, 1mM EDTA, 0.1% SDS, 0.5% Sodium deoxycholate, 1% NP-40 (v/v) (NP-40, # 2111-100 BioVision), *1x protease cocktail inhibitor

4x Laemmli Buffer	250mM Tris-HCl pH 6.8, 40% glycerol, 8% SDS, 20% β -mercaptoethanol, 1% bromophenol blue
10X Running Buffer	192mM Glycine, 25mM Tris, 0.1% SDS (w/v)
1X Running Buffer	10X diluted 10-fold in dH ₂ O
10X Transfer Buffer	192mM Glycine, 25mM Tris
1X Transfer Buffer	10X diluted 10-fold in dH ₂ O + 20% MeOH
Ponceau S	30% Trichloroacetic acid, 2% Ponceau S
1X PBST	0.05% Tween20, PBS 1X
10X TBS	137mM NaCl, 20mM Tris-HCl pH 7.6 (CST recipe)
1X TBST	0.1% Tween20, 10X TBS diluted 10-fold in dH ₂ O

2.2.5.1 Cell lysis

First, cells were cultured in 35mm or 60mm dishes until they reach the desired confluency. For cell lysis following transfection, cells were harvested after 48hrs (DNA transfection) or 72hrs/96hrs (siRNA transfection). Dishes were placed on ice and medium was carefully discarded. All following steps of cell lysis were performed on ice. Then, cells were washed twice with ice-cold PBS 1X. Ice-cold lysis buffer freshly supplemented with 1X protease cocktail inhibitor was added onto the cells. Volumes of lysis buffer used can be found in **Table 2.37**. Volumes were adjusted if necessary based on cell density. Cells were incubated in their wells with lysis buffer on ice for 15-20min. Afterwards, cells were then harvested using cell scrapers and cell lysate was transferred into an ice-cold 1.5mL tube. Lysis was carried out for 1hr on ice by vortexing the tube every 10min. Then, the lysate was cleared of cell debris by centrifugation for 15min at 16600xg at 4°C. The clear lysate (supernatant) was transferred into a new ice-cold 1.5mL tube, and the pellet was discarded. If necessary, protein concentration was measured using DC assay and samples were prepared with equal amount of proteins. 4X Laemmli Buffer (final concentration 1X) was added and the samples boiled for 5min at 98°C to denature proteins. Before loading on the gel, samples were briefly vortexed and spun to ensure proper homogenisation of proteins.

Table 2.37 | Volume of lysis buffer used depending on the application

Sample type	35mm dish/6-well plate	60mm dish
Untransfected cells	100-150 μ L	200-300 μ L
Overexpressing cells	250 μ L	/
Knockdown cells	150 μ L	/

2.2.5.2 Co-immunoprecipitation/pulldown

Co-immunoprecipitation (co-ip) or pulldown is a widely used technique to study protein-protein interactions. A target protein is transiently immobilised onto a solid support (agarose beads) coupled with a specific antibody that recognises either the protein or its tag. Cell lysate is incubated with these functionalised beads to allow protein-protein interactions. Beads are then precipitated by centrifugation which pulls-down the protein of interest along with the protein complex formed around it. Proteins are then detected using the western blotting technique.

Table 2.38 | Co-immunoprecipitation conditions for the interactions investigated

Interactions	Trap	Buffers
Flag-mMAGI-1B / V5-PTPN14	Flag antibody coupled to Protein A agarose resin	Lysis: HEPES 0.5% Triton Washes: HEPES 0.1% Triton
EGFP-mMAGI-1B / Myc-PTPN14 hMAGI-1Cβ1 / Myc-PTPN14	GFP-Trap®_A or Myc-Trap®_A	Lysis: HEPES 0.5% Triton Washes: HEPES 0.1% Triton
EGFP-mMAGI-1B / Flag-mMAGI-1B	GFP-Trap®_A	Lysis: HEPES 0.5% Triton Washes: HEPES 0.1% Triton
EGFP-mMAGI-1B / endogenous YAP	GFP-Trap®_A	Lysis: HEPES 0.5% Triton Washes: HEPES 0.1% Triton
Flag-mMAGI-1B / Myc-LATS1/2 EGFP-mMAGI-1B / Myc-LATS1/2	Myc-Trap®_A GFP-Trap®_A	Lysis: NETN 0.5% NP-40 Washes: NETN 0.1% NP-40
EGFP-mMAGI-1B / Myc-PTPN14 / Myc-LATS1/2	GFP-Trap®_A	Lysis: NETN 0.5% NP-40 Washes: NETN 0.1% NP-40
hMAGI-3b*-V5/His / Myc-PTPN14	Myc-Trap®_A	Lysis: HEPES 0.5% Triton Washes: HEPES 0.1% Triton
hMAGI-3b*-V5/His / Myc-LATS1/2	Myc-Trap®_A	Lysis: NETN 0.5% NP-40 Washes: NETN 0.1% NP-40

HEK293 cells were seeded at 3×10^5 cells/well in a 6-well plate 24hrs prior to transfection. 2-3 wells were seeded per sample. Cells were transfected/co-transfected according to Section 2.2.1.5 with 1µg total DNA per well, for 48hrs. Cell lysate (250µL/well) was harvested and the wells containing the same sample were pulled together. The volume was topped up to 1mL with Lysis buffer, this ensured optimal mixing during incubation with the beads. Detailed protocol for cell lysis can be found in Section 2.2.5.1. Lysates were cleared of cell debris by centrifugation for 15min at 16600xg at 4°C. 5-10% of the clear lysate were transferred into a new ice-cold 1.5mL tube, 4X Laemmli buffer was added and the samples were boiled for 5min at 98°C to denature the proteins. This fraction was referred to as INPUT and represented the total lysate (to ensure the presence of the proteins of interest). The rest of the clear lysate

was transferred into an ice-cold 1.5mL tube containing pre-equilibrated empty beads (10µL of slurry from either uncoupled Protein A-agarose resin or Binding control agarose beads) to pre-clear the lysate and control for unspecific binding.

Equilibration of beads to remove EtOH from the storage buffer (20% EtOH):

The commercial tube containing Protein A-agarose resin or control beads was thoroughly vortexed to resuspend beads completely and the desired amount of beads (referred to as slurry) was pipetted into an ice-cold 1.5mL tube. 25µL of slurry were used for Protein A-agarose resin and 10-15µL for Binding control agarose beads. Beads were washed with 200µL of ice-cold lysis buffer and tubes were centrifuged for 2min at 3615xg, 4°C. The supernatant was carefully discarded without disrupting the beads. The washing steps were carried out twice more. The last wash was only removed when the clear lysate was ready to be added on top to avoid beads drying out.

Tubes, containing the control beads and cell lysate, were tumbled end-over-end for 30min at 4°C. Beads were precipitated at the bottom of the tube by centrifugation for 2min at 3615xg, 4°C.

If performing co-immunoprecipitation with a specific antibody and Protein A-agarose resin:

The supernatant (pre-cleared cell lysate) was carefully transferred into a new ice-cold 1.5mL tube (1mL) and the desired antibody (1:500 dilution for the Flag-antibody) was added to the sample. Tubes were tumbled end-over-end for 1hr at 4°C to allow binding of the antibody to the protein of interest. The solution was transferred into an ice-cold 1.5mL tube containing pre-equilibrated Protein A-agarose resin (25µL of slurry).

If performing a pulldown using commercially available Myc-Trap[®] A or GFP-Trap[®] A:

The supernatant was carefully transferred to an ice-cold 1.5mL tube containing pre-equilibrated Myc-Trap[®]_A (20µL of slurry) or GFP-Trap[®]_A (10-15µL of slurry).

Tubes were tumbled end-over-end for 3-4hrs at 4°C to allow interaction of the protein of interest with the functionalised beads and formation of protein complexes. Next, beads were precipitated by centrifugation for 2min at 3615xg, 4°C. 5-10% of the supernatant were collected into a new ice-cold 1.5mL tube, 4X Laemmli buffer added and the samples were boiled for 5min

at 98°C to denature the proteins. This fraction was referred to as UNBOUND and represented the fraction of proteins that did not bind to the beads nor to the protein of interest. This step was only used during the optimisation phase and is not displayed in figures. The rest of the supernatant was carefully discarded without disrupting the beads. Beads were washed with 500µL of wash buffer and precipitated by centrifugation for 2min at 3615xg, 4°C. The supernatant was carefully discarded without disrupting the beads. The washing steps were carried out three more times (4 washes of the beads in total). After the last wash, beads were resuspended in 60µL of 2X Laemmli buffer. Pipetting up and down was avoided in order to avoid losing beads in the pipette tip; instead, the Laemmli buffer was pipetted at the bottom of the tube and the tip was slowly raised while mixing with circular movements. This fraction was referred to as PULLDOWN. Samples were denatured by boiling for 5min at 98°C. This step ensured dissociation of the protein of interest and protein complex pulled down from the beads. In the case of co-ip, the specific antibody dissociated as well from the beads and the heavy chains were visible on the western blot membrane at ~50kDa. Before loading on the polyacrylamide gel, INPUT (and UNBOUND) samples were briefly vortexed and spun to ensure proper homogenisation of proteins. PULLDOWN samples were centrifuged for 2min at 3615xg to precipitate beads at the bottom of the tube and only the supernatant was loaded on the gel.

2.2.5.3 Assessment of protein concentration: DC assay.

Protein concentration in cell lysate was assessed using the Bio-Rad DC Protein Assay based on the improved Lowry method. The assay was carried out according to the manufacturer's instructions and the absorbance was read at 740nm in a FluorSTAR OPTIMA microplate reader from BMG LabTech.

First, a standard curve was performed with serial dilutions of Albumin standard (stock concentration of 2mg/mL) into the same buffer as the samples to be measured, from 1.5mg/mL to 0mg/mL (6 points). Absorbance values (y-axis) were plotted against Albumin concentration (x-axis) and a linear regression was applied. If the R^2 value was above 0.95, the equation $ABS = a * concentration + b$ was used to determine the protein concentration of each samples based on their absorbance value. Measures were performed at least in duplicates and the absolute values averaged. Samples were prepared to contain the same amount of proteins (30-60µg) and volumes were adjusted using the appropriate buffer.

2.2.5.4 SDS-PAGE

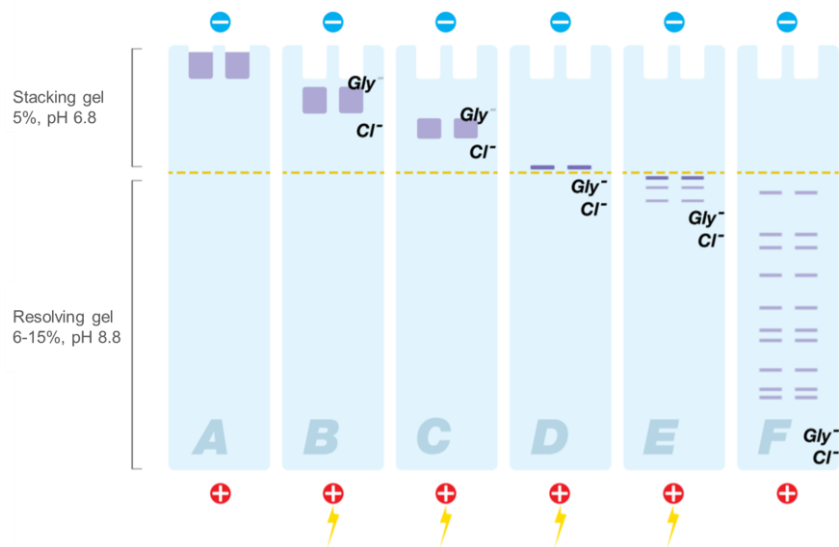


Figure 2.8 | Protein migration and ion fronts in a denaturing discontinuous system.

Adapted from Fig. 2.2 from BioRad Bulletin_6040. **A**, Samples are loaded into the wells. **B**, Voltage is applied to the system (50-90V) and the samples enter the gel. The Cl^- ions, present in the gel (Tris-HCl) move faster than the SDS-coated proteins and form an ion front. They are called leading ions. The glycine ions, present in the running buffer in a negative state, flow in the gel, predominantly lose their negative charge at pH 6.8, and form a lagging front behind the proteins. They are called trailing ions. **C**, A voltage gradient is formed in between the two fronts which constrains the proteins. **D**, The proteins are stacked between the narrow chloride and glycine fronts. At the interface between stacking and resolving gels, pH changes to 8.8 where glycine molecules are negatively charged which causes them to move more swiftly toward the positive electrode and to accelerate past the proteins. In the meantime, proteins are left in a very narrow line at the interface of the two gels. All proteins will enter the resolving gels together. **E**, As the resolving gel contains a higher acrylamide concentration, the movement of proteins will be slowed according to their molecular weight. **F**, At the end of the running, individual proteins are organised into band patterns according to their size.

Protein samples were run on SDS-PAGE (sodium dodecyl sulphate polyacrylamide gel electrophoresis) and subjected to an electrical current resulting in separation according to their molecular weight. As previously described, samples were prepared in Laemmli Buffer which contains β -mercaptoethanol and together with boiling, denatured proteins. SDS is present in the running buffer as well as in the gel composition and coats the proteins with a uniform negative charge, allowing them to move through the gel toward the positive electrode. To allow good resolution, a discontinuous buffer system was used relying on different pH and gel compositions (**Figure 2.8**).

SDS-PAGE were prepared according to the **Table 2.39**. The acrylamide percentage was chosen based on the molecular weight of the proteins to detect: 8% for 25-200kDa and 10%

for 15-100kDa. SDS-PAGE were run in the BioRad Mini-PROTEAN® Tetra Cell according to manufacturer's instructions.

Table 2.39 | Composition of stacking and resolving gels for SDS-PAGE

Components	Stacking gel	Resolving gel	
	10mL	10mL	
	5%	8%	10%
dH ₂ O	6.15mL	5.4mL	4.9mL
40% acrylamide 37.5:1 acrylamide/bis-acrylamide	1.25mL	2mL	2.5mL
Tris-HCl pH 6.8	2.5mL	/	/
Tris-HCl pH 8.8	/	2.5mL	2.5mL
10% SDS	100µL	100µL	100µL
10% APS (ammonium persulfate)	100µL	50µL	50µL
TEMED	10µL	5µL	5µL

Samples were loaded into the gel along with a PageRuler™ Prestained Protein Ladder (10-180kDa or 10-250kDa) and run with 1X running buffer. During the stacking phase, the voltage was set to 60V to allow complete concentration of the samples at the stacking/resolving interphase. Then, the voltage was increased to 120V for the entire run until the Laemmli Buffer, migrating with the Cl⁻ ions front, left the gel. The gel set-up was then disassembled and the proteins were transferred onto a membrane for Western Blot.

2.2.5.5 Protein transfer

Proteins were transferred onto a nitrocellulose membrane (0.2µm pore size) using Mini Trans-Blot® Electrophoretic Transfer Cells according to manufacturers' instructions. Similar to gel electrophoresis, electrical current was used to set proteins in motion. 250mA were applied for 90min, in 1X transfer buffer containing 20% MeOH, to allow the proteins to transfer horizontally from the gel to the membrane, creating a perfect copy of the gel.

The Prestained Protein Ladder allowed estimation of transfer efficiency. If necessary, further assessment of transfer efficiency was performed by staining the membrane with Ponceau S solution which was poured to cover the entire membrane and incubated at RT for 1min. Ponceau S was removed from the membrane which was then washed abundantly with dH₂O until the background became white again and only protein bands were stained in red. Ponceau S staining of proteins is reversible and was washed away using PBST 1X or TBST 1X

for 5min under constant rotation. It is important to note that Ponceau S staining can introduce some background during fluorescence detection.

2.2.5.6 Western Blotting procedure

To detect specific proteins of interest on the membrane, the western blotting technique was performed. All incubation steps were performed under gentle agitation.

Table 2.40 | List of antibodies used for Western blot and associated buffers

Antibody	Buffers	Dilution
β -tubulin (mouse)	Blocking and antibody incubation: 5% Milk/PBST 1X Washing: PBST 1X	1:5000
AMOT (rabbit)	Blocking and antibody incubation: 5% Milk/TBST 1X Washing: TBST 1X	1:1000
Flag (mouse)	Blocking and antibody incubation: 5% Milk/PBST 1X Washing: PBST 1X	1:500
GFP (rabbit)	Blocking and antibody incubation: 5% Milk/PBST 1X Washing: PBST 1X	1:2000
MAGI-1 (rabbit)	Blocking and antibody incubation: 5% Milk/PBST 1X Washing: PBST 1X	1:500
MAGI-2 (mouse)	Blocking and antibody incubation: 5% Milk/TBST 1X Washing: PBST 1X	1:200
MAGI-3 (mouse)	Blocking and antibody incubation: 5% Milk/PBST 1X Washing: PBST 1X	1:200
Myc (mouse)	Blocking and antibody incubation: 5% Milk/PBST 1X Washing: PBST 1X	1:1000
Phospho-YAP Ser127 (rabbit)	Blocking and antibody incubation: 5% BSA/TBST 1X Washing: TBST 1X	1:1000
PTPN14 (rabbit)	Blocking and antibody incubation: 5% Milk/TBST 1X Washing: TBST 1X	1:500
YAP (rabbit)	Blocking and antibody incubation: 5% BSA/TBST 1X Washing: TBST 1X	1:1000
YAP/TAZ (mouse)	Blocking and antibody incubation: 5% Milk/PBST 1X Washing: PBST 1X	1:200

After protein transfer, the membrane was cut according to the different proteins to detect. The membrane was blocked for 1hr at room temperature. The solution depended on the primary antibody and manufacturer's recommendations. **Table 2.40** lists the antibody used and associated buffers. The membrane was incubated with a primary antibody diluted in 1-3mL of the appropriate buffer overnight at 4°C. The excess and unbound antibody was

washed from the membrane for 3x 10min in PBST 1X or TBST 1X at RT. The membrane was incubated with a fluorescently-conjugated secondary antibody (**Table 2.4**), diluted in 5mL of the appropriate buffer, for 1hr at room temperature. For this step, tubes were covered with aluminium foil to limit light exposure of the membranes. The excess and unbound antibody was washed from the membrane for 3x 10min in PBST 1X or TBST 1X at RT. The membrane was allowed to dry for a few minutes in a dark environment. Proteins were detected (Section 2.2.5.7.1).

2.2.5.7 Protein detection and quantification

2.2.5.7.1 Protein detection

Proteins were detected using the Odyssey Sa[®] Infrared Imaging System from LI-COR with a 200µm resolution. Two infrared detection channels were available: 800nm and 700nm.

Membranes were scanned according to the secondary antibody species to detect: anti-rabbit-680nm and/or anti-mouse-800nm. The detector sensitivity for each channel was set to a default value of 5.0 but was adjusted, if necessary, to avoid saturation of the protein bands in the image. Image Studio™ Lite software was used to adjust brightness and contrast of the blots and to quantify protein bands (See below).

2.2.5.7.2 Western Blot quantification

Quantification was carried out using the Image Studio™ Lite software. Rectangles of the same surface area were drawn around the bands to quantify (**Figure 2.9**). Background was calculated by the software by taking the median intensity of a 3-pixel border around each rectangle. Depending on the shape of the band, the background was taken from top/bottom or right/left borders, not to overlap with other bands. This value was then automatically multiplied by the area of each shape and subtracted to the total intensity found in each rectangle, giving the protein signal.

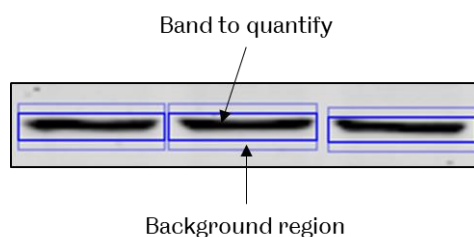


Figure 2.9 | Western blot quantification using Image Studio™ Lite software.

This was done for the loading control (β -tubulin) and the protein signal to quantify. First, β -tubulin signals were expressed as a ratio of the highest value. Then, the signal of the protein of interest for each sample was divided by the associated β -tubulin ratio.

2.2.5.8 Phosphorylation assay

In this section, all lysis buffers were supplemented with PhosSTOP phosphatase inhibitors.

2.2.5.8.1 Phosphospecificity of the antibody

Phosphospecificity of the PhosphoYAP Ser127 antibody was assessed prior to using it for characterisation. The protocol was supplied by Cell Signaling Technology.

First, total protein was extracted from DLD-1 WT and MAGI-1 knockout clones G1 8 (A) and G2 14 (B) using RIPA buffer supplemented with PhosSTOP tablet (Section 2.2.5.1). Samples were prepared with equal amount of total protein: 40 μ g (Section 2.2.5.3) and run in duplicate (WT_G1 8_G2 14 | WT_G1 8_G2 14) on a 8% SDS-PAGE (Section 2.2.5.4) and transferred onto a nitrocellulose membrane (Section 2.2.5.5). The membrane was cut in half, with each replicate on either side. Next, the phosphatase mixture was prepared as indicated in **Table 2.41**. Replicate membranes were either incubated with the phosphatase or the negative control mixtures in sealed bags overnight at 37°C under gentle mixing. Membranes were washed twice with TBST 1X for 5min and the Western blotting protocol was performed, starting from the blocking step, as described in Section 2.2.5.6 with the PhosphoYAP Ser127 primary antibody.

Table 2.41 | Phosphatase treatment after transfer

Components	CIP/ λ -Phosphatase	Negative control
ddH ₂ O	700 μ L	800 μ L
10X NEBuffer for Protein MetalloPhosphatases (PMP)	100 μ L	100 μ L
10X MnCl ₂	100 μ L	100 μ L
Alkaline Phosphatase Calf Intestinal (CIP, 10,000 units/mL)	50 μ L	/
Lambda Protein Phosphatase (400,000 U/mL)	50 μ L	/

2.2.5.8.2 PhosphoYAP Ser127 assay

The aim of this assay was to assess the proportion of phosphorylated YAP on the Ser127 residue with respect to cell density.

First, cells were seeded in 60mm dishes at 0.75×10^5 cells/cm² (medium density) and 2×10^5 cells/cm² (high density). 24hrs later, total protein was extracted with NETN Buffer (0.5% NP-40) supplemented with protease cocktail inhibitor and PhosSTOP (Section 2.2.5.1). Samples were prepared and run identically on two 8% SDS-PAGE (Sections 2.2.5.3 and 2.2.5.4). Western blot was performed with anti-PhosphoYAP Ser127 & anti- β -tubulin antibodies on one membrane, and anti-YAP (total YAP) & anti- β -tubulin antibodies on the other (Section 2.2.4.3.8.2). Quantification of PhosphoYAP Ser127 / Total YAP was performed as described in Section 2.2.5.7.2. PhosphoYAP Ser127 and total YAP were normalised to their respective β -tubulin signal. Then, the proportion of PhosphoYAP Ser127 (PhosphoYAP Ser127 / Total YAP) were represented as a percentage of either HIGH density for each sample or WT for each density. Statistical significance was assessed over at least three independent experiments (Section 2.2.7).

2.2.6 Immunofluorescence imaging

2.2.6.1 Coverslips coating

HEK293 cells do not adhere very strongly to their substrate and required coating of the glass coverslips with Poly-L-lysine to undergo the immunostaining process without too much cell loss. The following steps were performed under sterile conditions in a tissue culture hood. First, Poly-L-lysine 0.1% solution was diluted 10-fold in ddH₂O and 1mL of 0.01% Poly-L-lysine solution was added on top of each coverslip (in 12-well plate). The Poly-L-lysine was left to adsorb to the glass for 30min at room temperature, then, the solution was discarded and coverslips were allowed to dry under the hood for 1hr. Coverslips were washed three times with PBS 1X before use.

2.2.6.2 Density assay and YAP subcellular localisation

Density assays were performed to assess YAP cell density dependent subcellular localisation.

2.2.6.2.1 Density assay in wild-type cell lines

The density assays in wild-type cell lines (as shown in **Figure 3.1**) were performed as follow. First, cells were seeded in 12-well plates on coverslips (coated with Poly-L-lysine in the case of HEK293 cells – Section 2.2.6.1) at LOW, MEDIUM and HIGH densities and cultured for the

number of days indicated in **Table 2.42** before fixation. Immunostaining with anti-YAP or anti-YAP/TAZ antibodies was performed as described in Section 2.2.6.4. Images were acquired with either an epifluorescence or an Airyscan confocal microscope.

Table 2.42 | Seeding densities for density assay in wild-type cell lines

The surface area of a well in 12-well plate is 4cm².

WT cell lines	LOW	MEDIUM	HIGH	Days of culture
HEK293	0.125x10 ⁵ cells/cm ²	0.25x10 ⁵ cells/cm ²	0.75x10 ⁵ cells/cm ²	3 days
Caco-2	0.25x10 ⁵ cells/cm ²	0.5 x10 ⁵ cells/cm ²	1.25x10 ⁵ cells/cm ²	6 days
DLD-1	0.0625x10 ⁵ cells/cm ²	0.25x10 ⁵ cells/cm ²	0.75x10 ⁵ cells/cm ²	3 days
MDCK	0.125x10 ⁵ cells/cm ²	0.25x10 ⁵ cells/cm ²	0.75x10 ⁵ cells/cm ²	3 days

2.2.6.2.2 YAP subcellular localisation upon MAGI-1 knockdown at high density

YAP subcellular localisation was then assessed in Caco-2, HEK293 and DLD-1 cell lines upon MAGI-1 transient knockdown. Cells were seeded in 12-well plates on coverslips (coated with Poly-L-lysine in the case of HEK293 cells – Section 2.2.6.1) for siRNA transfection as indicated in **Table 2.16**. Then, siRNA transient transfection was performed using MAGI-1 siRNA and Scrambled siRNA (described in **Table 2.8**) as detailed in **Table 2.17**. Cells were fixed and subjected to anti-MAGI-1 and anti-YAP or anti-YAP/TAZ immunostaining (Section 2.2.6.4). Finally, images were acquired with either an epifluorescence or an Airyscan confocal microscope.

2.2.6.2.3 24hrs density assay in MAGI knockout clones

YAP subcellular localisation was assessed at medium and high densities in DLD-1 cells upon MAGI-1 and/or MAGI-3 stable knockout. Cells were seeded in 12-well plates on coverslips at MEDIUM and HIGH densities (as indicated in **Table 2.43**) and cultured for 24hrs. Anti-YAP immunostaining was performed as described in Section 2.2.6.4 and images were acquired with an Airyscan confocal microscope.

Table 2.43 | Seeding densities for 24hrs density assay in MAGI knockout cell lines

The surface area of a well in 12-well plate is 4cm².

MEDIUM	HIGH
0.75x10 ⁵ cells/cm ²	2x10 ⁵ cells/cm ²

2.2.6.3 Colocalisation study

The colocalisation study was performed with overexpressed proteins in DLD-1 cells. First, cells (DLD-1 WT cells or MAGI-1 KO clone G2 14) were seeded at 3×10^5 cells/well in 6-well plates. Transfection or co-transfection was performed 24hrs after seeding as described in Section 2.2.1.5. The next day, transfected cells were split and re-seeded on coverslips in 12-well plates at 3×10^5 cells/well to reach medium density. 48hrs after transfection, cells were fixed and subjected to immunostaining with relevant antibodies (Section 2.2.6.4). Three fluorochromes were used: EGFP/Alexa Fluor™ 488, Alexa Fluor™ 568 and Alexa Fluor™ 647. Finally, images were acquired with an Airyscan confocal microscope. For the colocalisation experiment in DLD-1 WT cells, a single slice was acquired in Airyscan mode while for the colocalisation experiment in MAGI-1 knockout clone G2 14 (B), Z-stacks were acquired in confocal mode.

2.2.6.4 Immunostaining

Table 2.44 | Buffer composition for immunostaining procedure

Buffers	Composition
PBS 1X	137mM NaCl, 2.7mM KCl, 10mM Na ₂ PO ₄ , 1.8mMKH ₂ PO ₄ , pH 7.4
4% PFA (paraformaldehyde)	4% PFA in PBS 1X, pH 7.4
Quenching solution	0.1M Glycine in PBS 1X
Permeabilization solution	0.1% Triton X-100 in PBS 1X
Washing solution	0.01% Tween20 in PBS 1X
Blocking and antibody incubation solution	0.5% FBS, 0.01% Tween20 in PBS 1X

Fixation step and following PBS wash were carried out under a chemical fume hood. Liquid wastes and tips were collected in appropriate containers and disposed of by the University Health and Safety Officer. All steps were performed at room temperature unless otherwise stated. Washing steps were carried out in the multi-well plate.

First, cells were seeded on coverslips. When ready to be fixed, cells were washed twice with PBS 1X before being fixed with 4% PFA/PBS 1X for 15min under a fume hood. Excess PFA was removed by washing the cells once with PBS 1X. Any unreacted aldehyde molecules were then quenched by incubating cells with 0.1M Glycine/PBS 1X for 5min. Cells were washed twice more with PBS 1X. Then, samples were permeabilised with 0.1% Triton/PBS 1X for 15min. Coverslips were washed three times with 0.01% Tween20/PBS 1X. Next, cells were blocked in 0.5% FBS/0.01% Tween20/PBS 1X for 1hr to reduce unspecific binding. Samples were incubated with primary antibody overnight in a humidity chamber at 4°C. A piece of Parafilm® was placed at the bottom of a petri dish. The antibody dilution was prepared in blocking buffer

(See **Table 2.3** for dilutions) and a 35 μ L drop of antibody dilution was pipetted, per coverslip, on the Parafilm[®]. Coverslips were removed from the multi-well plate using forceps and the extra blocking buffer was drained on tissue paper. Each coverslip was placed, cell side down, on the drop of antibody dilution. A wet tissue paper was placed on top of the petri dish before closing the lid to ensure good humidity and prevent coverslips from drying out. Coverslips were incubated overnight at 4°C. The next morning, coverslips were placed back (cell-side up) in the multi-well plate using forceps and the extra antibody solution was drained on tissue paper. To remove excess antibody, coverslips were washed three times with 0.01% Tween20/PBS 1X. Coverslips were then incubated with secondary antibodies (See **Table 2.4** for dilutions) diluted in blocking buffer, together with Hoechst 33342 nuclear counterstain (1:2000 dilution), for 1hr in a humidity chamber at room temperature. The petri dish was placed in a dark environment. Afterwards, coverslips were placed back in the multi-well plate and washed three times with 0.01% Tween20/PBS 1X to remove the excess antibody. Then, coverslips were washed once with PBS 1X and once with dH₂O to remove salts. At that point, coverslips were taken out from the multi-well plate and the excess moisture was removed by gently tapping the empty side of the coverslips on tissue paper. Coverslips were mounted onto glass slides with 6 μ L Prolong gold anti-fade mounting medium. Slides were left to cure (solidify) for 24hrs at room temperature in a dark environment. The next day, the excess mounting medium was gently removed with wet tissue paper, coverslips were secured by applying four dots of nail polish on the rim and slides were stored at 4°C up to a few months.

2.2.6.5 *Microscopy*

2.2.6.5.1 *Epifluorescence microscope*

Stained cells were observed with an epifluorescence microscope using a 60X oil immersion objective. Images were acquired with the Volocity software.

2.2.6.5.2 *Confocal microscope*

Stained cells were observed with a LSM880 Airyscan Confocal using a 63X oil immersion objective. Images were acquired with the ZEISS ZEN Digital imaging software.

2.2.6.6 *Image processing – Fiji*

After acquisition, images were exported as TIFF files and further processed with the Fiji software. All images from a same experiment were processed in the same way.

2.2.7 Statistical analysis

Where applicable, a statistical analysis of the results was performed.

Graphs were prepared in GraphPad Prism software and data were represented in scatter plots with bars of the mean \pm standard error to the mean (S.E.M.). Statistical significance was assessed using the appropriate test depending on the dataset.

Figure 3.18: The statistical analysis of the data presented in this figure could not be performed. A one-way ANOVA relies on two assumptions, normal distribution of the data and equal variance, that were both violated in this case. The former was due to the low number of data points. The latter, verified by Levene's test ($p < 0.05$), resulted from a wide variability of values between repeats. Moreover, the normalisation to either WT or one density condition, necessary to compare several western blots, artificially set the variance for the control group to zero. This prevented the use of a modified one-way ANOVA, robust to unequal variances, such as Brown-Forsythe test in SPSS Statistics software (IBM Corporation).

Figure 3.20: Statistical significance was assessed using the SPSS Statistics software (IBM Corporation). First, a one-way ANOVA was performed. However, the dataset violated the two assumptions with an ANOVA analysis: 1) Normal distribution (most likely due to the low n number) and 2) Equal variances (Levene's test). Moreover, the dataset presented unequal sample size. Therefore, a Brown-Forsythe one-way ANOVA was performed instead. A Brown-Forsythe one-way ANOVA consists in transforming the data by taking the absolute deviation of each data point from the median of the group (transformed value = $ABS(\text{original value} - \text{median of the group})$) before running a one-way ANOVA. This test indicated a statistically significant difference amongst cell lines (**a**: $F(6,6.018)=379.062$, $p<0.0001$ and **b**: $F(6,8.085)=290.310$, $p<0.0001$). To determine where this difference laid, a post hoc Games Howell multiple comparisons' test was performed. This test is the appropriate choice when comparing groups with unequal variances.

Figure A. 15: Statistical significance was assessed using the SPSS Statistics software (IBM Corporation). Once again, the dataset presented unequal variances (Levene's test, $p < 0.0001$) and unequal sample sizes. Therefore, a Brown-Forsythe one-way ANOVA was performed which indicated a statistically significant difference in nuclear YAP amongst micropatterns sizes ($F(5,914.161)=142.460$, $p<0.0001$). To determine where this difference laid, a post hoc Games Howell multiple comparisons' test was performed.

2.2.8 OrganoPlate® methods

All experiments in OrganoPlates® were performed at MIMETAS, the-organ-on-a-chip company.

2.2.8.1 Gut tubules in 3-lane design

2.2.8.2 3-lane design

The OrganoPlate® 3-lane design possesses three microfluidic channels that meet in the centre (**Figure 2.10**). Each one can be accessed by two wells: inlet (IN), on the left, and outlet (OUT), on the right. The design relies on an innovative technology called Phaseguides™ which are carefully designed barriers building on the property of liquid to form menisci. They guide the air-liquid interface and the capillary pressure is affected by the change in geometry. The appropriate design ensures that a liquid meniscus forms over the PhaseGuide™ in an outward curved shape and stops the liquid from flowing beyond. When used with a liquid that gelates, such as extracellular matrix, it creates a barrier-free boundary between the two channels. To obtain a gut tubule, the middle channel is filled with Collagen-I, cells are then seeded on the top channel against the extracellular matrix and the bottom channel serves for medium perfusion (**Figure 2.10b-d**).

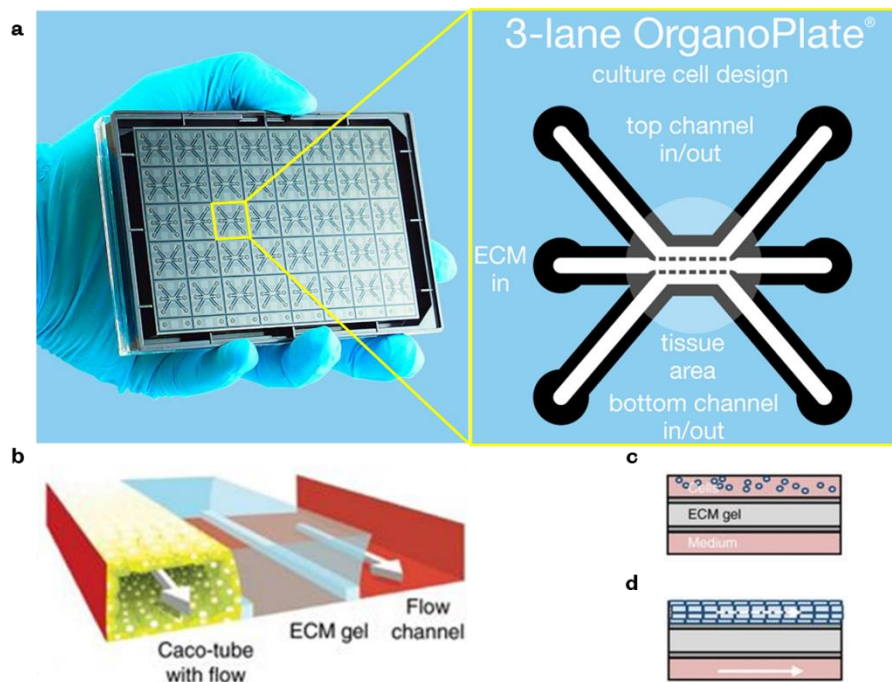


Figure 2.10 | OrganoPlate® 3-lane design.

a. Adapted from <https://mimetas.com/page/organoplate%C2%AE-3-lane>. (Left) Bottom of a 384-well plate with the forty 3-lane chips. (Right) Zoom-in on one of the microfluidic chips. The three channels meet in the centre. The access points are denominated inlet (IN) on the left and outlets (OUT) on the right. PhaseGuides™ are indicated by dotted lines. **b.** Example of a gut-tubule made with Caco-2 cells. The middle channel is used for the extracellular

matrix (ECM). Cells are then seeded in the top channel while the bottom channel is left free for medium perfusion. **c**, Schematics of the tissue area, where the three channels meet, right after seeding the cells. **d**, Schematics of the same chip a few days later when cells have formed a tubule. **b-d**, Taken from Figure 1 of (314).

2.2.8.2.1 Collagen-I coating

The Collagen-I (Culturex 5mg/mL, #3440-100-01, Lot# 42429E18) 4mg/mL solution was prepared on ice, as follow, immediately prior to dispensing it in the 3-lane middle channel. The final HEPES/NaHCO₃/Col-I ratio is 1:1:8, volume to volume.

First, HEPES 1M was mixed with NaHCO₃ 37g/mL. Salts were used to increase the solution's pH and allow polymerisation of Collagen-I. Then, Collagen-I 5mg/mL was added and the solution was homogenized by pipetting up and down before being spun briefly to allow air bubbles to collect at the surface. The tube was then kept on ice to slow down the polymerisation process and dispensed in the middle channel / gel inlets (2µL/chip) within ten minutes. Plates were incubated at 37°C, 5% CO₂ for 15min to allow polymerisation of the Collagen-I. Finally, 30µL of HBSS were added to the gel inlets to keep the ECM hydrated until cell seeding.

The gel channel is lined on both sides with Phaseguides™. Once the Collagen-I had polymerised, it created permeable barriers between channels (**Figure 2.11**).

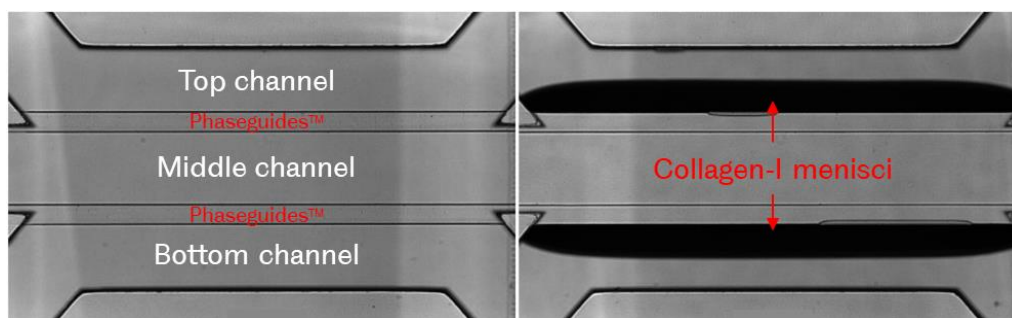


Figure 2.11 | Phase contrast images of a 3-lane design from the observation window (Top view).

(Left) Empty chip. (Right) Collagen-I has been dispensed in the middle channel allowing menisci to form on the Phaseguides™ lining the channel. The black areas correspond to the curved menisci of the gel/air interface.

2.2.8.2.2 Cell seeding in the OrganoPlate®

DLD-1 cells were used to form gut-tubules (**Table 2.45**).

Cells were trypsinised and collected into 15mL tubes. 10µL of cell suspension was mixed with 10µL of Trypan blue and half was added into each side of a counting slide (EVS-050, VWR). The cell number of each population was measured in duplicate using an automated cell

counter (EVE™, NANOENTEK). 1×10^6 cells for each population were aliquoted and pelleted (200xg, 5min) into micro-centrifuge tubes. Cells were resuspended in 100µL of RPMI complete medium to reach a concentration of 1×10^4 cells/µL. The cell suspension was then thoroughly homogenised prior to seeding in the channels. 2µL of cell suspension at 1×10^4 cells/µL were dispensed into the top channel inlet. One chip per plate was left cell-free to use as a negative control in assays. Next, 50µL of RPMI complete medium were added to the top inlets. Organoplates® were placed on a stand, at an angle of 105°, in the incubator (37°C, 5% CO₂) for 3hrs to force cells to sediment onto and attach first to the ECM. Once cells had attached to their substrate, 50µL of RPMI complete medium were added to the top outlets, bottom inlets and outlets. It was important to allow medium to flow from the inlets into the channels before adding more medium to the outlets to avoid trapping air bubbles. Finally, plates were placed horizontally, in the incubator, on a MIMETAS rocker alternating every 8min between +7° and -7° inclination, creating a bi-directional flow of medium. Over the following few days, cells were left to grow and form hollow tubules. Medium was refreshed every two days.

Table 2.45 | Cell lines cultured in the 3-lane OrganoPlate®.

Cell lines	Passage #	Genotype
DLD-1 WT	P32-38	WT
G1 8 (clone A)	P45-50	MAGI-1 KO
G2 14 (clone B)	P43-49	
G5+6 clone 28	P45-50	MAGI-3 KO
A5+6 clone 7	P55-60	MAGI1/MAGI3 double KO derived from MAGI-1 KO clone A or B
B5+6 clone 2	P53-58	

2.2.8.3 Barrier integrity assay

Epithelial tissues are characterised by their ability to form a selective barrier between their apical and basal sides. Cells are sealed to one another by tight junctions that restrict the paracellular passage of molecules. Therefore, substances that go through the epithelial layer have to enter the cells, by diffusion or active transport, which grants high selectivity to these tissues.

Barrier integrity (BI) assays were performed to assess the leak-tightness of the tubules. It consisted in monitoring the diffusion of two fluorescent compounds through the bottom cell layer of the tubules into the gel and bottom channels. A healthy epithelial tissue should be leak-tight to both FITC-Dextran 150kDa and TRITC-Dextran 4.4kDa fluorescent probes. The cell-free chip served as positive control for a leaky chip.

BI assays were performed as follow. First, all channels were washed with medium prior to the assay to ensure proper liquid flow. A working solution of both dyes were prepared by diluting FITC-Dextran 150kDa (Sigma, 46946) and TRITC-Dextran 4.4kDa (Sigma, T1037) in RPMI complete medium to a final concentration of 0.5mg/mL. Then, 40 μ L of fluorescent solution were dispensed in the top inlets and while only 30 μ L were pipetted to the outlets to allow quick perfusion. The middle and bottom channel inlets and outlets were filled with 20 μ L of complete RPMI complete medium. Leakage of the fluorescent compounds through the cell layer was monitored as quickly as possible by automatic and sequential imaging of the observation windows using an ImageXpress microscope (Molecular Devices). For each chip, pictures for both wavelengths were acquired every 2min over a total period of 14min. The analysis was then performed using ImageJ and a MIMETAS plugin that compared and normalised the fluorescence in the middle (ECM) to that of the top (cells) channel for each wavelength overtime. The ratio $Fluo_{GEL}/Fluo_{TOP}$ was plotted overtime (**Figure 2.12**). Due to the many cell lines to compare, the last time point (14min) alone was considered and represented.

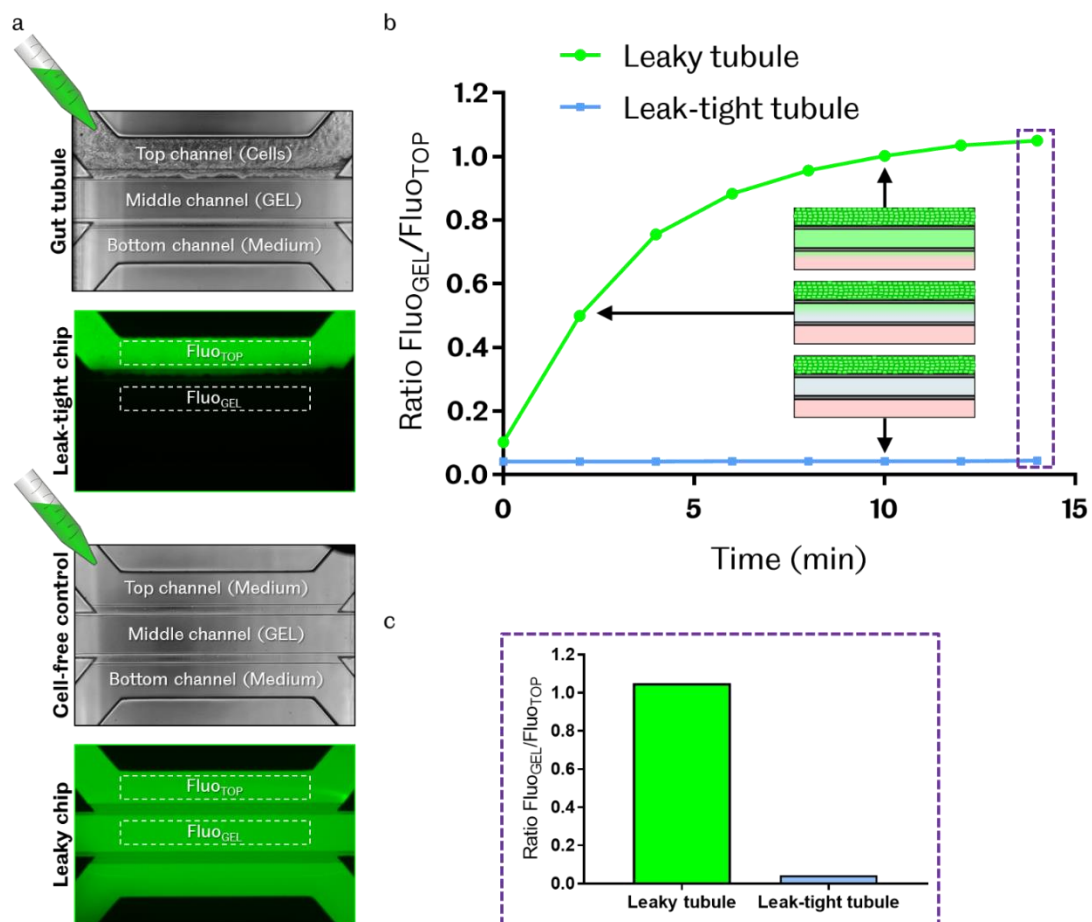


Figure 2.12 | Example of quantification of the barrier integrity assay in OrganoPlate®.

a. Example of leak-tight (gut tubule – Top) and leaky (cell free control – Bottom) 3-lane Organoplate® chips. Phase contrast and fluorescent images of the top (cells), middle (ECM) and bottom (medium) channels after dispensing fluorescent Dextran (FITC in this case) in the tubule (top channel). The white dotted boxes correspond to the regions considered during quantification. The fluorescence measured in the gel (middle) channel (Fluo_{GEL}) is normalised to the fluorescence in the top channel (Fluo_{TOP}) and the ratio is plotted over time (**b**). The fluorescence ratio for a leak-tight tubule stays very low (Blue), as no Dextran passes through the cell barrier. However, the ratio for a leaky vessel increases overtime, as the Dextran diffuses into the gel channel, until reaching a value of ~1.0 at steady-state. **c.** Bar graph representing the value of the fluorescence ratio at the last time point considered (**b** – purple dotted box).

2.2.8.4 EdU proliferation assay

An EdU assay (ThermoFisher Scientific, Click-iT™ Plus EdU Alexa Fluor™ 647 Imaging Kit, #C10640) was used to determine the number of cells proliferating in early (Day4) and late (Day10) stages DLD-1 tubules. This assay relies on the incorporation of a modified thymine analogue, EdU, into newly synthesised DNA. The detection is then possible through a click reaction catalysed by copper, between the alkyne residue of the EdU and the azide from the Alexa Fluor® dye, creating a covalent bond between the two molecules (**Figure 2.13**) (315-317).

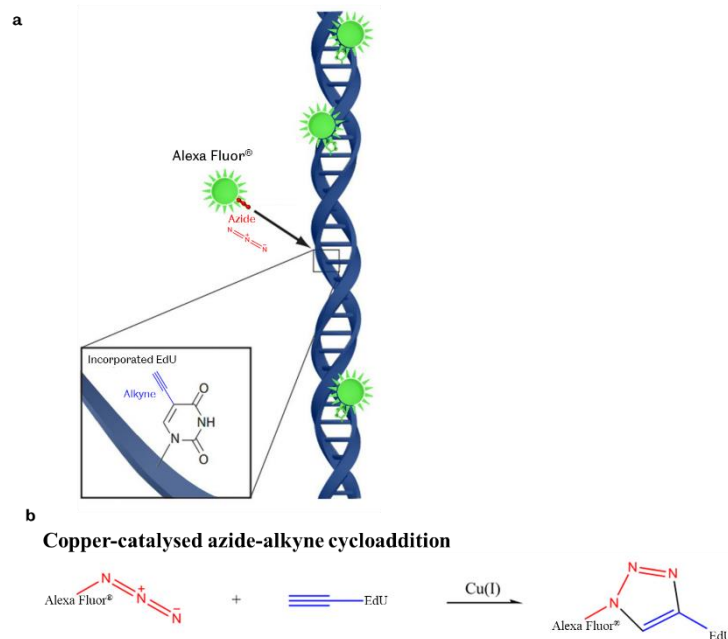


Figure 2.13 | Edu incorporation in DNA and easy detection via click reaction.

a. Adapted from <https://www.genecopoeia.com/product/tracking-new-dna-synthesis/>. The alkyne-containing thymidine analogue, EdU, is incorporated in the DNA of proliferating cells and can be easily detected by the addition of an Alexa Fluor® probe containing an azide residue. Copper catalyses the click reaction between the two moieties, linking them covalently. **b.** Illustration of the click cycloaddition. Adapted from (45,318).

The first 3-lane OrganoPlate[®] was seeded with all 6 cell lines to characterise (**Table 2.45**). Six days later, the second plate was seeded in a similar manner, with triplicates of each cell lines. The EdU assay was performed simultaneously on both plates, on Day10 and Day4 respectively (described below).

Table 2.46 | Click-iT[®] Plus reaction cocktail.

Click-iT [®] Plus reaction cocktail
Click-iT [®] EdU reaction buffer
Copper protectant
Alexa Fluor [®] 647
Reaction buffer additive

The EdU concentration and incubation time were adapted from manufacturer's instructions and MIMETAS protocol. First, the EdU compound was fed to the cells and incubated for 4hrs (37°C, 5% CO₂, bi-directional flow), during which it was incorporated in newly synthesised DNA at each replication. For each cell line, one chip was used as control and was only fed DMSO (vehicle). Tubules were then fixed with 3.7% formaldehyde in HBSS for 15min and washed twice with a 3% BSA solution in HBSS for 3min. Then, cells were permeabilised in 0.5% Triton X-100 in HBSS for 20min at room temperature before being washed twice with a 3% BSA solution in HBSS for 3min. The Click-iT[®] Plus reaction cocktail (**Table 2.46**) was added to the cells and the plate incubated on the rocker for 30min at room temperature, wrapped in aluminium foil to avoid light exposure. Cells were washed twice with a 3% BSA solution in HBSS for 3min. Then, cells nuclei were stained with Hoechst[®] 33342 (supplied in the kit) at a working concentration of 5µg/mL in HBSS, for 30min on the rocker, protected from light. Cells were washed twice with a 3% BSA solution in HBSS for 3min and HBSS was added to all channels to allow imaging. Z-stacks of each chip with Cy5 and DAPI filters were taken using a MoIDev (Molecular Devices) confocal microscope. Only the sum projection of each stacks was saved. Data processing was conducted with Fiji using plugins developed by MIMETAS (**Table 2.47**). First, the number of nuclei per image was assessed using the nuclear counterstain Hoechst. Then, the total intensity of the EdU signal (Cy5 channel) was determined. Finally, the intensity per nucleus was calculated for each picture and averaged, whenever possible, among duplicates. Some chips had a very low Hoechst signal, probably due to a technical issue during the immunostaining procedure, which impaired the quantification. These samples were excluded.

Table 2.47 | Parameters used in the MIMETAS plugin to process EdU assay.

Nuclei size	7µm
Magnification/ binning (20x confocal)	0.36
Background correction	40
Background average intensity	8000

2.2.8.5 Viability assay

A WST-8 based viability assay (Sigma, Cell counting kit-8, #96992) was used to assess the number of viable cells in the DLD-1 tubules on Day7 after seeding. The water-soluble tetrazolium salt, WST-8, is reduced in living cells by dehydrogenases, producing a water-soluble yellow-coloured product, called formazan. The amount of formazan dye generated can be measured by absorbance at 450nm in a Plate reader, and is directly proportional to the living cell number.

The assay was conducted according to the manufacturer's instruction and MIMETAS protocol. Two types of negative controls were used: cell-free control and no WST-8 reagent control.

First, a 1:10 working dilution of WST-8 in HBSS was added to the cells and the plate was placed on the rocker inside the incubator for 30min. In the no WST-8 control chip, only HBSS was added. Perfusion inside the channels was stopped by leaving the plate still in the incubator for an extra 5min. Then, absorbance at 450nm was measured in each chip with a Plate reader, preheated at 37°C. Finally, analysis was performed by subtracting the blank measurement (cell-free chip) to the absorbance value for each chip.

2.2.8.6 Immunostaining

Table 2.48 | Primary antibodies used for immunostaining in the OrganoPlate®.

Antibody	Dilution	Cat#, Company
Occludin (rabbit)	1:100	71-1500, Invitrogen™
ZO-1 (rabbit)	1:250	617300, Invitrogen™
E-cadherin (mouse)	1:300	610181, BD Biosciences
MAGI-1 (rabbit)	1:250	M5691, SIGMA Aldrich (Merk) (previously described in Table 2.3)
YAP/TAZ (mouse)	1:200	Sc-101199, Santa Cruz Biotechnologies (previously described in Table 2.3)

Immunostaining of cells in the OrganoPlate[®] was performed according to MIMETAS protocol. All steps, except for the secondary antibodies incubation, were performed using differential volumes between the cell (top) inlet and other wells to ensure perfusion through the cell channel and the whole chip.

First, cells were fixed with 3.7% formaldehyde in HBSS for 15min, then, washed twice with PBS for 5min and once with the washing solution (4% FBS/PBS). Next, cells were permeabilised for 10min in 0.3% Triton X-100 in PBS and washed with the washing solution for 5min. The blocking step was performed in a solution of 2% FBS / 2%BSA / 0.1% Tween in PBS (blocking buffer) for 45min. Cells were incubated with primary antibodies in blocking buffer overnight at 4°C (**Table 2.48**). Cells were washed twice with the washing solution for 5min. and then incubated with secondary antibodies, nuclear counterstain (Hoechst) and ActinGreen[™] ReadyProbes[®] when needed (**Table 2.49**). Cells were washed twice with the washing solution for 5min and an extra PBS 1X wash was carried out for 5min. Next, all wells were filled with PBS 1X to allow imaging. Z-stacks of the tubules were acquired using a MolDev confocal microscope, 20x air objective (**Figure 2.14**). Images were processed in Fiji using a MIMETAS plugin. All images were processed with the same parameters.

Table 2.49 | Fluorescent antibodies used for immunostaining in the OrganoPlate[®].

Antibody/Probe	Dilution	Cat#, Company
ActinGreen [™] 488 ReadyProbes [®]	2 drops/mL	R37110, LifeTechnologies
Goat anti-rabbit IgG (H+L) Cross-Adsorbed Secondary Antibody, Alexa Fluor [®] 555	1:250	A21428, Invitrogen [™]
Goat anti-Mouse IgG (H+L) Cross-Adsorbed Secondary Antibody, Alexa Fluor [®] 488	1:250	A-11001, Invitrogen [™]
Hoechst 33342	1:2000	H3570, Invitrogen [™]

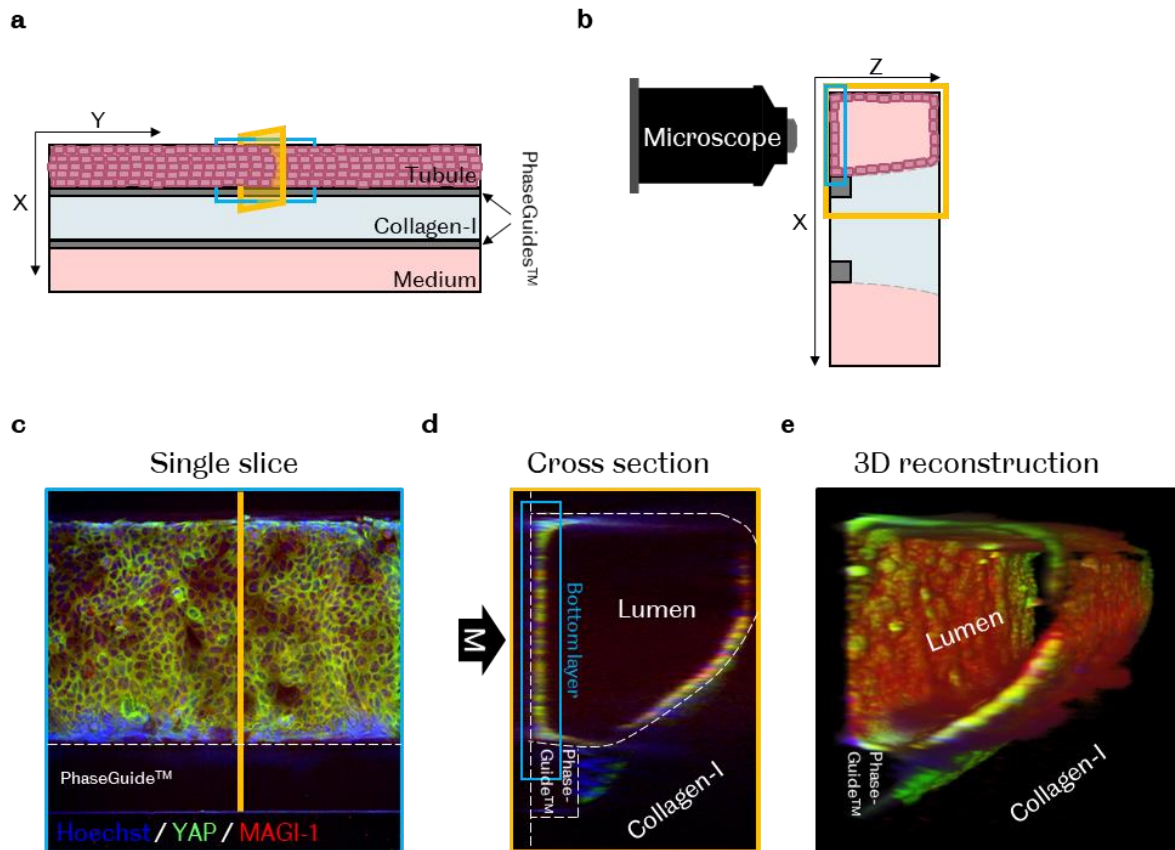


Figure 2.14 | Confocal imaging of gut tubules in a 3-lane OrganoPlate®.

a, Top view of a 3-lane chip (schematic representation) with the top (Tubule), middle (Collagen-I) and bottom (Medium) channels, separated by PhaseGuides™. The turquoise box indicates the bottom layer of cells (XY plane) that is imaged with an inverted microscope (example shown in **c**). The orange box shows a cross-section of the tubule, along the XZ plane (example shown in **d**). **b**, Schematic representation of the entire cross-section of a chip along the XZ plane. The objective of an inverted microscope is positioned below the plate and images are acquired through the glass bottom. Z-stacks of tubules are acquired along the Z axis. **c**, **d** & **e**, Day4 DLD-1 WT tubule stained with Hoechst (nuclear counterstain, Blue), anti-YAP (Green) and anti-MAGI-1 (Red) antibodies. Images acquired with a confocal microscope, 20x objective. Scale bar: 50µm. The images show only the top channel, containing the tubule and part of the gel channel. The positions of the lumen, PhaseGuide™ and Collagen-I are indicated. **c**, Single slice showing the bottom cell layer of a tubule (turquoise box in **c**). **d**, Orthogonal view of the tubule generated from a Z-stack (taken along the Z axis). The arrow indicates the position of the microscope. **e**, 3D reconstruction of the entire tubule from the Z-stack in Fiji.

3 Chapter 3: MAGI-1 and MAGI-3 regulate the Hippo-YAP pathway's response to cell density and YAP cytoplasmic retention

3.1 Introduction

YAP/TAZ subcellular localisation is thought to be regulated via a phosphorylation-dependent mechanism (8,63). Cell density has been shown to be an important regulator of YAP/TAZ localisation (8,66). Indeed, in sparse cultures, YAP/TAZ undergoes nucleocytoplasmic shuttling but accumulates preferentially in the nucleus where it promotes transcription of target genes through association with various transcription factors (319). As cells grow denser and establish proper cell-cell contacts, the Hippo cascade activates, promoting YAP/TAZ phosphorylation by the LATS1/2 kinases. Upon phosphorylation, YAP/TAZ are gradually sequestered in the cytoplasm via several regulator proteins such as 14-3-3 (8,20,30,33), PTPN14 (71-75) and AMOT (76,77,137,138). In dense culture, YAP/TAZ are completely excluded from the nucleus resulting in contact-inhibition of proliferation (8,69).

MAGI-1, a tight junction and multi-PDZ domain protein, was recently identified in a Hippo pathway kinome RNAi screen (160). Their findings indicate that MAGI-1 affects YAP subcellular localization in a cell density-dependent manner in HaCaT and HEK293 cells. However, the mechanisms at play remain to be elucidated.

3.2 Aims

Here, we aimed at investigating the mechanism governing MAGI-1 regulation of YAP subcellular localisation. First, we asked whether MAGI-1 was a universal regulator of cell density-dependent Hippo signaling in epithelial cells. Then, we established a stable system to study the effects of MAGI-1 on YAP Ser127 phosphorylation status and subcellular localisation in response to cell density using CRISPR/Cas9 gene editing technique.

In front of the high similarity among the members of the MAGI family, we aimed at investigating the role of MAGI-2 and MAGI-3 in YAP regulation.

3.3 Results

3.3.1 MAGI proteins play a role in YAP nuclear exclusion at high cell density

MAGI-1, a multi-PDZ and tight junction protein, was identified by Mohseni and collaborators and shown to affect YAP subcellular localisation at high cell density in HaCaT and HEK293 cells (160). However, the mechanism of MAGI-1's link to the Hippo-YAP pathway remains elusive.

3.3.2 YAP localisation is cell density dependent in epithelial cells

The nucleocytoplasmic shuttling of the Hippo pathway downstream effector, YAP, directly correlates with its activity as a transcriptional co-activator. We therefore intended to use this feature as a direct read-out of YAP's activity. We first established a reliable immunofluorescence qualitative assay to assess YAP subcellular localisation across different cellular densities. Two kidney and two colon adenocarcinoma epithelial cell lines, namely HEK293, MDCK-II, Caco-2 and DLD-1 (**Table 3.1**), were seeded at low, medium and high cell density and subjected to anti-YAP immunostaining (**Figure 3.1**). All four cell lines tested displayed the same phenotype, in line with the literature: 1) in sparse cultures, YAP shuttles between nucleus and cytoplasm but mainly accumulates in nuclei to promote cell proliferation; 2) as density increases, cell-cell contacts activate the Hippo cascade which results in progressive sequestration of YAP in the cytosol; 3) at high cell density, YAP is excluded from nuclei (White arrows). When sequestered in the cytoplasm, YAP is spatially prevented to fulfil its role of transcriptional co-activator (8). In addition, in MDCK-II, Caco-2 and DLD-1 cells we observed that YAP was enriched at cell-cell contacts (White arrowheads) already in sparse cultures. Taken together, our results show that YAP subcellular localisation is cell-density dependent in HEK293, MDCK-II, Caco-2 and DLD-1 cell lines. This density assay provides a clear and qualitative read-out of YAP activity.

Table 3.1 | Epithelial cell lines

Cell line	Organism	Tissue	Morphology	Disease
HEK293 Human Embryonic Kidney	Human	Embryonic kidney	Epithelial Adherent	Normal
MDCKII Madin-Darby Canine Kidney	Dog	Kidney	Epithelial Adherent	Normal
Caco-2 AdenoCArcinoma of the COlon	Human	Colon	Epithelial Adherent	Colorectal adenocarcinoma
DLD-1 Daniel L. Dexter	Human	Colon	Epithelial Adherent	Dukes' type C, colorectal adenocarcinoma

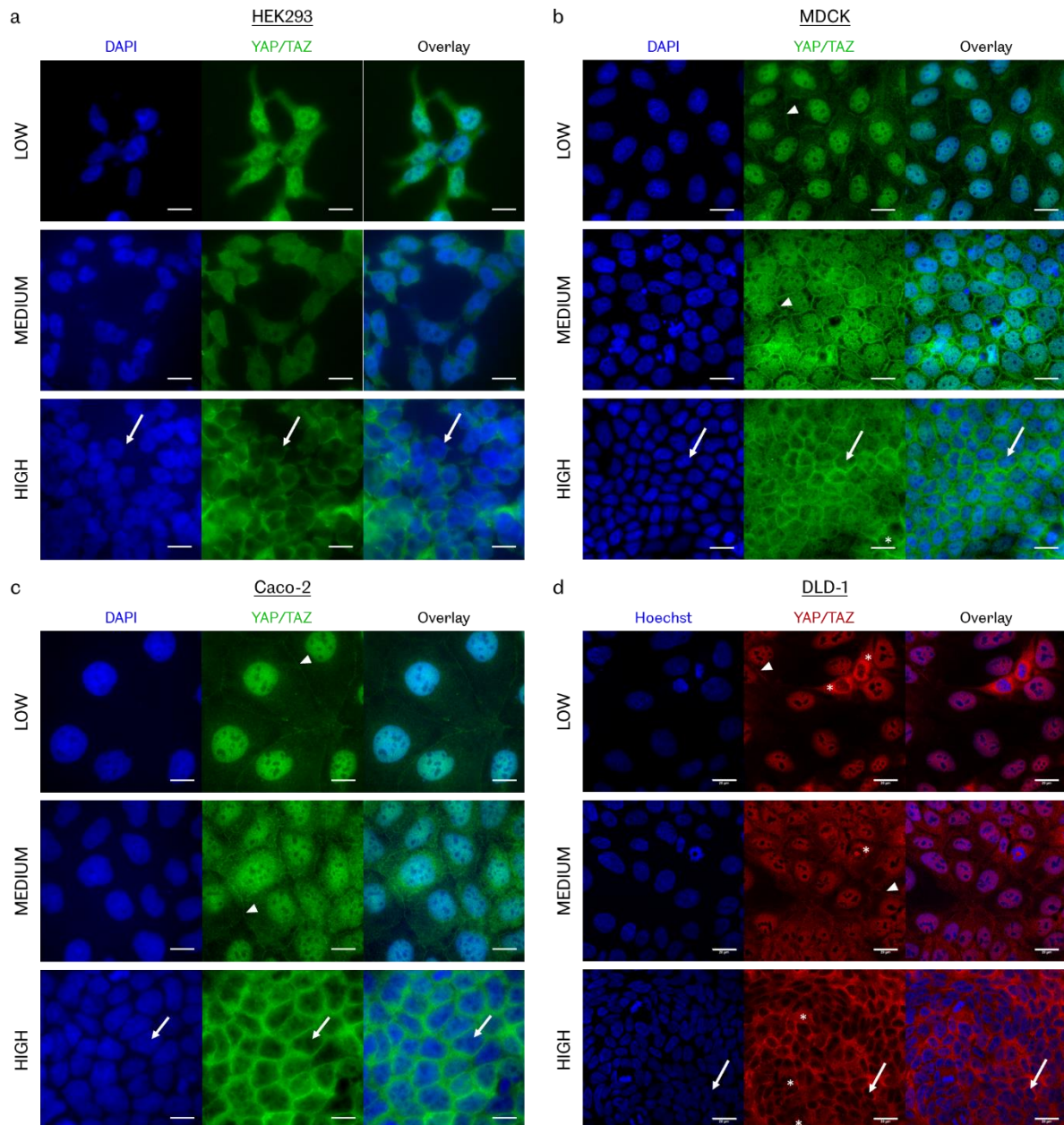


Figure 3.1 | YAP subcellular localisation is cell density dependent in epithelial cells.

HEK293 (n=3) (a), MDCK-II (n=1) (b), Caco-2 (n=3) (c) and DLD-1 (n=3) (d) cells were seeded on coverslips at low, medium and high density. Immunostaining was performed using an anti-YAP/TAZ antibody. Images were acquired with an epifluorescence (a-c) or a confocal (d) microscope. Scale bars: 20µm. At low cell density (LOW), YAP is mostly nuclear. When density increases (MEDIUM), YAP becomes distributed between nucleus and cytosol and in dense cultures (HIGH), YAP is excluded from the nucleus (arrows). In MDCK-II (b), Caco-2 (c) and DLD-1 (d) cells, YAP is localised at cell-cell contacts (arrowheads) already in sparse cultures. White asterisks (*) indicate dividing cells for which YAP is localised in the whole cell volume around the DNA. MDCK-II (b) images taken by Dhruv Ritesh Shah, undergraduate student. Secondary-only controls are shown in [Figure A. 2](#).

3.3.3 MAGI-1 depletion drives YAP into the nucleus at high cell density

3.3.3.1.1 MAGI-1 transient knockdown promotes YAP nuclear localisation at high cell density

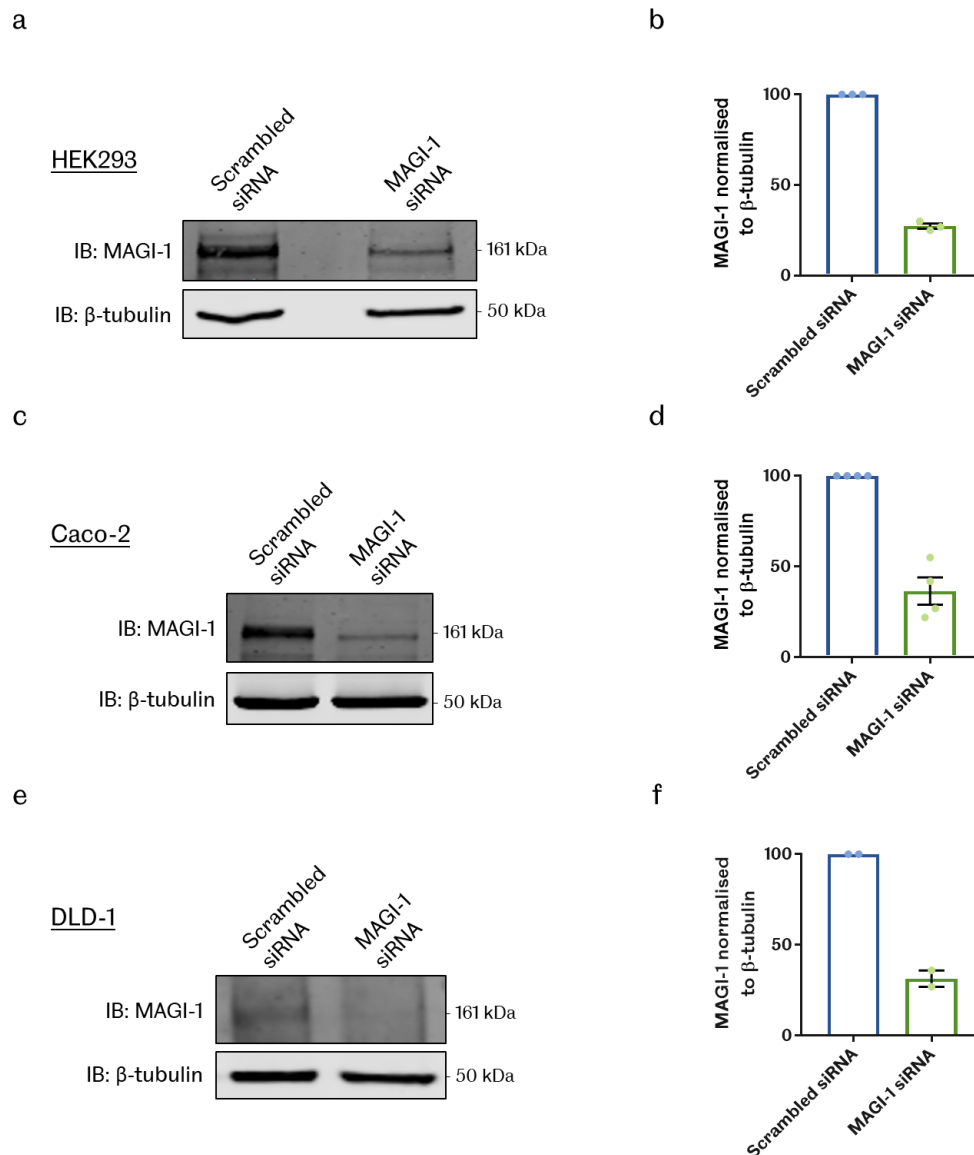


Figure 3.2 | MAGI-1 transient knockdown in HEK293, Caco-2 and DLD-1 cells.

HEK293 (n=3) (a & b), Caco-2 (n=4) (c & d) and DLD-1 (n=2) (e & f) cells transiently transfected with either MAGI-1 or Scrambled siRNA as indicated. Scrambled siRNA was used as a negative control. MAGI-1 knockdown efficiency was assessed by western blot using an anti-MAGI-1 antibody and β -tubulin was used as loading control (b, d & f). Quantification of MAGI-1 knockdown efficiency was performed in each cell line. Individual data points are shown and the bars represent the mean value \pm S.E.M. MAGI-1 levels were first normalised to the associated β -tubulin signal. Scrambled siRNA control represent 100%.

Next, we investigated the consequence of MAGI-1 transient depletion on YAP nucleocytoplasmic shuttling using the previously described density read-out assay. HEK293, Caco-2 and DLD-1 cells were seeded to reach high density within 96hrs or 120hrs, depending on the cell line (See Chapter 2, Section 2.2.6.2.2 for protocol details). Transient transfection

was performed with either MAGI-1 or Scrambled siRNA. Knockdown efficiency was assessed by western blotting using an anti-MAGI-1 antibody and β -tubulin as a loading control (**Figure 3.2**). We reached, in all three cell lines, a 70% reduction of the MAGI-1 expression levels upon siRNA transfection.

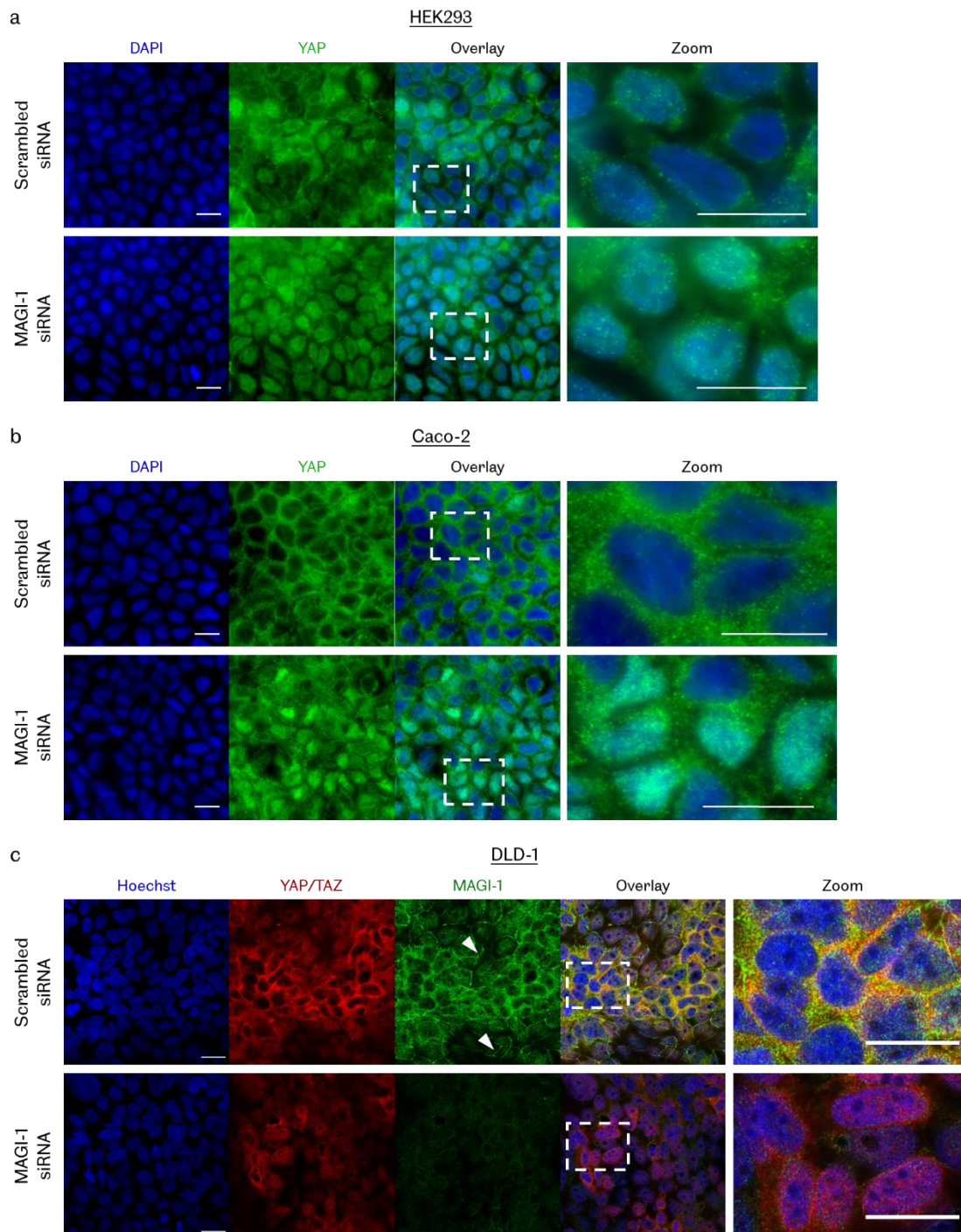


Figure 3.3 | MAGI-1 transient knockdown induces nuclear localisation of YAP at high cell density.

HEK293 (n=2) (a), Caco-2 (n=3) (b) and DLD-1 (n=2) (c) cells were seeded to reach high density and transiently transfected with either MAGI-1 or Scrambled siRNA as indicated. Scrambled siRNA was used as a negative control. MAGI-1 knockdown efficiency was assessed by western blot (Figure 3.2). Immunostaining was performed using an

anti-YAP antibody to investigate YAP subcellular localisation in dense cultures. Images were acquired with an epifluorescence (a & c) or a confocal (d) microscope. Scale bars: 20µm. In samples transfected with the Scrambled siRNA, YAP localisation is mainly cytoplasmic as expected. However, MAGI-1 transient depletion drives YAP to the nucleus at high density in all three cell lines. The white arrowheads (d) indicate MAGI-1 junction localisation. Secondary-only controls are shown in **Figure A. 2**

In parallel, immunostaining with an anti-YAP antibody was performed on the Scrambled and MAGI-1 siRNA transfected cells (**Figure 3.3**). HEK293 and Caco-2 cells were imaged with an epifluorescence microscope (**Figure 3.3a & b**). Both cell lines displayed YAP nuclear accumulation at high density, contrary to control (Scrambled siRNA). DLD-1 cells were stained with anti-YAP/TAZ and anti-MAGI-1 antibodies and imaged with a confocal microscope. We observed the same YAP phenotype in confirmed MAGI-1 knocked-down cells. Our results are in line with the work of Mohseni and co-workers (160) and show that transient depletion of MAGI-1 drives YAP into the nucleus at high cell density. Taken together, our data show that MAGI-1 plays a role in the regulation of YAP subcellular localisation. We therefore hypothesized that MAGI-1 could either act by promoting LATS-mediated phosphorylation of YAP, first step toward its exclusion from the nucleus, or by being involved in YAP sequestration in the cytosol.

3.3.3.1.2 MAGI-1 overexpression does not promote cytoplasmic retention of YAP in sparse cells

Next, we asked whether overexpression of MAGI-1 could provoke YAP cytoplasmic retention, much like other well-characterised negative regulators of YAP (73,74,76). As YAP is normally cytoplasmic in dense cells, this experiment was conducted at low cell density to be able to evidence a change in localisation from nuclear to cytoplasmic, should there be one. PTPN14 was used here as a positive control. First, HEK293 cells were transiently transfected with either Flag-mMAGI-1B or V5-PTPN14 expression constructs. Cells were cultured at low density and subjected to immunostaining to assess localisation of endogenous YAP upon overexpression of either protein (**Figure 3.4a**). In WT cells, YAP was found, as expected, in the nucleus (Top panel). Upon overexpression of PTPN14, YAP was driven out of the nuclei and sequestered in the cytosol, as reported in the literature (73,74). However, MAGI-1 overexpression did not induce translocation of YAP from nucleus to cytoplasm. We observed the same behaviour in DLD-1 cells (**Figure 3.4b**). Interestingly, we noticed that overexpression of MAGI-1 in HEK293 was enriching YAP at cell-cell contacts (Arrowheads) which is not the case in WT cells (**Figure 3.1a** and **Figure 3.4a** top panel). In DLD-1 cells, on the other hand, as noticed previously (**Figure 3.1d**), YAP was already enriched at the plasma membrane at low density regardless of MAGI-1 overexpression (**Figure 3.4b** arrows). Taken together, our

results indicate that MAGI-1 is not sufficient to induce cytoplasmic retention of YAP at low cell density, unlike PTPN14. MAGI-1, being a tight junction protein, we hypothesised that the cellular context in which it exerts a negative regulation on YAP was not recapitulated at low cell density and therefore the trigger of density was missing from this experiment. Our data also suggests that MAGI-1 contributes to YAP being enriched at cell-cell contacts in HEK293 cells.

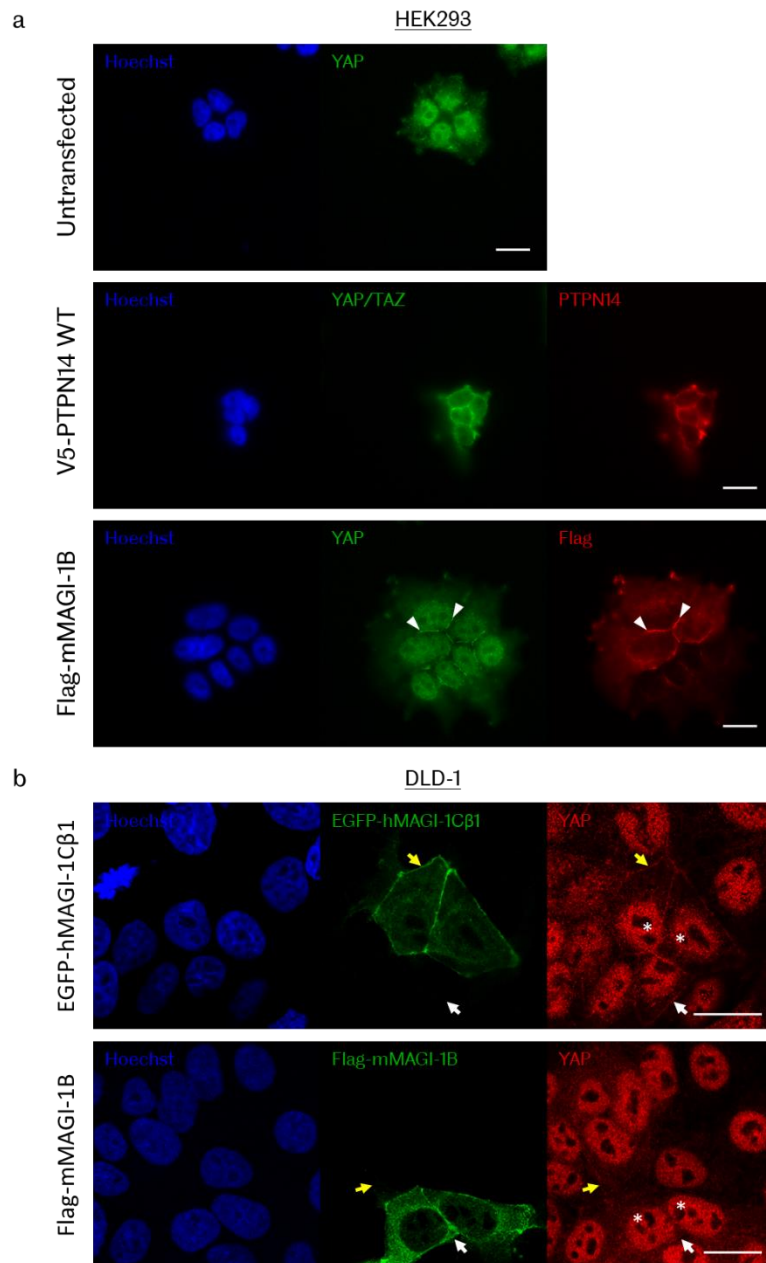


Figure 3.4 | MAGI-1 overexpression does not induce exclusion of YAP from the nucleus in sparse cells.

a. HEK293 cells were transiently transfected with either V5-PTPN14 (used as positive control) or Flag-mMAGI-1B (n=1). Untransfected HEK293 cells (Top panel) were used as negative control. Cells were cultured at low density and subjected to immunostaining with anti-YAP (endogenous), anti-YAP/TAZ (endogenous), anti-PTPN14 or anti-Flag antibodies as indicated. Hoechst was used as nuclear counterstain. Images were acquired with an epifluorescence microscope. Scale bars: 20µm. In untransfected cells, YAP is normally nuclear in sparse cells. Upon

overexpression of PTPN14, YAP is forced out of the nucleus, corroborating literature (73,74). mMAGI-1B overexpression does not induce YAP exclusion from the nucleus at low cell density. Arrowheads point at enriched YAP at the cell-cell contacts upon MAGI-1 overexpression. **b**, DLD-1 cells were kept at low density and transiently transfected with either EGFP-hMAGI-1C β 1 or Flag-mMAGI-1B constructs as indicated (n=1). Immunostaining was performed with an anti-YAP antibody (endogenous) and anti-Flag antibody when appropriate. Hoechst was used as nuclear counterstain. Images were acquired with a confocal microscope. Scale bars: 20 μ m. The white asterisks indicate cells overexpressing MAGI-1. Here again, MAGI-1 overexpression does not affect YAP nuclear localisation at low cell density. In DLD-1 cells, YAP is enriched at the plasma membrane regardless of MAGI-1 overexpression (yellow (with) and white (without) arrows).

3.3.3.1.3 Generation of stable MAGI-1 knockout cell lines using CRISPR/Cas9 technique

Based on the promising results of MAGI-1 transient depletion, we aimed at generating MAGI-1 stable knockout cell lines using CRISPR/Cas9 technique to further characterise the nature and mechanism of MAGI-1 regulation of YAP.

The DLD-1 colon adenocarcinoma cell line was selected as a model cell line based on the following criteria:

- 1) Forms epithelial monolayer with proper tight junctions (**Figure 3.5**)
- 2) Proper localisation of MAGI-1 at tight junctions (**Figure 3.5**)
- 3) Expresses high levels of MAGI-1 (320)
- 4) YAP nucleocytoplasmic shuttling based on cell density is conserved (**Figure 3.1d**)
- 5) DLD-1 cells are 90-95% diploid (321) which make them suitable for CRISPR/Cas9 technique.

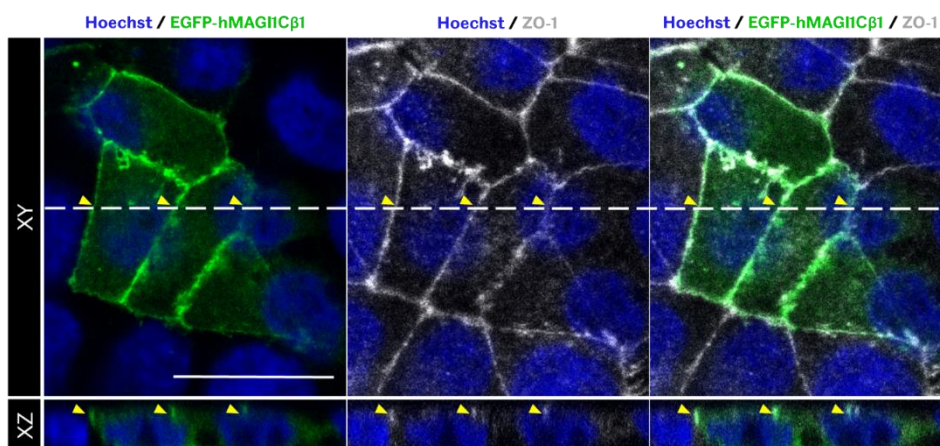


Figure 3.5 | MAGI-1 colocalises with ZO-1 at tight junctions.

Confocal images of DLD-1 cells acquired with a 60x objective. DLD-1 cells were transiently transfected with EGFP-hMAGI-1C β 1 (Green) construct. Immunostaining with an anti-ZO-1 (Greys) antibody was performed. Hoechst was used as a nuclear counterstain. XY view corresponds to a single slice of the Z-stacks, corresponding to the apical

view. XZ represents the orthogonal view taken along the white dotted line. DLD-1 cells form proper tight junctions and MAGI-1 colocalises with ZO-1. Scale bars: 20µm.

We aimed at generating complete MAGI-1 knockout in DLD-1 cells, using the CRISPR NHEJ (Non-homologous end-joining) repair mechanism. We therefore designed single guide RNAs within Exon1 to generate STOP codons as early as possible within the gene, while targeting all isoforms (**Figure 3.6**). We selected two sgRNAs (**Figure 3.6 & Table 3.2**), G1 and G2, that were sufficiently far apart within Exon1 to increase the chances of efficiency. Primers to amplify the targeted region were designed using NCBI Primer Blast tool (Primers #19 and #20 from **Table 2.7**, Chapter 0). Each sgRNA was cloned into a PX458-Cas9-GFP vector (See Chapter 0 for detailed protocol).

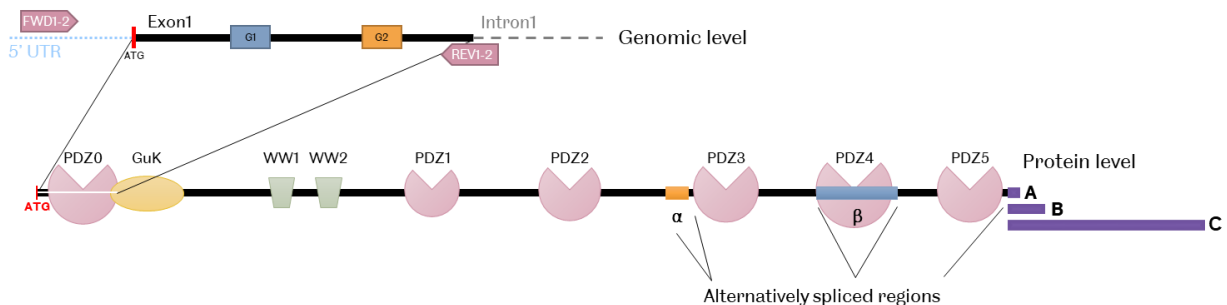


Figure 3.6 | Design of two sgRNAs targeting MAGI-1 Exon1.

(Top) Map of MAGI-1 5'-UTR, Exon1 and beginning of Intron1, illustrating the position of G1 and G2 as well as of the primer pair (FWD: forward and REV: reverse) designed to amplify the region targeted by the sgRNAs. (Bottom) Schematic representation of MAGI-1 alternatively spliced regions: α, β and C-terminal tail. Targeting Exon1, far upstream of the first alternatively spliced domain, ensures that all MAGI-1 isoforms will be affected by the CRISPR/Cas9 gene editing.

Table 3.2 | MAGI-1 sgRNAs targeting Exon1

Table recapitulating the two single guide RNAs selected to induce MAGI-1 knockout along with the primers designed to amplify the targeted region (illustrated in **Figure 3.6**). BbsI site. Oligonucleotide numbers (#) refer to Table 2.9 (sgRNAs) and Table 2.7 (primers) of Chapter 0.

Single guide RNA	Targeted Sequence_PAM	Exonic off-targets
sgRNA1 (G1) (#1 & #2)	GGAGTTTCCGTACGTCGGAG_CGG Top: 5' - CACCGGGAGTTTCCGTACGTCGGAG - 3' Bottom: 5' - AACCTCCGACGTACGGAACTCC - 3' Duplex: 5' - CACCGGGAGTTTCCGTACGTCGGAG - 3' 3' - CCTCAAAGGCATGCAGCCTCCAAA - 5'	None

Figure 3.7 | Validation of MAGI-1 knockout clones G1 8 (A) and G2 14 (B).

a, Sequencing results of G1 8 (A) and G2 14 (B) MAGI-1 knockout (KO) clones. Alignment with WT sequence of the targeted region. G1 8, a homozygote clone, counts a one-nucleotide addition that leads to a frameshift and a premature STOP codon after 85aa. G2 14 is a heterozygote KO clone. One allele (A1) suffered a two-base pair deletion while the other (A2) underwent a five-nucleotide deletion. Both alleles have a premature STOP codon at 125 and 124aa respectively. The numbers in red indicate the extent of the mutation in nucleotides. **b**, Proteins were extracted from MAGI-1 KO clones and DLD-1 WT and samples were subjected to western blotting with an anti-MAGI-1 antibody. β -tubulin was used as a loading control. The red arrow points at the MAGI-1 band which is gone in the KO clones. **c**, MAGI-1 KO clones and DLD-1 WT cells were cultured on coverslips and subjected to anti-MAGI-1 immunostaining. Images were acquired with a confocal microscope. Hoechst was used as a nuclear counterstain. Scale bars: 20 μ m. The white arrow indicates MAGI-1 junction localisation which is no longer visible in MAGI-1 KO clones.

DLD-1 WT cells were transfected with either PX458-G1 or PX458-G2 vectors and sorted into single cells by FACS. Clone screening consisted in the (1) characterisation of CRISPR-induced indels at the targeted site by sequencing and (2) validation at the protein level using western blotting and immunostaining. The validation of two of the MAGI-1 knockout clones, G1 8 (A) and G2 14 (B), originating from either guides, is shown in **Figure 3.7**. The sequencing results predicted the occurrence of premature STOP codons. The absence of protein was confirmed with western blotting and immunofluorescence. These two clones were therefore used for further study.

The two predicted off-targets of G2, SIPA1 and CNTN5, were checked by sequencing in G2 14. No mutation was found in either of these genes.

3.3.3.1.4 MAGI-1 stable depletion mildly affect YAP subcellular localisation at high cell density

Using the freshly generated MAGI-1 knockout clones, we repeated the density assay. DLD-1 WT cells alongside G1 8 (A) and G2 14 (B) MAGI-1 KO clones were seeded at low, medium and high density. Having a stable cell line system allowed for a better control of the final densities. Cells were subjected to anti-YAP/TAZ immunostaining (**Figure 3.8**). DLD-1 WT and MAGI-1 KO clones alike showed nuclear YAP/TAZ at low cell density. However, some divergences appeared at higher densities. While there was a striking difference between medium and high density in WT cells, MAGI-1 KO clones looked similar in both, with YAP being distributed between nucleus and cytoplasm. These results could indicate a higher threshold for maximum density. Surprisingly, the YAP defect in dense cultures observed in MAGI-1 KO clones (**Figure 3.8**) was milder than in MAGI-1 transiently depleted cells (**Figure 3.3**). We therefore hypothesised that with the stable character of a knockout, cells had time to adapt and partially compensate for MAGI-1 depletion.

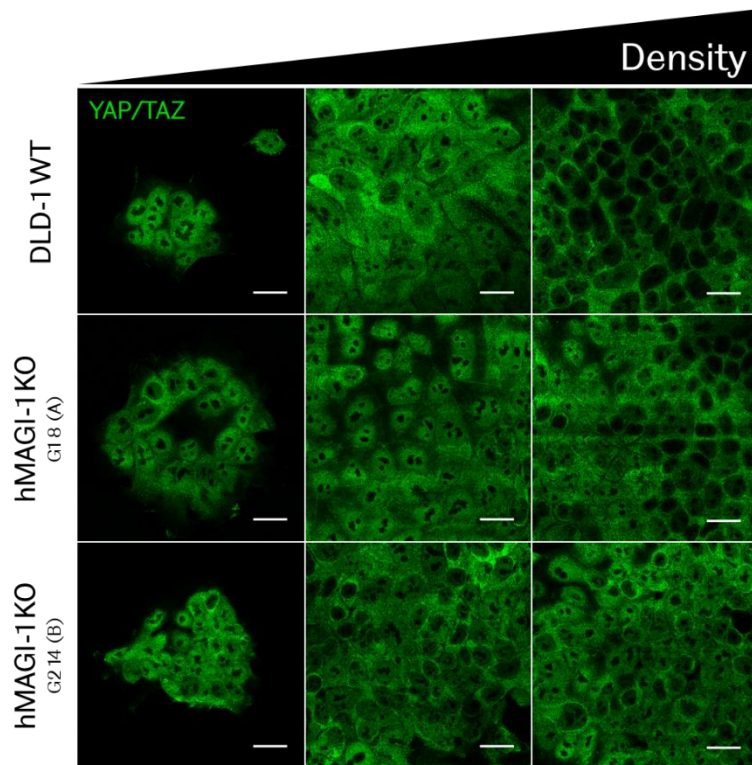


Figure 3.8 | MAGI-1 knockout mildly affects YAP subcellular localisation at high cell density.

MAGI-1 KO clones and DLD-1 WT cells were cultured on coverslips and subjected to anti-YAP/TAZ immunostaining (n=3). Images were acquired with a confocal microscope. Scale bars: 20µm. DLD-1 WT cells display the normal YAP phenotype with a nuclear localisation in sparse cells and a progressive cytoplasmic retention increasing with density. In MAGI-1 KO clones, in dense cultures, YAP is still distributed between nucleus and cytoplasm. This phenotype is milder than in MAGI-1 transiently depleted cells (**Figure 3.2**).

Our results suggest a biologically robust system and a potential compensatory mechanism. In *Drosophila*, there is a single MAGI protein against three in mammals (FlyBase). The other MAGI family members are thereby primary candidates for redundancy or compensation as they share high similarity in protein modular structures and interacting networks (Chapter 4). Interestingly, Hammad et al. observed a compensation effect between MAGI-1 and MAGI-3 for the regulation of Corticotropin-releasing factor receptor1 (CRFR1) endocytosis in HEK293 cells (322). To investigate the potential compensatory mechanism or redundancy between MAGI proteins, we generated double MAGI1/MAGI2 and MAGI1/MAGI3 knockouts.

3.3.4 Depletion of MAGI-1 and MAGI-2 in DLD-1 cells

MAGI-2 has mostly been studied and characterised in kidney and brain. However, a study reported a negative regulation of MAGI-2, also known as S-SCAM, on VPAC₁, a GPCR, in intestinal epithelial cells (323).

3.3.4.1.1 Expression of MAGI-2 in DLD-1 cells

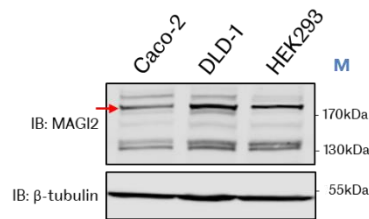


Figure 3.9 | MAGI-2 expression in Caco-2, DLD-1 and HEK293 cell lines.

MAGI-2 expression in Caco-2, DLD-1 and HEK293 cell lines. Cells were lysed and 60µg of total proteins were loaded on an 8% PAGE. The membrane was probed with anti-MAGI-2 antibody and β-tubulin was used as loading control. The band above the 170kDa marker (Red arrow) is present in all three cell lines and matches the size of MAGI-2 (158kDa). M = protein ladder.

MAGI-2 expression in gut cells has been reported by Gee and co-workers who were able to detect and knockdown MAGI-2 in T84 cells (323). These cells are immortalised colon adenocarcinoma cells that had metastasised to the patient's lungs. Our cell line, DLD-1, is also from a colon adenocarcinoma. To verify MAGI-2 expression in DLD-1 cells, proteins were extracted alongside two other cell lines, Caco-2 and HEK293. Samples were subjected to western blotting with an anti-MAGI-2 antibody. MAGI-2 theoretical molecular weight is 158kDa. A prominent band, above the 170kDa marker, was observed in all three cell lines (**Figure 3.9**, red arrow). As a point of comparison, MAGI-1 protein of 161kDa also runs above the 170kDa marker (Example in **Figure 3.7b**). DLD-1 cells appear to have a higher expression of MAGI-2 than HEK293 and Caco-2.

3.3.4.1.2 Generation of stable MAGI-2 and MAGI1/MAGI2 knockout cell lines using CRISPR/Cas9 technique

In Annex 3, we describe the generation of MAGI-2 single and MAGI1/MAGI2 double knockouts bulk populations and isogenic clones in DLD-1 cells.

Unfortunately, MAGI-2 knockout in clones could only be confirmed at the genomic level (Annex 3). In the meantime, a recently submitted thesis work reported correlation between cancer metastasis and reduction of MAGI-2 expression levels in their cohort of patients suffering from colon adenocarcinoma. However, they evidenced the absence of MAGI-2 mRNA expression in three colorectal cancer cell lines, namely HT-115, RKO and HRT-18 (265). Interestingly, the DLD-1 and HRT-18 cell lines were found to have the same genetic origin and to be derived from the same individual (324). According to Dr. Khanzada thesis work, MAGI-2 may not be expressed in DLD-1 cells either (265). To properly answer the question of

expression of MAGI-2 in DLD-1 cells, further experiments would be required such as qPCR. However, due to time restriction, we did not investigate the MAGI-2 track further.

3.3.5 Depletion of both MAGI-1 and MAGI-3 accentuates YAP defect at high cell density

MAGI-3 is the third member of the MAGI family. Its expression is ubiquitous in epithelial cells and has been shown to localise at tight junctions (242). MAGI-3 has been implicated as a potential new regulator of the Hippo-YAP in breast cancer cells (301). Moreover, as investigated in Chapter 4, MAGI-1 and MAGI-3 share many binding partners within the Hippo pathway which further suggest a potential compensatory mechanism or redundancy.

3.3.5.1.1 Expression of MAGI-3 in DLD-1 cells

First, we checked MAGI-3 expression in DLD-1 cells. Total protein was extracted from DLD-1 cells along with Caco-2 and HEK293 cells. Samples were subjected to western blotting with an anti-MAGI-3 antibody. A band was detected in all three cell lines (**Figure 3.10**, Red arrow) which size matched the longest MAGI-3 isoform, MAGI-3a (**Figure 3.12a**). The most prominent band in HEK293 cells was running just above the 130kDa marker (**Figure 3.10**, Orange arrow) and would correspond to the shortest isoform, MAGI-3b. MAGI-3 expression levels were altogether low in Caco-2. However, in DLD-1 cells, a good signal was observed for MAGI-3a which we can speculate is the predominant isoform in this cell line.

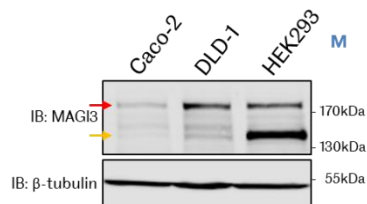


Figure 3.10 | MAGI-3 expression in Caco-2, DLD-1 and HEK293 cell lines.

Cells were lysed and 60µg of total proteins were loaded on an 8% PAGE. The membrane was probed with anti-MAGI-3 antibody and β-tubulin was used as loading control. The band above the 170kDa marker (Red arrow) is present in all three cell lines and matches the size of MAGI-3a (163kDa), the longest isoform. A second band, prominent only in HEK293 cells (Orange arrow) corresponds to the short isoform (~125kDa). M = protein ladder.

Next, we asked whether MAGI-3 protein expression levels were affected upon MAGI-1 knockout. Total protein was extracted from DLD-1 WT and MAGI-1 KO clones, G1 8 (A) and G2 14 (B) and subjected to anti-MAGI-1 and anti-MAGI-3 western blotting (**Figure 3.11**). Surprisingly, MAGI-3 protein levels were not increased as a consequence of MAGI-1 knockout. On the contrary, they appeared slightly decreased in G1 8 (A) clone. However, the other clone

showed no difference. MAGI-3 expression levels have been reported to be down-regulated in colon adenocarcinoma tissues and correlate with cancer progression (289). It is possible that the single cells from which originated G1 8 and G2 14 clones respectively, already displayed different levels of MAGI-3 protein. Our hypothesis therefore shifted towards redundancy rather than compensation between MAGI-1 and MAGI-3, as no up-regulation was observed.

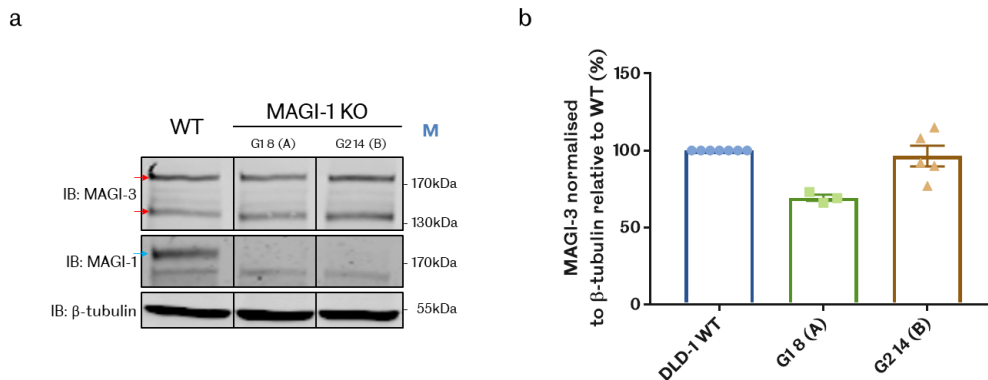


Figure 3.11 | MAGI-3 protein levels are not upregulated upon MAGI-1 knockout.

MAGI-3 expression in MAGI-1 knockout clones. Cells were lysed and samples were subjected to western blotting using anti-MAGI-1 and anti-MAGI-3 antibodies. β -tubulin was used as loading control. **a**, Example of membrane showing MAGI-3 protein levels in MAGI-1 knockout clones. The membrane contained more samples that have been cropped out. The full western blot is shown in **Figure 3.13a**. Red arrows: MAGI-3a and **b**. Turquoise arrow: MAGI-1 band. M = protein ladder. **b**, Quantification of three western blots for G1 8 (A) (n=3) and five for G2 14 (B) (n=5). The whole MAGI-3 signal (as shown in **a**) was taken into account for the quantification. MAGI-3 signal was normalised to its β -tubulin signal and is represented as a percentage of DLD-1 WT. Bars represent mean \pm S.E.M. MAGI-3 is not upregulated in MAGI-1 knockout clones.

3.3.5.1.2 Generation of stable MAGI-3 and MAGI1/MAGI3 knockout cell lines using CRISPR/Cas9 technique

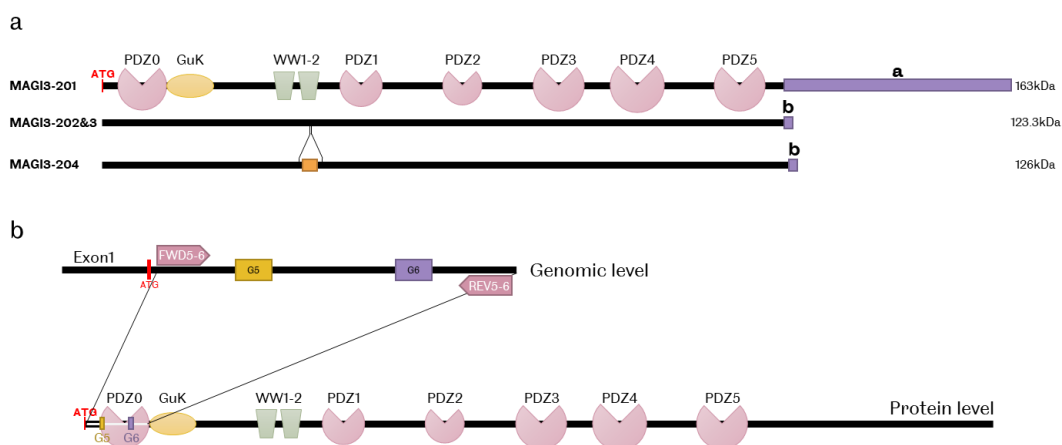


Figure 3.12 | Two sgRNAs targeting Exon1 and all isoforms of MAGI-3.

a. Ensembl lists four MAGI3 transcripts giving rise to three isoforms. The C-terminal is the main alternatively spliced region with a long (a: 372aa) and a short (b: 17aa) versions. Exon8 (75bp) is also alternatively spliced and is present only in MAGI3-204 where it disrupts WW2 domain. **b.** (Top) Schematic representation of the MAGI-3 targeted genomic region with associated sgRNAs, G5 and G6, and primer pair (FWD5-6 and REV5-6). (Bottom) At the protein level, the targeted region corresponds to the beginning of the protein and spans the PDZ0 domain.

In order to be able to study the potential redundancy between MAGI-1 and MAGI-3 in the regulation of the Hippo-YAP pathway, we aimed at generating MAGI-3 single and MAGI1/MAGI3 double knockout cell lines. Similar to MAGI-1, MAGI-3 has a few alternatively spliced regions (**Figure 3.12a**). To target all isoforms and increase the chances of generating a STOP codon as early as possible to completely knockout the protein, we designed two guides in Exon1, namely G5 and G6 (**Figure 3.12b & Table 3.3**). The 5-6 primer pair was designed with the CRISPOR tool to amplify the targeted region (#23 and #24 from **Table 2.7**). Each sgRNA was cloned into a PX459-Cas9-Puro vector (See Chapter 0 for detailed protocol).

Table 3.3 | MAGI-3 sgRNAs targeting Exon1

Table recapitulating the two single guide RNAs selected to induce MAGI-3 knockout along with the primers designed to amplify the targeted region (illustrated in **Figure 3.12b**). **BbsI** site. Oligonucleotide numbers (#) refer to Table 2.9 (sgRNAs) and Table 2.7 (primers) of Chapter 0.

Single guide RNA	Targeted Sequence_PAM	Exonic off-targets
sgRNA5 (G5) (#9 & #10)	GACTTCGGCGCGGAGATCCG_CGG Top: 5' - CACCGGACTTCGGCGCGGAGATCCG - 3' Bottom: 5' - AAACCGGATCTCCGCGCCGAAGTCC - 3' Duplex: 5' - CACCGGACTTCGGCGCGGAGATCCG - 3' 3' - CCTGAAGCCGCGCCTCTAGGCCAAA - 5'	GON4L (NM_032292.5) CCTCGGAGCGCCGCGCCGAGTG LINC00543 (NR_135254.1) lncRNA CCCCGCACCTCCGCGCCGTAGTT RP1-118J21.25 (No protein) GGCCTCGGCGCAGAGATCCTAGG RP11-401P9.7 (No protein) CCTCAGGTCTCCGCACTGAAGTC
sgRNA6 (G6) (#11 & #12)	GTAAACGGGACGCCTGTCAG_CGG Top: 5' - CACCGGTAAACGGGACGCCTGTCAG - 3' Bottom: 5' - AAACCTGACAGGCGTCCCGTTTACC - 3' Duplex: 5' - CACCGGTAAACGGGACGCCTGTCAG - 3' 3' - CCATTTGCCCTGCGGACAGTCCAAA - 5'	PLCL1 (NM_006226.4) CCGCTGCCGGGCGTCCCGCTTTC CPA1 (NM_001868.4) CCTATGAAGGGCGTCCCATTTAC LINC01134 (NR_024455.1) lncRNA CCCCTGAGAGGCTTACCGTTTCC
Sequences of primers to amplify the sgRNAs targeted region		
FWD5-6 (#23)	5' - AGACGCTGAAGAAGAAGAAGCA - 3'	Exon1
REV5-6 (#24)	5' - GTCTTGAGACGGATGGGCTC - 3'	Exon1

First, we aimed at generating bulk populations by Puromycin selection. DLD-1 WT, G1 8 (A) and G2 14 (B) were transfected with both PX459-G5 and PX459-G6 together. By combining the two guides, we hoped to increase the likelihood of inflicting indels that would lead to a premature STOP codon. From now on, MAGI-3 KO bulk population and clones derived from WT cells will be referred to as G5+6 while MAGI1/MAGI3 double KO bulk population and clones, A5+6 or B5+6 when derived from MAGI-1 KO clones G1 8 (A) or G2 14 (B) respectively. After Puromycin selection, the efficiency of the bulk MAGI-3 knockout was assessed by western blotting (**Figure 3.13a**). The intensity of both MAGI-3 bands (Red arrows) substantially decreased in both MAGI1/MAGI3 bulk populations, indicating very efficient bulk MAGI-3 knockouts. However, the G5+6 MAGI-3 bulk population showed a less pronounced reduction of MAGI-3 signal.

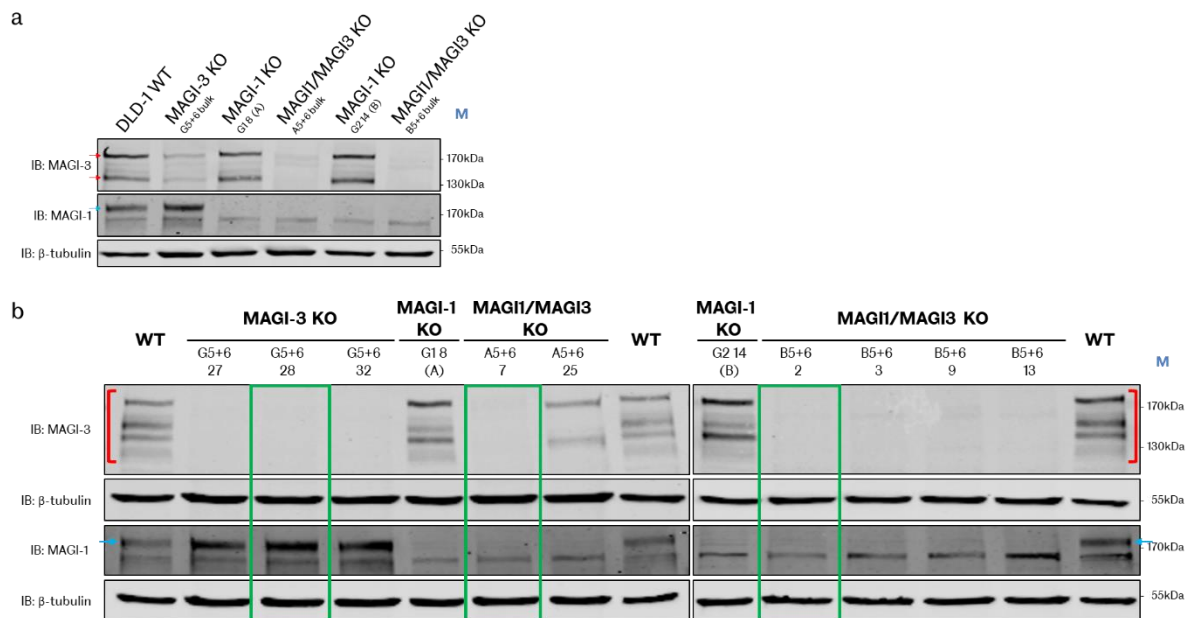


Figure 3.13 | Validation of MAGI-3 single and MAGI1/MAGI3 double knockout at the protein level. Western blot analysis of MAGI-3 single and MAGI1/MAGI3 double knockout bulk populations (**a**) or isogenic clones (**b**). Proteins were extracted from each cell line (as indicated). Samples were subjected to western blotting with anti-MAGI3, anti-MAGI1 and anti- β -tubulin antibodies. M indicates the molecular weights of the protein ladder used. MAGI-1 knockout is confirmed in all clone A or B-derived populations (Blue arrow). Red arrows/brackets: MAGI3 a and b isoforms. **a**, MAGI-3 bulk KO was very efficient in A5+6 and B5+6 bulk populations but less in G5+6 population. **b**, Validation of isogenic clones. The randomly selected clones are indicated by green boxes.

Then, the G5+6, A5+6 and B5+6 bulk populations were sorted into single cells by FACS to obtain isogenic populations. As previously for MAGI-1, clones were screened at the genomic level using sequencing and at the protein level with western blotting (**Figure 3.13b**). Among the validated MAGI-3 single and MAGI1/MAGI3 double knockout clones, one from each

population was randomly chosen: G5+6 28, A5+6 7 and B5+6 2 (**Figure 3.13b**, green boxes). Mutations at the genomic level for the selected clones are recapitulated in **Figure 3.14**.

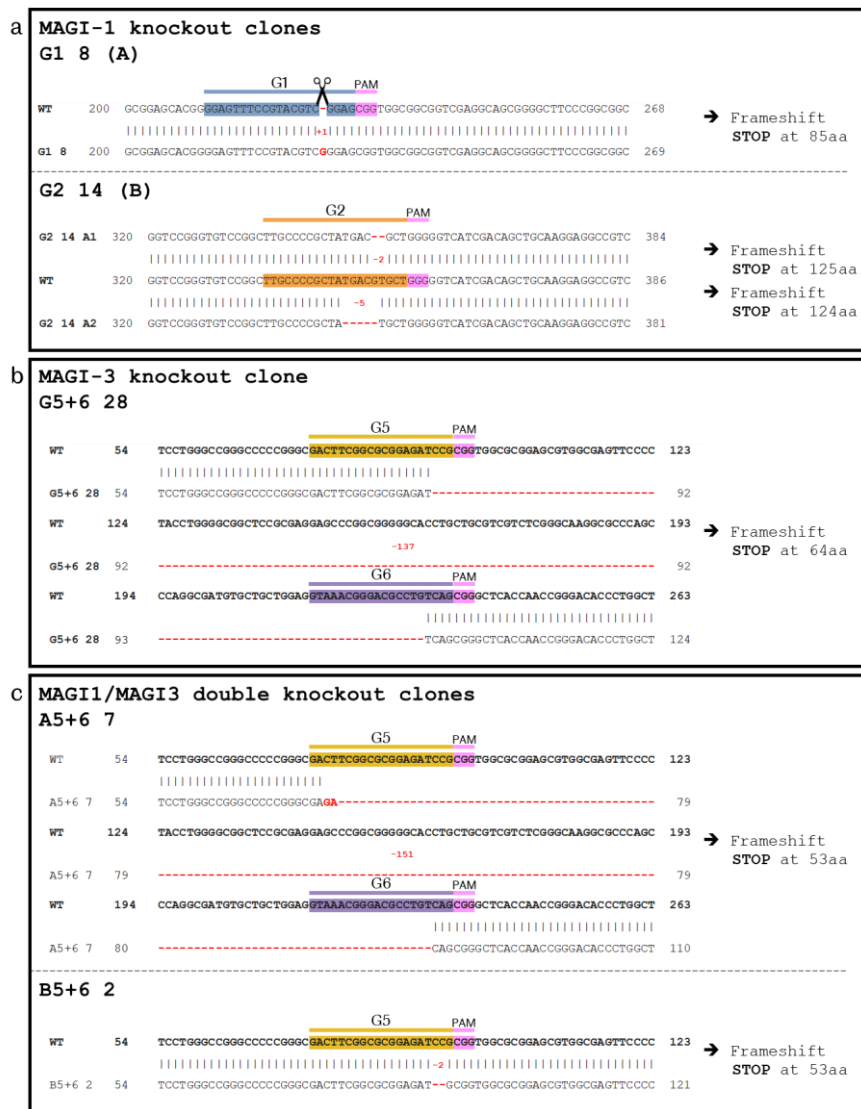


Figure 3.14 | Mutations of MAGI-3 single and MAGI1/MAGI3 double knockout clones.

Sequencing results of MAGI-1, MAGI-3 and MAGI1/MAGI3 knockout clones. **a**, Alignment of G1 8 (A) and G2 14 (B) MAGI-1 KO clones with WT sequence at the targeted region (MAGI-1 Exon1). **b-c**, Alignment of G5+6 28 MAGI-3 (b) and A5+6 7 & B5+6 2 MAGI1/MAGI3 (c) KO clones with WT sequence at the targeted site (MAGI-3 Exon1). In the case of G5+6 28 and A5+6 7, the whole fragment of DNA between G5 and G6 has been deleted. All three isogenic clones have a premature STOP codon terminated the protein sequence after 53 or 64aa. The numbers in red indicate the extent of the mutation in nucleotides.

3.3.5.1.3 MAGI1/MAGI3 double depletion drives YAP in the nucleus at high cell density

Next, we asked whether MAGI1/MAGI3 double knockout presented a stronger YAP defect at high cell density compared to single MAGI-1 knockout. We started by testing the MAGI-3 and MAGI1/MAGI3 bulk populations (**Figure 3.13a**) with the density assay presented

in Section 3.3.2. Cells at medium and high density were subjected to anti-YAP immunostaining (**Figure 3.15**). MAGI-3 KO bulk population displayed a mild defect with YAP being equally distributed between nucleus and cytoplasm in dense cells. On the other hand, both MAGI1/MAGI3 bulk populations displayed a more serious defect in YAP localisation. Indeed, the double knockout appeared to enhance YAP nuclear localisation at high cell density.

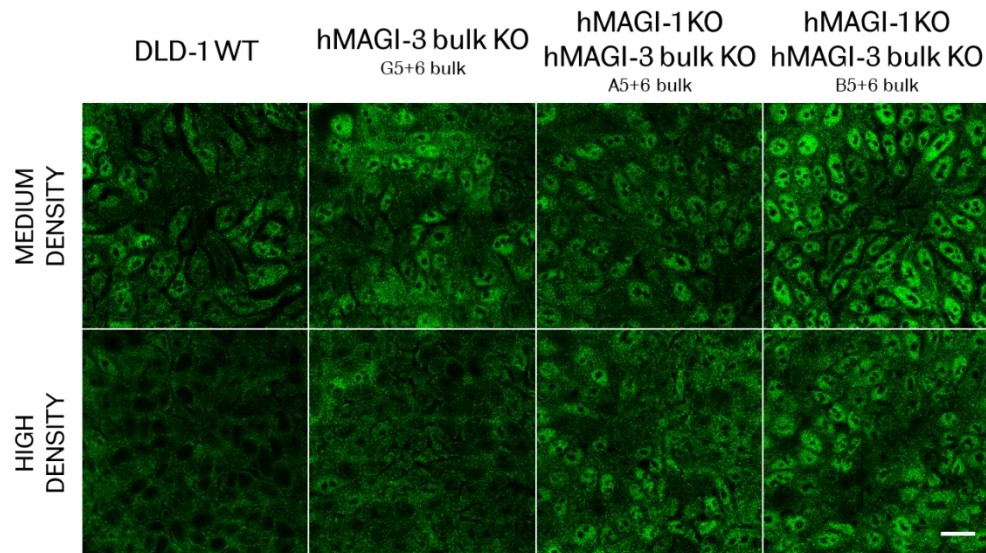


Figure 3.15 | MAGI1/MAGI3 double knockout enhances YAP defect at high cell density.

MAGI-3 and MAGI1/MAGI3 bulk populations (**Figure 3.13a**) and DLD-1 WT cells were cultured on coverslips and subjected to anti-YAP/TAZ immunostaining (n=2). Images were acquired with a confocal microscope. Scale bar: 20µm. In DLD-1 WT cells, YAP is normally distributed between nucleus and cytoplasm at medium density and completely excluded from the cytosol at high density. MAGI-3 KO bulk population still presents equally distributed YAP, much like MAGI-1 KO clones (**Figure 3.8**). MAGI1/MAGI3 double KO bulk population show mainly nuclear YAP at high cell density. All images shown, per density, have a very similar number of cells.

This YAP defect was also confirmed in the isogenic clones (**Figure 3.16**). All CRISPR clones, single and double knockout, presented a YAP defect at high cell density. In the MAGI1/MAGI3 double knockout, the phenotype was slightly accentuated with YAP being equally distributed between nucleus and cytosol much like DLD-1 WT at medium density. B5+6 2 clones also displayed intense nuclear YAP at medium density. Taken together, our data further support the existence of redundancy between MAGI-1 and MAGI-3 in their regulation of YAP subcellular localisation at high cell density. As YAP localisation in clones did not change much between medium and high density, these results further support our hypothesis that MAGIs depletion modifies the density threshold for YAP complete exclusion from the nucleus.

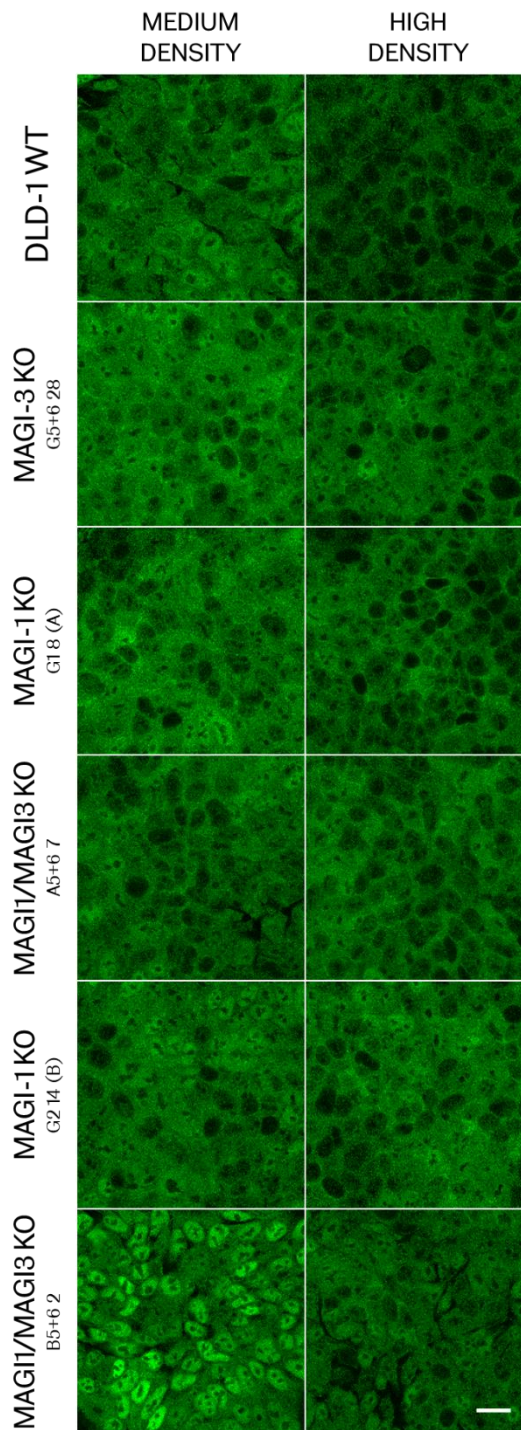


Figure 3.16 | MAGIs single and double knockout appear to push back to threshold for high cell density sensing.

MAGI-1, MAGI-3 and MAGI1/MAGI3 knockout clones (**Figure 3.13a**) as well as DLD-1 WT cells were cultured on coverslips and subjected to anti-YAP/TAZ immunostaining (n=3). Images were acquired with a confocal microscope. Scale bar: 20µm. In DLD-1 WT cells, YAP is normally distributed between nucleus and cytoplasm at medium density and completely excluded from the cytosol at high density. In MAGI knockout clones, YAP is distributed between nucleus and cytoplasm in dense cells, comparable to the medium density phenotype. Clone B5+6 2 shows brighter nuclear YAP at medium density.

3.3.6 MAGI-1/MAGI-3 double depletion reduces LATS1/2-mediated phosphorylation of YAP Ser127 at high cell density

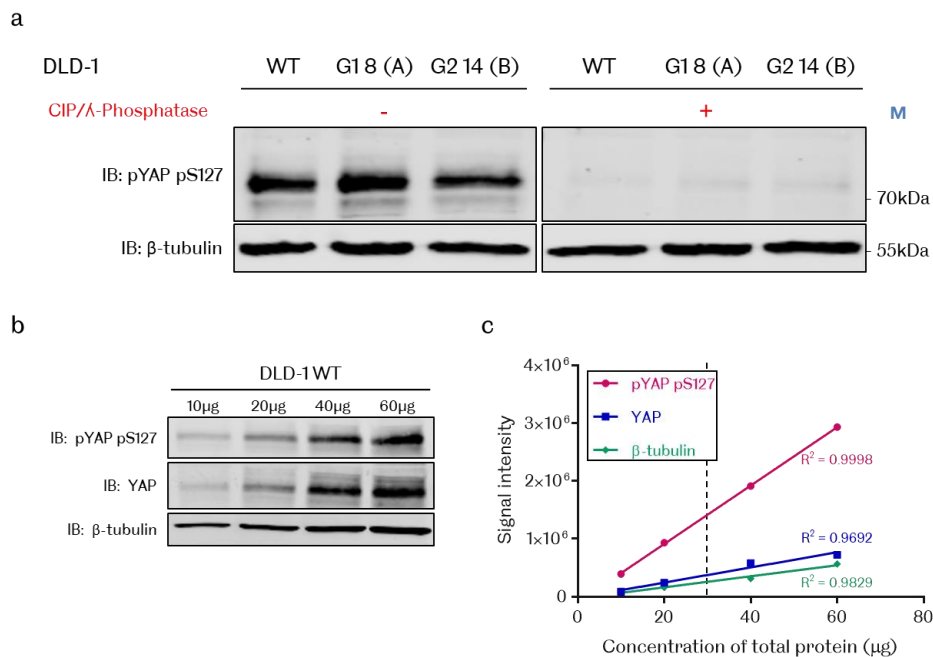


Figure 3.17 | Validation of antibodies.

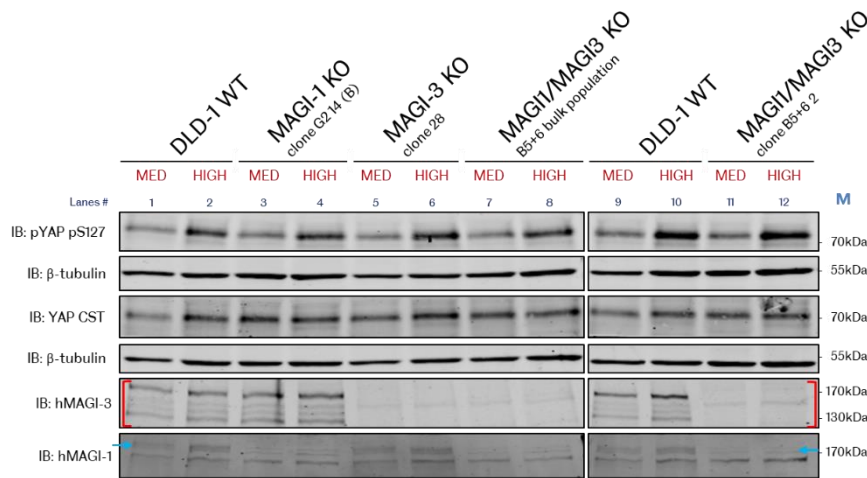
a, pYAP pS127 antibody is phosphospecific. DLD-1 WT and MAGI-1 KO clones, G1 8 (A) & G2 14 (B), lysates were run on an 8% SDS-PAGE in duplicates and transferred onto a nitrocellulose membrane. The right part of the membrane was subjected to phosphatase treatment (CIP and λ -phosphatase) to release phosphate groups from phosphorylated Ser, Thr and Tyr residues. Membranes were probed with the anti-pYAP pS127 antibody. β -tubulin was used as a loading control. The anti-pYAP pS127 antibody signal is lost upon phosphatase treatment, validating its phosphospecificity. **b-c**, Determination of the linear range of antibodies used for quantification of the phosphorylation assay (**Figure 3.18**). Different amounts of DLD-1 WT lysate, ranging from 10 to 60 μ g of total protein, were subjected to western blotting with anti-pYAP pS127, anti-YAP and anti- β -tubulin antibodies (**b**). The signal intensity of each band was plotted against the total protein concentration (**c**). Linear regression was performed for each antibody and the R² values are indicated. All three antibodies were being used in their linear range (R² > 0.95). The dotted line represents 30 μ g of total protein used in the phosphorylation assays (**Figure 3.18**).

YAP contains five HxRxxS consensus sequences for LATS1/2 phosphorylation (31). LATS-mediated phosphorylation of YAP Ser127 residue is believed to regulate its subcellular localisation in response to cell density cues (8,20,22,148). Upon activation of the Hippo cascade by cell-cell contacts, Ser127 is phosphorylated which leads to the subsequent sequestration of YAP in the cytosol by cytoplasmic anchors such as 14-3-3 or PTPN14 (8,20,72,148,325). There are some reports of YAP degradation following phosphorylation by the LATS kinases (63). YAP Ser127 phosphorylation status can therefore be considered a direct read-out of the activation of the Hippo-LATS cascade in response to cell density (20). Mohseni and collaborators reported a decrease of phosphoSer127 upon transient depletion of MAGI-1 (160).

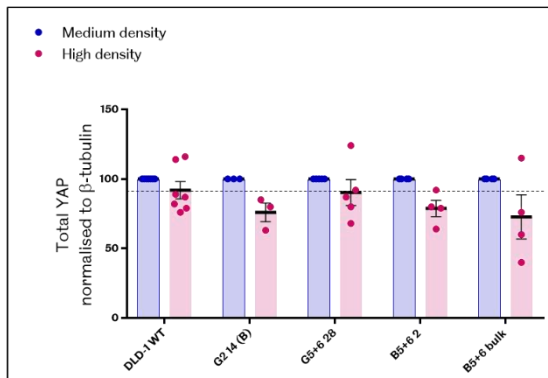
Given that MAGI1/MAGI3 double knockout leads to an accumulation of YAP in the nucleus in dense cultures, we asked whether it resulted from a decreased LATS-mediated phosphorylation of Ser127. DLD-1 WT cells, MAGI-1 KO clone G2 14 (B), MAGI-3 KO clone G5+6 28 and MAGI1/MAGI3 double KO clone B5+6 2 and bulk population B5+6 bulk were cultured at medium and high densities. Cells were lysed and 30µg of total protein per sample were subjected to western blotting with anti-pYAP pS127, phosphospecific for phosphoSer127 residue (**Figure 3.17a**), and anti-YAP antibodies. β-tubulin was used as a loading control for quantification. Antibodies used to detect PhosphoYAP, Total YAP and the housekeeping gene, β-tubulin, were previously shown to be within their respective linear ranges (**Figure 3.17b**). Two identical gels were run and one membrane was probed for pYAP pS127, MAGI-1 and β-tubulin while the other was stained with anti-YAP (Total YAP), anti-MAGI-3 and anti-β-tubulin antibodies. **Figure 3.18a** shows a representative western blot. MAGI-1 and MAGI-3 knockouts were confirmed using their respective antibodies. The data was processed using GraphPad Prism software. PhosphoYAP and Total YAP were each normalised to their respective β-tubulin signals. Total YAP levels were represented as a percentage of each samples' medium density condition (**Figure 3.18b**) or as a percentage of WT for each density considered (**Figure 3.18c**). The ratio of PhosphoYAP over Total YAP was represented as a percentage of each samples' high density condition (**Figure 3.18d**) or as a percentage of WT for each density considered (**Figure 3.18e**). No statistical analysis could be performed due to the wide variability of values collected from one experiment to the other. Indeed, one-way ANOVA and multi-comparison tests such as Tukey's are based on the assumption that the samples have equal variance and normal distributions. A Brown-Forsythe test revealed that the standard deviations between samples were significantly different ($P < 0.05$) indicating that the "equal variance" assumption was violated. The following interpretation is therefore based on the global trend of mean values. Total YAP levels did not show much variation in DLD-1 WT cells between medium and high density indicating close to no degradation in this cell line. CRISPR clones globally showed slightly lower total YAP levels at high density than both their respective medium density (**Figure 3.18a**) and WT (**Figure 3.18b**). The ratio of phosphorylated YAP over total YAP slightly increased with cell density in WT (**Figure 3.18d**), as expected. Surprisingly, we found a higher increase of the proportion of phosphorylated YAP in CRISPR clones (**Figure 3.18d**). When comparing with WT, we observed an overall lower YAP phosphorylation in CRISPR clones at medium density; yet high density levels were similar to WT (**Figure 3.18e**). This is intriguing as our immunofluorescence data showed an increased pool of nuclear YAP at high density in MAGI knockout clones (**Figure 3.15** and **Figure 3.16**). Our data therefore

showed that phosphoSer127 is not the only mechanism regulating YAP nucleocytoplasmic shuttling at high density.

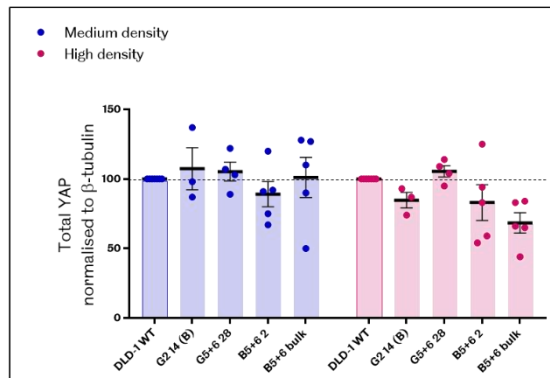
a



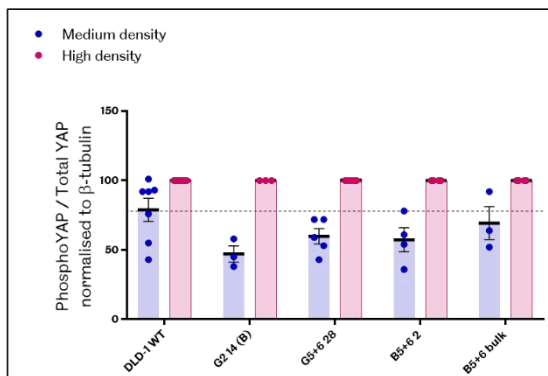
b



c



d



e

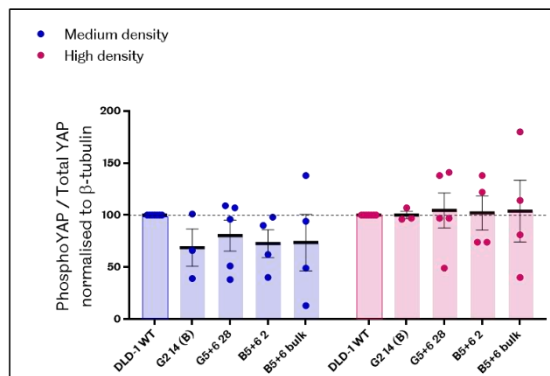


Figure 3.18 | MAGIs knockout reduces YAP Ser127 phosphorylation at medium density.

a. Example of western blot (30 μ g of total protein) showing YAP Ser127 phosphorylation status in MAGI KO clones at medium (MED) and high (HIGH) density. Red brackets: MAGI-3. Turquoise arrow: MAGI-1 band. M = protein ladder. **b-e.** Quantification from western blots. Total YAP and PhosphoYAP signals were normalised to their respective β -tubulin signals. Each data point is represented ($n \geq 3$). Mean \pm S.E.M. The dotted lines indicate the WT mean values. **b.** For each sample, total YAP levels are represented as a percentage of medium density (lined bars). In WT cells, total YAP levels at medium and high density are similar. In MAGI1 (G2 14) and MAGI1/MAGI3 (B5+6 2 and bulk) KO populations, YAP levels at high density appear slightly lower than at medium density. **c.** For each density,

total YAP levels are represented as a percentage of DLD-1 WT (lined bars). At medium density, total YAP levels are very similar in WT and MAGI KO clones. At high density, levels in MAGI-1 KO clone and MAGI1/MAGI3 double knockout appear slightly reduced compared to WT. **d**, For each sample, PhosphoYAP/Total YAP is represented as a percentage of high density (lined bars). In MAGI KO clones, the increase in phosphorylation between medium and high density is more substantial than in WT. **e**, For each density, PhosphoYAP/Total YAP is represented as a percentage of DLD-1 WT. At medium density, YAP pS127 phosphorylation appears reduced compared to DLD-1 WT while at high density, the levels are comparable in clones and WT.

Taken together, our results indicate a complex mechanism of regulation from the MAGI proteins on YAP. First, MAGIs appear to exert a role on LATS-mediated phosphorylation of YAP Ser127 residue. The lower phosphorylated YAP levels at medium density in MAGIs knockout correlates with our previous hypothesis of a higher threshold for cell density. Second, as pYAP pS127 is reported to be able to enter the nucleus (186), our data point toward a role of MAGIs in regulating phosphorylated YAP cytoplasmic retention.

3.3.7 MAGI knockout DLD-1 cells form 3D leak-tight tubules in OrganoPlate[®]

Epithelial tissues are characterised by their ability to form a selective barrier between their apical and basal sides. Cells are sealed to one another by tight junctions that restrict the paracellular passage of molecules. Therefore, substances that go through the epithelial layer have to enter the cells, by diffusion or active transport, which grants high selectivity to these tissues. However, this essential feature of epithelial tissues is often disrupted in diseases, such as in Crohn's disease for intestinal tissues (326) or more generally, cancer which gives way to metastasis. Assessing the leak-tightness of an epithelium is therefore an essential step of its characterisation as it represents the critical integrity of tight-junctions.

MAGIs, as tight junction and multi-PDZ domain scaffolding proteins, play a crucial role in ensuring epithelial integrity (252). Knocking out either or both MAGI-1 and MAGI-3 proteins could have an impact on other tight junction proteins, on polarisation or on the actin cytoskeleton integrity. All three are known regulators of the Hippo-YAP pathway (See Section 1.2.2). This prompted us to ask whether the YAP defect observed in MAGI knockouts was an indirect effect from disturbing cell polarisation or junctions. To assess these paramount epithelial properties, we cultured our cell lines in 3D in OrganoPlates[®] (MIMETAS, The organ-on-a-chip company, NL).

3.3.7.1 DLD-1 cells form tubules within four days of culture in the OrganoPlate®

Based on our parental cell line, DLD-1, we used a 3-lane OrganoPlate® design, to best mimic colon. This design, as indicated by its name, possesses three microfluidic channels that meet in the centre (**Figure 3.19a**). For a gut-on-a-chip model, the middle channel was filled with Collagen-I, cells were then cultured in the top channel, against the ECM, and the bottom channel was only used, in our case, for medium perfusion (314). The different steps of seeding are schematically represented in **Figure 3.19b-h**. The tubule formation was monitored by phase contrast images from Day0 (seeding) to Day7 of culture (**Figure 3.19i**). The images mirror the schematics. A DLD-1 WT tubule, growing under bilateral flow, was complete on Day4.

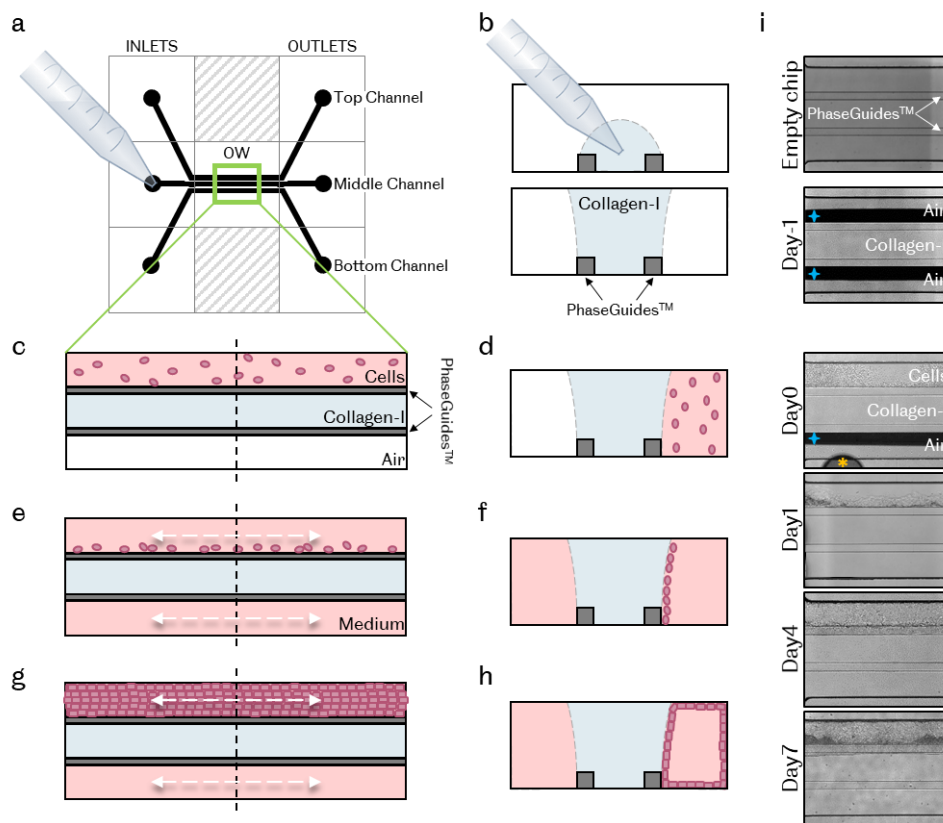


Figure 3.19 | Formation of tubules in 3-lane OrganoPlate®.

a. The OrganoPlate® is based on a 384-well plate. Each chip of the 3-lane design spans over 9 wells. Each 384-well plate contains 40 chips. In this model, cells are cultured in the top channel against an extracellular matrix, Collagen-I here, which is in the middle channel. The bottom channel was only used for medium perfusion in this study. All three channels meet in the centre of the chip and are delineated by Phaseguides™ at the interface. The left and right wells are denominated INLETS and OUTLETS respectively. The middle well is the observation window (OW) and allows to visualise the three lanes through the glass bottom of the plate. **b.** First the ECM is dispensed in the middle channel and left to polymerise and form, thanks to the PhaseGuide™ technology, a seamless barrier. Then the cells are seeded in the top channel (**c & d**), and the plate is angled so as to force cells against the ECM. After a few hours the plate is incubated on a rocking platform, subjecting cells to bilateral flow (white dotted arrows) (**e &**

f). Finally, cells proliferate until forming a leak-tight tubule (**g & h**). **c, e, g**, Top views from the observation window (green square). **d, f, h**, Cross sections along the dotted lines of the steps described in **c, e & g** respectively. Inspired from Figure 1 of (314) and Supplementary figure 2 of (327). **i**, Phase contrast images, acquired with a MolDev confocal microscope through the OW, of DLD-1 WT cells in a 3-lane OrganoPlate® over several days. Day0 corresponds to the day of seeding (picture taken directly after cells were dispensed, the bottom channel was not filled with medium yet). On Day4, the tubule is complete. *: Air bubble in the Observation Window. †: Air/Collagen-I curved interface created over the PhaseGuides™. This interface become invisible once the top and bottom channels are filled with liquid (medium).

We, then, cultured DLD-1 WT cells as well as MAGI-1, MAGI-3 and MAGI1/MAGI3 knockout clones in a 3-lane OrganoPlate®. An EdU assay (Described in Annex 4) revealed that all cell lines considered had very similar numbers of cells per tubules on Day4 of culture and suggested no effect of MAGI knockouts on cell proliferation.

3.3.7.2 *DLD-1 cells form leak-tight tubules and single MAGI knockout does not impair barrier function*

MAGI-1 and MAGI-3 are both tight junction proteins and MAGI-1 has been shown to be involved in their maintenance (242,250). As TJs are used to sense density and we showed a defect in YAP's response to cell density in 2D cultures upon MAGI proteins knockout (**Figure 3.16**), we asked whether tight junction's integrity was affected.

To assess the tight junction integrity in 3D tubules, we performed a barrier integrity assay (BI) developed and optimised by MIMETAS. This assay consists in dispensing fluorescent molecules in the cell channel (top channel), namely FITC-Dextran 150kDa and TRITC-Dextran 4.4kDa, and monitoring their diffusion through the cell layer into the gel and bottom channels overtime (usually 15min) (See full protocol in Chapter 0 Section 2.2.8.3). The fluorescence in the middle (ECM) channel was compared and normalised to that of the top channel (Cells), using a MIMETAS plugin in Fiji, and plotting the fluorescence ratio overtime. A ratio close to 0 corresponds to a leak-tight tubule while a final ratio of 1 indicates complete diffusion of the fluorescent molecule to the gel channel (**Figure 2.12**). The barrier function of the epithelium is considered lost when the fluorescence ratio exceeds 0.4 (314).

Based on previous experiments (314), we decided to perform our barrier integrity assays on Day4. Each cell line was seeded in a 3-lane OrganoPlate® in at least duplicates or triplicates, with one chip per plate being left without cells to serve as a cell-free control. Four days after seeding, a BI assay was performed using FITC-Dextran 150kDa and TRITC-Dextran 4.4kDa fluorescent compounds. Due to the many cell lines considered, only the 15min (after adding

the fluorescent compounds) time point was represented (**Figure 3.20**). The DLD-1 WT tubule and the cell-free chip represent the two extreme outcomes of this assay: leak-tight with a fluorescence ratio close to 0 and completely leaky with a ratio close to 1. Representative images of the mean fluorescence ratio for each population are shown in **Figure 3.20c & d**. MAGI-1 and MAGI-3 single knockout clones were as consistently leak-tight to both fluorescent compounds as DLD-1 WT cells (**Figure 3.20**). However, the MAGI1/MAGI3 double knockout clones displayed opposite behaviours. A5+6 7 was leak-tight while B5+6 2 presented an elevated fluorescence ratio (above 0.4), indicative of leaky tubules. We later found that this clone (B5+6 2) presented a defect in Occludin staining that could explain the loss of barrier function (Annex 4, **Figure A. 12**). Taken together, our results show that neither MAGI-1 nor MAGI-3 single knockout affected the barrier integrity of the tubules. At this point, we cannot conclude on the effect of MAGI1/MAGI3 double knockout on barrier function as the two clones show two extreme and opposite scenarios.

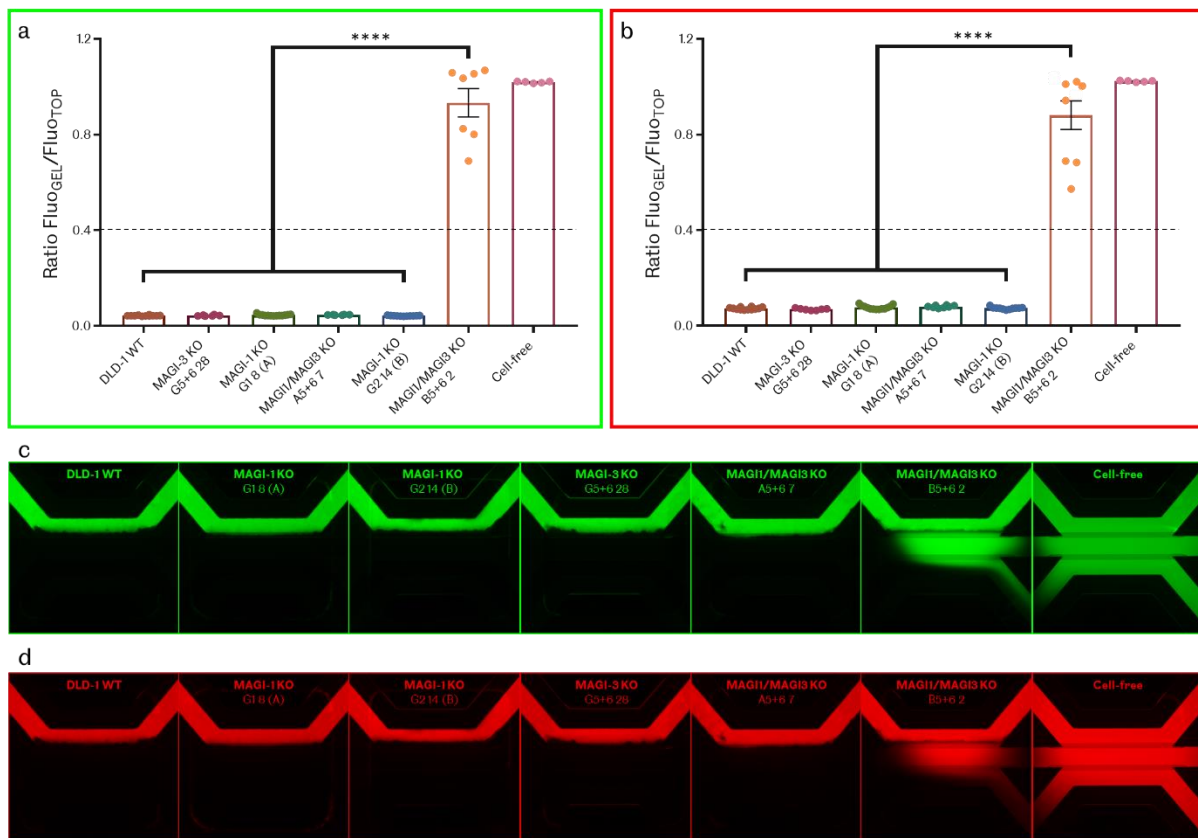


Figure 3.20 | MAGI1 and MAGI3 single knockouts do not affect barrier integrity of the tubules.

DLD-1 derived cell lines were cultured in 3-lane OrganoPlates® for 4 days before being subjected to a barrier integrity assay. Two fluorescent compounds, namely FITC-Dextran 150kDa and TRITC-Dextran 4.4kDa were dispensed into the top channel of the chips, containing the tubule. One chip per plate was left without cells to constitute a cell-free (leaky) control. Measurements were taken 15min after perfusion with the fluorescent probes. The assay was conducted on 5 plates with n numbers ranging from 7 to 13 per cell line (WT n=12, G1 8 n=13, G2 14 n=11, G5+6 28 n=7, A5+6 7 n=8, B5+6 2 n=9, cell-free control n=5). Data processing was carried out using a Fiji plugin

from MIMETAS. It consisted in normalising the fluorescent signal from the middle (Gel) channel to that of the top (Cells) channel, as described in **Figure 2.12. a & b**, Left and right quadrants represent FITC and TRITC fluorescence ratios following the barrier integrity assay. Each graph contains individual data points as well as the mean value (height of the bars) \pm S.E.M. A Brown-Forsythe one-way ANOVA was performed (a: $F(6,6.018)=379.062$, $p<0.0001$ and b: $F(6,8.085)=290.310$, $p<0.0001$) followed by the multiple comparisons Games Howell's test. ****: significant (p values < 0.0001). The dotted lines represent the threshold (ratio of 0.4) for loss of barrier function. MAGI-1 and MAGI-3 individual knockouts do not affect barrier integrity. MAGI1/MAGI3 double knockout could be dramatically impairing the barrier function but the two clones display opposite behaviour. **c & d**, Fluorescent images of FITC and TRITC respectively corresponding to the mean fluorescence ratio of each population (both channels represent the same chip).

In Annex 4, we present a gross characterisation of the CRISPR cell lines by immunostaining with epithelial markers such as ZO-1, E-cadherin and Occludin. At first glance, no defect was observed in F-actin cytoskeleton, ZO-1 or E-cadherin localisation. Only B5+6 2, MAGI1/MAGI3 double knockout clone, displayed no Occludin staining at cell-cell contacts, coherent with the loss of epithelial barrier function (**Figure 3.20**).

3.3.7.3 MAGI knockouts do not affect YAP nuclear exclusion in 3D tubules

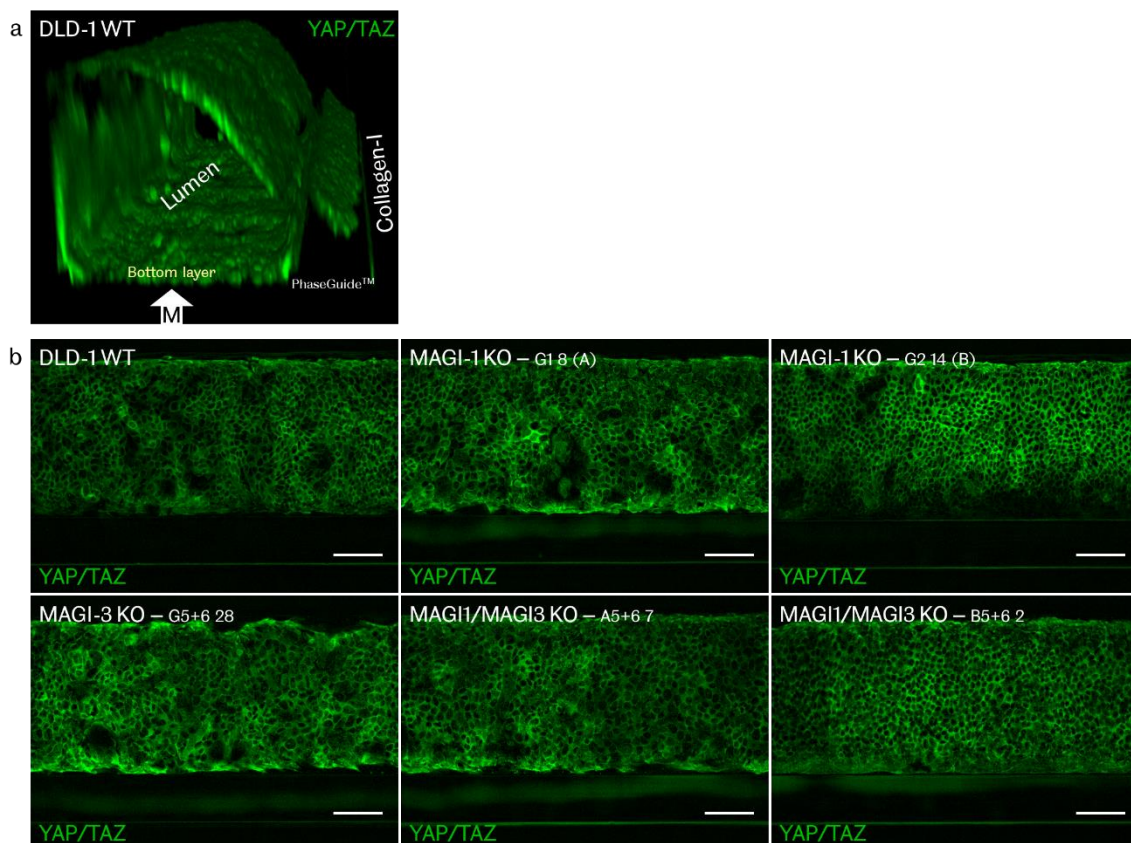


Figure 3.21 | YAP cytoplasmic localisation in DLD-1 tubules cultured under flow in OrganoPlate®.

Day4 DLD-1 tubules were stained with an anti-YAP/TAZ (Green) antibody (n=1). Scale bars: 50µm. Z-stacks were acquired using a confocal microscope, with a 20x objective. **a**, 3D reconstruction of the full Z-stack for DLD-1 WT cells. The “M” indicates the microscope objective imaging the tubules from below. **b**, A single slice is shown: apical view of the bottom cell layer of the tubules. YAP staining is cytoplasmic in all cell lines.

We have found in 2D cultures that MAGI knockouts impaired the nuclear exclusion of YAP at high cell density. We asked whether this defect was occurring in 3D, fully-formed tubules. DLD-1 cells along with MAGI single and double knockout clones were cultured in a 3-lane OrganoPlate[®] under bilateral flow. Immunostaining was performed with an anti-YAP/TAZ antibody on Day4 of culture. Z-stacks were taken using a confocal microscope with a 20x objective. Images were acquired and processed identically. A single slice corresponding to the bottom layer of cells (**Figure 2.14**) for each population is shown in **Figure 3.21b**. YAP was clearly cytoplasmic in DLD-1 WT and MAGI knockouts alike. We previously showed that on Day4 of culture, all tubules had similar number of cells (Annex 4) that we can extrapolate as having similar densities. The difference of YAP localisation in clones between 2D (**Figure 3.16**) and 3D culture (**Figure 3.16b**) could arise from the fluid flow in OrganoPlate[®].

3.4 Discussion

3.4.1 Redundancy among the MAGI family of proteins

In this study, we have further established MAGI-1 and MAGI-3 as regulators of YAP subcellular localisation. MAGI-1 was reported to perturb YAP localisation at high cell density when knocked-down (160). Our data corroborated the study and showed that MAGI-1 transient knockdown was promoting YAP nuclear localisation at high cell density in HEK293, Caco-2 and DLD-1 cells. To better characterise the mechanism of MAGI-1 negative regulation of YAP, we used the CRISPR/Cas9 gene editing technique to generate MAGI-1 stable knockout cell lines. However, our experiments with MAGI-1 KO clones (**Figure 3.8**) only showed a mild defect at high cell density with YAP being distributed between nucleus and cytoplasm, usually indicative of medium density. The difference between transient knockdown and stable knockout results suggested a biologically robust system and a potential compensatory mechanism. *Drosophila* possess a sole MAGI protein in against three in mammals (FlyBase). The other MAGI family members were therefore primary candidates as they share very high similarity in overall domain structures and thereby in their protein interaction networks (Investigated in Chapter 4). Interestingly, Hammad et al. observed a compensation effect between MAGI-1 and MAGI-3 for the regulation of Corticotropin-releasing factor receptor1 (CRFR1) endocytosis in HEK293 cells (322). We therefore generated MAGI-3 and MAGI1/MAGI3

knockouts. Lack of both MAGI-1 and MAGI-3 proteins appeared to enhance the phenotypes observed (discussed below) further supporting partial redundancy and overlap of functions among the MAGI family with respect to the Hippo-YAP pathway.

3.4.2 Lack of both MAGI-1 and MAGI-3 impairs Hippo-YAP response to cell density cue in 2D cultures

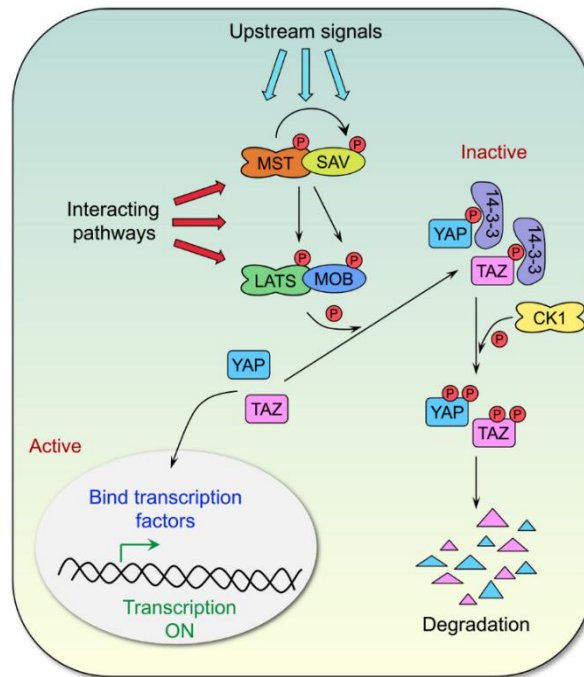


Figure 3.22 | Canonical view of the core mammalian Hippo pathway.

Figure 1 from (45,328). In response to cell density, the core Hippo cascade activates to inhibit YAP transcriptional activity and sequester it in the cytosol. At low cell density, YAP is accumulated in the nucleus where it interacts with transcription factors such as TEADs (35,329) to promote cell proliferation, survival and differentiation. As density increases, the core Hippo kinase cascade is activated: MST1/2 kinases, with the help of the Sav1 adaptor protein, activates LATS1/2 via phosphorylation (23). Then, the LATS1/2 kinases recruit MOB1 to assist in the phosphorylation of YAP (8,20,211) on Ser127. Phosphorylated YAP is then sequestered in the cytoplasm by 14-3-3 protein binding or subsequently degraded (8,63,64,211). TJs: Tight junctions. AJs: Adherens junctions.

The canonical view of the mammalian Hippo pathway refers to the conserved kinase cascade of phosphorylation concluding with YAP cytoplasmic sequestration (**Figure 3.22**): 1) Upon activation by upstream signals such as cell density, the MST1/2 kinases, together with the adaptor Sav1, phosphorylate and activate the LATS1/2 kinases (23) which in turn 2) recruit the adaptor protein MOB1 to assist phosphorylation of YAP (8,20,211) on its Ser127 residue; 3) Phosphorylation of Ser127 triggers YAP nuclear exclusion and cytoplasmic retention by the 14-3-3 protein or protein degradation (8,63,64,211). In recent years, this classic model has been

expanded, adding more and more players to the Hippo pathway. Here, we focused our study on YAP's response to cell density.

We found that, MAGI-1 and MAGI-3 proteins, played a role in the regulation of YAP subcellular localisation in response to cell density. Our data showed that double knockout of MAGI1 and MAGI3 resulted in a defect in nuclear exclusion at high cell density. Indeed, knockout clones displayed a YAP localisation corresponding to a medium density in WT cells: evenly distributed between nucleus and cytoplasm. We therefore suggest that MAGI knockouts result in a modified threshold for sensing cell density. During contact inhibition of proliferation, LATS-mediated phosphorylation of the YAP Ser127 residue is believed to be an important step leading to its nuclear exclusion and cytoplasmic retention by the 14-3-3 protein (8). We therefore examined the status of this Serine residue in our MAGI knockouts. We observed lower levels of YAP Ser127 phosphorylation in MAGI knockout clones at medium density, consistent with a modified threshold of density sensing. Surprisingly, we found that Ser127 phosphorylation levels were similar to that in DLD-1 WT cells at high cell density in contrast with Mohseni and collaborators (160). These results indicate that YAP pSer127 is located in the nucleus in our MAGI knockout cells. This phenomenon has been reported by Wada and co-workers who showed that although YAP Ser127 phosphorylation is required for cytoplasmic exclusion, it is not by itself sufficient (186). Our results do not fully shed light on the entire mechanism at play since no enhancement of the PhosphoYAP defect was observed in double compared to single MAGI knockouts. Taken together, our data suggest that regulation of YAP by the MAGI proteins is two-fold: 1) early phase cell density sensing and activation of the Hippo pathway through LATS kinases and 2) involvement in YAP cytoplasmic retention at high cell density (Further discussed in Chapter 5).

Sensing of cell density encompasses two components: 1) cell-cell contacts and 2) the reduction of the surface area available for each cell. The latter has been shown to be Hippo-independent. Indeed, several studies reported that single cells cultured on islands with decreasing available adhesive areas displayed cytoplasmic YAP past a given threshold (180,188). Their results pointed at a role of the actin cytoskeleton in regulating YAP nuclear exclusion under such circumstances. It would be interesting to examine the behaviour of MAGI knockout clones' single cells on micropatterns. We have established a system (described in Annex 5) that will be used to further study the effect of MAGI-1 knockout on YAP cytoplasmic retention on small adhesive areas.

3.4.3 YAP localisation in 3D tubules under bilateral fluid flow

Next, we completed our study by a gross characterisation of the MAGI knockout clones in 3D cultures which recapitulate more closely physiological conditions. The OrganoPlate® constitute a microfluidic platform that enables 3D cell culture subjected to bilateral medium perfusion. We successfully grew gut tubules against Collagen-I in a 3-lane OrganoPlate® from the 6 cell lines considered: DLD-1 WT, MAGI-1 knockouts (G1 8 & G2 14), MAGI-3 knockout (G5+6 28) and MAGI1/MAGI3 double knockouts (A5+6 7 & B5+6 2).

We looked at YAP subcellular localisation in the 3D gut tubules. Our results showed cytoplasmic YAP in all DLD-1 tubules grown in a 3-lane OrganoPlate® under fluid flow conditions, regardless of MAGI knockouts (**Figure 3.21**). Data from an EdU assay showed that on Day4 of culture, tubules from all cell lines considered had similar cell numbers and thereby comparable density. However, in 2D cultures, we found that MAGI knockouts impaired YAP nuclear exclusion at high cell density (**Figure 3.16**) in contrast with our 3D data. Tubules were subjected to fluid flow that is known to exert two types of forces: 1) shear stress and 2) mechanical strains on the tube walls (330). YAP localisation has been reported to be affected by shear stress in endothelial cells (200-202,331,332). Upon initiation of the flow, YAP is transiently translocated to the nucleus *in vitro* (~24hrs) but becomes cytoplasmic again under sustained flow conditions. This response to shear stress is believed to be Hippo-independent and rather stem from cytoskeleton reorganisation (202). In our experimental set-up, on Day4 of culture, cells were under sustained bilateral flow which could explain YAP nuclear exclusion in MAGI knockout clones.

As MAGI-1 knockdown was reported by Zaric and co-workers to induce a defect in actin stress fibres (252), we grossly observed F-actin staining in DLD-1 cells in 3D culture in the OrganoPlate®. At first glance, no obvious defect in stress fibres nor in the actin circumferential belt was observed in MAGI knockouts (Annex 4), though a more thorough analysis would be required.

Taken together, YAP localisation in 3D tubules cultured in the OrganoPlate® and subjected to bilateral flow might be governed solely by the actin cytoskeleton and not need MAGI proteins to trigger cytoplasmic retention. This constitutes preliminary results and further investigation is required to conclude. Unfortunately, due to limited time, this was not investigated further.

3.4.4 Single MAGI knockout does not affect epithelial barrier integrity in the tubules

MAGI proteins are known to play a role in tight junctions' maintenance. TJs are a paramount component in the assembly of epithelial tissues with signalling and barrier functions (333). We therefore asked if the epithelial barrier function was compromised in the MAGI knockout cell lines. We used a barrier integrity assay using fluorescent compounds to assess the paracellular diffusion through the gut tubules cultured in OrganoPlate[®]. We found, that DLD-1 WT tubules were leak-tight to high and low molecular weight fluorescent Dextran on Day4 (**Figure 3.20**), in line with reports for the Caco-2 cell line (314). DLD-1 WT cells and MAGI1/3 single and double knockout clones displayed similar cell numbers at Day4 of culture (Annex 4 and **Figure A. 10**). Our data showed that MAGI-1 and MAGI-3 single knockouts were leak-tight to the two fluorescent dyes after 15min, indicating that the barrier integrity was unaffected in this timeframe. Unfortunately, no conclusion can be given so as to the effect of MAGI1/MAGI3 double knockout on barrier integrity. Indeed, the two isogenic clones tested displayed opposite behaviours: A5+6 7 was as consistently leak-tight as WT while B5+6 2 was consistently leaky. We later found that B5+6 2 clone had a defect in Occludin (Annex 4 and **Figure A. 12**) which could explain the loss of barrier integrity. Interestingly, Occludin was found to be recruited to JAM-4 junctions in a MAGI-1 dependent manner in L cells (mouse fibroblast) (235). Moreover, based on our gross characterisation in the OrganoPlate[®], other epithelial markers such as ZO-1, E-cadherin and F-actin did not appear to be affected by MAGI knockouts (Annex 4 and **Figure A. 14**).

Interestingly, Dr. Khanzada thesis work reports a small but statistically significant decrease of trans-epithelial electrical resistance (TEER) in HT-115 and RKO MAGI-1 knockdown cells compared to WT (265). TEER measurements give a quantitative indication of cells barrier integrity while the barrier integrity assay used in this thesis provides a qualitative insight. As intestinal epithelial cells, such as Caco-2 and DLD-1 cells, possess a high TEER value to begin with, MAGI-1 depletion may indeed decrease the barrier integrity but not enough to be detected by a qualitative assay, or in such a short timeframe.

Interestingly, lower MAGI-1 and MAGI-3 expression levels have been reported in patients suffering from Microscopic colitis (266) and inflammatory bowel disease (267) respectively. Both diseases are associated with increased epithelial paracellular permeability. It would therefore be interesting to assess whether MAGI knockout tubules respond differently to cytokines stimulation. Patients with inflammatory bowel diseases (IBDs) are more likely to develop colorectal cancer (334-336). As both MAGI-1 and MAGI-3 proteins have reportedly

lower expression levels in both IBDs and colorectal cancers (252,266,267,289), they could provide a molecular link between the two conditions.

4 Chapter 4: MAGI-1 and MAGI-3 form a complex with essential players of the Hippo cascade at tight junctions

4.1 Introduction

Proteins are the essential players that drive most of cell processes but they rarely work alone. Indeed, they tend to assemble into macromolecular complexes to perform intricate tasks. In most cases, those proteins are part of signalling pathways that cooperate to transmit a signal through the cell and modulate a given function, such as division or death, in response to environmental cues. This process is called signal transduction and consists in a series of intracellular events such as interactions and post-translational modifications to activate or inhibit the next protein. Cells respond by altering their activity or changing their gene expression. Through evolution, signalling cascades, such as the Hippo pathway, have become more complex by acquiring more layers of regulation (337-339). It is, indeed, paramount that signalling pathways, controlling essential functions, be tightly regulated, otherwise, it can lead to the development of diseases such as cancer.

Tandem WW domains are particularly recurrent interaction modules within the Hippo pathway. WW domains are named after two highly conserved and characteristic tryptophan residues. These modules intervene in the upstream as well as downstream regulation of the pathway (340,341). Although WW domains are very short (~38 amino acids), and the human proteome only counts about two hundred of them, they present a versatile platform to a vast repertoire of more than 1,890 putative interactors containing proline-rich motifs (56). WW domains from closely related proteins can have different specificities for protein ligands and thereby hold the role of linking individual proteins to a physiologically relevant function (55,342). WW domains are sorted in different classes depending on their ligand preference (52,53). MAGI-1 possesses two of such domains that belong to Class I associating with [L/P]PxY motifs, same as YAP (54,55).

When investigating the role of a protein, it is useful to identify its interacting network. In our case, to further establish MAGI-1 as a negative regulator of YAP, we investigated MAGI-1's molecular interactions with players of the Hippo pathway. Indeed, a large scale proteomic screen identified MAGI-1 among the proteins being in close proximity of the LATS1/2 kinases within cells (221,343). This could indicate a potential interaction and requires validation by co-

immunoprecipitation experiments. Similarly, two separate proteomics studies identified MAGI-1 in PTPN14 interactome (344,345). This interaction also requires validation by co-immunoprecipitation.

Co-immunoprecipitation experiments consist in immobilising a protein of interest, most of the time overexpressed and fused to a tag, on agarose beads functionalised to bind to the tag, and isolate its cohort of binding partners. When the cell lysate is incubated with beads, the protein of interest attaches to the resin along with its interactors. The choice of buffer here is crucial to maintain and preserve 3D conformation of proteins and their interaction complexes. The beads are then washed several times with a milder buffer, usually containing less detergent, to get rid of all non-specific interactions. The protein of interest and its binding partners are then eluted from the beads and denatured to allow separation on a SDS-PAGE, followed by western blotting detection.

4.2 Aims

The aim of this chapter was to further establish MAGI-1 within the Hippo signalling pathway and shed some light on a potential regulatory mechanism. We used co-immunoprecipitation (or pulldown) experiments to validate and map the interactions of MAGI-1 with key players of the Hippo-YAP pathway: PTPN14 and the LATS1/2 kinases. Moreover, we completed the study with immunostaining to further support the legitimacy of these interactions *in vitro*.

In front of the high similarity between the proteins of the MAGI family and potential redundancy with respect to YAP regulation, we assessed whether MAGI-1 and MAGI-3 shared Hippo-YAP binding partners.

In this chapter, we decided to work with HEK293 cells for immunoprecipitation experiments as they reach high transfection efficiency.

4.3 Results

4.3.1 MAGI-1 interacts with PTPN14, a well-established negative regulator of YAP

MAGI-1 was identified among PTPN14's interactome by two independent proteomic studies using affinity capture coupled by mass spectrometry (344,345). In this section, we used co-immunoprecipitation (or pulldown) experiments to validate and map the interaction between MAGI-1 and PTPN14.

4.3.1.1 *mMAGI-1 interacts with PTPN14.*

First, we aimed at confirming the interaction between MAGI-1 and PTPN14. HEK293 cells were transiently co-transfected with V5-PTPN14 and Flag-mMAGI-1B constructs. A pull-down experiment using Flag-functionalised agarose beads was performed and the samples were run on a SDS-PAGE. Western blot analysis was carried out with anti-PTPN14 and anti-Flag antibodies. V5-PTPN14 was detected in Flag-mMAGI-1B pull-down complex (**Figure 4.1a**, lane 2). The reciprocal pull-down was performed using Myc-PTPN14 and GFP-mMAGI-1B expression constructs and Myc-trap[®] resin. GFP-mMAGI-1B was detected in PTPN14 pull-down complex (**Figure 4.1b**, lane 2). Taken together, our results show that the two proteins interact either in a direct or indirect manner.

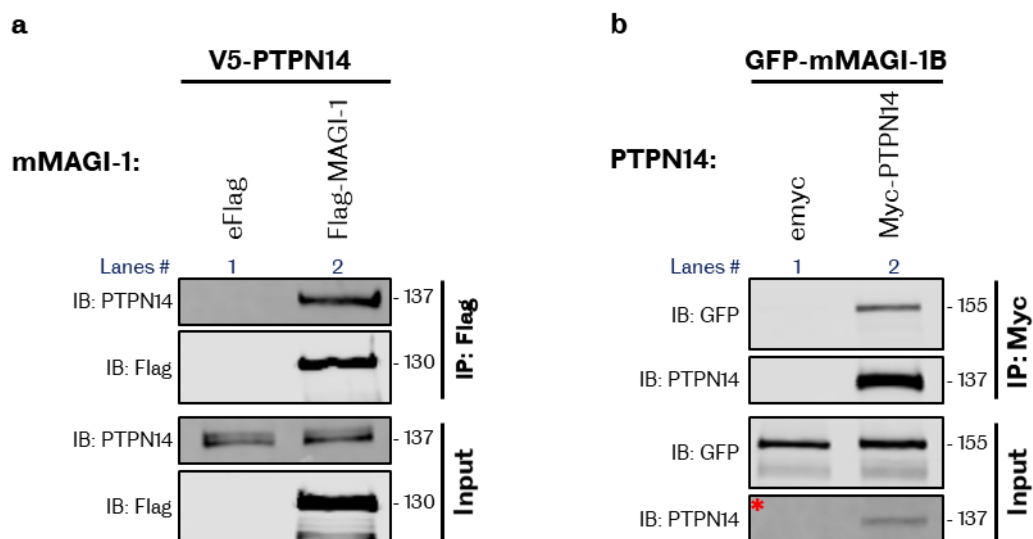


Figure 4.1 | MAGI-1 interacts with PTPN14.

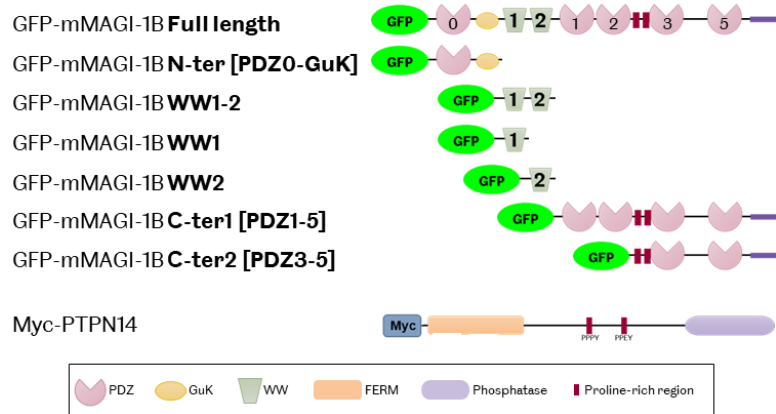
The indicated plasmids were transiently transfected into HEK293 cells. Cell lysates were subjected to immunoprecipitation (IP) and western blotting (IB) as indicated. Empty vectors (eFlag and emyc) were used as control. Protein expression levels are confirmed in the input fractions (1.5% of total cell lysates). Theoretical molecular weights are indicated in kDa on the right side of the western blots. *: increased brightness and contrast compared to the corresponding IP fraction. **a**, Co-immunoprecipitation experiment of V5-PTPN14 with Flag-mMAGI-1B using agarose beads coated with Flag antibody (Same one as used for WB detection) (n=3). PTP14 is found in mMAGI-1's protein complex. **b**, Co-immunoprecipitation experiment of GFP-mMAGI-1B with Myc-PTPN14 WT using Myc-trap[®] resin (n=2). MAGI-1 is found in PTPN14's protein complex.

4.3.1.2 *mMAGI-1 WW domains are sufficient to interact with PTPN14.*

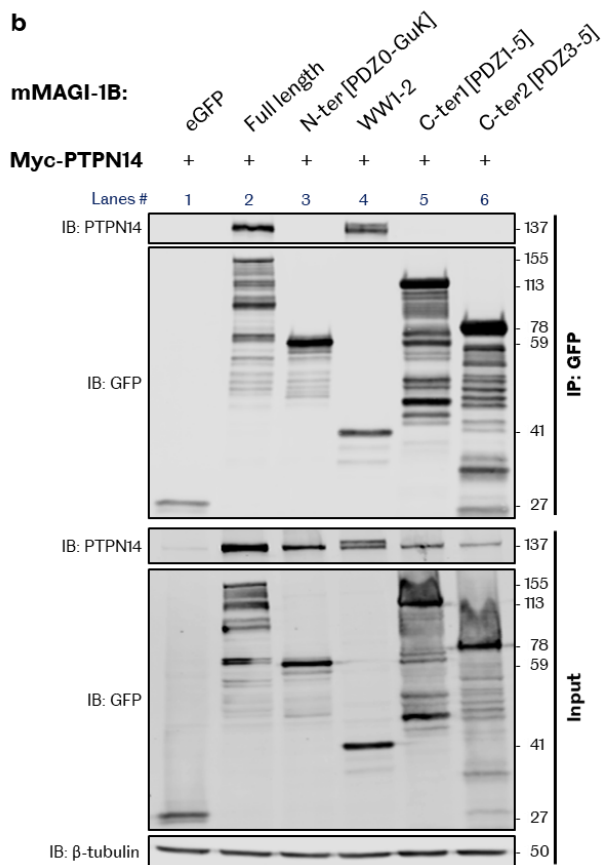
Next, we aimed at dissecting the interaction and identifying the respective protein-protein interaction domains involved. We started by asking, on MAGI-1 side, which domain(s)

was/were needed for the interaction with PTPN14. Several GFP-tagged truncated mMAGI-1B constructs were generated: PDZ0-GuK, WW1-2, PDZ1-5, PDZ3-5 for the study (**Figure 4.2a**).

a



b



c

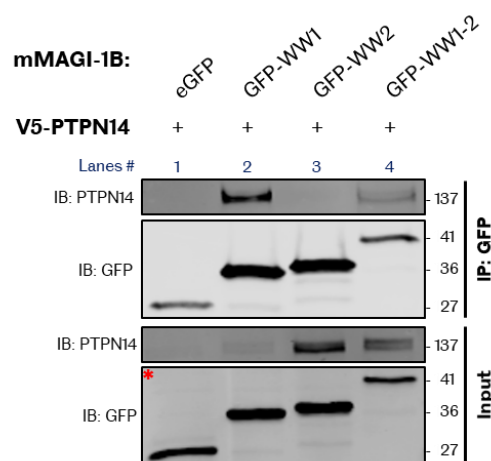


Figure 4.2 | MAGI-1 WW1 domain interacts with PTPN14.

The indicated plasmids were transfected into HEK293 cells. Cell lysates were subjected to immunoprecipitation (IP) and western blotting (IB) as indicated. An empty vector (eGFP) was used as control. Protein expression levels are confirmed in the input fractions (1.5% of total cell lysates). Theoretical molecular weights are indicated in kDa on the right side of the western blots. *: increased brightness and contrast compared to the corresponding IP fraction. **a**, mMAGI-1B and PTPN14 constructs used in this figure. Details on the constructs can be found in Chapter 2. PDZ: Repeat of 80-100 amino acids that was first identified in PSD-95/Dlg/ZO-1/2 (346-348); GuK: Guanylate

kinase domain; WW: Domain with two conserved tryptophan residues; FERM: Named after 4.1, Ezrin, Radixin and Moesin proteins, this domain is involved in plasma membrane localisation of the protein (349). **b**, Co-immunoprecipitation experiment of Myc-PTPN14 with GFP-mMAGI-1B full length or constructs using GFP-trap[®] resin (n=2). PTPN14 was found in mMAGI-1B WW domains protein complex indicating that they are sufficient for the interaction with PTPN14. **c**, Co-immunoprecipitation experiment of Myc-PTPN14 with GFP-WW domains constructs of mMAGI-1B using GFP-trap[®] resin (n=2). PTPN14 interacts more specifically with MAGI-1 WW1 domain.

HEK293 cells were transiently co-transfected with the aforementioned GFP-constructs and Myc-PTPN14. A GFP-trap[®] pulldown was performed and the samples were analysed by western blotting with anti-GFP and anti-PTPN14 antibodies. PTPN14 was only pulled-down by mMAGI-1 full length and WW domains-only construct (**Figure 4.2b** lanes 2 and 4 respectively). Our results therefore indicate that MAGI-1 WW domains are sufficient to pulldown PTPN14.

We also noticed that PTPN14 appeared as a doublet upon overexpression of WW1-2 (**Figure 4.2b** lane 4), most likely due to a post-translational modification; this did not affect the binding as both forms were pulled-down by mMAGI-1B WW domains. We did not investigate further the nature of this modification due to time restriction.

To further map the interaction, we asked whether both WW domains were required to pulldown PTPN14. Two more truncated mMAGI-1B GFP-constructs were made, WW1 and WW2, to assess the necessity of each individual WW domain for the interaction. Another GFP-trap[®] pulldown was performed with GFP-WW1, GFP-WW2 or GFP-WW1-2 and Myc-PTPN14 expression constructs transiently co-transfected in HEK293 cells. Membranes were subjected to western blotting with anti-GFP and anti-PTPN14 antibodies. PTPN14 was detected in GFP-WW1 and GFP-WW1-2 protein complexes but was absent from GFP-WW2 pulldown lane (**Figure 4.2c** lanes 2, 4 and 3 respectively). Taken together, our findings indicate that only the first WW domain is sufficient to interact with PTPN14.

4.3.1.3 *PTPN14 PPxY motifs are necessary for the binding of mMAGI-1 WW domains.*

We have established that the interaction between MAGI-1 and PTPN14 was mediated by MAGI-1 WW domains. WW domains are short amino acid sequences containing two characteristic and conserved tryptophan residues. These domains are known to associate with proline-rich motifs (55). Interestingly, PTPN14 possesses two such proline-rich regions, referred to as PPxY motifs. This type of interactions is common in signal transduction, especially within the Hippo pathway (340,341). We therefore speculated that PTPN14's PPxY motifs were involved in the interaction with MAGI-1 WW domains. We used a PTPN14 construct for which the proline-rich regions had been mutated to alanines (AAAA) (75). HEK293 cells

were transiently co-transfected with either V5-PTPN14 WT or PPxY mutant and Flag-WW1-2 expression constructs. A Flag-pulldown was performed and the samples were subjected to western blotting with anti-PTPN14 and anti-Flag antibodies. Our results confirmed that Flag-WW1-2 was sufficient to precipitate PTPN14 WT (**Figure 4.3b** lane 2). However, the PTPN14 PPxY mutant was not present in Flag-WW1-2 pulldown complex (**Figure 4.3b** lane 4). Mutation of the PPxY motifs abolished the interaction with mMAGI-1B WW domains. Taken together, our findings strongly suggest a direct interaction between mMAGI-1B WW domains and PTPN14 PPxY motifs.

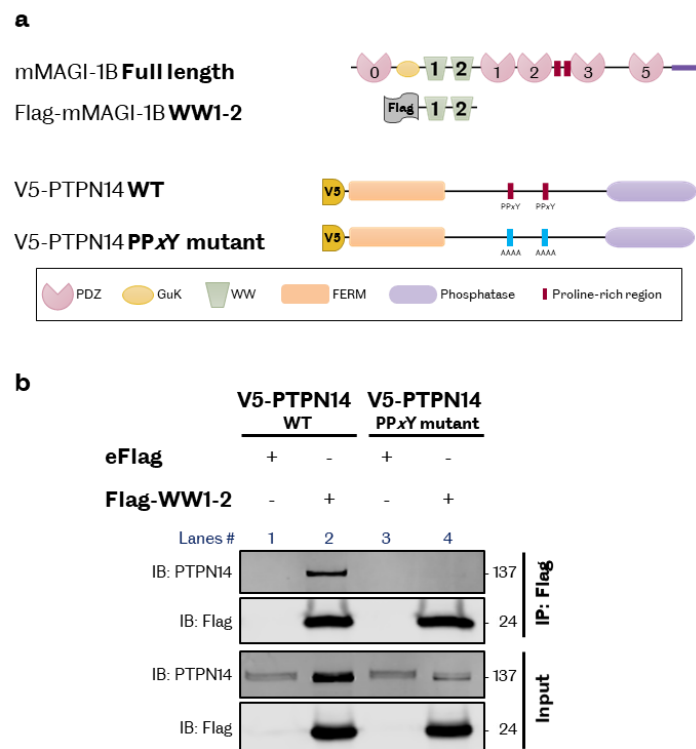


Figure 4.3 | PTPN14 PPxY motifs are necessary for the binding of MAGI-1 WW domains.

a, mMAGI-1B and PTPN14 constructs used in this figure. Details on the constructs can be found in Chapter 2. **b**, HEK293 cells were transiently co-transfected with either V5-PTPN14 WT or PPxY mutant and Flag-WW1-2. Cell lysates were subjected to Flag immunoprecipitation (IP) and western blotting (IB) as indicated (n=2). An empty vector (eFlag) was used as control. Protein expression levels are confirmed in the input fractions (1.5% of total cell lysates). Theoretical molecular weights are indicated in kDa on the right side of the western blots. Mutation of the PTPN14 proline-rich regions (PPxY motifs) to alanines (AAAA) abolishes the interaction with mMAGI-1B WW domains.

4.3.1.4 Potential second binding site between mMAGI-1 and PTPN14.

After establishing the main binding site between MAGI-1 and PTPN14, we asked whether there was a second binding site to the interaction. Indeed, we showed that mMAGI-1B WW domains were sufficient to pulldown PTPN14 through its PPxY motifs. However, the WW

domains might not be necessary for the interaction. To test that hypothesis, we generated GFP-mMAGI-1B deletion constructs: Δ WW1, Δ WW2 and Δ WW1-2. HEK293 cells were transiently co-transfected with the aforementioned GFP constructs and Myc-PTPN14 WT. A GFP-trap[®] pulldown was carried out and the samples were subjected to western blotting with anti-PTPN14 and anti-GFP antibodies. GFP- Δ WW2 was able to pulldown PTPN14 (**Figure 4.4b** lane 4) which corroborates our previous finding that MAGI-1 WW1 domain was sufficient to interact with PTPN14 (**Figure 4.2c** lane 2). Surprisingly, GFP- Δ WW1 and GFP- Δ WW1-2 constructs were still capable of precipitating a small amount of PTPN14 (**Figure 4.4b** lanes 3 and 5 respectively). This result suggests that MAGI-1 WW domains are required to bind to PTPN14 but do not account for the entire interaction. The residual binding in the absence of the WW domains could result from an indirect interaction or indicate the presence of a secondary binding site.

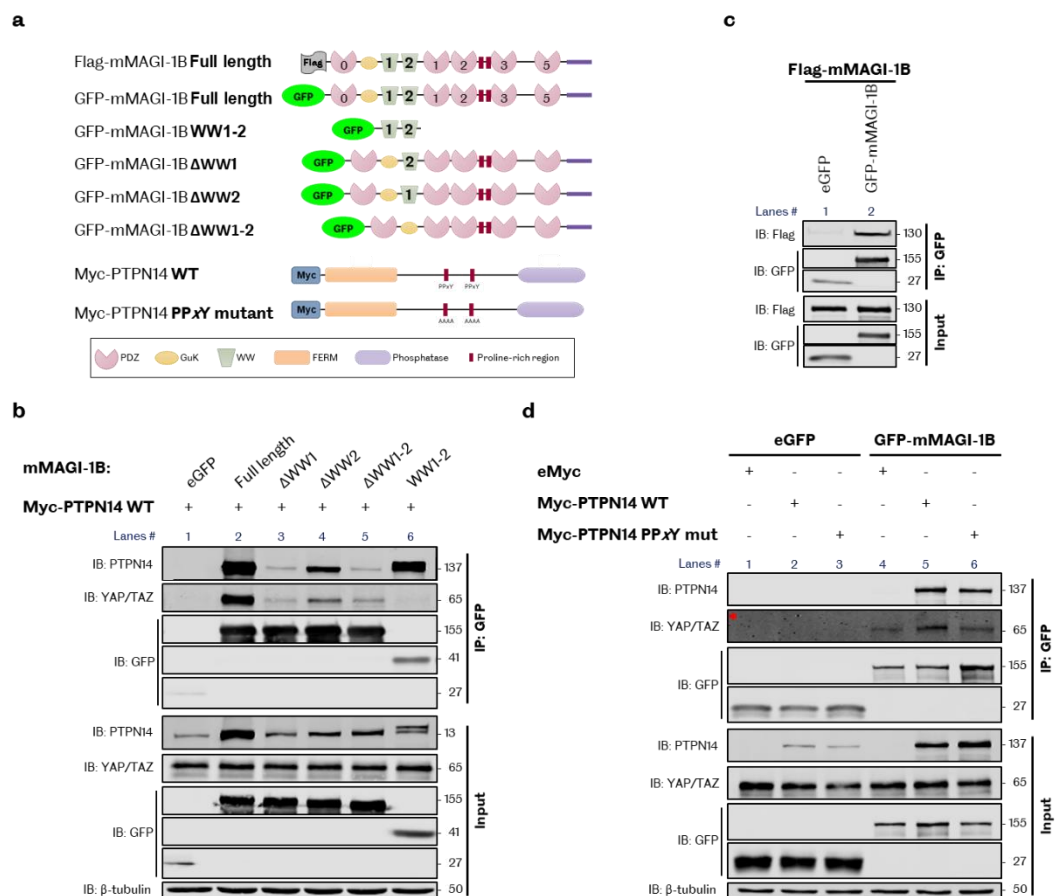


Figure 4.4 | Potential second binding site between mMAGI-1 and PTPN14.

The indicated plasmids were transfected into HEK293 cells. Cell lysates were subjected to immunoprecipitation (IP) and western blotting (IB) as indicated. An empty vector (eGFP) was used as control. Protein expression levels are confirmed in the input fractions (1.5% of total cell lysates). Theoretical molecular weights are indicated in kDa on the right side of the western blots. *: increased brightness and contrast compared to the corresponding input fraction. **a**, mMAGI-1B and PTPN14 constructs used in this figure. Details on the constructs can be found in Chapter 2. **b**, Co-immunoprecipitation experiment of Myc-PTPN14 WT with GFP-mMAGI-1B full length (FL) or WW-domains

deletion constructs using GFP-trap[®] resin (n=2). Deletion of WW1 or WW1-2 domains is not sufficient to abolish the interaction of MAGI-1 with PTPN14, suggesting the presence of a second binding site. YAP is found in the protein complex with MAGI-1 FL and PTPN14. **c.** Co-immunoprecipitation experiment of Flag-mMAGI-1B with GFP-mMAGI-1B using GFP-trap[®] resin (n=1). MAGI-1 oligomerises with itself. **d.** Co-immunoprecipitation experiment of Myc-PTPN14 WT or PPxY mutant with GFP-mMAGI-1B FL using GFP-trap[®] resin (n=2). MAGI-1 is found in PTPN14's protein complex regardless of the mutation of the PPxY motif, although the affinity is greatly reduced. mMAGI-1B is able to pull down YAP independently of PTPN14 overexpression.

First, we addressed the possibility that the observed residual binding could arise from the formation of MAGI-1 oligomers. Indeed, MAGI-1 contains many PDZ domains that are known to form oligomers (301,350-352). The MAGI-1 deletion-constructs could potentially oligomerise with the endogenous MAGI-1 protein, much less abundant, and thereby pull down small amounts of PTPN14. To test that hypothesis, we performed a pull down experiment with two different tagged versions of mMAGI-1B full length. HEK293 cells were transiently transfected with Flag-mMAGI-1B and GFP-mMAGI-1B. A GFP-trap[®] pull down was performed and samples were subjected to western blotting with anti-Flag and anti-GFP antibodies. Flag-mMAGI-1B was strongly detected in GFP-mMAGI-1B protein complex indicating that MAGI-1 is capable of oligomerising with itself (**Figure 4.4c** lane 2). It could explain the residual PTPN14 binding in the MAGI-1 WW domains deletion constructs protein complex. Another possibility would be that MAGI-1 and PTPN14 are part of a bigger protein complex that may be disturbed but still occur in the absence of MAGI-1 WW domains. Lastly, one might also consider the existence of another secondary binding site.

To investigate the presence of a potential second binding site for the MAGI-1/PTPN14 interaction, we built on previous results. Indeed, we had shown that mutation of PTPN14 PPxY motifs impeded the binding to the MAGI-1 GFP-WW1-2 construct (**Figure 4.3b** lane 4). We therefore asked whether PTPN14 PPxY mutant could still interact with the full length MAGI-1 protein. HEK293 cells were transiently transfected with Myc-PTPN14 WT or PPxY mutant and GFP-mMAGI-1B full length (FL). A GFP-trap[®] pull down was performed and samples were subjected to western blotting with anti-Myc and anti-GFP antibodies. Surprisingly, PTPN14 mutant was detected in MAGI-1 FL protein complex (**Figure 4.4d** lane 6). The band intensity was reduced to about 20% compared to WT (lane 5). Mutation of the proline-rich regions was checked once again by sequencing. This new finding further suggests the existence of a second binding site for the MAGI-1/PTPN14 interaction, independent of the WW domains and PPxY motifs. However, due to time restriction this second, minor, binding site was not investigated further.

4.3.1.5 Is mMAGI-1B stabilising PTPN14?

Over all the pull-downs performed, we noticed that the exogenous PTPN14 protein levels were increasing along with MAGI-1 overexpression. The pattern varied depending on which MAGI-1 sub-construct was co-expressed. For example, the overexpression of MAGI-1 WW domains together with PTPN14 WT appeared to enhance PTPN14 protein levels. This effect was obliterated upon mutation of PTPN14 PPxY motifs (**Figure 4.3b**, input lanes). This effect could be occurring at the mRNA or at the protein level. We hypothesised that MAGI-1 interaction with PTPN14 was stabilising the latter protein. This question is addressed in Annex 6.

4.3.1.6 PTPN14 interaction is conserved with the human isoform: hMAGI-1Cβ1.

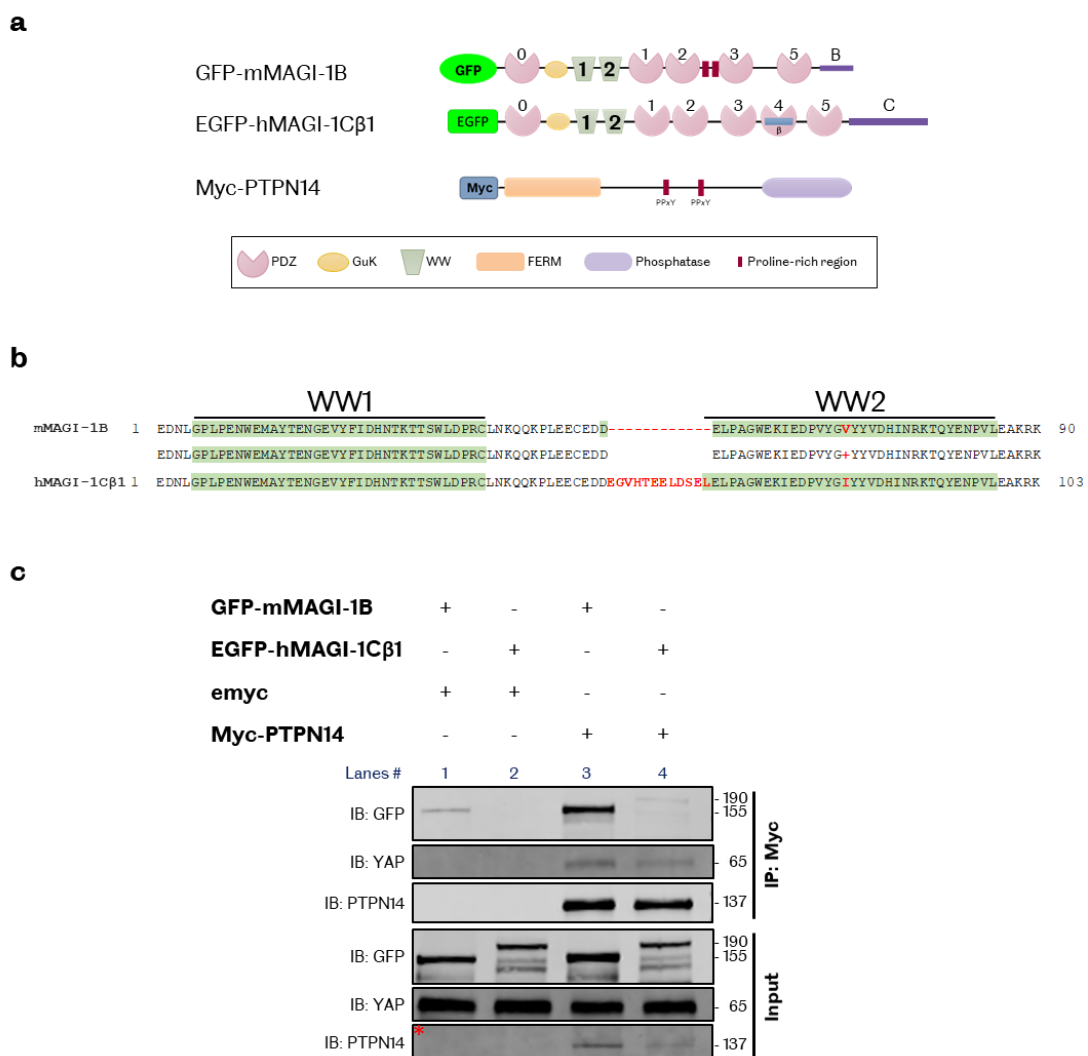


Figure 4.5 | PTPN14 interaction is conserved with the human isoform: hMAGI-1Cβ1.

a. MAGI-1 and PTPN14 constructs used in this figure. Details on the constructs can be found in Chapter 2. **b.** NCBI protein blast between the mouse and human MAGI-1 WW domains. The first WW domain is 100% conserved and the second one shares very high similarity. However, in the human form, the linker region between the two WW

domains is longer, which could affect the 3D structure of this area. **c**, HEK293 cells were transiently co-transfected with either GFP-mMAGI-1B or EGFP-hMAGI-1C β 1 and Myc-PTPN14. Cell lysates were subjected to Myc-trap[®] immunoprecipitation (IP) and western blotting (IB) as indicated (n=1). An empty vector (emyc) was used as control. Protein expression levels are confirmed in the input fractions (1.5% of total cell lysates). Theoretical molecular weights are indicated in kDa on the right side of the western blots. *: increased brightness and contrast compared to the corresponding IP fraction. The interaction with PTPN14 is conserved in human (lane 4), although it appears less strong.

So far, all the MAGI-1 constructs used in the study were derived from the mouse MAGI-1B isoform. We later generated a human hMAGI-1C β 1 construct which is the endogenous isoform to epithelial cells (See Annex 1). Our two constructs, namely mMAGI-1B and hMAGI-1C β 1, on top of being from different species, constituted two different isoforms. However, excluding the alternatively spliced β and C-terminal regions, the protein sequences share 95% identity. WW1 domain is entirely conserved between mouse and human species while the linker between both WW domains is longer by 12 aa in the human version (**Figure 4.5b**). We therefore asked whether the interaction was conserved with the human MAGI-1. HEK293 cells were transiently co-transfected with GFP-mMAGI-1B or EGFP-hMAGI-1C β 1 and Myc-PTPN14 WT. A Myc-Trap[®] pulldown was performed and the samples were subjected to western blotting with anti-GFP and anti-Myc antibodies. EGFP-hMAGI-1C β 1 could be detected in PTPN14 protein complex, however, the amount pulled-down was much lower than that of GFP-mMAGI-1B (**Figure 4.5c** lanes 4 and 3 respectively). The PTPN14 interaction with human MAGI-1 seemed less strong than with its mouse counterpart. This could be due to the longer linker region affecting the 3D conformation of the protein in this area.

4.3.1.7 *PTPN14 localises with hMAGI-1C β 1 at cell-cell contacts*

To consolidate the biochemistry results on the MAGI-1/PTPN14 interaction, we asked whether both proteins were colocalising in epithelial cells. DLD-1 WT cells were transiently co-transfected with Myc-PTPN14 and EGFP-hMAGI-1C β 1 expression constructs. Immunostaining was performed with an anti-PTPN14 antibody. We found that PTPN14 was localised at the plasma membrane as reported in the literature (104) (**Figure 4.6a**). However, upon EGFP-hMAGI-1C β 1 overexpression, the pool of PTPN14 localised at the plasma membrane appeared enriched. Taken together, our immunostaining data further supports that legitimacy of MAGI-1/PTPN14 interaction. Moreover, MAGI-1 may be involved in recruiting PTPN14 to the membrane.

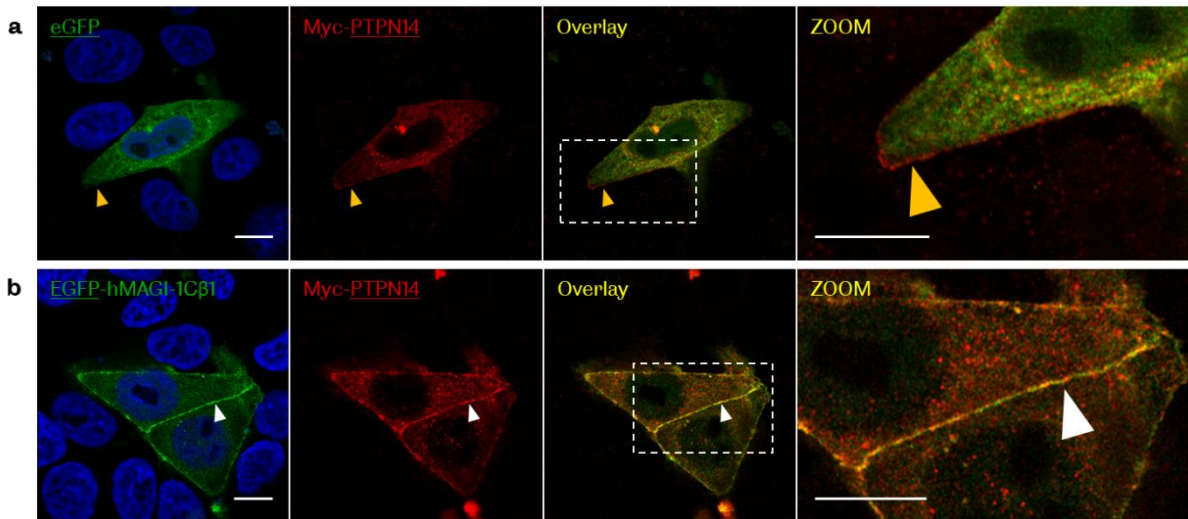


Figure 4.6 | MAGI-1 appears to enhance PTPN14 plasma membrane localisation.

DLD-1 WT cells were transiently transfected with the indicated constructs (n=1). Anti-PTPN14 immunostaining was performed. Hoechst was used as DNA counterstain. Images were acquired with a confocal microscope in Airyscan mode. Scale bars: 10µm. The 'ZOOM' corresponds to the area delineated by the white dotted box. **a**, PTPN14 is present at the membrane (Orange arrowheads). **b**, Upon overexpression of MAGI-1, PTPN14 signal at cell-cell contacts is enriched (White arrowheads).

4.3.1.8 PTPN14 interacts with MAGI-3

The MAGI family contains three members: MAGI-1, MAGI-2 and MAGI-3, that share high similarity in terms of modular domains, leading to overlapping protein interaction networks. Moreover, Hammad and co-worker observed a compensatory mechanism within the MAGI family (322). Based on our data, we strongly suspected, at least partial, redundancy of MAGI-1's function within the Hippo-YAP pathway (See Chapter 3). We focused our complementary interaction study on MAGI-3.

MAGI-3 was suggested to interact with PTPN14 by a large-scale proteomics study (345). Here, we aimed at confirming the interaction with co-immunoprecipitation experiments. To that end, we used an expression construct containing the hMAGI-3b* isoform fused at the C-terminal with V5 and 6xHis tags, courtesy of Prof. Randy Hall (**Figure 4.7a**). This version of the protein possesses only the first WW domain as the presence of the alternatively spliced * region disrupts WW2. Because of the high similarity between MAGI-1 and MAGI-3, we ask whether the MAGI-3/PTPN14 interaction was mediated by the WW domains and PPxY motifs, as with MAGI-1. HEK293 cells were transiently co-transfected with hMAGI-3b*-V5/His and either Myc-PTPN14 WT or PPxY mutant constructs. A Myc-trap[®] pulldown was performed and samples were subjected to western blotting with anti-MAGI-3 and anti-PTPN14 antibodies. We found hMAGI-3b* present in both PTPN14 WT and mutant protein complexes (**Figure 4.7b**

lanes 2 and 3). Mutation of PTPN14's proline-rich regions did not completely abolish, but clearly disturbed its interaction with hMAGI-3b (lane 3). Our results confirmed the MAGI-3/PTPN14 interaction and suggested that the binding is mainly mediated by the WW/PPxY regions, similarly to MAGI-1 interaction.

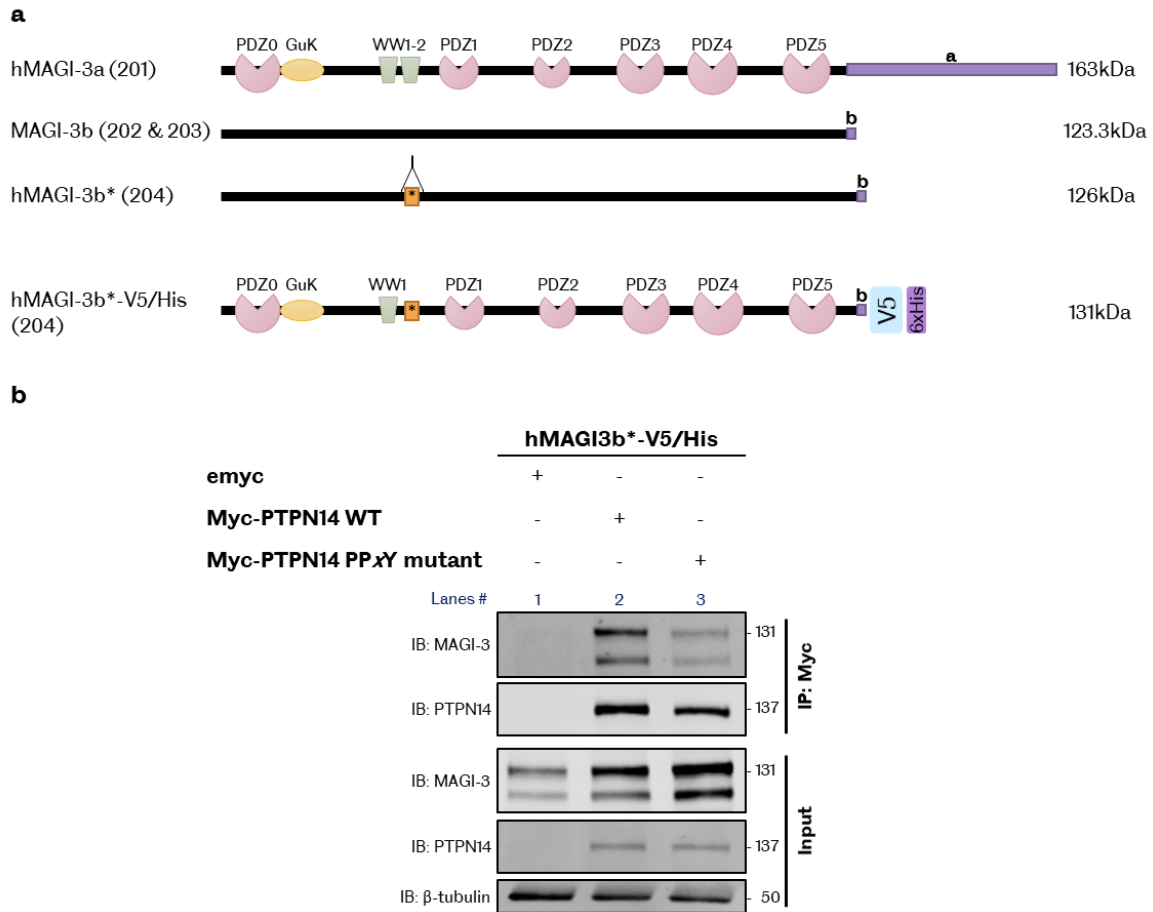


Figure 4.7 | MAGI-3 interacts with PTPN14.

a. Modular structures of MAGI-3 isoforms. The numbers correspond to the transcripts from Ensembl. Two regions are alternatively spliced: the C-ter part (a or b) and a short region that disrupt the WW2 domain, that we will refer to as * (Top). The fusion protein used in this study is the b* isoform with C-terminal V5 and 6xHis tags, courtesy of Prof. Randy Hall (Bottom). **b.** HEK293 cells were transiently co-transfected with hMAGI3b*-V5/His and either Myc-PTPN14 WT or PPxY mutant, as indicated. Cell lysates were subjected to Myc-trap® immunoprecipitation (IP) and western blotting (IB) as indicated (n=2). An empty vector (emyc) was used as control. Protein expression levels are confirmed in the input fractions (1.5% of total cell lysates). Theoretical molecular weights are indicated in kDa on the right side of the western blots. MAGI-3 interacts with PTPN14 and the binding is reduced with the PPxY mutant, indicating that, similarly to MAGI-1, the WW-domains and PPxY motifs may be involved.

4.3.2 YAP is in MAGI-1 protein complex.

4.3.2.1 YAP is part of MAGI-1/PTPN14 complex

PTPN14 is a well-known negative regulator of YAP (71-75). We therefore asked whether YAP was part of the MAGI-1/PTPN14 protein complex. We re-probed membranes from previous pulldown experiments with an anti-YAP antibody to detect the endogenous protein. YAP was found in the protein complex pulled-down with MAGI-1 full length and containing PTPN14 (**Figure 4.4b** lane 2). Varying amounts of YAP were also precipitated with MAGI-1 WW-domains deletion constructs (**Figure 4.4b** lanes 3, 4 and 5) with a pattern that resembled that of PTPN14. Indeed, YAP WW domains are reported to interact with PTPN14 PPxY (74). However, YAP was completely absent from GFP-WW1-2 construct pulldown complex (**Figure 4.4b** lane 6). Given that both MAGI-1 and YAP are interacting with PTPN14 PPxY motifs, it was reasonable to assume that upon overexpression of the GFP-WW1-2 construct, MAGI-1 WW domains saturated PTPN14 PPxY motifs, out-competing that of YAP. These results suggest that YAP might be pulldown indirectly in MAGI-1 protein complex via PTPN14. However, YAP was still found in MAGI-1 protein complex regardless of PTPN14 WT or PPxY mutant overexpression (**Figure 4.4d** lanes 4, 5 and 6). Yet, mutation of PPxY motifs in PTPN14 was reported to abolish its interaction with YAP, using the same construct as used in our study (75). Taken together, our results suggest an interaction between MAGI-1 and YAP independently of PTPN14.

4.3.2.2 YAP interacts with MAGI-1 C-terminal PDZ domains

Next, we examined whether MAGI-1 and YAP were interacting directly. HEK293 cells were transfected with GFP-mMAGI-1B or GFP-truncated constructs: PZ0-GuK, WW1-2, PDZ1-5, PDZ3-5. A GFP-trap[®] was performed and samples were subjected to western blotting with anti-GFP and anti-YAP antibodies. Endogenous YAP was found in the protein complexes of the full length MAGI-1 and that of the constructs harbouring PDZ domains (**Figure 4.8b** lanes 2, 3, 5 and 6). The strongest interaction was detected with the C-ter2 construct containing mMAGI-1B PDZ3 and PDZ5 domains. PDZ4 domain, corresponding to the alternatively spliced β -region, is spliced out in the mMAGI-1B isoform. We noticed that YAP, when pulled-down with either C-ter1 or C-ter2 construct was detected higher by the antibody than its usual size. The higher molecular weight could be due to a post-translational modification. However, since it did not occur in presence of the full length mMAGI-1B, we speculated that it resulted from the ectopic expression of a truncated protein and did not investigate further. YAP was barely detectable in the pulldown complex of mMAGI-1B WW1-2 domains. This most likely represents the fraction

of YAP precipitated indirectly by other WW domain-interactors of MAGI-1 such as PTPN14 or AMOT (74,223,224). In summary, our results further suggest a direct interaction between MAGI-1 PDZ3 or PDZ5 domains and YAP.

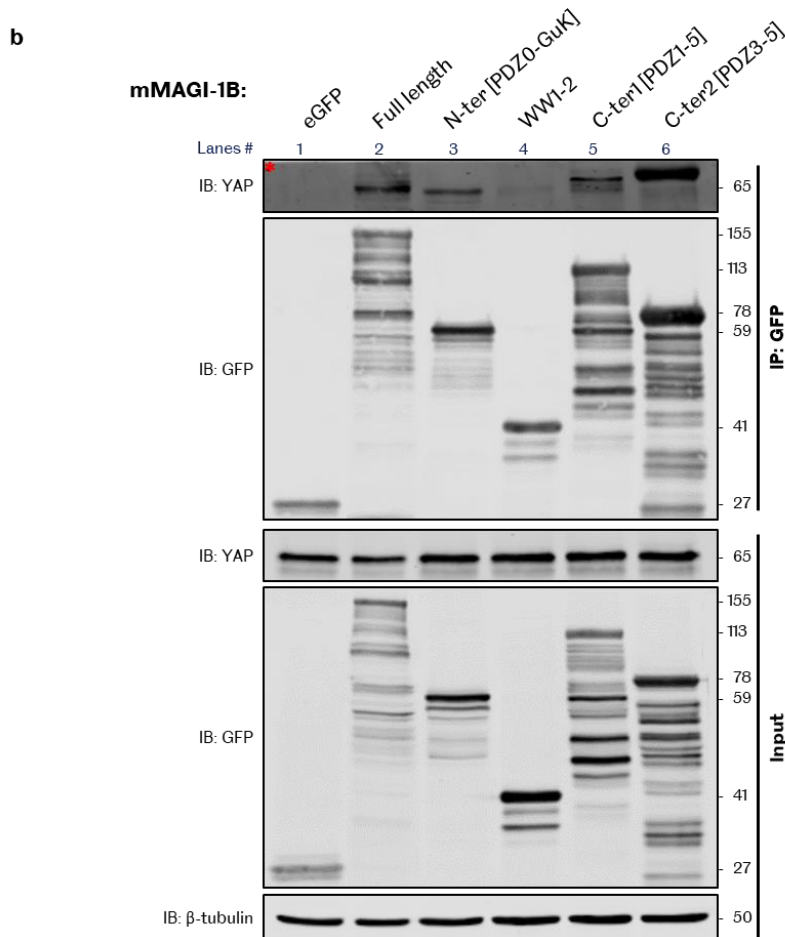
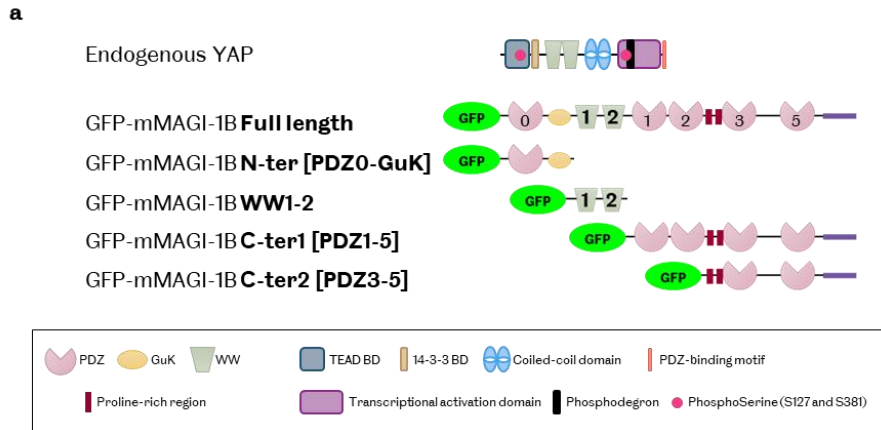


Figure 4.8 | YAP interacts with MAGI-1 C-terminal PDZ domains.

a, YAP protein-protein interaction domains. BD: binding domain. MAGI-1 expression constructs used in this figure. In mMAGI-1B, the PDZ4 domain (β -region) is spliced out. Details on the constructs can be found in Chapter 2. **b**, HEK293 cells were transiently co-transfected with either of the GFP-mMAGI-1B constructs, as indicated. Cell lysates were subjected to GFP-trap[®] immunoprecipitation (IP) and western blotting (IB) as indicated (n=1). An empty

vector (eGFP) was used as control. Protein expression levels are confirmed in the input fractions (1.5% of total cell lysates). Theoretical molecular weights are indicated in kDa on the right side of the western blots. *: increased brightness and contrast compared to the corresponding input fraction. YAP was found in the pull-down complexes with the MAGI-1 subconstructs harbouring PDZ domains. There is an obvious preference for construct C-ter2 containing only PDZ3 and PDZ5. The band detected by the anti-YAP antibody is higher in this protein complex than the baseline band, suggesting a post-translational modification.

4.3.2.3 YAP is enriched at cell-cell contacts with MAGI-1

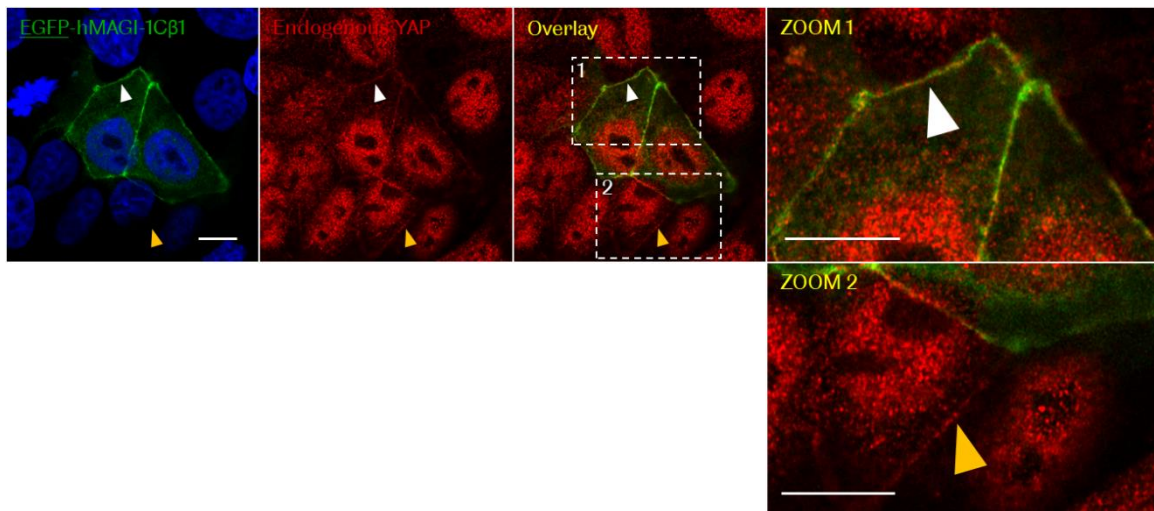


Figure 4.9 | MAGI-1 and YAP are both localised at cell-cell contacts.

DLD-1 WT cells were transiently transfected with the indicated constructs (n=1). Anti-YAP immunostaining was performed to detect the endogenous protein. Hoechst was used as DNA counterstain. Images were acquired with a confocal microscope in Airyscan mode. Scale bars: 10 μ m. The 'ZOOM' corresponds to the area delineated by the white dotted boxes. YAP is localised at cell-cell contacts with (ZOOM 1 – white arrowheads) and without (ZOOM 2 – orange arrowheads) MAGI-1 overexpression.

To gain more insight on a potential regulatory mechanism, we looked whether MAGI-1 and YAP were colocalising at cell-cell contacts. DLD-1 WT cells were transiently transfected with EGFP-hMAGI-1C β 1 and anti-YAP immunostaining was performed to detect the endogenous protein. Corroborating our previous data (Chapter 3, **Figure 3.1** and **Figure 3.4**), we found that YAP is localised in the nucleus at a low cell density and is also enriched at the cell-cell contacts. Overexpression of EGFP-hMAGI-1C β 1 did not affect YAP nuclear localisation. Moreover, YAP enrichment at the plasma membrane occurred regardless of MAGI-1 overexpression. To summarise, our immunofluorescence results indicate that YAP is enriched at the cell-cell contacts where MAGI-1 is localised, consolidating the potential direct interaction between the two proteins. In addition, MAGI-1 does not appear to recruit YAP to

the junctions but we cannot rule-out the role of the endogenous MAGI-1 pool in this experiment.

4.3.3 MAGI-1 interacts with LATS1/2, key players of the Hippo pathway

MAGI-1 was found to be in close vicinity of LATS1/2 by a large-scale proteomics study aiming at unravelling the Hippo pathway interactome (221). Indeed, MAGI-1 was found among the biotinylated proteins when either of the LATS kinases was used as bait using a technique of proximity-dependent biotinylation, called BioID (343). Based on the BioID mechanism, MAGI-1 could be either of the following: (1) a direct interactor, (2) an indirect interactor or (3) simply a neighbouring protein which does not interact with the LATS kinases (343). Here, we aimed at validating and dissecting this potential interaction between MAGI-1 and LATS1/2 using co-immunoprecipitation experiments.

4.3.3.1 MAGI-1 is in a protein complex with either of the LATS kinases.

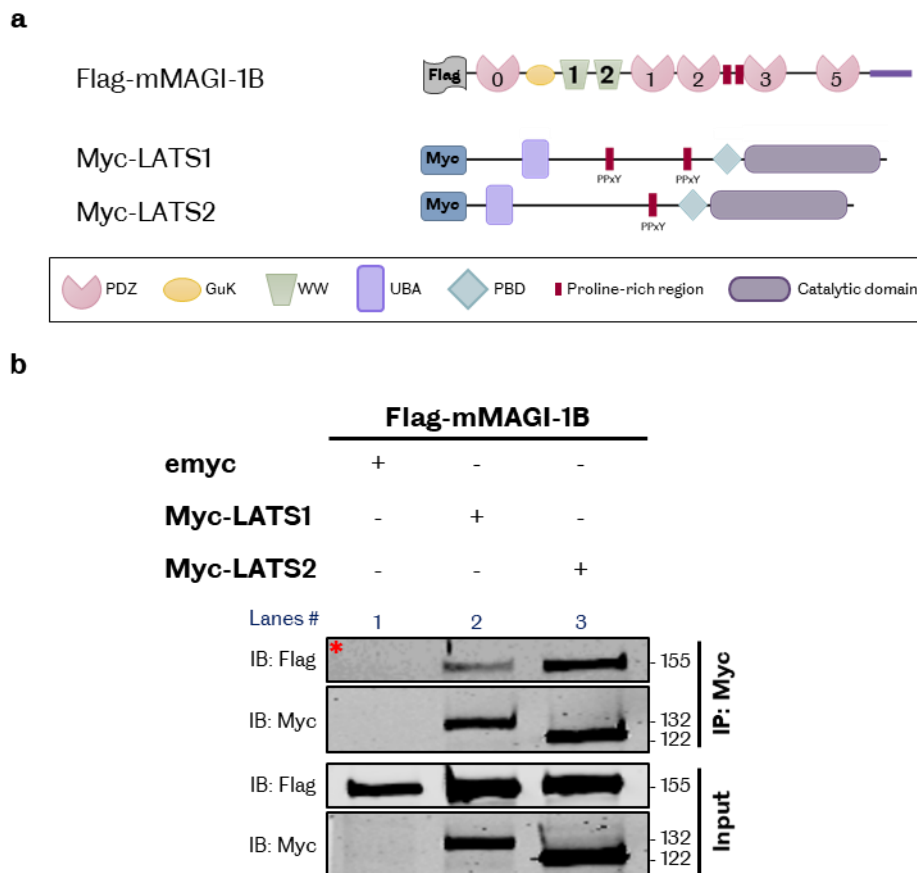


Figure 4.10 | MAGI-1 is in a protein complex with either of the LATS kinases.

a. mMAGI-1B and LATS1/2 constructs used in this figure. Details on the constructs can be found in Chapter 2. PDZ: Repeat of 80-100 amino acids that was first identified in PSD-95/Dlg/ZO-1/2; GuK: Guanylate kinase domain; WW: Domain with two conserved tryptophan residues; UBA: Ubiquitin-associated domain; PDB: Protein binding domain.

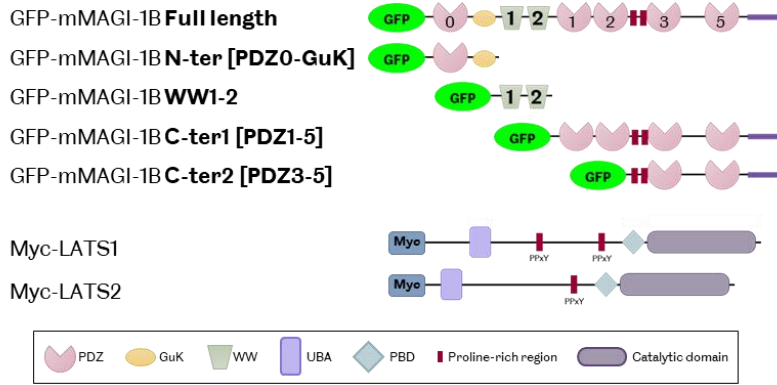
b. HEK293 cells were transiently co-transfected with Myc-LATS1 or Myc-LATS2 and Flag-mMAGI-1B, as indicated. Cell lysates were subjected to Myc-trap[®] immunoprecipitation (IP) and western blotting (IB) as indicated (n=2). An empty vector (emyc) was used as control. Protein expression levels are confirmed in the input fractions (1.5% of total cell lysates). Theoretical molecular weights are indicated in kDa on the right side of the western blots. *: increased brightness and contrast compared to the corresponding input fraction. MAGI-1 interacts with both LATS kinases and seems to have a stronger affinity for LATS2.

First, we aimed at confirming the interaction between MAGI-1 and either of the LATS kinases. To that end, HEK293 cells were transiently co-transfected with either Myc-LATS1 or Myc-LATS2 and Flag-mMAGI-1B. A Myc-trap[®] pulldown was performed and samples were subjected to western blotting with anti-Myc and anti-Flag antibodies. This interaction required milder pulldown buffer conditions than with PTPN14 to be detected. Optimisation steps are described in Annex 7. Flag-mMAGI-1B was found in both Myc-LATS1 and Myc-LATS2 pulldown complexes (**Figure 4.10b** lanes 2 and 3 respectively). Our results confirm that MAGI-1 is in a protein complex with either of the LATS kinases and further suggest that these proteins interact in a direct or indirect manner.

4.3.3.2 *MAGI-1 WW domains are sufficient to bind to the LATS kinases.*

Next, we aimed at further characterising the interaction between MAGI-1 and the LATS kinases. Similar to our study with PTPN14, we used MAGI-1 truncated constructs: PDZ0-GuK, WW1-2, PDZ1-5 and PDZ3-5, to pin point the domain(s) sufficient to pulldown LATS1 and LATS2. HEK293 cells were transiently co-transfected with either Myc-LATS1 or Myc-LATS2 and the aforementioned GFP-tagged truncated mMAGI-1B constructs. A GFP-trap[®] was performed and the samples were subjected to western blotting with anti-Myc and anti-GFP antibodies. Firstly, LATS1 and LATS2 individually were found in mMAGI-1B protein complex, evidencing the reciprocity of the interaction (**Figure 4.11b** lanes 2 and 8 respectively). Interestingly, both kinases were strongly present in GFP-WW1-2 pulldown lanes (lanes 4 and 10), most likely thanks to their PPxY motifs. We also noticed distinctive behaviours between LATS1 and LATS2. Indeed, only the latter protein was found associated with PDZ domains-containing mMAGI-1B constructs (lanes 9, 11 and 12), with a preference for C-terminal PDZ domains (lanes 11 and 12). Taken together, our results show that once again, mMAGI-1B WW domains appeared to be the main binding site for the MAGI-1/LATS interaction. In addition, LATS2 might be interacting with mMAGI-1B C-terminal PDZ domains.

a



b

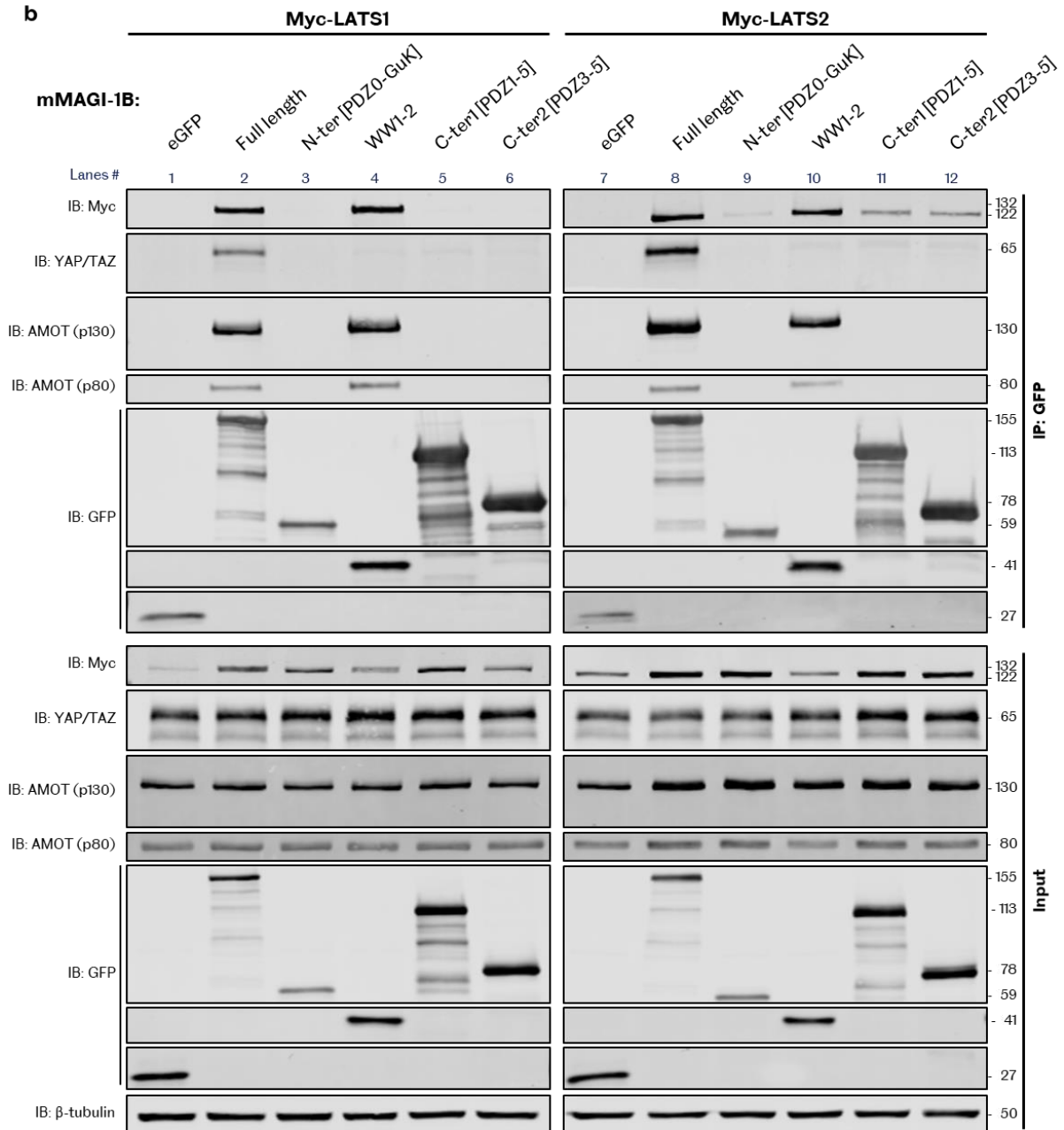


Figure 4.11 | MAGI-1 WW domains are sufficient to bind to the LATS kinases.

a. mMAGI-1B and LATS1/2 constructs used in this figure. In mMAGI-1B, the PDZ4 domain (β -region) is spliced out. Details on the constructs can be found in Chapter 2. PDZ: Repeat of 80-100 amino acids that was first identified in PSD-95/Dlg/ZO-1/2; GuK: Guanylate kinase domain; WW: Domain with two conserved tryptophan residues; UBA: Ubiquitin-associated domain; PDB: Protein binding domain. **b.** HEK293 cells were transiently co-transfected with Myc-LATS1 or Myc-LATS2 and GFP-mMAGI-1B truncated constructs, as indicated. Cell lysates were subjected to GFP-trap[®] immunoprecipitation (IP) and western blotting (IB) as indicated (n=2). An empty vector (eGFP) was used as control. Protein expression levels are confirmed in the input fractions (1.5% of total cell lysates). Theoretical molecular weights are indicated in kDa on the right side of the western blots. The reciprocal interaction between the LATS kinases and mMAGI-1B is confirmed. mMAGI-1B WW domains are sufficient to bind to both kinases. LATS2 also display affinity for the PDZ-rich constructs of mMAGI-1B. Both AMOT isoforms are precipitated along with MAGI-1 full length and WW-only constructs.

4.3.3.3 LATS1/2 interaction is conserved with the human isoform: hMAGI-1C β 1.

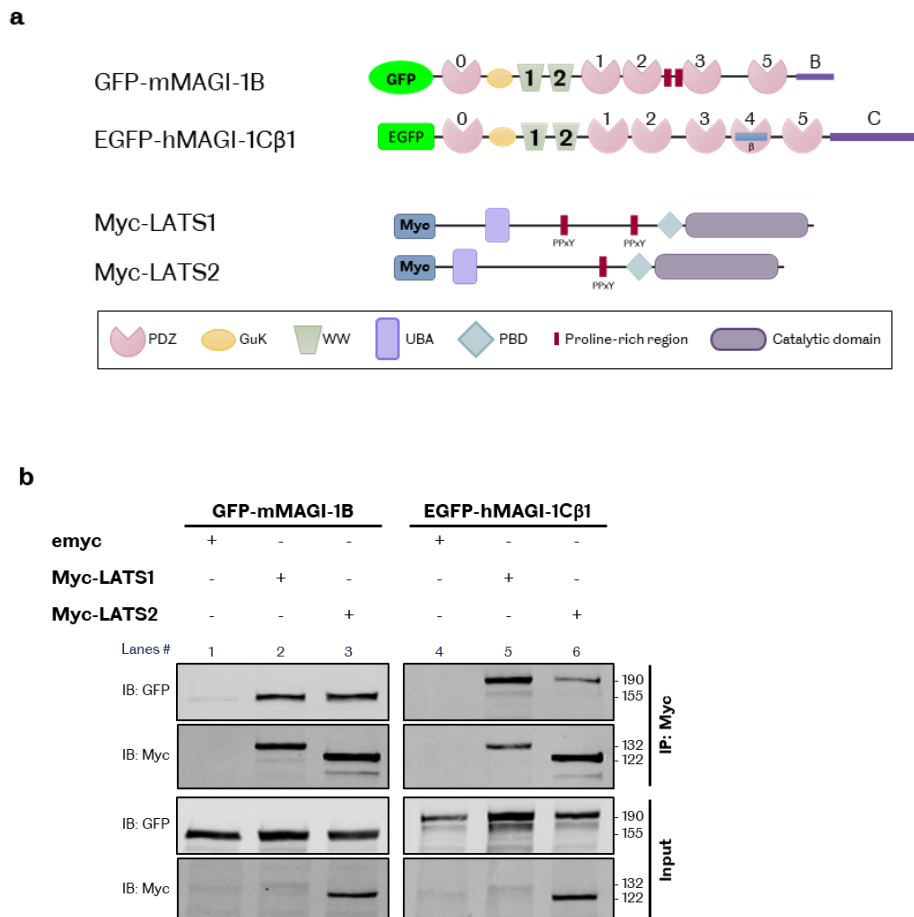


Figure 4.12 | LATS1/2 interaction is conserved with the human isoform: hMAGI-1C β 1.

a. mMAGI-1B and LATS1/2 constructs used in this figure. In mMAGI-1B, the PDZ4 domain (β -region) is spliced out. Details on the constructs can be found in Chapter 2. PDZ: Repeat of 80-100 amino acids that was first identified in PSD-95/Dlg/ZO-1/2; GuK: Guanylate kinase domain; WW: Domain with two conserved tryptophan residues; UBA: Ubiquitin-associated domain; PDB: Protein binding domain. **b.** HEK293 cells were transiently co-transfected with

Myc-LATS1 or Myc-LATS2 and EGFP-hMAGI-1C β 1 or GFP-mMAGI-1B, as indicated. Cell lysates were subjected to Myc-trap[®] immunoprecipitation (IP) and western blotting (IB) as indicated (n=1). An empty vector (emyc) was used as control. Protein expression levels are confirmed in the input fractions (1.5% of total cell lysates). Theoretical molecular weights are indicated in kDa on the right side of the western blots. Similar to the mouse version, human MAGI-1C β 1 interacts with both LATS1 and LATS2 kinases. While mMAGI-1B seems to have similar affinity for both kinases, hMAGI-1C β clearly has a preference for LATS1.

We then asked whether the interaction between MAGI-1 and the LATS1/2 was conserved with the human version hMAGI-1C β 1, endogenous isoform of epithelial tissues. To that end, HEK293 cells were transiently co-transfected with either Myc-LATS1 or Myc-LATS2 and EGFP-hMAGI-1C β 1. GFP-mMAGI-1B was used in parallel as a positive control. A Myc-trap[®] was performed and samples were subjected to western blotting with anti-Myc and anti-GFP antibodies. The human MAGI-1 was found in both LATS1 and LATS2 protein complexes (**Figure 4.12b** lanes 5 and 6). However, hMAGI-1C β 1 showed a stronger affinity for LATS1 (lane 5).

4.3.3.4 *The LATS kinases are enriched at cell-cell contacts upon hMAGI-1C β 1 overexpression*

Next, we asked whether the LATS kinases localisation was affected by MAGI-1. DLD-1 WT cells were therefore transiently co-transfected with EGFP-hMAGI-1C β 1 and either Myc-LATS1 or Myc-LATS2 expression constructs. We observed that LATS1 appeared to be recruited and enriched at the cell-cell contacts upon overexpression of EGFP-hMAGI-1C β 1, from an otherwise cytoplasmic localisation (**Figure 4.13a & b**). On the other hand, LATS2 was present at the plasma membrane, regardless of MAGI-1 overexpression (**Figure 4.13c & d**). To summarise, our immunofluorescence data further supports the validity of the MAGI1/LATS interaction *in vitro*. Moreover, we found that MAGI-1 may have a role in recruiting one of the kinases, LATS1, to the cell-cell contacts, coherent with a stronger interaction (**Figure 4.12**).

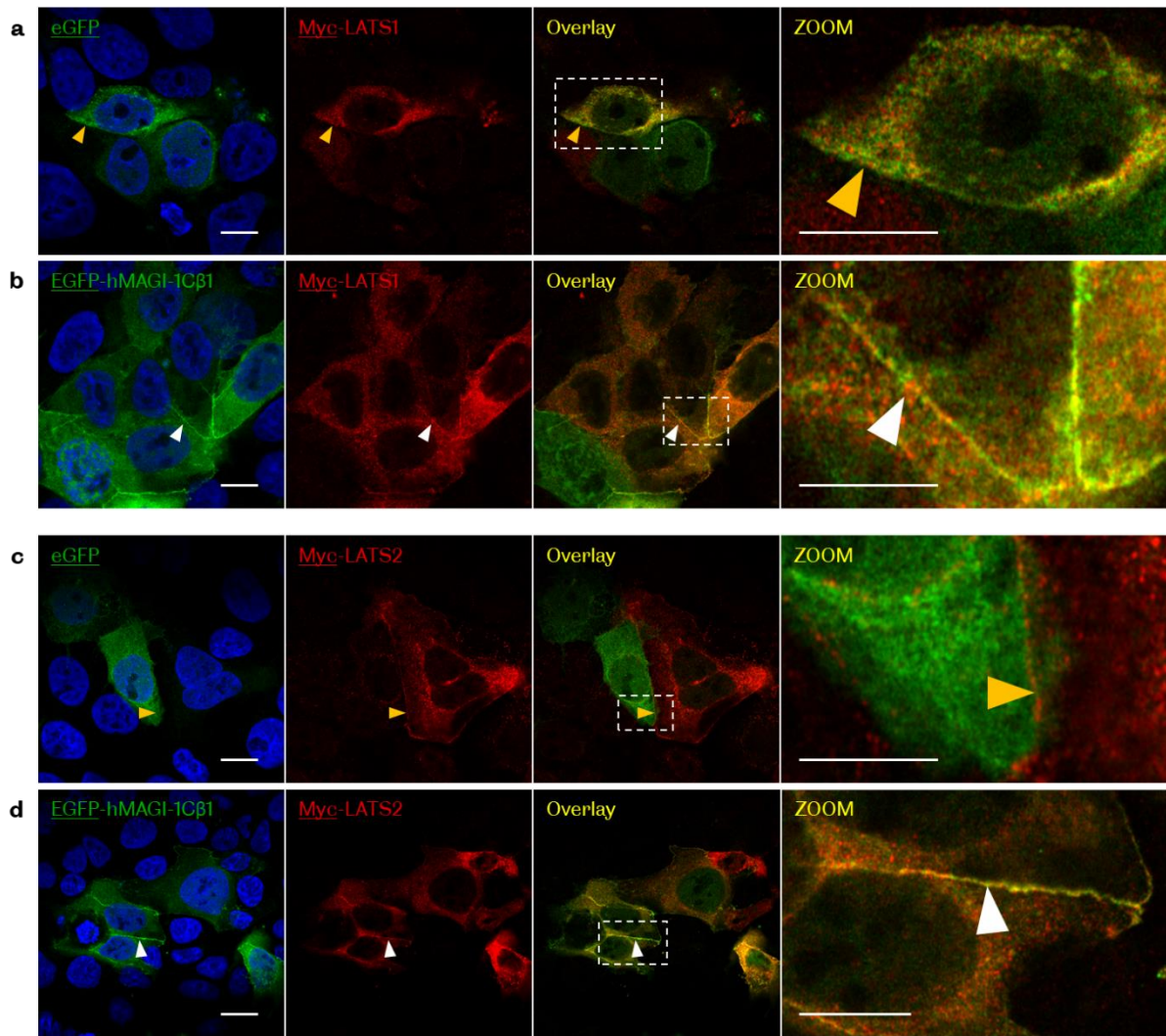


Figure 4.13 | MAGI-1 and the LATS kinases are localised at the cell-cell contacts.

DLD-1 WT cells were transiently transfected with the indicated constructs (n=1). Anti-Myc immunostaining was performed. Hoechst was used as DNA counterstain. Images were acquired with a confocal microscope in Airyscan mode. Scale bars: 10 μ m. The 'ZOOM' corresponds to the area delineated by the white dotted box. **a.** LATS1 staining is cytoplasmic and not particularly enriched at the cell-cell contacts (orange arrowheads). **b.** Upon overexpression of EGFP-hMAGI-1C β 1, LATS1 is recruited to the plasma membrane where it overlaps with MAGI-1 (white arrowheads). **c.** LATS2 is enriched at the plasma membrane (orange arrowheads). **d.** LATS2 and MAGI-1 staining overlap at the cell-cell contacts.

4.3.3.5 LATS1/2 interact with MAGI-3

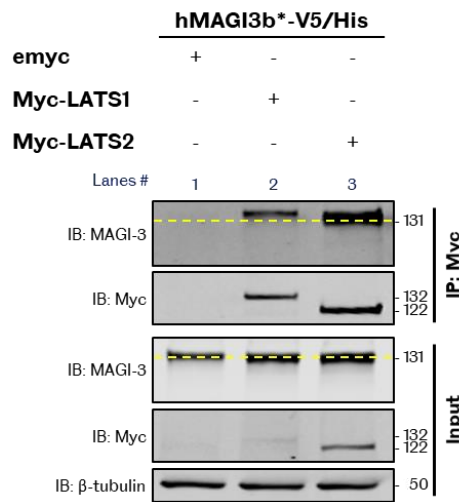


Figure 4.14 | MAGI-3 interacts with the LATS kinases.

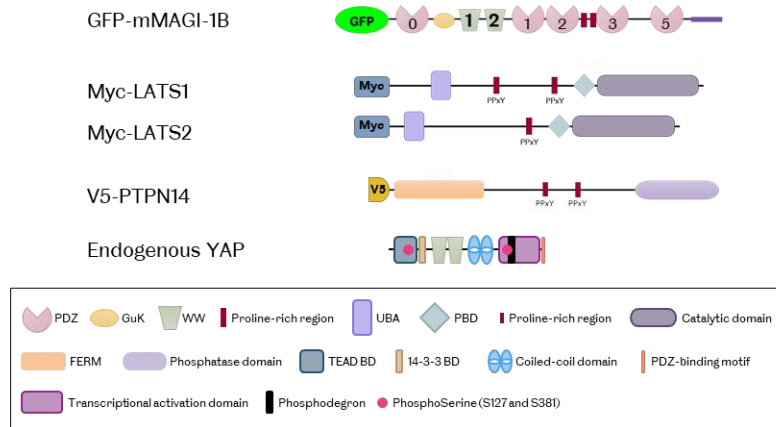
HEK293 cells were transiently co-transfected with hMAGI3b*-V5/His and either Myc-LATS1 or Myc-LATS2, as indicated. Cell lysates were subjected to Myc-trap[®] immunoprecipitation (IP) and western blotting (IB) as indicated (n=2). An empty vector (emyc) was used as control. Protein expression levels are confirmed in the input fractions (1.5% of total cell lysates). Theoretical molecular weights are indicated in kDa on the right side of the western blots. MAGI-3 interacts with both LATS1 and LATS2. The yellow dotted line indicates the input protein. In the pulldown lanes, MAGI-3 appears to be running higher. The protein could therefore be phosphorylated by the LATS kinases.

Next, we asked whether MAGI-3 could also interact with the LATS1/2 kinases. Indeed, a study, using a WW-domains array, suggested that LATS1 interacted with MAGI-3 WW domains (353). Here, we aimed at confirming this interaction with co-immunoprecipitation experiments. HEK293 cells were transiently transfected with hMAGI-3b*-V5/His and either Myc-LATS1 or Myc-LATS2 expression constructs. A Myc-trap[®] pulldown was performed and samples were subjected to western blotting using anti-MAGI-3 and anti-Myc antibodies. MAGI-3 was found in both LATS1 and LATS2 protein complexes (**Figure 4.14** lanes 2 and 3), similarly to MAGI-1 (**Figure 4.10** lanes 2 and 3). Moreover, MAGI-3 seemed to have a preference for LATS2 (**Figure 4.14** lane 3). In the pulldown lanes, we noticed that the band for MAGI-3 was slightly higher in LATS1 protein complex (lane 2). After adjusting the brightness and contrast settings of the image processing software, MAGI-3 actually appeared in the INPUT fraction as a single band while in LATS2 pulldown fraction it was a doublet (lane 3). In LATS1 pulldown lane, MAGI-3 was clearly a single band, above the baseline (yellow dotted line – lane 2). This could potentially indicate a post-translational modification, such as phosphorylation. However, due to limited time, this was not investigated further. Taken together, our results show that, similarly to MAGI-1, MAGI-3 interacts with both LATS kinases.

4.3.4 PTPN14, LATS1/2, AMOT and YAP are co-precipitated by MAGI-1

4.3.4.1 PTPN14 competes with LATS1/2 for the binding of mMAGI-1B WW domains.

a



b

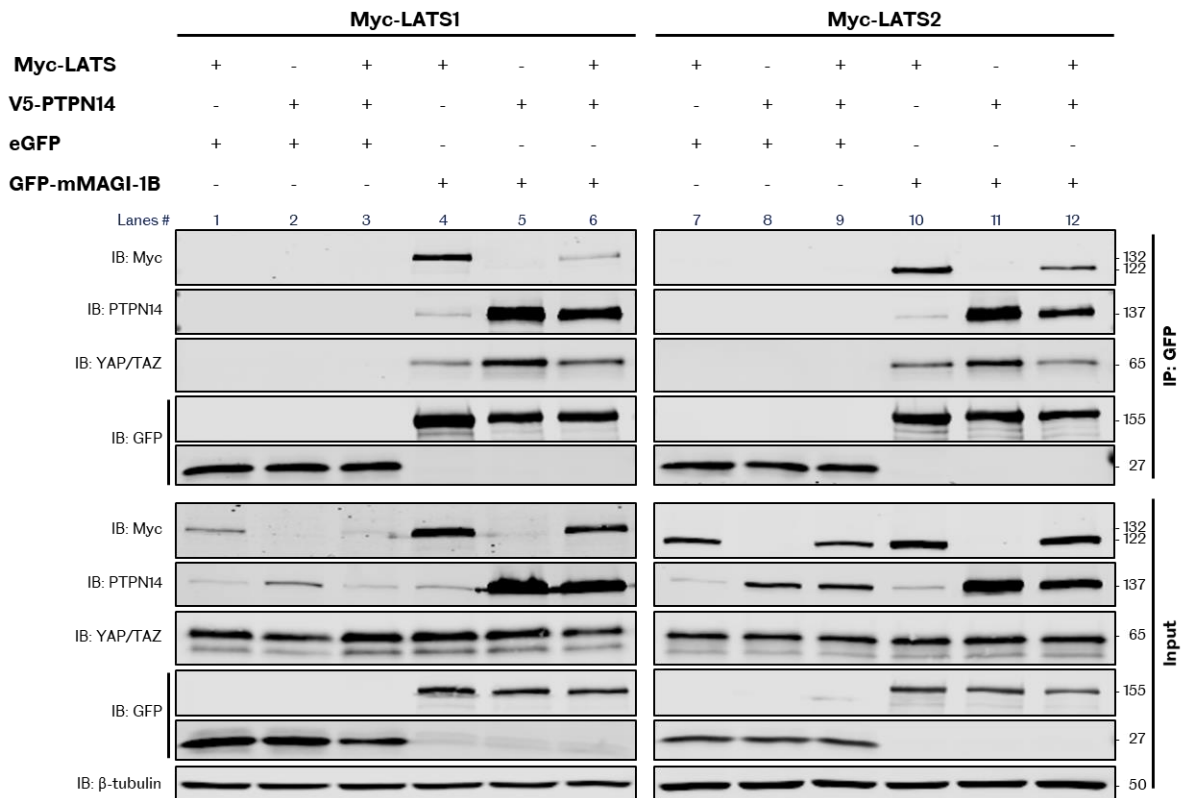


Figure 4.15 | PTPN14 competes with LATS1/2 for the binding of mMAGI-1B WW domains.

a. mMAGI-1B, LATS1/2 and PTPN14 constructs used in this figure. Details on the constructs can be found in Chapter 2. Endogenous YAP protein-protein interaction domains. PDZ: Repeat of 80-100 amino acids that was first identified in PSD-95/Dlg/ZO-1/2; GuK: Guanylate kinase domain; WW: Domain with two conserved tryptophan residues; UBA: Ubiquitin-associated domain; PDB: Protein binding domain. BD: binding domain; FERM: Named after 4.1, Ezrin, Radixin and Moesin proteins, this domain is involved in plasma membrane localisation of the protein. **b.** HEK293 cells were transiently co-transfected with GFP-mMAGI-1B, Myc-LATS1 (Left) or Myc-LATS2 (Right), and/or V5-PTPN14, as indicated. Cell lysates were subjected to GFP-trap® immunoprecipitation (IP) and western blotting (IB)

as indicated (n=2 with LATS1 and n=1 with LATS2). An empty vector (eGFP) was used as control. Protein expression levels are confirmed in the input fractions (1.5% of total cell lysates). Theoretical molecular weights are indicated in kDa on the right side of the western blots. The individual MAGI-1/PTPN14 and MAGI-1/LATS interactions are confirmed. In the triple pulldown lanes (#6 and #12), both LATS1/2 and PTPN14 are pulled-down with MAGI-1. However, there seem to be competition for MAGI-1 WW domains binding and PTPN14 shows the strongest affinity. YAP is present in all pulldown complexes with mMAGI-1B.

So far, we have shown that PTPN14 and the LATS1/2 kinases interact with mMAGI-1B WW domains. We then asked whether these proteins were competing to bind to the WW domains of MAGI-1. We therefore performed triple pulldown experiments of mMAGI-1B/PTPN14/LATS1 or mMAGI-1B/PTPN14/LATS2. HEK293 cells were transiently co-transfected with GFP-mMAGI-1B, V5-PTPN14 and either Myc-LATS1 or Myc-LATS2. GFP-trap[®] co-immunoprecipitation was performed and samples were subjected to western blotting with anti-GFP, anti-PTPN14 and anti-Myc antibodies. These experiments confirmed the individual mMAGI-1B/PTPN14 and mMAGI-1B/LATS interactions that were used as controls (**Figure 4.15b** lanes 5 & 11, and 4 & 10 respectively). When considering the triple mMAGI-1B/PTPN14/LATS pulldowns, similar results were obtained with LATS1 (left side, lane 1-6) and LATS2 (right side, lanes 7-12). Indeed, both PTPN14 and LATS1/2 were found simultaneously in mMAGI-1B protein complexes (**Figure 4.15b** lanes 6 and 12 respectively). However, PTPN14 was strongly present in the complex (lanes 6 and 12, similarly to mMAGI1B/PTPN14 in lanes 5 and 11) whereas the amount of LATS precipitated was greatly reduced compared to mMAGI1B/LATS (lanes 4 and 10). Moreover, we were able to detect the endogenous PTPN14 in the mMAGI-1B/LATS pulldown lanes (lanes 4 and 10). Taken together, our results suggest that LATS1/2 and PTPN14 are partially competing to bind to mMAGI-1B WW domains and PTPN14 is showing the strongest affinity.

4.3.4.2 *YAP is part of mMAGI-1B protein complex, alongside PTPN14 and LATS1/2.*

We have previously shown evidence that YAP might interact directly with one of MAGI-1 C-terminal PDZ domains (Section 4.3.2.2). Moreover, literature extensively reports interaction of PTPN14 and LATS1/2 respective PPxY motifs with YAP WW domains (31,57,71-75,354). We therefore asked whether YAP was part of the complex with MAGI-1 and PTPN14 and/or LATS1/2 kinases. We probed the membranes of the triple pulldowns with anti-YAP/TAZ antibody (**Figure 4.15b**). YAP was found in all mMAGI-1B protein complexes (lanes 4, 5, 6, 10, 11 and 12). However, the amount of YAP precipitated along with mMAGI-1B and PTPN14 (lanes 5 and 11) was greater than that pulled-down in the presence of LATS1/2 (lanes 4, 6, 10 and 12). Taken

together, our results show that YAP is precipitated by MAGI-1 alongside PTPN14 and LATS1/2, suggesting that they might be in a complex together.

4.3.4.3 AMOT proteins are part of mMAGI-1B complex, alongside LATS1/2, PTPN14 and YAP.

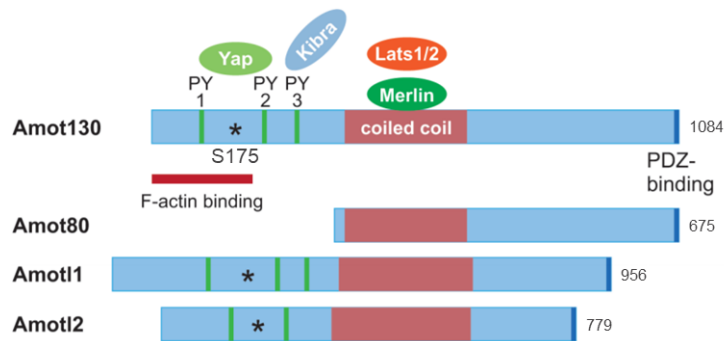


Figure 4.16 | AMOT family of proteins.

Modular structure and known Hippo pathway interactors of the AMOT family. It comprises four members: the two angiominin (AMOT) isoforms p130 and p80, angiominin-like1 (AMOTL1) and angiominin-like2 (AMOTL2) proteins. PY indicates the presence of proline-rich regions or [L/P]PxY motifs (green bars). *: indicate the conserved consensus sequence for LATS1/2 phosphorylation. Taken and adapted from Figure 1b of (45,355).

Next, we turned our interest to the motin family, composed of AMOT p130 and p80 as well as AMOTL1 and AMOTL2 (**Figure 4.16**) (further described in Section 1.2.2.1.6). According to Patrie's and Bratt's teams, AMOT p130, AMOTL1 and AMOTL2 are interactors of MAGI-1 WW domains (223,224). The interaction requires the motifs' [L/P]PxY motifs, which the p80 isoform lacks thereby preventing interaction with MAGI-1 (224) and other WW-domains containing proteins such as YAP (76). The AMOT family of proteins are well known regulators of the Hippo YAP pathway (described in Section 1.2.2.1.6) and both angiominin isoforms interact with and exert differential role on LATS (96,140). Moreover, AMOT was identified as a PTPN14-associated protein by tandem affinity purification and mass spectrometry analysis (74,356).

We therefore asked whether the AMOT family was part of the protein complex we were studying. Membranes of the triple mMAGI-1B/LATS/PTPN14 pulldown were re-probed with an anti-AMOT antibody (**Figure 4.17b** – original experiment in Section 4.3.4.1). This antibody recognises the endogenous AMOT C-terminal region and therefore detects both p80 and p130 isoforms, but does not cross-react with AMOTL1/2 (Cell Signaling Technology). Both isoforms were precipitated with mMAGI-1B/PTPN14, mMAGI-1B/LATS1 and mMAGI-1B/PTPN14/LATS1 complexes (**Figure 4.17b** lanes 4, 5 and 6 respectively). The presence of the p130 isoform in the pulldown lanes could be due to both direct and indirect binding to MAGI-1, through LATS1

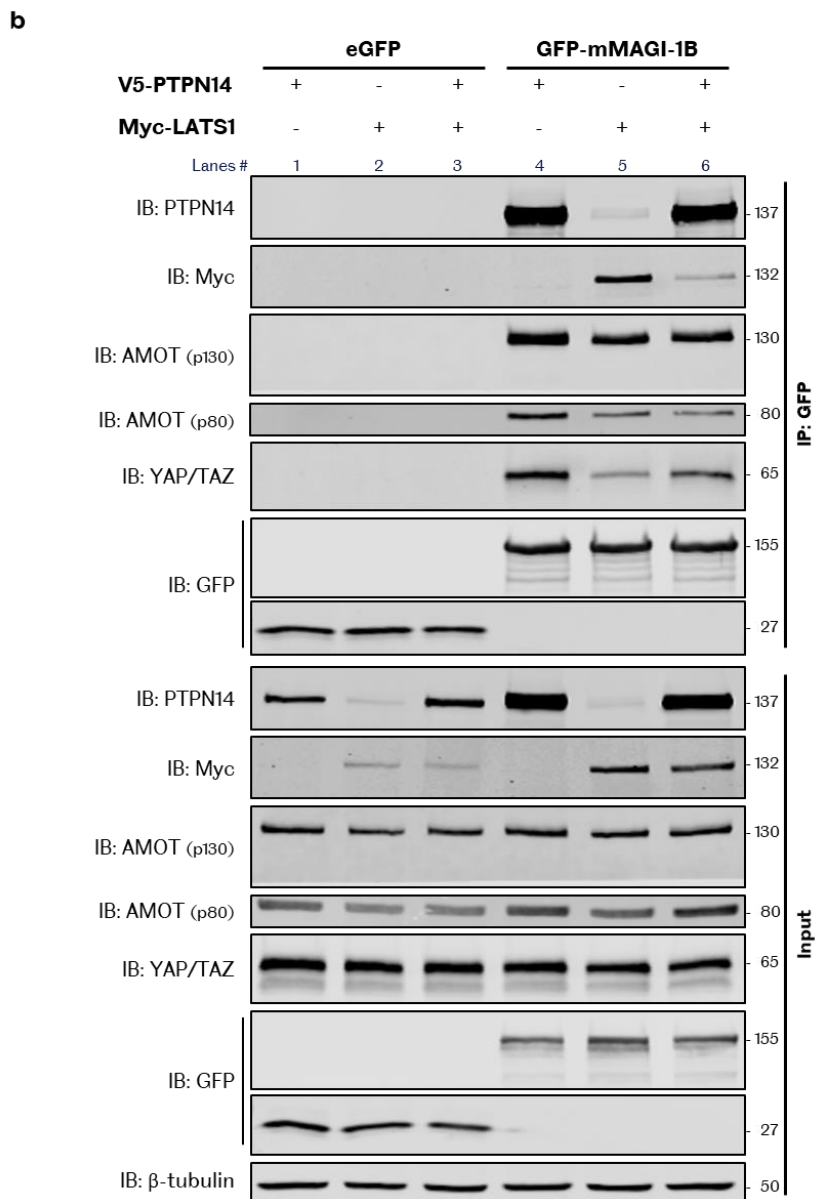
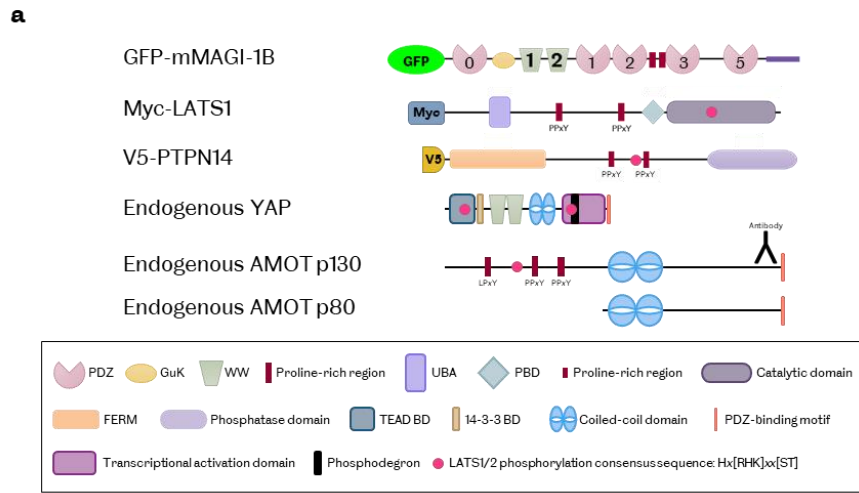


Figure 4.17 | AMOT proteins are part of mMAGI-1B complex, alongside LATS1/2, PTPN14 and YAP.

a, mMAGI-1B, LATS1 and PTPN14 constructs used in this figure. Details on the constructs can be found in Chapter 2. Endogenous YAP and AMOTs protein-protein interaction domains. The antibody schematics approximately locates

the anti-AMOT epitope. PDZ: Repeat of 80-100 amino acids that was first identified in PSD-95/Dlg/ZO-1/2; GuK: Guanylate kinase domain; WW: Domain with two conserved tryptophan residues; UBA: Ubiquitin-associated domain; PDB: Protein binding domain. BD: binding domain; FERM: Named after 4.1, Ezrin, Radixin and Moesin proteins, this domain is involved in plasma membrane localisation of the protein. **b**, HEK293 cells were transiently co-transfected with GFP-mMAGI-1B, Myc-LATS1, and/or V5-PTPN14, as indicated. Cell lysates were subjected to GFP-trap® immunoprecipitation (IP) and western blotting (IB) as indicated. An empty vector (eGFP) was used as control. Protein expression levels are confirmed in the input fractions (1.5% of total cell lysates). Theoretical molecular weights are indicated in kDa on the right side of the western blots. Membranes were probed with an anti-AMOT antibody which recognises both AMOT isoforms (n=1). AMOT p130 and p80 isoforms are present in all pulldown complexes with mMAGI-1B (lanes 4-6).

or PTPN14. As AMOT possesses a PDZ-binding motif at its C-terminal, common to both isoforms, we could have reasonably expected to see an interaction with one of MAGI-1 numerous PDZ domains. However, we probed for AMOT in the mMAGI-1B/LATS mapping pulldown experiment and only found both of AMOT isoforms precipitated along with the FL MAGI-1 and the WW-domain construct, with LATS1/2, while none was detected in association with the PDZ-domain constructs (**Figure 4.11**). It therefore suggests that AMOT PDZ-binding motif is not able to interact with MAGI-1. The p80 isoform was therefore most likely precipitated indirectly. Our results thereby suggest that PTPN14, similarly to LATS1/2, can interact with both angiotensin isoforms but the binding site has not yet been elucidated and would require further investigation. To summarize, our data show that both angiotensin isoforms are part of the protein complex formed around mMAGI-1B.

4.3.4.4 *AMOT does not appear to be precipitated alongside MAGI-3.*

Next, we asked whether endogenous AMOT was also part of protein complexes with MAGI-3. To that end, we re-probed membranes from the previous pulldown experiments between MAGI-3 and either PTPN14 or the LATS kinases. Interestingly, neither of AMOT isoforms were found in the protein complexes precipitated with PTPN14 nor LATS1/2 and associated with MAGI-3 (**Figure 4.18a** and **Figure 4.18b** lanes 2 & 3). Our results therefore suggest that AMOT is not part of the complex forming around MAGI-3, unlike MAGI-1.

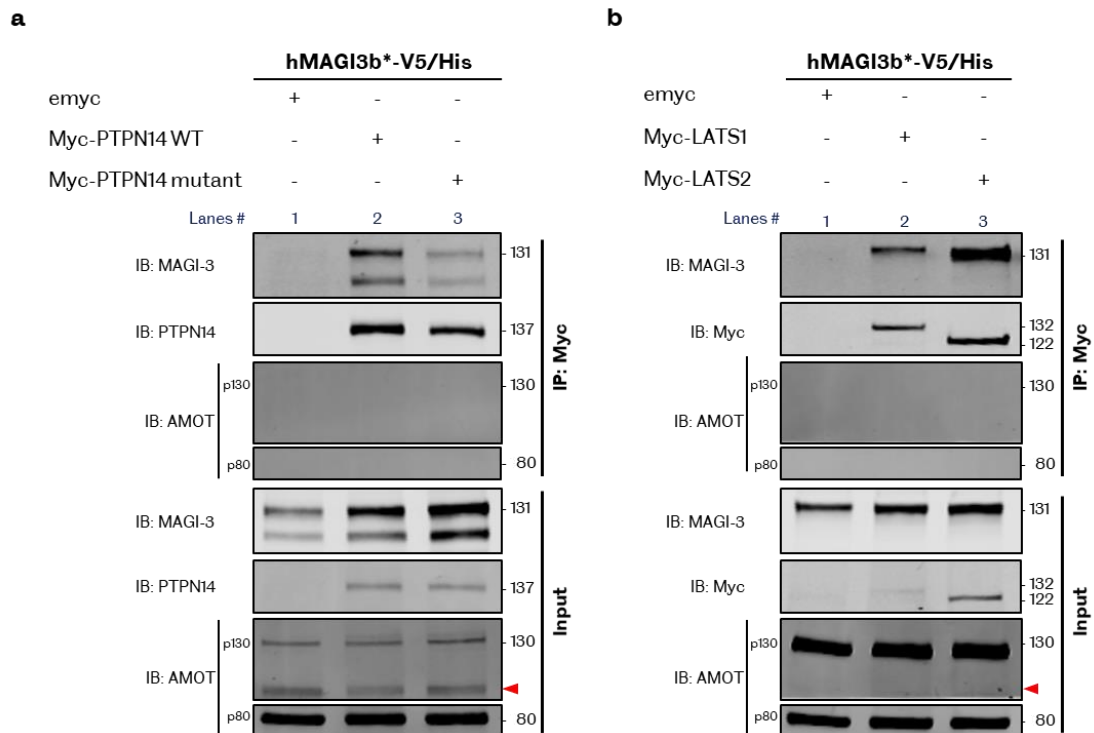


Figure 4.18 | AMOT was not detected in pull-down complexes in the presence of MAGI-3.

Same experiments and blots as **Figure 4.7b** and **Figure 4.14c**. In both cases, membranes were re-probed with an anti-AMOT antibody to detect endogenous AMOT. Theoretical molecular weights are indicated in kDa on the right side of the western blots. **a**, Co-immunoprecipitation experiment, in HEK293 cells, of hMAGI3b*-V5/His with Myc-PTPN14 WT or PPxY mutant using Myc-trap[®] resin (n=1). The angiominin isoform p130 appears much less abundant. The red arrowhead designates an extra band appearing just above 100kDa marker in this experiment. **b**, Co-immunoprecipitation experiment, in HEK293 cells, of hMAGI3b*-V5/His with Myc-LATS1 or Myc-LATS2 using Myc-trap[®] resin (n=1).

4.3.5 MAGI-1 localises with its binding partners at tight junctions

We have shown that MAGI-1 interacts with key players of the Hippo-YAP pathway: PTPN14, LATS1/2 and YAP itself. In addition, we have some evidence that all the aforementioned proteins localise at the cell-cell contacts in DLD-1 WT cells (**Figure 4.6**, **Figure 4.9** and **Figure 4.13**). MAGI-1 being a tight junction protein, we hypothesised that it acts as a scaffolding protein to assemble part of the Hippo cascade at the tight junctions. To test that hypothesis and rule out the role of the endogenous MAGI-1 in the membrane localisation of its binding partners, we used the generated MAGI-1 knockout clone G2 14 (B) and endogenous ZO-1 as a tight junction marker.

4.3.5.1 MAGI-1 is recruiting PTPN14 to tight junctions

First, we investigated the localisation of PTPN14. G2 14 cells were transiently transfected with Myc-PTPN14 alone or together with EGFP-hMAGI-1C β 1. Immunostaining was performed with anti-PTPN14 and anti-ZO-1 antibodies. We found that PTPN14 did not colocalise with ZO-1 at tight junctions in cells lacking MAGI-1 (**Figure 4.19a**). However, in MAGI-1 overexpressing cells, PTPN14 was enriched at tight junctions and colocalising with ZO-1 and MAGI-1. Our results indicate that MAGI-1 is recruiting PTPN14 to tight junctions.

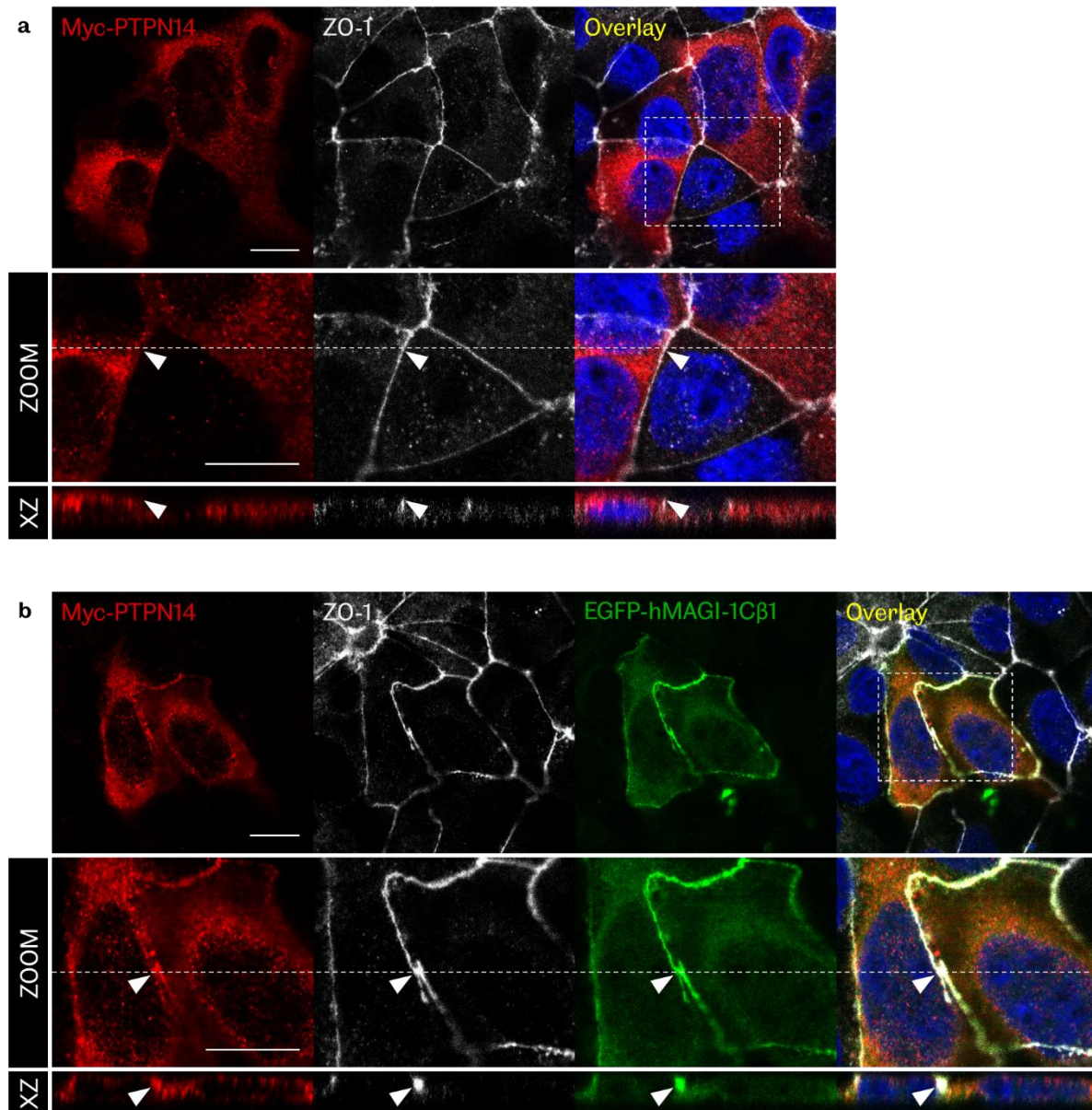


Figure 4.19 | PTPN14 is recruited to tight junctions by MAGI-1.

DLD-1 MAGI-1 knockout cells, clone G2 14 (B), were transiently transfected with Myc-PTPN14 alone or with EGFP-hMAGI-1C β 1 (n=1). Anti-PTPN14 and anti-ZO-1 immunostaining was performed. Z-stacks images were acquired with a confocal microscope. Hoechst was used as a nuclear counterstain. Scale bars: 10 μ m. The 'ZOOM' images correspond to the area delineated by the dotted white box. The XZ views were taken along the dotted line. The

white arrowheads point at ZO-1-positive tight junctions. **a**, In MAGI-1 knockout cells, PTPN14 is overall cytoplasmic and is not enriched at tight junctions (as indicated by the arrowhead in the XZ view). **b**, Upon overexpression of MAGI-1, PTPN14 is enriched at the tight junctions indicating that MAGI-1 is involved in PTPN14 recruitment.

4.3.5.2 YAP is enriched at tight junctions regardless of MAGI-1 expression

Second, we looked whether the YAP pool localised at the cell-cell contacts early on (**Figure 3.1** and **Figure 4.9**) was MAGI-1 dependent. G2 14 were transiently transfected with EGFP-hMAGI-1C β 1. Anti-YAP and anti-ZO-1 immunostaining was performed to detect the endogenous proteins. YAP was found to be enriched at ZO-1 positive tight junctions regardless of MAGI-1 expression (**Figure 4.20**). Our results indicate that MAGI-1 is not necessary to target YAP to tight junctions.

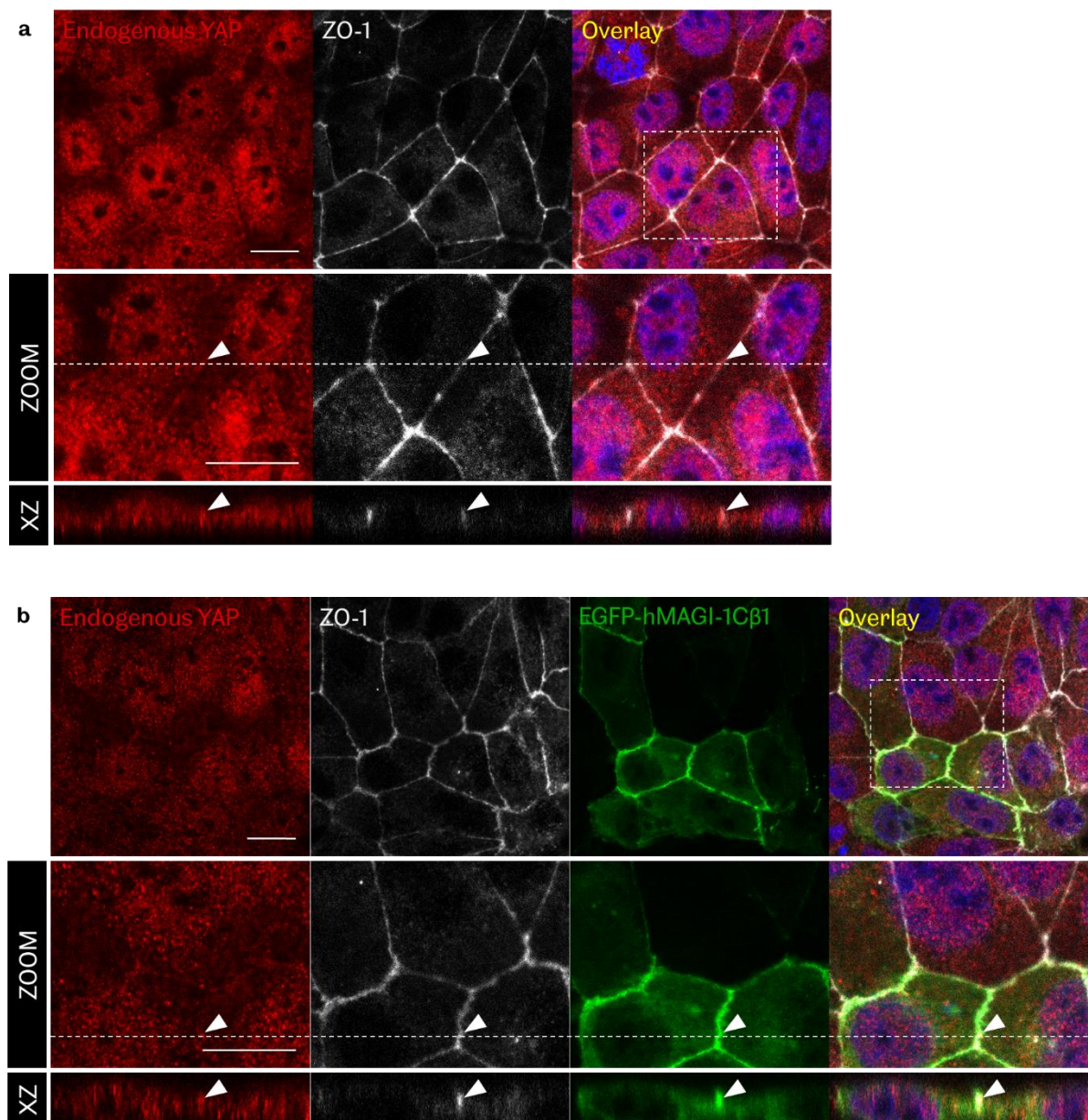
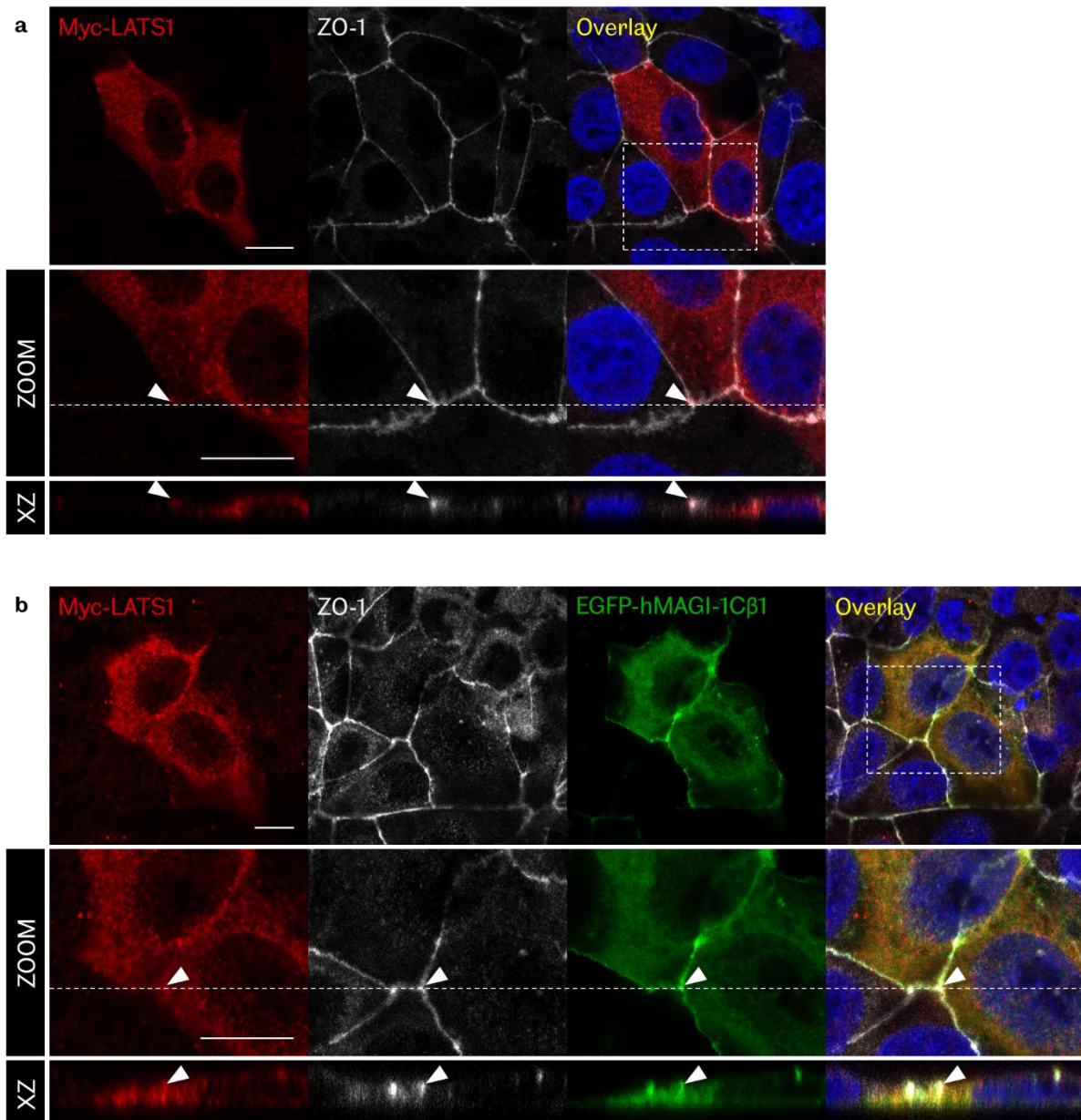


Figure 4.20 | YAP is enriched at the tight junctions regardless of MAGI-1 expression..

DLD-1 MAGI-1 knockout cells, clone G2 14 (B), were transiently transfected with EGFP-hMAGI-1C β 1 (n=1). Anti-YAP and anti-ZO-1 immunostaining was performed. Z-stacks images were acquired with a confocal microscope. Hoechst was used as a nuclear counterstain. Scale bars: 10 μ m. The 'ZOOM' images correspond to the area delineated by the dotted white box. The XZ views were taken along the dotted line. The white arrowheads point at ZO-1-positive tight junctions. YAP signal is enriched at the tight junctions regardless of MAGI-1 depletion (a) or overexpression (b).

4.3.5.3 MAGI-1 is recruiting both LATS kinases to tight junctions



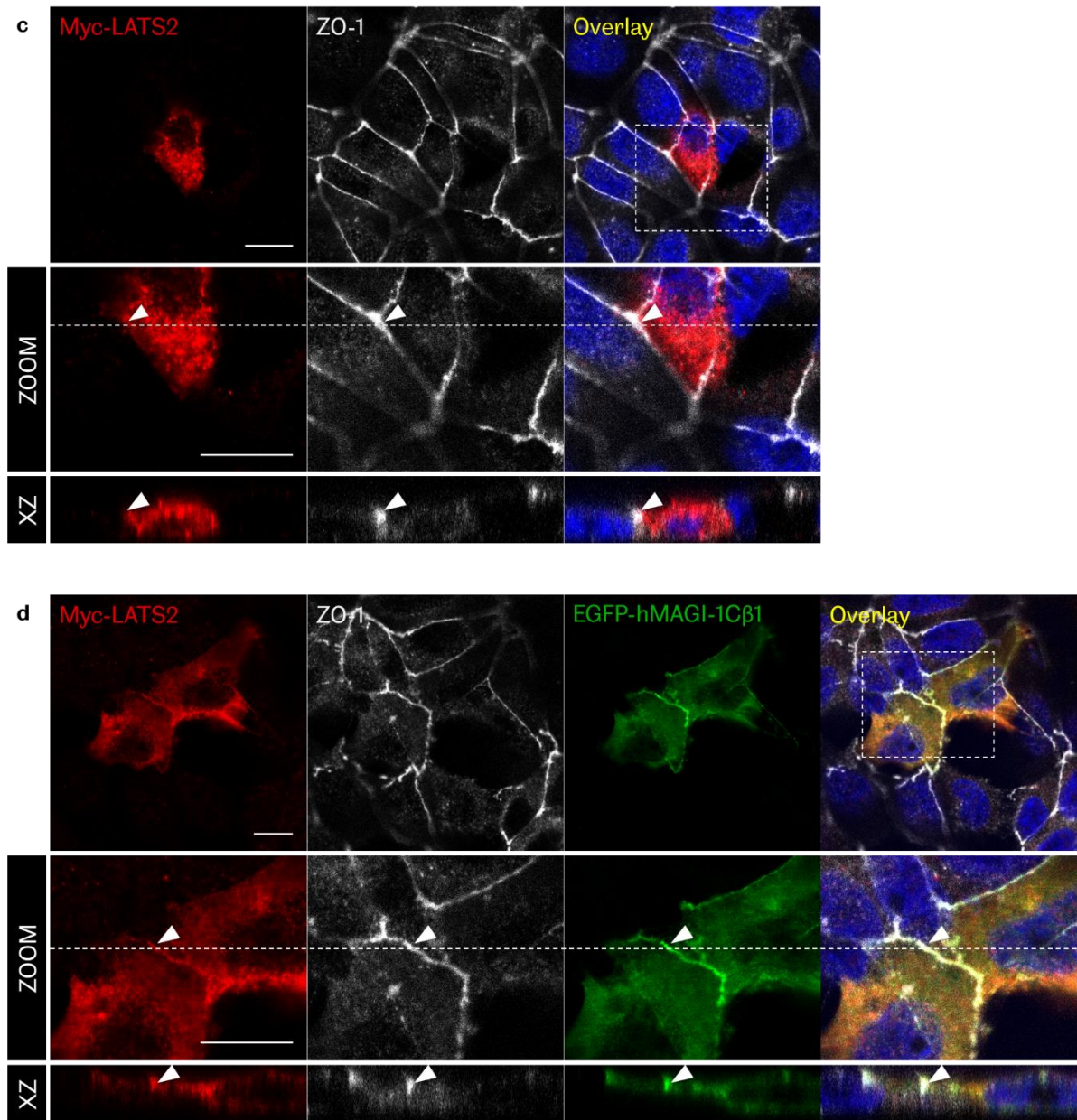


Figure 4.21 | LATS1/2 kinases are recruited to tight junctions by MAGI-1.

DLD-1 MAGI-1 knockout cells, clone G2 14 (B), were transiently transfected with either Myc-LATS1 or Myc-LATS2 alone or with EGFP-hMAGI-1C β 1 (n=1). Anti-Myc and anti-ZO-1 immunostaining was performed. Z-stacks images were acquired with a confocal microscope. Hoechst was used as a nuclear counterstain. Scale bars: 10 μ m. The 'ZOOM' images correspond to the area delineated by the dotted white box. The XZ views were taken along the dotted line. The white arrowheads point at ZO-1-positive tight junctions. **a**, In MAGI-1 knockout cells, LATS1 is faintly present at the membrane. **b**, Upon overexpression of MAGI-1, LATS1 becomes enriched at the tight junctions indicating that MAGI-1 is involved in LATS1 recruitment. **c**, In MAGI-1 knockout cells, LATS2 was completely absent from the membrane. **d**, Upon overexpression of MAGI-1, LATS2 is enriched at ZO-1 positive tight junctions, colocalising with EGFP-hMAGI-1C β 1.

Last, we asked whether the LATS kinases were also colocalising with MAGI-1 at tight junctions. G2 14 cells were transiently transfected with either Myc-LATS1 or Myc-LATS2 alone

or together with EGFP-hMAGI-1C β 1. Immunostaining was performed with anti-Myc and anti-ZO-1 antibodies. We found that neither LATS1 nor LATS2 was present at tight junctions in MAGI-1 knockout cells. However, overexpression of EGFP-hMAGI-1C β 1 resulted in enrichment of both kinases at ZO-1-positive tight junctions. Our data indicates that MAGI-1 is recruiting LATS1/2 at tight junctions.

4.3.5.4 AMOT is not expressed in colon cancer cell lines

We did not investigate the localisation of AMOT as this protein is not expressed in DLD-1 cells (**Figure 4.22**).

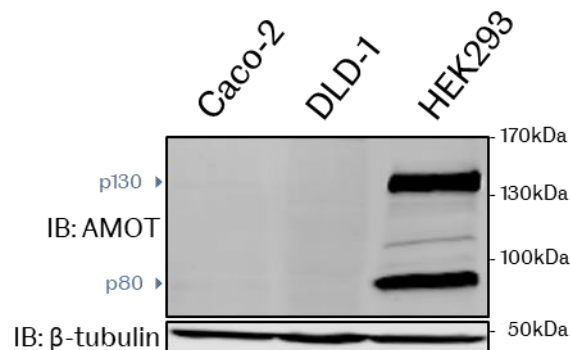


Figure 4.22 | AMOT is not expressed in DLD-1 cells.

Total protein was extracted from Caco-2, DLD-1 and HEK293 cells. Samples were subjected to anti-AMOT immunoblotting. β -tubulin was used as a loading control. The molecular weights indicated in kDa on the right side of the western blots correspond to the protein ladder. In HEK293 cells, both AMOT isoforms, p130 and p80, are abundantly expressed. AMOT is completely absent in colon cancer cell lines, Caco-2 and DLD-1.

Taken together, our immunofluorescence results indicate that MAGI-1 is involved in the recruitment of PTPN14 and LATS1/2 and colocalises with YAP at the tight junctions. Based on our biochemistry data, we hypothesise that this recruitment occurs by direct interaction of MAGI-1 with PTPN14 and LATS1/2.

4.4 Discussion

4.4.1 MAGI-1 interacts with key players of the Hippo pathway

4.4.1.1 *The WW domains, pivotal to mediate these interactions*

Using co-immunoprecipitation experiments, we confirmed and mapped interactions of MAGI-1 with key regulators of the Hippo pathway. We found that MAGI-1's WW domains played a pivotal role in mediating those interactions. WW domain-mediated complexes are abundant within the Hippo signalling pathway and these modules and their cognate binding motifs, [L/P]PxY, have drawn much attention in recent years (357). Indeed, such interaction modules offer a versatile platform, linking proteins to a physiologically relevant function. To add to the high modularity, researchers believe that tyrosine phosphorylation of either of the cognate domains can act as a negative switch for the interaction. For example, Chen et al. used a SPOTs peptide array to determine the binding requirements of the proline-rich region of WBP-1 to YAP's WW domains. They reported that phosphorylation of the tyrosine residue PPP_pY abrogated the interaction of WBP-1 with YAP *in vitro* (54). In addition, tyrosine residues within WW domains can also regulate binding with their cognate motifs. Li and co-workers reported that Tyr188 residue located within YAP WW1 domain played an important role in YAP regulation. Indeed, they suggested that phosphorylation of the Tyr188 was disrupting YAP interaction with its upstream negative regulators PTPN14 and LATS1/2 (358). This further suggests a critical role for tyrosine phosphorylation in the regulation of WW-containing proteins (359). However, not much is known about the tyrosine kinases that would control WW domain-mediated interactions. It is interesting to note that Nishimura et al. identified a tyrosine phosphorylation site (Tyr373) within MAGI-1 WW2 domain and suggested that it may regulate the binding properties of this domain (234). This particular tyrosine residue within MAGI-1 WW2 domain was later found to be dephosphorylated by the protein tyrosine phosphatase receptor z (Ptpz) (360). Although the functional significance of this phosphorylation site is not known yet, it is suggested to affect MAGI-1 binding properties. It would be interesting to investigate whether phosphorylation of this Tyr373 site regulates MAGI-1 interaction with the identified players of the Hippo pathway.

4.4.1.1.1 **MAGI-1 and PTPN14.**

We found that PTPN14 PPxY motifs were interacting with MAGI-1 WW domains, with a clear preference for WW1 (**Figure 4.23**). Moreover, our results suggested the presence of a second, minor, binding site between the two proteins, independent of the WW-PPxY

interaction. Apart from the WW1-2 domains constructs, no other part of MAGI-1, N-ter or C-ter individually, was sufficient to precipitate PTPN14 (**Figure 4.2b** lanes 3, 5 and 6). We therefore speculated that if a second binding site indeed existed, it required both N-ter and C-ter parts of MAGI-1 together, in a 3D conformation.

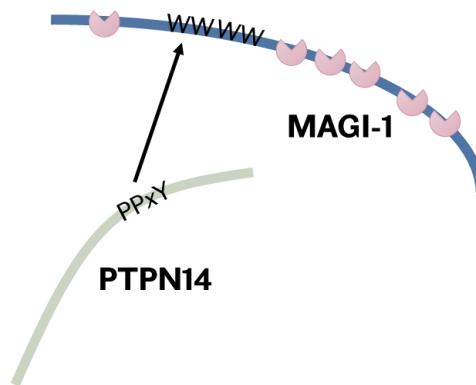


Figure 4.23 | MAGI-1 interacts with PTPN14.

PTPN14 possesses two PPxY motifs that interact with MAGI-1 WW domains, preferentially with WW1. Another, weaker, secondary binding site could not be ruled out.

4.4.1.1.2 MAGI-1 and LATS1/2.

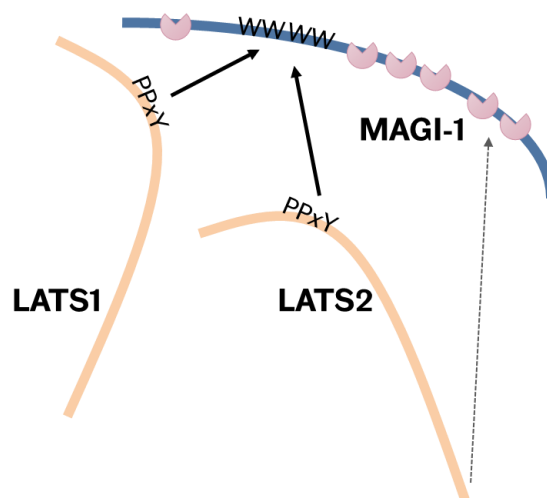


Figure 4.24 | MAGI-1 interacts with both LATS kinases.

LATS1 and LATS2 possess two and one PPxY motifs respectively, which interact with MAGI-1 WW domains (solid arrows). LATS2 C-ter may also interact with MAGI-1 PDZ3 or PDZ5 domains (dotted arrow).

We found that both LATS kinases were interacting with the WW domains of MAGI-1 (**Figure 4.24**). LATS1 and LATS2 possess two and one PPxY motifs, respectively. Such motifs are known to associate with WW domains. In addition, LATS2 seemed to show an affinity for MAGI-1 PDZ domains, especially those from the C-terminal constructs. If we analyse the last few amino acids of LATS2, we find the following sequence: CQPVYV which does not *per se*

correspond to any consensus sequence for a PDZ binding motif (361). However, several PDZ-domain proteins are listed in Biogrid as interactors of LATS2 alone, such as MPDZ, STXBP4 and ZO-1 (221).

LATS1 and LATS2 kinases, as paralogues, share very similar structures and thereby overlap on some of their basic functions. However, as we have found here, they display slight differences that demonstrates that the two kinases are not simply a genomic duplication. Each of them have unique characteristics which supports a more complex pathway with many more layers of regulation than in *Drosophila* for example.

4.4.1.1.3 mMAGI-1B versus hMAGI-1Cβ1.

Expression constructs derived from the mouse MAGI-1B protein were used for the characterisation and mapping of the interactions with PTPN14 and LATS1/2. Excluding alternatively split regions, the mouse and human MAGI-1 protein sequences share 95% identity. We have confirmed the conservation of the interaction of both PTPN14 and LATS1/2 with the human MAGI-Cβ1 version (**Figure 4.5b** and **Figure 4.12b** respectively). Slight differences were observed in the binding properties of the human and mouse MAGI-1 proteins. First, we found that the interaction with PTPN14 was less strong with hMAGI-1Cβ1 than with mMAGI-1B. Second, our results showed that, contrary to mMAGI-1B which displayed similar affinities for both kinases, the human hMAGI-1Cβ1 presented a stronger interaction with LATS1. The WW domains sequence is extremely well conserved between the two species. However, the linker region between the tandem WW domains is longer by 12 amino acids in the human form. This extra length might affect the 3D conformation and/or flexibility and affect the binding properties of the WW domains (**Figure 4.25**).



Figure 4.25 | hMAGI-1 WW domains are farther apart than in the mouse protein.

Protein alignment of mMAGI-1B and hMAGI-1Cβ WW domain-tandem regions. In the human protein, the linker region between the two WW domains is longer (12 amino acids), potentially allowing more flexibility to the structure.

4.4.1.1.4 MAGI-1 and AMOT.

Most of AMOT family members, AMOT p130, AMOTL1 and AMOTL2, have been reported to associate with MAGI-1 via its WW-domains (223,224). Here, we focused on angiominin isoforms p130 and p80. Surprisingly, we found that both AMOT isoforms were precipitated in

MAGI-1 protein complexes. AMOT p130 was reported to bind to MAGI-1 via a [L/P]PxY motifs–WW domains interaction (**Figure 4.26**) (224). However, the presence of AMOT p80 most likely resulted from an indirect interaction since Bratt and co-worker's found that due to its lack of [L/P]PxY motifs, this isoform was unable to bind to MAGI-1 (224).

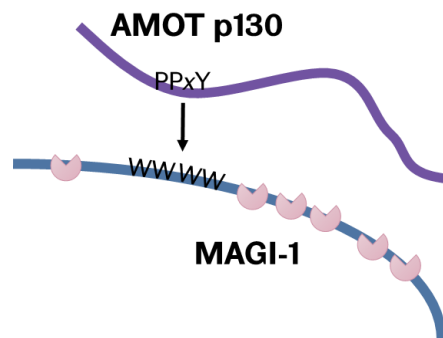


Figure 4.26 | MAGI-1 interacts with AMOT p130.

AMOT p130 possesses three [L/P]PxY motifs that interact with MAGI-1 WW domains (224).

4.4.1.2 *MAGI-1 interacts with the Hippo pathway downstream effector: YAP*

We found the Hippo pathway downstream effector, YAP, to be precipitated by MAGI-1, alongside PTPN14. As PTPN14 is a well-known interactor of YAP WW domains (71-75), we first thought that it was indirectly pulled-down by MAGI-1. Yet, YAP could still be precipitated regardless of PTPN14 overexpression or PPxY mutation (**Figure 4.4d** lanes 4 and 6), which had been reported to abolish their interaction (74). We therefore investigated whether there could be a direct interaction between MAGI-1 and the Hippo pathway downstream effector. Endogenous YAP presented the strongest affinity for mMAGI-1B C-ter2 construct harbouring PDZ3 and PDZ5 domains (**Figure 4.8b** lane 6), which had not been sufficient to precipitate PTPN14 (**Figure 4.2b** lane 6). From MAGI-1 and YAP domains, we identified two potential ways the proteins could interact in a direct manner: (1) mMAGI-1B possesses two LPxY motifs between its PDZ3 and PDZ5 domains that could bind to YAP WW domains, and (2) YAP has a PDZ-binding motif on its C-terminal tail which could interact with one of MAGI-1 PDZ domains. The first scenario is the less likely as these LPxY motifs are not conserved in the human form of the MAGI-1 protein. The second option, on the other hand, appears more likely. Indeed, a study reported the interaction of MAGI-3 last PDZ domain with YAP PDZ-binding motif (301). They had, before confirming the interaction by co-immunoprecipitation, utilized a computational predictor to screen YAP PDZ-binding motif against all human PDZ domains (362). MAGI-3 last PDZ domain was ranked first amongst the highest-scoring predicted interactors of YAP PDZ-binding domain; hMAGI-1 last PDZ domain, PDZ5, was ranked seventh.

Alignment of mMAGI-1, used in this thesis, and hMAGI-1, predicted by Ni and collaborators, PDZ5 domain protein sequences yielded 99% identity. Our results are in accordance with the prediction (301) and further suggest a legitimate direct interaction between MAGI-1 C-terminal PDZ domains and YAP (**Figure 4.27**).

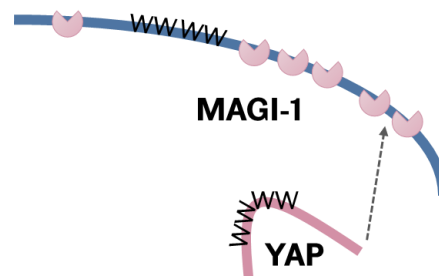


Figure 4.27 | MAGI-1 interacts with YAP.

YAP may interact with MAGI-1 PDZ5 via its C-terminal PDZ-binding motif.

4.4.1.3 *MAGI-1 and Kibra, differential upstream regulators of the Hippo-YAP pathway?*

As discussed previously, we have shown that both PTPN14 and LATS1/2 interact with mMAGI-1B WW domains. Interestingly, it has been reported in the literature that both PTPN14 and LATS1 are interacting with Kibra's WW domains. In addition, PTPN14 interacts with LATS1 C-terminus. Wilson et al. therefore suggested that PTPN14, LATS1 and Kibra form a trimeric complex as they did not find signs of competition for Kibra's WW domains (75). Moreover, AMOT p130, as well as AMOTL1 and AMOTL2, were identified as strong binding partners of Kibra, also called WWC1 (**Figure 4.28a**) (363). Collectively, MAGI-1 shares a lot of similarities with Kibra in terms of [L/P]PxY-containing binding partners: PTPN14, LATS1/2, AMOT p130, AMOTL1 and AMOTL2 (**Figure 4.28a & b**). The difference between Kibra and MAGI-1 resides in their other modular domains (**Figure 4.28c**). Indeed, MAGI-1 is a multi-PDZ domain protein that localises at tight junctions while Kibra is associated with apical domain and cell-cell junctions in epithelial cells (364). Such similarity in Hippo pathway binding partners and yet such distinct modular structures and cellular functions, led us to hypothesize that both proteins are regulators of the Hippo pathway but depending on the upstream signal, one complex preferentially forms.

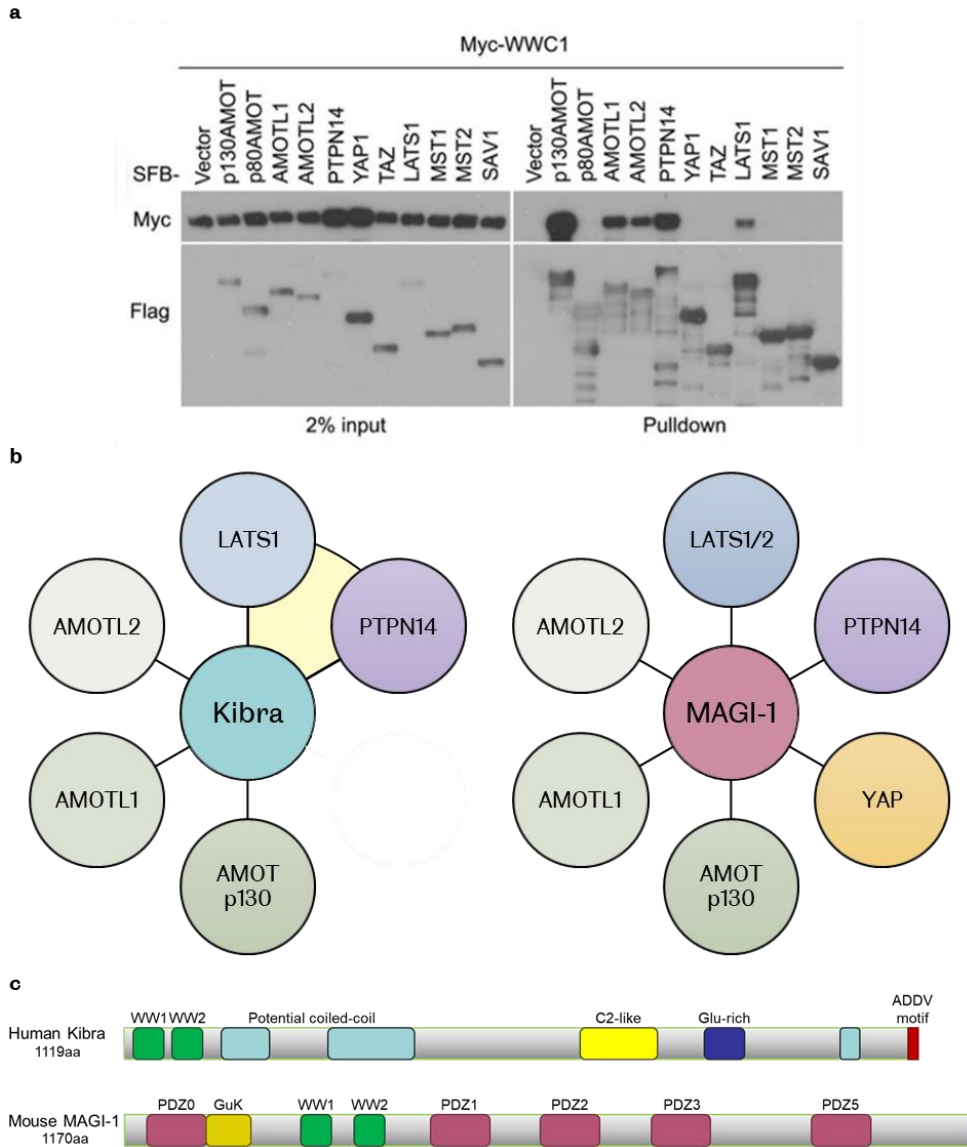


Figure 4.28 | Kibra (WWC1) shares many binding partners with MAGI-1 due to their tandem WW domains but have, otherwise, very different structures.

a, Figure 4B from (363). Pull-down experiment of Myc-WWC1, also known as Kibra, with the indicated proteins. The strongest affinity is demonstrated by AMOT p130. Kibra also interacts with the other members of the motin family, AMOTL1 and AMOTL2, with PTPN14 and LATS1. All the interacting proteins possess [L/P]PxY motifs. **b**, Comparison of Kibra and MAGI-1 Hippo pathway interacting networks. Kibra, LATS1 and PTPN14 form a tripartite complex (75). **c**, Modular structures of the Human Kibra and Mouse MAGI-1 proteins. Apart from their tandem WW domains, MAGI-1 and Kibra shared very little similarities in terms of other modular domains. Adapted from Figure 2 of (365).

4.4.2 MAGI-1 and MAGI-3 share the same Hippo pathway interactors

Signalling cascades such as the Hippo-YAP pathway have gotten more complex with evolution. Indeed, several players in the *Drosophila* pathway, for example Yorkie or Warts, have multiple homologues in the mammalian pathway: YAP/TAZ and LATS1/2 respectively. In

Drosophila Melanogaster, only one MAGI protein exists, while in human, it is a family of three members: MAGI-1, -2 and -3 (Flybase). All three human MAGI family members share high similarity of modular protein-protein interaction domains. Here, we investigated whether they also shared some of MAGI-1 binding network. Based on results obtained and discussed in Chapter 3, we focused exclusively our interaction study on MAGI-3.

Firstly, we have shown that MAGI-3 interacts with PTPN14 and that mutation of PTPN14 PPxY motifs greatly impaired the binding. We therefore hypothesise that, similarly to MAGI-1, MAGI-3 WW domains interact with PTPN14 PPxY motifs.

Secondly, our results show that both LATS kinases interact with MAGI-3, although LATS2 displayed a higher affinity. It appeared that after prolonged proximity with a set of proteins, potentially the LATS kinases, MAGI-3 may have been subjected to post-translational modifications. Since we were investigating the interaction with LATS1/2 which are kinases, we hypothesised that MAGI-3 might be one of their substrates. We looked for the LATS/NDR consensus sequence, Hx[RHK]xx[ST] (31), within the MAGI-3 protein sequence (Uniprot ID: Q5TCQ9) using the Protein Data Bank Protein Feature View. Unfortunately, no such consensus sequence was found. However, the following consensus sequence was identified, RxRxx[ST], about 70aa ahead of the first WW domain; it is known as the archetypal motif for Akt phosphorylation (366-368). Interestingly, MAGI-3 was reported to interact with PTEN and together regulate Akt (283), similarly to the other MAGI family members (227,253). The two consensus sequences are rather similar and Akt has been shown to phosphorylate YAP on Ser127 on an unusual sequence, corresponding to that of the LATS kinases: HxRxxS (33).

Thirdly, literature reports a direct interaction between MAGI-3 PDZ6 domain (numbered 1-6 as opposed to 0-5 for MAGI-1) and YAP C-terminal PDZ-binding motif. Moreover, Ni and co-workers investigated the regulatory role of MAGI-3 on YAP and found a truncated form of MAGI-3 protein in breast cancer cells. They encountered a new mechanism by which alteration of the mRNA can lead to the formation of an oncogenic dominant negative protein (301). Indeed, in MDA-MB-231 breast cancer cells, a portion of MAGI-3 mRNA was prematurely cleaved and polyadenylated, giving rise to a truncated form of the protein lacking the last four PDZ domains. That abnormal protein was no longer able to bind to YAP but could interact with its full length self, creating a dominant-negative complex unable to negatively regulate YAP activity. We did not detect this truncated version of MAGI-3 protein in any of the cell lines tested, Caco-2, DLD-1 and HEK293 (**Figure 3.10**).

Overall, MAGI-3 shares not only similarities with MAGI-1 in terms of modular structure but also in terms of Hippo pathway binding partners. **Figure 4.29** summarises the MAGI-3

interactions investigated in this chapter. These results further reinforce the bases for the potential existence of redundancy or of a compensatory mechanism between the members of the MAGI family (Chapter 3).

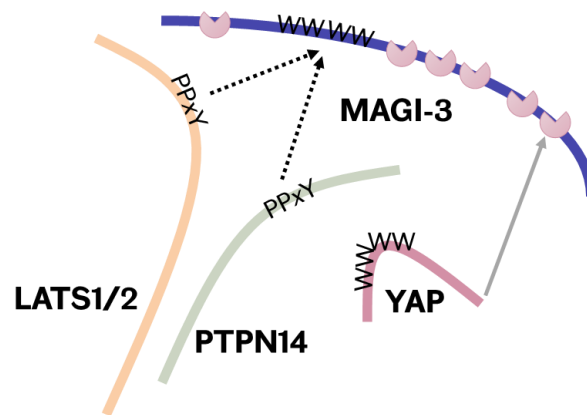


Figure 4.29 | MAGI-3 interacts with key players of the Hippo pathway.

PTPN14 and LATS1/2 interact with MAGI-3. Due to its similarities with MAGI-1, these interactions are probably mediated by MAGI-3 WW domains and cognate PPxY motifs (dotted arrows). YAP C-terminal domain interacts with MAGI-3 PDZ5 domain (301).

4.4.3 The MAGIs, scaffolding proteins, assembling part of the Hippo signal transduction machinery

4.4.3.1 *MAGI-1, a scaffolding protein, assembling PTPN14, LATS1/2, YAP and AMOT at tight junctions*

We have shown that MAGI-1 interacts with PTPN14, LATS1/2 and YAP individually. Literature reports another interactor of MAGI-1 WW domains: AMOT p130 (224). Since three of these Hippo pathway interactors bind to MAGI-1 WW domains, namely PTPN14, LATS1/2 and AMOT p130, we asked if there was competition over the binding. We performed triple pulldown experiments where MAGI-1, PTPN14 and/or LATS1/2 were overexpressed and MAGI-1 was used as bait. Endogenous YAP and AMOT presence was also checked in the pulled-down complexes. Our results combined to literature led us to believe that MAGI-1 is in a complex with all the aforementioned interactors.

Firstly, our results showed that the MAGI-1/PTPN14 interaction was stronger than the MAGI-1/LATS one. We found less LATS1/2 precipitated by MAGI-1 in the presence of PTPN14, while PTPN14 levels were unchanged, suggesting the occurrence of a partial competition (**Figure 4.15b** lanes 6 and 12). As mentioned previously, Wilson and co-workers reported a trimeric complex occurring between PTPN14, Kibra and LATS1. They found that Kibra is able to bind to PTPN14 and LATS1 PPxY motifs via its WW domains while PTPN14 interacts with

LATS1 via its C-terminal phosphatase domain (75). We hypothesise that a similar complex could form around MAGI-1, depending on the upstream signal.

Secondly, in our triple pulldown experiments, we found endogenous YAP present in all protein complexes, alongside PTPN14, LATS1/2 and AMOT. However, the levels precipitated varied depending on the other proteins overexpressed (**Figure 4.15b** and **Figure 4.17**). Indeed, the amount of YAP was greater when pulled-down with MAGI-1/PTPN14 than with MAGI-1/LATS. YAP is known to interact with PTPN14 (74), LATS1/2 (31,57-59) and AMOT p130 (138,139,369). All the aforementioned interactions are mediated by YAP WW domains. We could therefore imagine competition happening between MAGI-1 and YAP WW domains for the binding of PTPN14, LATS1/2 or AMOT's PPxY motifs. Yet, MAGI-1, being overexpressed, should prevail as we saw in MAGI-1/PTPN14 mapping (**Figure 4.4b** lane 4). The amount of YAP precipitated with MAGI-1/PTPN14 or MAGI-1/LATS, would therefore solely result from the direct interaction between MAGI-1 PDZ domains and YAP. However, this hypothesis does not explain the variability in the levels of pulled-down YAP. Since they are greater in the MAGI-1/PTPN14 pulldown lane, it suggests that YAP is pulled-down both in a direct and indirect manner, via MAGI-1 and PTPN14 respectively. We therefore hypothesise that MAGI-1, PTPN14 and YAP can be in a tripartite complex.

Thirdly, we detected both isoforms of AMOT in our protein complexes precipitated by MAGI-1 (**Figure 4.16** lanes 4-6). Angiomotin p130 has been reported to interact with MAGI-1 WW domains through its [L/P]PxY motifs. However, p80, lacking this N-terminal region, failed to bind to MAGI-1 (224). The shortest isoform was therefore most likely pulled-down indirectly, for example via PTPN14 or LATS1/2. AMOT was identified as a PTPN14-associated protein by tandem affinity purification and mass spectrometry analysis (74,356). Moreover, both p130 and p80 were reported to interact with LATS2. The study showed that both isoforms of AMOT antagonise each other over LATS2 activation and subsequent YAP phosphorylation (140). Based on Paramasivam and co-workers' results, we can hypothesise that our protein complex accommodates both AMOT isoforms that cancel each other out until an upstream signal determines whether to activate or inhibit the LATS-mediated Hippo pathway. We could therefore imagine a similar mechanism of differential regulation of PTPN14 by the AMOT isoforms.

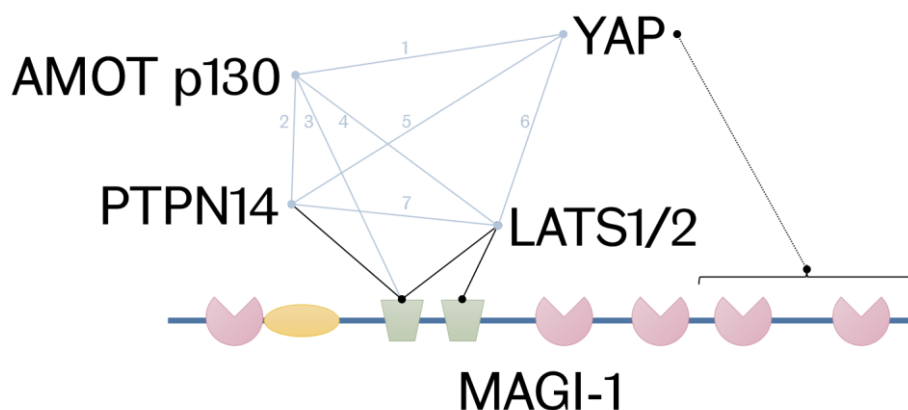


Figure 4.30 | Hippo multi-protein complex assembled around MAGI-1.

MAGI-1 interacts and might be in a complex with LATS1/2, PTPN14, AMOT and YAP. Black lines indicate the interaction identified (dotted) and mapped (solid) in this thesis chapter. Light blue lines represent the interactions reported in the literature. 1: AMOT/YAP – (138,139,369), 2: AMOT/PTPN14 – (74,356), 3: AMOTp130/MAGI-1 – (223,224), 4: AMOT/LATS – (96,140,221), 5: PTPN14/YAP – (71-75), 6: LATS/YAP – (31,57-59), 7: PTPN14/LATS – (75,221).

To summarise, all the proteins considered in this study interact with each other, as well as with MAGI-1 (**Figure 4.30**). Even though most of these proteins bind to its WW domains, we showed that MAGI-1 is able to oligomerise and could thereby accommodate several interactors at once. We suggest that MAGI-1 acts as a scaffolding protein, assembling PTPN14, LATS1/2, YAP and AMOT.

4.4.3.2 *MAGI-3, a scaffolding protein, assembling PTPN14, LATS1/2 and YAP*

The discussion around MAGI-3 is similar to the one for MAGI-1, as it regards the same pool of interactors: PTPN14, LATS1/2 (this study) and YAP (301). MAGI-3 was also reported to oligomerise by Ni and collaborators (301). However, AMOT was not found amongst the proteins pulled-down by PTPN14/MAGI-3 nor LATS/MAGI-3 (**Figure 4.18**). This was surprising as literature reports interaction of AMOT with at least LATS independently of MAGI-1 (140) and suggests interaction with PTPN14 (74,356). Moreover, due to the similarity between MAGI-1 and MAGI-3 modular structures as well as their WW domains binding partners (PTPN14 and LATS1/2), we could have expected MAGI-3 to interact with AMOT p130. Competition of AMOT with the Myc-tagged overexpressed proteins over MAGI-3 WW domains would not fully explain why AMOT p130 and p80 are not pulled-down via LATS or PTPN14 directly, similarly to what was happening with MAGI-1 (**Figure 4.17b**). Indeed, as far as the LATS kinases are concerned,

the binding sites for MAGI and AMOT are not overlapping. Paramasivam and co-workers reported that the first 307 amino-acids of LATS2 were required to bind AMOT's coiled-coil domain (140), while the PPxY motifs, needed for the MAGI interaction, are located at ~375aa and ~555aa for LATS1 and ~515aa for LATS2. In all previous pulldown experiments that were probed for endogenous AMOT, GFP-mMAGI-1B was the bait immobilised on the beads. In the present experiments, LATS (or PTPN14), with N-terminal Myc tags, were being used as baits. We can therefore speculate that the amino-termini of these bait-proteins were rather close to the beads and when MAGI3b*-V5/His binds to LATS PPxY motifs, it created steric hindrance and hid LATS N-termini from AMOT, and/or other putative interactors. With respect to PTPN14's pulldown complex, the same hypothesis could apply. However, the potential binding site is still unknown between PTPN14 and AMOT. Indeed, the interaction was only reported in proteomics screens and has not yet been confirmed nor mapped with co-immunoprecipitation experiments (74,356). To summarise, we suggest a similar complex assembling around MAGI-3 and involving several players of the Hippo pathway: PTPN14, LATS1/2 and YAP (**Figure 4.31**).

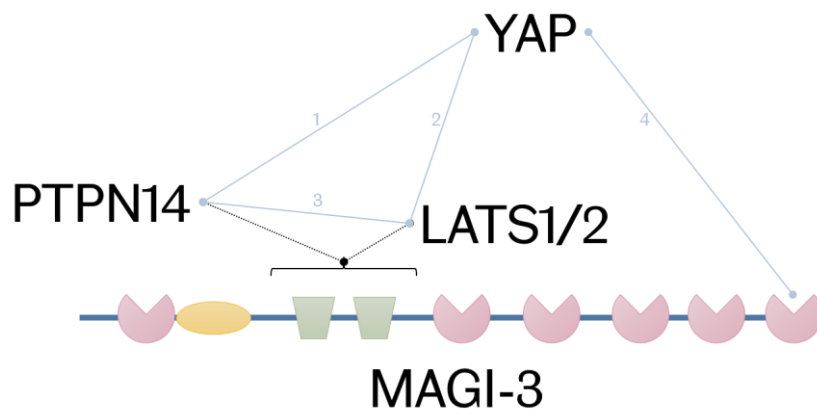


Figure 4.31 | Hippo multi-protein complex assembled around MAGI-3.

MAGI-3 interacts with LATS1/2, PTPN14 and YAP. Black dotted lines indicate the interactions identified in this thesis chapter; we hypothesise that they are mediated by MAGI-3 WW domains. Light blue lines represent the interactions reported in the literature. 1: PTPN14/YAP – (71-75), 2: LATS/YAP – (31,57-59), 3: PTPN14/LATS – (75,221), 4: YAP/MAGI-3 – (301).

4.4.3.3 MAGI proteins assemble part of Hippo cascade at tight junctions

In this chapter, we investigated the interaction networks of two members of the MAGI family, namely MAGI-1 and MAGI-3. We found that MAGI-1 WW domains were crucial to mediate

interactions with PTPN14 and the LATS kinases (**Figure 4.2b** and **Figure 4.11b** respectively). AMOT p130 isoform was reported to interact with MAGI-1 WW domains (223,224) and was detected in our protein complexes along with MAGI-1, PTPN14, LATS1/2 and YAP (**Figure 4.17**). In addition, our results suggest that YAP could bind to MAGI-1 PDZ5 domain (**Figure 4.8b**). This last PDZ domain is also the one binding to β -catenin and targeting MAGI-1 to cell-cell junctions. With so many protein-protein interaction domains, MAGI-1 is believed to act as a scaffold. Yet, in our study alone, we found four Hippo pathway proteins interacting with MAGI-1 WW domain, with little competition between them. We have evidenced that MAGI-1, as many multi-PDZ proteins (301,350-352), can oligomerise with itself and thereby allow different proteins to bind to its WW domains.

We found that all PTPN14, LATS1/2 and YAP were enriched at tight junctions upon overexpression of MAGI-1 (Section 4.3.5). Our results indicate that MAGI-1 is recruiting PTPN14, LATS1 and LATS2 to ZO-1 positive tight junctions. Indeed, the aforementioned binding partners were absent from apical cell-cell contacts in MAGI-1 knockout DLD-1 cells. Regarding YAP localisation, our data showed that YAP was enriched at tight junctions regardless of MAGI-1 expression. As Ni and co-workers reported interaction of MAGI-3 and YAP (301) and MAGI-3 is known to localise at tight junctions, we could hypothesise that YAP enrichment at tight junctions is partially governed by MAGI-3. Other proteins such as AMOT or ZO-2 are also believed to sequester YAP at tight junctions (69,76).

We showed that MAGI-3 could also interact with PTPN14 and LATS1/2 kinases (**Figure 4.7b** and **Figure 4.14** respectively). Ni et al. reported oligomerisation of MAGI-3 and interaction with YAP via its last domain (301). AMOT could not be detected in PTPN14 nor LATS complexes the presence of MAGI-3, potentially due to steric hindrance (**Figure 4.18**). It would be interesting to investigate the colocalisation of PTPN14, LATS1/2 and YAP in the MAGI1/MAGI3 double knockout cell lines generated in Chapter 3.

Our findings further establish MAGI-1 and MAGI-3 as potential regulators of the Hippo pathway. The fact that MAGI-1 and MAGI-3 share so many binding partners amongst the Hippo cascade further support a potential compensatory mechanism or redundancy among the MAGI family. We propose a model whereby the MAGIs act as scaffolds, bringing together part of the Hippo-YAP pathway machinery to the tight junctions (**Figure 4.32**) upon a given upstream signal.

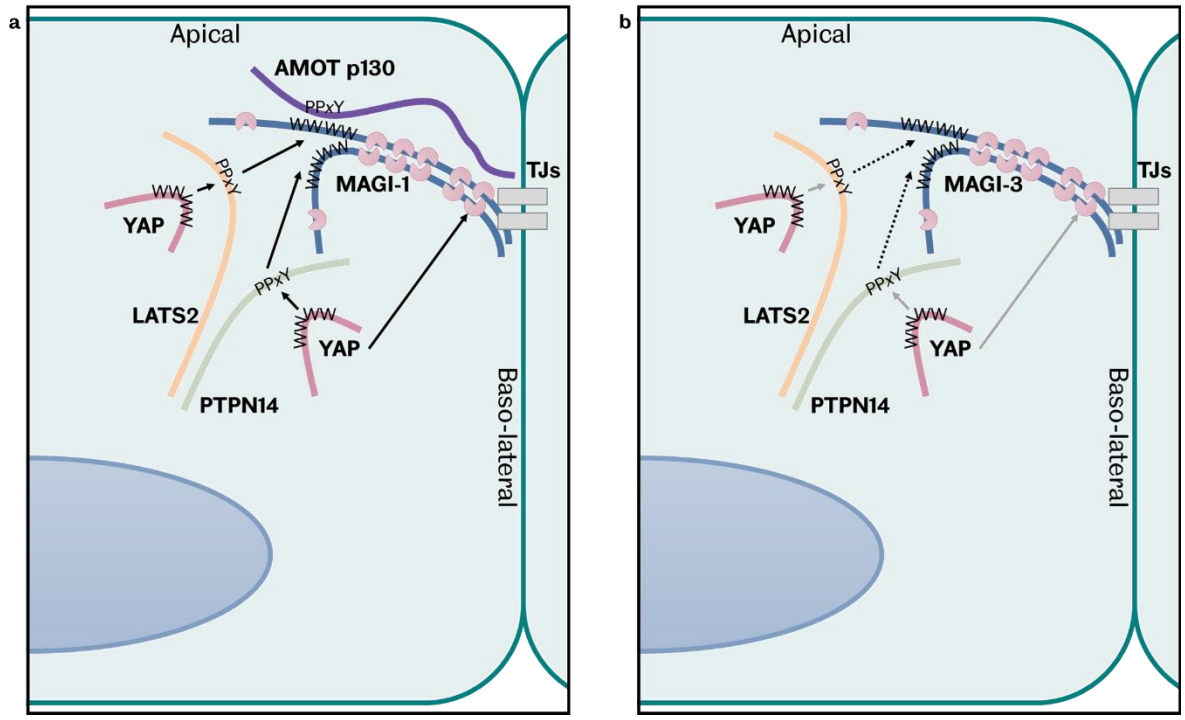


Figure 4.32 | MAGI proteins assemble part of the Hippo signal transduction machinery at the plasma membrane. Partial assembly of the Hippo-YAP pathway around MAGI-1 (a) and MAGI-3 (b). Dotted arrows indicate the speculated binding domains based on the similarity between MAGI-1 and MAGI-3. Grey arrows were used for YAP in the MAGI-3 complex as this was not directly evidenced by western blotting in this study.

5 Discussion and future perspectives

In this study, we provided new evidence that MAGI-1 and MAGI-3 proteins are involved in the regulation of YAP in response to cell density. We further established these scaffolding proteins within the Hippo pathway with a thorough biochemical analysis of their interacting networks. In the following discussion, we bring together our results and attempt to shed light on MAGI-1/3 mechanisms of regulation of the Hippo-YAP pathway.

5.1 WW domains at the centre of Hippo signal transduction

In the Hippo signalling pathway, there are four WW-containing proteins (excluding NEDD4 family of E3 ligases): KIBRA, SAV1, YAP and TAZ (44). Here, we report two other WW-domain containing proteins, namely MAGI-1 and MAGI-3, as regulators of the Hippo cascade.

We found that MAGI-1 WW-tandem interacts with the LATS kinases and PTPN14 PPxY motifs using co-immunoprecipitation experiments. Moreover, we showed that similar interactions were occurring between MAGI-3 and the aforementioned Hippo pathway players. MAGI-1 WW domains have also been previously reported to interact with the AMOT proteins (223,224). Taken together, three known regulators of the Hippo signalling pathway are binding to MAGI-1 WW-tandem. This strongly suggests that the WW-WW unit is pivotal for MAGI-1's role in the regulation of the Hippo-YAP pathway.

Interestingly, KIBRA and YAP have been reported to bind to PTPN14 (71-75), LATS1/2 (31,57-59,109,370) and AMOT (138,139,363,369) via WW-PPxY interaction. This raises the questions of specificity and cue: How can KIBRA, YAP and MAGI-1 all bind to the same subset of proteins from the Hippo pathway? What triggers favour one complex over the other?

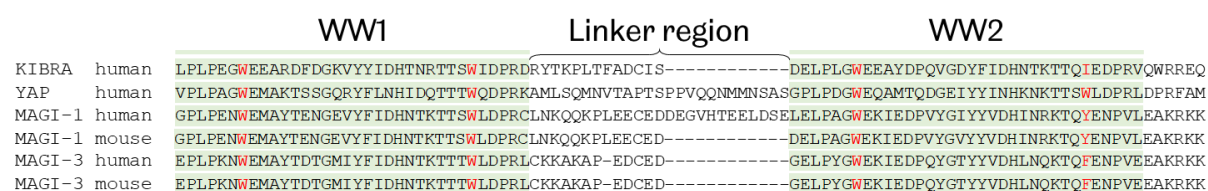


Figure 5.1 | Alignments of WW-tandems of the Hippo pathway

Alignment of the WW-tandem regions of KIBRA, YAP and MAGI-1/3 proteins. The characteristic tryptophan residues (or substitutes) are written in red. YAP and hMAGI-1 have a larger linker region that affect 3D conformation of the area and binding affinity (371).

A recent study published in BioRxiv (371) provided quantitative measurements of each of these interactions. Their isothermal titration calorimetry assays using purified WW-tandem

and PY motifs confirmed interaction of MAGI-1/3 with PTPN14 and LATS1/2. However, in contrast to our study, they showed that the PPxY motifs in PTPN14 contributed very little to these interactions. Indeed, the main binding site were two Φ PxY motifs (Φ = any uncharged amino acid) separated by three amino acids on PTPN14 ahead of the known PPxY consensus motifs. Discrepancies between our and their work, might arise from 3D native conformation and accessibility of the domains and motifs. Their findings are intriguing as they show that PTPN14 and LATS have a higher affinity for KIBRA and MAGI-3 WW-tandems than for YAP's or hMAGI-1's by at least an order of magnitude (K_d) due to the tandem conformation (**Figure 5.1**). They suggest that PTPN14 or the LATS kinases would primarily bind to KIBRA or MAGI-3 instead of YAP. Their study highlights that the system is extremely specific and sensitive to protein abundance. Additional work is needed to study the formation of the protein complexes under different conditions. However, given that many of the pathway interactions rely on the same WW-PPxY binding, it is challenging to use point mutations to investigate the role of one protein as this is bound to disrupt several interactions.

5.2 Regulation of the Hippo pathway by the MAGI proteins in response to cell density

MAGI-1 and MAGI-3 proteins have been reported to have reduced expression levels in colorectal cancer (252,289). Here, we investigated the effect of complete MAGI-1 and/or MAGI-3 knockout in a colorectal cancer cell line, DLD-1, with respect to the Hippo-YAP pathway. This particular cell line has been reported to have high levels of MAGI-1 protein (252,320). We found that YAP was abnormally accumulated in the nucleus in dense knockout cells, which usually correlates with its hyperactivity. However, levels of YAP Ser127 phosphorylation were similar to that in WT cells at high cell density. Interestingly, we observed that YAP pSer127 levels were decreased at medium density in cells lacking either or both aforementioned MAGI proteins. These results suggest a complex and 2-fold role of the MAGI proteins in the regulation of YAP.

As MAGI-1 was studied in more details in this work, we primarily discuss the role of MAGI-1 in the regulation of the Hippo-pathway.

5.2.1 Role of MAGI proteins in the early phase activation of the Hippo cascade upon cell density cue

First, the lower YAP pSer127 levels in cells cultured at medium density upon MAGI knockout denotes a defect in the Hippo-LATS cascade activation. We can therefore hypothesise that MAGIs, being tight junction proteins, are implicated in the early onset of Hippo pathway activation, potentially as soon as TJs are formed.

We found that MAGI-1 and MAGI-3 interact *in vitro* with PTPN14 and the LATS1/2 kinases via WW-PPxY binding. Moreover, our data suggest that MAGI-1, PTPN14, LATS1/2 and YAP are in a complex together, with little competition between PTPN14 and LATS. PTPN14 was reported to interact with LATS1, promote its activation, independently of the MST1/2 kinases, and subsequent phosphorylation of YAP Ser127 (75).

We found that MAGI-1 is implicated in PTPN14, LATS1 and LATS2 recruitment to ZO-1 positive tight junctions at medium density where they colocalise. Interestingly, translocation of the LATS kinases to the plasma membrane is reported to facilitate its phosphorylation and activation by the MST1/2–Sav1 complex (27) or by the MOB1A adaptor protein (26,372). Couzens et al. found PTPN14 in close proximity to the LATS kinases, MOB1A and MOB1B proteins (221). Taken together, these results suggest that MAGI-1, by recruiting PTPN14 and LATS at the plasma membrane, activate the Hippo-LATS cascade.

We hypothesise that, early on, when tight junctions start forming, MAGI-1 recruits PTPN14 and LATS1/2 at the TJs to promote LATS activation. In a progressive manner, LATS kinases phosphorylate YAP on the Ser127 residue which spatially prevents its interaction with the TEAD transcription factors as it unveils the 14-3-3 protein binding site for cytoplasmic retention.

We further speculate that in MAGI-1 depleted cells, this early onset of LATS activation does not occur. However, as density increases, other mechanisms, later on, activate the LATS kinases which catch up on YAP Ser127 phosphorylation. Amongst the proteins that have been reported to activate the Hippo-LATS cascade resulting in YAP inhibition upon density cues are the E-cadherin/ β -catenin complex (97), the AMOT family of proteins (76,96,143), PTPN14 (72,75), Kibra (75,109), ZO-2 (69) and Nf2 (27,188) together with the circumferential actin belt (66). Lack of MAGIs and the associated early onset activation of LATS results in a shift in density threshold for YAP nuclear exclusion. Taken together, this suggests that the MAGIs are assisted by other mechanisms in the cell density dependent Hippo pathway activation.

One of the outstanding question in the field, in front of the many reported junctional proteins involved in the activation of the signalling cascade, is whether these events occur in parallel or represent interdependent regulatory layers. At least some mechanisms must be interdependent otherwise depletion of a single of these proteins would not lead to such severe defects in the pathway activation. Our results suggest that activation of the LATS kinases, indirectly monitored by YAP pSer127 phosphorylation, requires a MAGI-dependent event followed by at least an additional mechanism, potentially involving any of the proteins mentioned above.

5.2.2 MAGI proteins implicated in YAP cytoplasmic retention

Our results showed that YAP pSer127 was inefficiently sequestered in the cytosol leading to an abnormal nuclear localisation in cells lacking one, the other or both MAGI-1/3 proteins. This led us to hypothesise that MAGI-1 is implicated in YAP cytoplasmic retention either directly or indirectly in dense cells.

1) Directly: We have shown that MAGI-1 and YAP colocalises at tight junctions, although MAGI-1 does not appear to be involved in YAP's recruitment. Yet, we have evidenced that MAGI-1 interacts with YAP in a PDZ-dependent manner. Ni and co-workers, reported an interaction between MAGI-3 last PDZ domain and YAP PDZ-binding motif. They showed that MAGI-3 was involved in the regulation of YAP cytoplasmic localisation through direct interaction in breast cancer cells and thereby acted as a tumour suppressor (301). However, they found that overexpression of MAGI-3 was sufficient to induce YAP cytoplasmic retention in HEK293 cells while our results show that it is not the case for MAGI-1. This points at distinct mechanisms of regulation of YAP for MAGI-1 and MAGI-3. It might explain the accentuated defect in YAP subcellular localisation we experienced in the MAGI1/MAGI3 double knockout cells, rather that it being due to a compensatory mechanism or redundancy. Although it might be through different mechanisms, both proteins are involved in the regulation of YAP subcellular localisation in response to cell density. As the interaction of YAP with the MAGIs is via its PDZ-binding motif, it is probable that it would occur regardless of the Ser127 phosphorylation status. This raises the question about the trigger for cytoplasmic retention which might occur upon post-translational modification of MAGI-1.

2) Indirectly: If considering an indirect regulation of YAP cytoplasmic retention by the MAGI proteins, it potentially implicates other known cytosolic anchors such as PTPN14 or AMOT. Our results suggested that MAGI-1 was increasing PTPN14 expression levels at high cell density. We hypothesised that it occurred through stabilisation of the protein. Thorough

investigation of this speculation is required and could not be done here due to time restriction. However, such a hypothesis is in line with our other results. If MAGI-1 indeed increases PTPN14 protein levels at high cell density, more PTPN14 molecules are available to activate LATS1 and sequester YAP in the cytoplasm. Interestingly, Wilson and collaborators found that PTPN14 was stabilising LATS1 (75). We can therefore hypothesise that MAGI-1 stabilises PTPN14 which in turns stabilises LATS1, ensuring activation and maintenance of activated Hippo pathway, as well as cytoplasmic retention of YAP, following a cell density trigger.

Based on the results from this work alone, we cannot conclude on the nature of the involvement of MAGI-1 in YAP cytoplasmic retention at high cell density. However, since we did not observe a defect of YAP cytoplasmic retention at medium density upon MAGI knockout, our findings suggest that it is regulated by different mechanisms at medium and high density pointing at the existence of an additional trigger or density threshold. The latter could be sensed by the surface area of each cell in a dense monolayer and thereby implicate the actin cytoskeleton as suggested by Aragona and colleagues (Section 1.2.2.3) (188).

5.2.3 Shape change, additional density trigger?

Colon epithelium is naturally columnar. When cell lines derived from such an epithelium are cultured *in vitro* in 2D, such as DLD-1, individual cells artificially go through three shapes that can be related to squamous, cuboidal and columnar with increasing cell density. Indeed, in an epithelial monolayer, contractile forces, exerted by the actomyosin cytoskeleton on the extracellular matrix, balance adhesion forces such as cell-cell or cell-matrix interactions (373). When density increases, intercellular adhesion prevails and induces a shape change, first from squamous to cuboidal and then from cuboidal to columnar. In the latter shape, cells are tall with a large lateral membrane and a higher expression of adhesion molecules (374,375) while the apical and basal domains are restricted. Each shape change triggers a rearrangement of the cytoskeleton (188).

In this work, the medium density condition corresponded to close-to cuboidal cells with established cell-cell junctions and polarisation of the ZO-1 protein at tight junctions (**Figure 4.19, Figure 4.20, Figure 4.21**). Several studies report that upon establishment of cell-cell contacts such as adherens junctions, the Hippo cascade is activated and YAP is driven out of the nucleus (80,94-97). Yet, in cells cultured at medium density, we and others find YAP distributed between nucleus and cytoplasm (**Figure 3.1**). Therefore, the presence of intercellular junctions and even apical-basal polarisation alone are not enough to induce

complete exclusion of YAP from the nucleus. It is possible that the effect of cell-cell contacts on the Hippo pathway is strongly increased with the establishment of more junctional complexes and a higher abundance of adhesion molecules as it is the case in columnar epithelial cells (374,375). The establishment of more cell-cell junctions, the spatial confinement or the reorganisation of the cytoskeleton, recapitulated in a shape change, with the increase in cell density could therefore constitute additional density triggers in YAP regulation.

One study, by Furukawa and collaborators, reports that contraction of the actin circumferential belt due to high cell density triggers YAP inhibition (66). This contraction could result from a shape change from cuboidal to columnar. Indeed, they found that increased tension between adjacent cells through contraction of the actin bundle, induced remodelling of the adherens junctions, releasing Merlin from its interactions with E-cadherin and F-actin. Merlin subsequently enters the nucleus and forces YAP to translocate to the cytoplasm (66) where it will be phosphorylated by the LATS kinases (8,31) if not already, and sequestered by cytoplasmic anchors such as 14-3-3 (8), PTPN14, AMOT (76-79), CRB (95) and potentially the MAGI proteins ((301) and this thesis).

Independently of cell-cell contacts, Dupont's and Aragona's teams found that single cells cultured on small adhesive areas, recapitulating the spatial confinement of high cell density, displayed cytoplasmic YAP (180,188). Their studies point at a mechanism regulating YAP subcellular localisation based on cell spreading and independent from junctional cues. They proposed a model of contact inhibition of proliferation in two steps: 1) junctional proteins activate the Hippo-LATS cascade upon establishment of cell-cell contacts resulting in YAP Ser127 phosphorylation and initiating its cytoplasmic retention, 2) as density continues to increase slowly, cells are confined to small areas which greatly limit their spreading ; the resulting remodelling of the actin cytoskeleton fully leads to YAP exclusion from the nucleus and growth arrest (188). The latter step most likely corresponds to a shape change, this time not driven by intercellular adhesions but by forced reduction of the cell's basal domain to match the substrate.

The part played by the junctional complexes in YAP regulation in 2D cultures is most likely progressive until a critical confinement of each individual cell is achieved. We speculate that this threshold is reached upon a shape change and remodelling of the cytoskeleton to columnar epithelium. Once it is reached, YAP is fully excluded from the nucleus.

5.2.4 Our model

Capitalising on our results and literature, we established a model of MAGI-1 regulation of the Hippo-YAP pathway which represents our hypotheses (**Figure 5.2**):

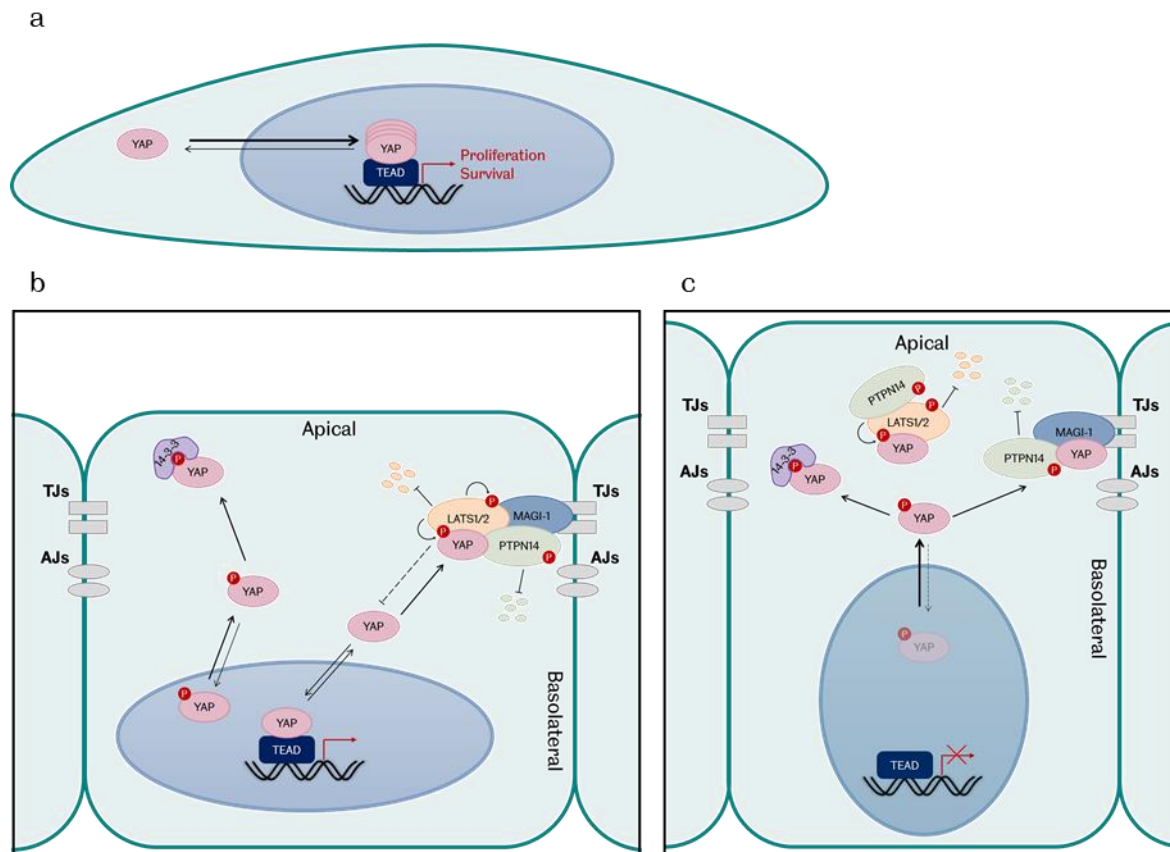


Figure 5.2 | Hypothetical view of MAGI-1 role in the regulation of the Hippo-YAP pathway

a. At low cell density, YAP shuttles between nucleus and cytoplasm but accumulates preferentially in the nucleus where it binds to transcription factors such as TEAD1-4 to promote cell proliferation and survival. **b.** When cells start establishing contacts with one another and upon a given density threshold, MAGI-1 recruits PTPN14 and the LATS kinases at tight junctions for activation. LATS, in turn phosphorylate YAP on its Ser127 residue which starts to affect the nucleocytoplasmic shuttling of YAP. The unphosphorylated YAP pool slowly gets depleted in favour of pYAP pSer127 which is retained in the cytoplasm by the 14-3-3 protein. **c.** In dense cells, most YAP molecules are phosphorylated and sequestered in the cytoplasm by 14-3-3, PTPN14 and other proteins. MAGI-1 stabilises PTPN14, thereby increasing its protein levels and ability to retain YAP in the cytoplasm. Moreover, PTPN14 in turns stabilises LATS1 (75).

1) Upon formation of tight junctions, MAGI-1 recruits PTPN14 and LATS1/2 kinases for an early onset activation of the Hippo cascade. Membrane localisation allows for activation of the LATS kinases through PTPN14 (75) which can subsequently phosphorylate YAP on its Ser127 residue. This step is progressive and features a pool of unphosphorylated YAP still capable to promote cell proliferation and a pool of phosphorylated Ser127 YAP being retained in the cytosol by the 14-3-3 protein (8,20,30,33).

2) As density increases, the space available for each cell decreases. The pool of phosphorylated YAP outweighs that of unphosphorylated YAP.

3) Upon a shape change to columnar epithelium or an additional trigger as discussed in Section 5.2.3, YAP is fully phosphorylated and sequestered in the cytoplasm by pSer127-dependent and independent mechanisms such as via 14-3-3, PTPN14 or AMOT.

MAGI-1 stabilises PTPN14 which in turns stabilises LATS1 ensuring continuous and sustained activity of the Hippo cascade to repress YAP activity.

Our results suggest several layers of regulation of YAP activity in response to cell density with multiple steps, all of which appear to be MAGI-1-dependent to some degree.

Based on the evidence collected in this thesis and information from the literature, we suggest that MAGI-1 and MAGI-3 both play a role in the regulation of YAP through partially overlapping functions.

5.2.5 MAGIs in colorectal cancer

The expression of MAGI proteins has been reported to be altered in cancer. For example, they are targeted and degraded by the human papillomavirus (240,261,262,264). In colorectal cancers, both MAGI-1 and MAGI-3 were found downregulated (252,289). Interestingly, NHERF2, a Na⁺/H⁺ exchanger regulatory factor and PDZ containing protein, was reported to oppose MAGI-3 for the binding of the lysophosphatidic acid receptor LPA₂. In colon adenocarcinoma, Lee and co-workers found NHERF2 levels upregulated, while MAGI-3 expression was lower than in healthy tissue (289); the NHERF2-LPA₂ interaction is therefore favoured and together they induce expression of COX2 (294) which is reported to, in turn, downregulate MAGI-1 expression (252). NHERF2 was described as an oncogenic protein and the blocking of its second PDZ domain with a small peptide reduced cancer cell proliferation (376). Interestingly, YAP was reported to interact with NHERF1 PDZ2 domain (377), NHERF2 ortholog, and found to bind with NHERF2 as well by several high throughput proteomic screens (221,222,344,378). It would be interesting to investigate whether NHERF2 interaction with YAP, combined with the NHERF2-dependent downregulation of several YAP negative regulators such as the MAGI-1/3 proteins (252,294) and PTPN14 (376), play a role in colorectal carcinogenesis or cancer progression.

5.3 Concluding remarks and future perspectives

In this thesis, we investigated the role of MAGI-1 and MAGI-3 proteins in the regulation of the Hippo-YAP pathway. We provided evidence that MAGI-1 and MAGI-3 are involved in controlling YAP subcellular localisation in response to cell density, both in the early onset of LATS activation and YAP cytoplasmic retention. In parallel, we further established MAGI-1 and MAGI-3 within the Hippo pathway by dissecting their interaction with several known players, namely PTPN14, LATS1/2 and YAP. We also showed colocalisation of MAGI-1 with these binding partners at tight junctions. Rescue of MAGI-1 expression was sufficient to recruit PTPN14 and the LATS kinases at tight junctions. Taken together, these results indicate a novel role of MAGI-1 in the Hippo pathway in relaying cell density cues to regulate YAP subcellular localisation and activity.

This work lays the foundations towards understanding the role of MAGI-1 within the Hippo signalling pathway in response to cell density cue. It provides insights on how signal transduction occurs between tight junctions and nucleus. We presented a novel layer of regulation of the Hippo-YAP pathway. MAGI-1 and MAGI-3 proteins have been reported to be downregulated in colorectal cancers which promotes migration and invasiveness, two hallmarks of metastasis (252,289). They therefore emerge as potential tumour-suppressors.

MAGIs are multi-PDZ domain scaffolding proteins, however, in this study, we report a role mainly mediated via their WW-tandem. It will be interesting to investigate the potential cross-talk between PDZ-binding and WW-binding proteins. Indeed, MAGI-1 PDZ-binding partners provide a link between tight junctions and RhoA, Wnt, Erk, Akt and Nf- κ B signalling pathways. MAGI proteins stand at the centre point, integrating and transducing signals from many different natures. They therefore present great potential as anti-cancerous therapeutic targets.

ANNEX 1: Generation of hMAGI-1Cβ1 cDNA using overlapping PCR

I. Overlapping PCR

Overlapping PCR is a technique used to assemble individual DNA fragments together. In this thesis, overlapping PCR was used to synthesize hMAGI-1Cβ1 (workflow shown in **Figure A. 1**).

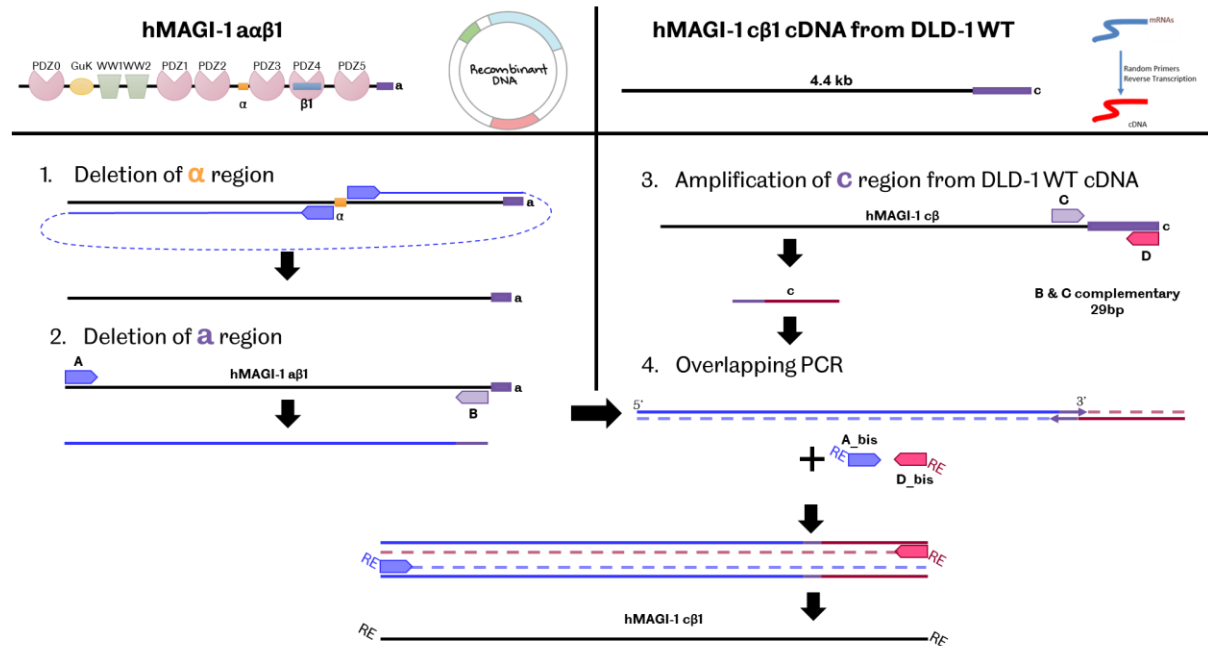


Figure A. 1 | Synthesis of hMAGI-1Cβ1 using overlapping PCR.

First, the α region was deleted from pFN21A HaloTag-hMAGI-1 Aαβ1 using Phusion® polymerase and primers #22 and #23 from **Table 2.5**. Then, hMAGI-1 β1 was amplified (excluding the C-terminal region A) using Phusion® polymerase (amplicon AB) and primers A (#24) and B (#26 from **Table 2.5**). In parallel, the C-terminal region C of hMAGI-1 Cβ was amplified from DLD-1 WT cDNA using GoTaq® polymerase (amplicon CD) and primers C (#27) and D (#28 from **Table 2.5**). Primers B and C are complementary over 29bp. As amplification with GoTaq® polymerase generates 3' end A overhangs, primer C was designed to start after a T base.

To assemble together the hMAGI-1 β1 (AB) and C-ter region C (CD) parts, overlapping PCR using Phusion® polymerase was performed. A mixture of 1:1 molar ratio of AB:CD was prepared in ddH₂O using the following formula:

$$ng\ of\ AB * \frac{length\ of\ CD\ (837bp)}{length\ of\ AB\ (3587bp)} = ng\ of\ CD$$

The PCR reaction mix, as described in **Table A. 1**, was prepared (without primers).

Table A. 1 | Reaction mix for Phusion® overlapping PCR.

Primers were added later.

Components	50µL reaction
5X Phusion Green HF Buffer	10µL
dNTPs (10mM)	1µL
Template DNA (1:1 molar ratio of AB:CD)	10ng AB + 2.3ng CD
DMSO	1.5µL
Phusion® High-Fidelity Polymerase (2U/µL) * Added last	0.5µL
ddH ₂ O	Up to 45µL

The overlapping 29bp of the AB and CD fragments were annealed and Phusion® polymerase created double stranded fragments (no amplification yet) using the following programme in a thermocycler:

- i. Heat lid to 110°C
- ii. Temp. 95.0°C for 3min – initial denaturation
- iii. Start cycle, 3x
 1. Temp. 95°C for 10s – denaturation step
 2. Temp. 60°C for 30s – annealing step
 3. Temp. 72°C for 30s/kb (2min) – extension step
- iv. Close cycle
- v. Hold at 8°C

Then, primers A_KpnI (#25) and D_EcoRI (#29 from **Table 2.5**), containing restriction sites, were added to the reaction mix (2.5µL namely 0.5µM final concentration each). Double stranded AD fragments were amplified by Phusion® polymerase using the following programme in a thermocycler:

- i. Heat lid to 110°C
- ii. Temp. 98.0°C for 30s – initial denaturation
- iii. Start cycle, 35x
 1. Temp. 98°C for 10s – denaturation step
 2. Temp. 68°C for 30s – annealing step
 3. Temp. 72°C for 30s/kb (2min30s) – extension step
- iv. Close cycle
- v. Temp. 72°C for 10min – final extension
- vi. Hold at 4°C

Finally, the AD PCR product was purified on an agarose gel before being subcloned with restriction enzymes into the desired vector, here pcDNA3.1(+) EGFP.

II. Site-directed mutagenesis

Site-directed mutagenesis is a common technique to introduce or correct point mutations in an expression vector.

Following hMAGI-1Cβ1 cloning in pcDNA3.1(+) EGFP vector and sequencing verification, a point mutation, 3635A>G - Glu1212Gly, was detected in the portion that had been amplified by the GoTaq® polymerase. This point mutation was corrected using the *QuikChange II XL Site-Directed Mutagenesis Kit* from Agilent Technologies and Pfu Ultra High-Fidelity DNA polymerase.

Table A. 2 | Reaction mix for mutagenesis.

Conversion of nanograms into picomoles of oligonucleotides was achieved using the following equation:

$$\frac{125\text{ng of oligo}}{330 * \# \text{ of bases in oligo}} * 1000 = X \text{ pmoles of oligonucleotide}$$

Components	Amounts
10X Reaction Buffer	5µL
dsDNA template (plasmid)	10ng
Forward primer	125ng
Reverse primer	125ng
dNTP mix (10mM)	1µL
QuickSolution	3µL
PfuUltra HF DNA Polymerase (2.5U/µL)	1µL
* Added last	
ddH ₂ O	Up to 50µL

First, mutagenesis primers #1 and #2 (**Table 2.6**) were designed using the QuickChange Primer Design Programme (www.agilent.com/genomics/qcpd). Both primers contained the desired mutation flanked by 15bp of correct DNA sequence and annealed to opposite strands of the plasmid. The melting temperature of the primer-pair should be ≥78°C. The following reaction described in **Table A. 2** was prepared and site-directed mutagenesis was carried out in a thermocycler using the following programme:

- a. Temp. 95°C for 1min – initial denaturation step
- b. Start cycles, 18x
 - i. Temp. 95°C for 50s – denaturation step
 - ii. Temp. 60°C for 50s – annealing step
 - iii. Temp. 68°C for min/kb (11min) – extension step

- c. Close cycle
- d. Temp. 68°C for 7min – final extension step
- e. Hold at 4°C (for at least 2min)

The parental methylated template was subsequently digested by the DpnI endonuclease by adding 1µL of DpnI enzyme (10U/µL) directly to the amplification reaction followed by an incubation of 1hr at 37°C. Mutated plasmids were then purified by column purification. Finally, the purified DNA was transformed into E. coli NovaBlue, isolated and verified by sequencing.

ANNEX 2: Supplement to **Figure 3.1** and **Figure 3.4**

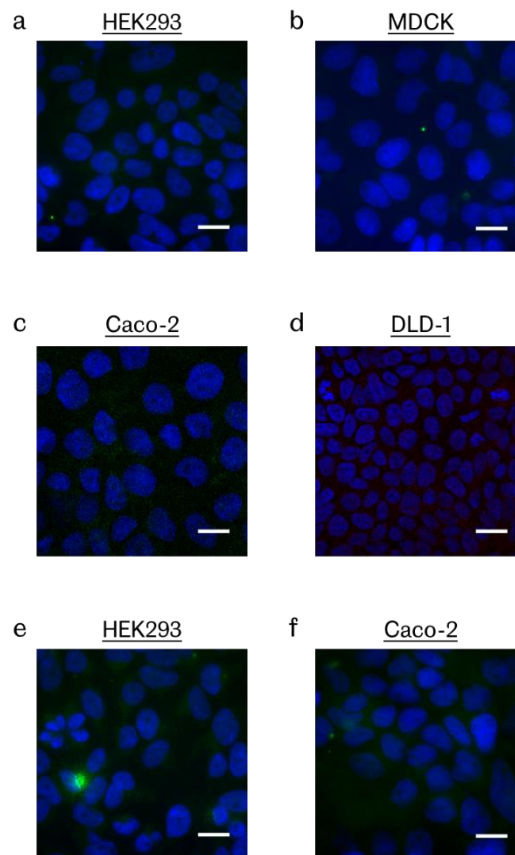


Figure A. 2 | Specificity of the YAP antibody for immunofluorescence

Immunofluorescence images showing the secondary-only controls.

Supplement to **Figure 3.1**: **a-c**, HEK293 (**a**), MDCK (**b**) and Caco-2 (**c**) cells were stained only with DAPI (blue) and the secondary antibody Goat anti-mouse IgG (H+L) Alexa Fluor® 488 (green) (**Table 2.4**). Images acquired with an epifluorescent microscope. Scale bars: 20µm. **d**, DLD-1 cells were stained only with Hoechst (blue) and the secondary antibody Donkey anti-mouse IgG (H+L) Alexa Fluor® 594 (red) (**Table 2.4**). Images were acquired with a confocal microscope. Scale bars: 20µm. Secondary antibodies tested do not give any unspecific staining indicating that the results presented in **Figure 3.1** reflect YAP/TAZ (Santa Cruz Biotechnology sc-101199, **Table 2.3**) subcellular localisation.

Supplement to **Figure 3.4**: HEK293 (**e**) and Caco-2 (**f**) cells were stained only with DAPI and the secondary antibody Donkey anti-rabbit IgG (H+L) Alexa Fluor® 488 (green) (**Table 2.4**). No unspecific staining was detected from the secondary antibody tested indicating that the results presented in **Figure 3.4** reflect YAP (Cell Signaling Technology #4912, **Table 2.3**) subcellular localisation.

ANNEX 3: Generation of MAGI2 single and MAGI1/MAGI2 double knockout in DLD-1 cells

I. Single guide RNA design for MAGI-2 knockout

We aimed, once again, at reaching a complete knockout of all MAGI-2 isoforms. Ensembl lists only two isoforms of the protein with an alternatively spliced Exon13. However, Hirao and co-workers found in CHO cells two alternative START codons yielding three isoforms that they denominated α , β and γ (**Figure A. 3**) (241). As even the shortest isoform, γ , still possesses the WW domains and PDZ domains, it is highly probable that it would conserve most of MAGI-2 full length interactions and function. We decided to design sgRNAs targeting Exon5 of the gene, after all potential alternative START codons. We selected two sgRNAs targeting MAGI-2 Exon5: G9 and G4 (**Figure A. 4 & Table A. 3**). G9 in the first half of Exon5 and G4 that coincided with the beginning of WW1 domain (**Figure A. 4**). A primer pair was designed to amplify the G9 and G4 targeted region, FWD9-4 and REV9-4 (#21 and #22 in **Table 2.7**). G9 and G4 were individually cloned into PX459-Cas9-Puro vectors.

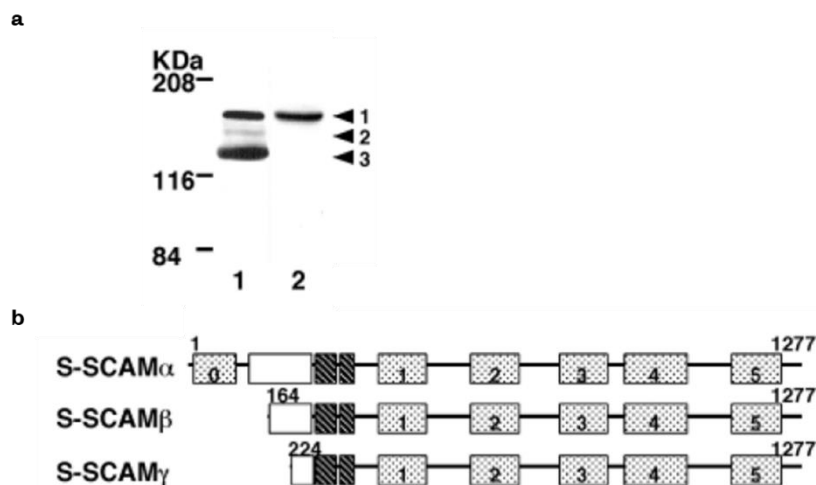


Figure A. 3 | Potential MAGI-2 alternative START codons and three isoforms.

Adapted from Figure 1 of (241). **a**, Immunoblot showing MAGI-2 in the synaptic plasma membrane fraction of CHO cells recognised either by an anti-WW (lane 1) or an anti-PDZ0 antibody (lane 2). **b**, Three MAGI-2 isoforms with two alternative START codons leading to proteins of 159, 140 and 134kDa (theoretical molecular weights). S-SCAM is an alternative name of MAGI-2.

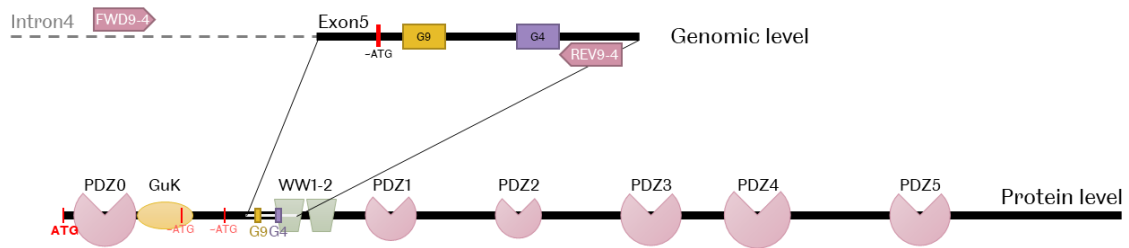


Figure A. 4 | Two sgRNAs targeting MAGI-2 Exon5.

Top. Schematic representation of the MAGI-2 targeted genomic region with associated sgRNAs, G9 and G4, and primer pair (FWD9-4 and REV9-4). **Bottom.** At the protein level, Exon5 codes for the part just before WW1 and almost spans the whole domain.

Table A. 3 | MAGI-2 sgRNAs targeting Exon5

Table recapitulating the two single guide RNAs selected to induce MAGI-2 knockout along with the primers designed to amplify the targeted region (illustrated in **Figure A. 4**). *Bbs*I site. Oligonucleotide numbers (#) refer to Table 2.9 (sgRNAs) and Table 2.7 (primers) of Chapter 0. (\Rev) indicates that G9 targets the reverse strand of DNA.

Single guide RNA	Targeted Sequence_PAM	Exonic off-targets
sgRNA9 (G9) (#5 & #6)	GGCTGACTGTACTGGTGC_AGG (\Rev) Top: 5' - CACCGGGCTGACTGTACTGGTGC - 3' Bottom: 5' - AACGCACCAGTGTACAGTCAGCC - 3' Duplex: 5' - CACCGGGCTGACTGTACTGGTGC - 3' 3' - CCCGACTGACATGTGACCACGCAA - 5'	DEPDC5 (NM_014662.5) CCTGCACCAGTATGAAGTCAGCA KCNN4 (NM_002250.3) CCAGCACCAGTGCCAGCCGGCC SGSM2 (NM_014853.3) CCTGCACCAGTCTGCAGAGAGCC PER1 (NM_002616.3) GGCTGACTGTTCACTGCTGCGGG EPHA10 (NM_001099439.2) CCTTGCCAGTGTCCAGTCAGCC FOXO3 (NM_001455.4) CCAGCAGCAGTCTCCTGTCAGCC KIF13B (NM_015254.4) GGCTGACTGCACCATGATGCGGG SMTNL1 (NM_001105565.2) GGCTGACTGTGCTCAGCTGCTGG ARHGEF38 (NM_001242729.2) GGCTTACTCCACACTTGTGCCGG
sgRNA4 (G4) (#7 & #8)	CAGACCCATTGCCTGATAAC_TGG Top: 5' - CACCGCAGACCCATTGCCTGATAAC - 3' Bottom: 5' - AACGTTATCAGGCAATGGGTCTGC - 3' Duplex:	/

	5' - CACCGCAGACCCATTGCCTGATAAC - 3' 3' - CGTCTGGGTAACGGACTATTGCAAA - 5'	
Sequences of primers to amplify the sgRNAs targeted region		
FWD9-4 (#21)	5' - GACGAGTGAAAGGAGAGCTCA - 3'	Intron4
REV9-4 (#22)	5' - CGCCCTTCTCTGTATAGGCC - 3'	Exon5

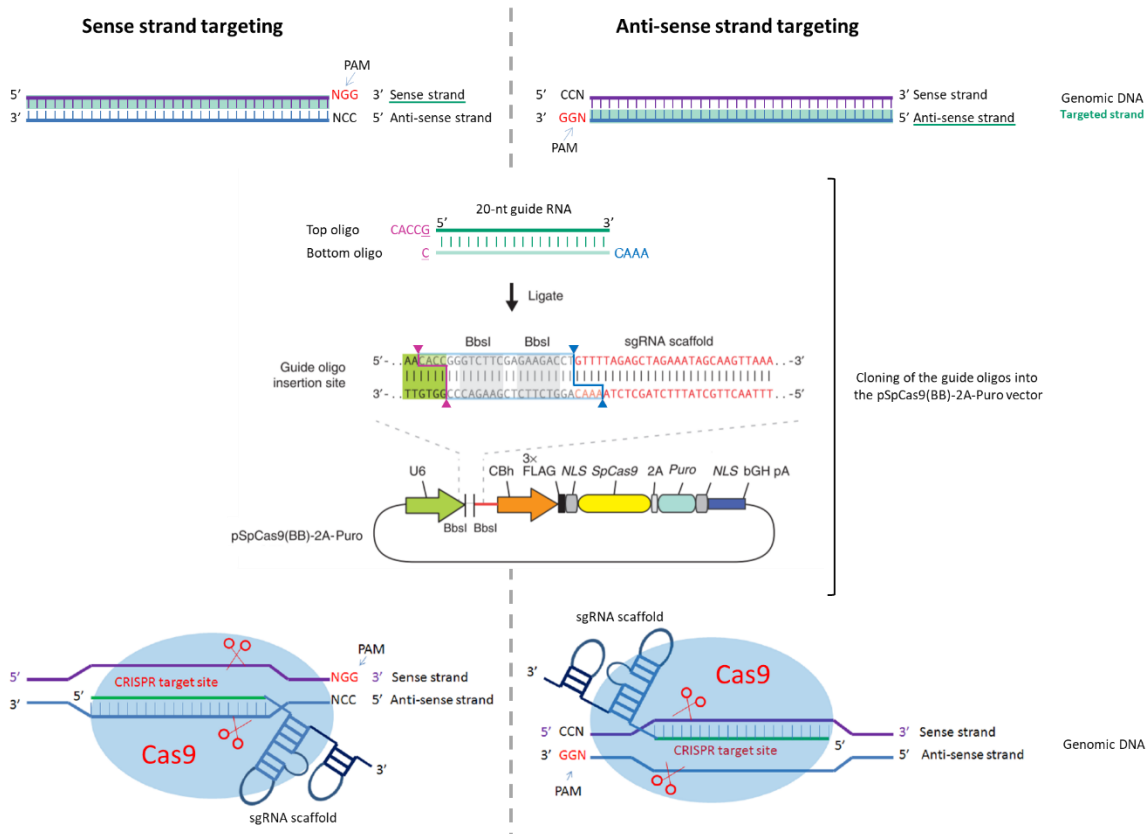


Figure A. 5 | Sense and anti-sense strand targeting and sgRNA oligo design.

sgRNAs predicted by the CRISPOR webtool can be targeting either the sense (Left) or the anti-sense (Right) strand of genomic DNA. The targeted sequence needs to be followed by a PAM motif (NGG). When cloning the sgRNAs into the Cas9 vector, the targeted sequence (either sense or anti-sense) becomes the Top oligo sequence (5' to 3') and the Bottom oligo is then the reverse complement. Both oligos are supplemented with the BbsI restriction sites to allow easy insertion in the recipient vector. The top strand of the sgRNA in the vector is directly followed by the sgRNA scaffold sequence which allows the Cas9 enzyme to dock and cut the targeted sequence approximately three nucleotides ahead of the PAM. Adapted from Figure 4 of (303) and Figure 2 of (379).

One of the selected guide, G9, was targeting the reverse strand of the genomic DNA. **Figure A. 5** shows how to design sgRNA targeting either the sense or the anti-sense strand of a target. In both cases, the targeted strand is the one containing the PAM motif (NGG). The top oligo then corresponds to the 5' to 3' sequence of the targeted region; the bottom oligo is the reverse complement. That way, once annealed and inserted into the Cas9 vector via BbsI

restriction sites, the targeted region is followed by the sgRNA scaffold that allow binding to the Cas9 enzyme.

II. Generation of MAGI-2 and MAGI1/MAGI2 knockout bulk populations

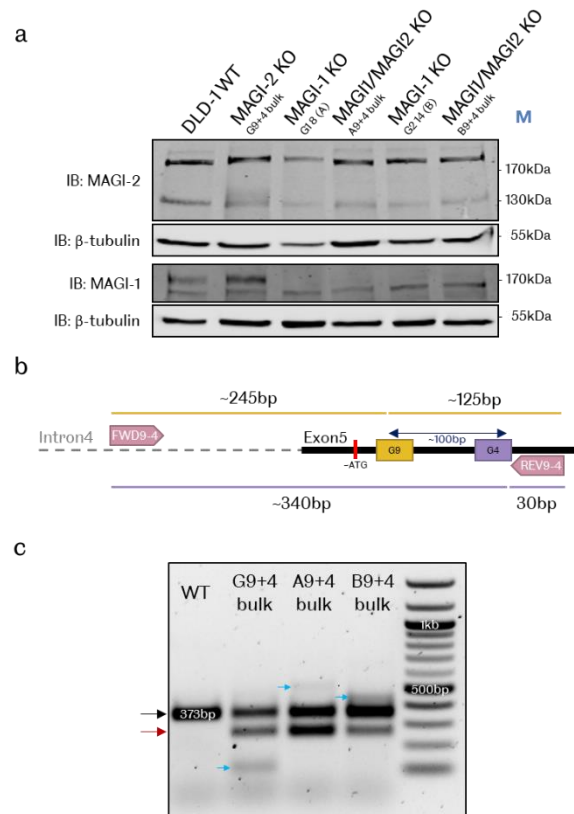


Figure A. 6 | Assessment of MAGI2 and MAGI1/MAGI2 bulk populations.

a, Western blot analysis of the MAGI-2 single and MAGI1/MAGI2 double KO bulk populations with the anti-MAGI-2 (m) antibody. It confirms that the MAGI-1 clones, A=G1 8 and B=G2 14, used to generate the subsequent cell populations, are still complete knockouts. On the other hand, the MAGI-2 antibody detects two bands that could correspond to the α and γ isoforms. However, the blot does not show much difference between the WT cells and the bulk populations. M = protein ladder. **b**, Schematic representation of G4 and G9 targeting Exon5 along with the 9-4 primer pair to amplify the targeted region. The total amplicon size is 373bp. The values indicated represent the predicted sizes of cleavage fragments by the T7 endonuclease enzyme. **c**, PCR products from DLD-1 WT cells, G9+4, A9+4 or B9+4 bulk populations, amplified with the 9-4 primer pair. The WT sample was used as a negative control and shows the complete PCR amplicon of 373bp (black arrow). The bulk populations, on the other hand, show multiple PCR products, with potential big insertions or deletions (red and blue arrows), suggesting good efficiency of the sgRNAs. The main lower band (red arrow) is present in all bulk populations and is approximately 100bp lower than the WT band. It could correspond to a deletion of the whole region between the two guides.

To improve efficiency, we used both G9 and G4 simultaneously. DLD-1 WT, G1 8 or G2 14 cells were co-transfected PX459-G9 and PX459-G4 vectors to obtain MAGI-2 single and MAGI1/MAGI2 double knockouts. The populations were denominated as follow: G9+4 for single

MAGI-2 KO, A9+4 and B9+4 for MAGI1/MAGI2 double KO obtained from G1 8 (A) and G2 14 (B) clones respectively.

Following Puromycin selection, proteins were extracted and samples were subjected to western blotting with an anti-MAGI-2 antibody (**Figure A. 6a**). The results obtained did not show much variation in the MAGI-2 presumed band between WT and bulk populations. The antibody used against MAGI-2 recognises the middle of Exon10, between PDZ1 and PDZ2 domains. One possibility would be that our guides are inefficient. The other possibility would be that the antibody is not specific, although it recognises two bands that could correspond with MAGI-2 α and γ isoforms. The third isoform, β , was much less abundant in Hirao and co-workers' study (241) and could be below the detection levels here.

To assess the gene-editing efficiency of G9 and G4 guides, we prepared samples for a T7 assay. Genomic DNA was extracted from DLD-1 WT and bulk populations and the targeted region was amplified by PCR using the 9-4 primer pair. When checking PCR products purity on agarose gel (**Figure A. 6c**), we already observed doublets and noticed that the lower band (other than the WT one – red arrow) was always the same size. We therefore hypothesised that since we used both guides simultaneously, a long fragment of approximately the distance between the two guides was removed in most cases. Products of other sizes were observed suggesting additional substantial indel mutations in the bulk populations. We did not proceed with a T7-assay as we would be comparing fragments of various sizes that would not be able to anneal properly. Analysis of the bulk populations at the genomic level revealed the introduction of substantial indel mutations at the site targeted by the CRISPR/Cas9 system. One hypothesis would be that the ~100bp-deletions evidenced were not inducing frameshifts and therefore did not affect protein synthesis.

III. Generation of isogenic clones from bulk populations

Despite the mixed results from the gene editing efficiency of the guides, we decided to sort the bulk populations into single cells. Having isogenic clones will allow better characterisation of the mutations induced and assess antibody specificity. G9+4, A9+4 and B9+4 bulk populations were sorted into single cells by FACS.

Clones were first screened by sequencing. **Figure A. 7** recapitulates the mutations of one validated genomic knockout clone per population. Proteins were then extracted from DLD-1 WT, G9+4 derived validated clones, G2 14 (B) and B9+4 10 clone. G9+4 3, 4, 8 and 12 all had the same genomic mutation and must have originated from the same cell during the

Puromycin selection. Once again, the top band recognised by MAGI-2 did not vary in intensity. Our western blot results were therefore inconclusive and pointed towards antibody unspecificity.

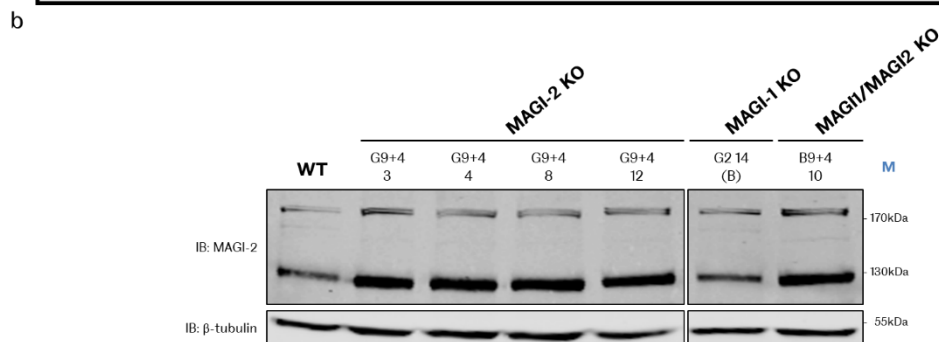
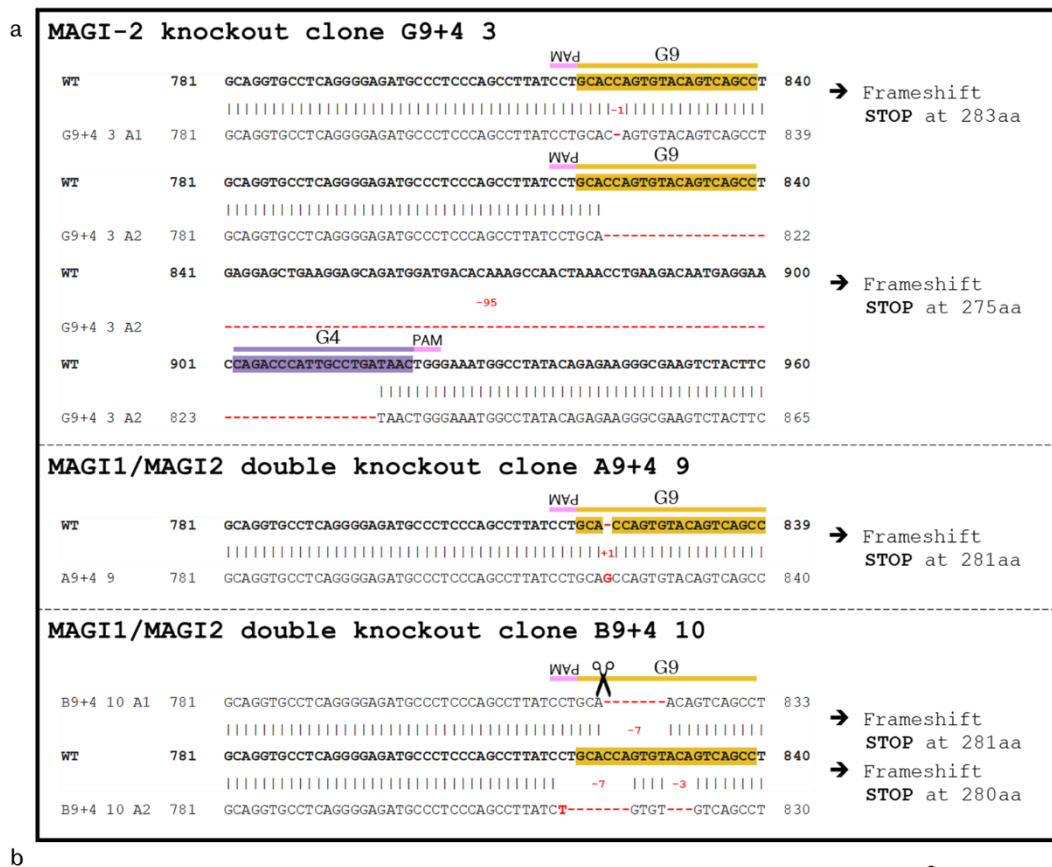


Figure A. 7 | Screening of MAGI-2 single and MAGI1/MAGI2 double knockout clones.

a. Sequencing results of MAGI-2 and MAGI1/MAGI2 clones. Alignment of the targeted region (Exon5) of the validated clones against WT sequence. A1 = allele 1, A2 = Allele 2, arbitrarily numbered. All frameshifts occur before the start of the first WW domain (302aa). **b.** Cells from clones validated at the genomic level were lysed and 60 μ g of total protein were run on an 8% PAGE. Western blot was performed and the membrane was detected with anti-MAGI-2 and anti- β -tubulin (loading control) antibodies. The bands that we considered as MAGI-2 are still present in the genomic KOs. M1 = MAGI-1, M2 = MAGI-2, KO = knockout. M = protein ladder, the molecular weights indicated correspond to the protein marker.

In parallel, we further tested the anti-MAGI-2 antibody using an HA-MAGI2 construct (Courtesy of Prof. Hall) and comparing the detection of the endogenous and overexpressed MAGI-2 proteins. HEK293 cells were transiently transfected with the HA-MAGI2 construct and proteins were extracted, alongside HEK293 untransfected cells. Samples were subjected to western blotting with anti-MAGI2 or anti-HA antibodies. This experiment confirmed that the band detected in the untransfected cells by the anti-MAGI2 antibody corresponded to the size of the HA-MAGI2 construct (**Figure A. 8c**, red dotted line). Indeed, molecular weight difference brought in by the HA tag is negligible (**Figure A. 8b**). These new results would tend toward specificity of the antibody contrary to the CRISPR results.

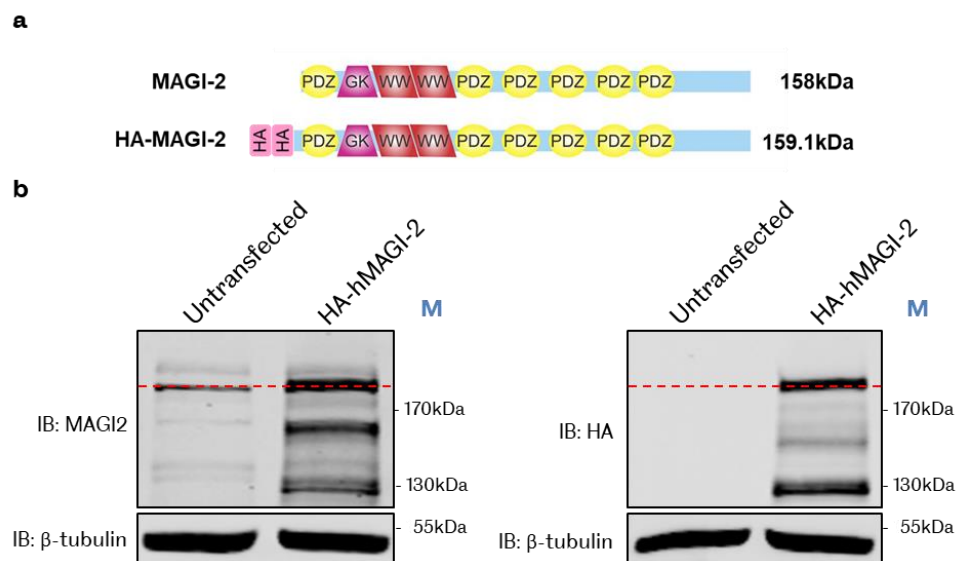


Figure A. 8 | MAGI-2 overexpression and antibody specificity.

a, Schematic representation of MAGI-2 full length and HA-tagged construct, kindly provided by Dr. Randy Hall. Adapted from Figure 1 of (380). **b**, HA-MAGI2 construct was transfected into HEK293 cells, followed by cell lysis 48hrs later. 60 μ g of total protein were loaded on an 8% PAGE. The membrane was probed with either anti-MAGI-2 (Left) or anti-HA (Right) antibodies and β -tubulin was used as loading control. The anti-MAGI2 antibody recognises something in the untransfected cells of the same size as the construct (red dotted line) that would most likely be the endogenous protein. M = protein ladder.

To summarise, we managed to identify MAGI2 single and MAGI1/MAGI2 double knockout clones at the genomic level but unfortunately, we were unable to confirm MAGI-2 KO at the protein level.

ANNEX 4: Proliferation and immunostaining in the OrganoPlate®

I. Balance between cell proliferation and cell death to maintain tubules

Before proceeding with functional assays, we aimed at monitoring cell growth and tubule maintenance of the various cell lines. MAGI-1, MAGI-3 and MAGI1/MAGI3 CRISPR knockout clones were cultured alongside DLD-1 WT cells in the OrganoPlate®.

First, we aimed at assessing the proportion of proliferating cells at an early (Day4) and relatively late stage (Day10) of the tubule using an EdU assay (Chapter 2 Section 2.2.8.4). Each cell line was seeded in triplicates in the first 3-lane OrganoPlate®. Six days later, the second plate was seeded in a similar manner, with triplicates of each cell lines. The EdU assay was performed simultaneously on both plates, on Day10 and Day4 respectively (**Figure A. 9**). This experiment was carried out once and therefore constitute preliminary data which are presented in **Figure A. 10**.

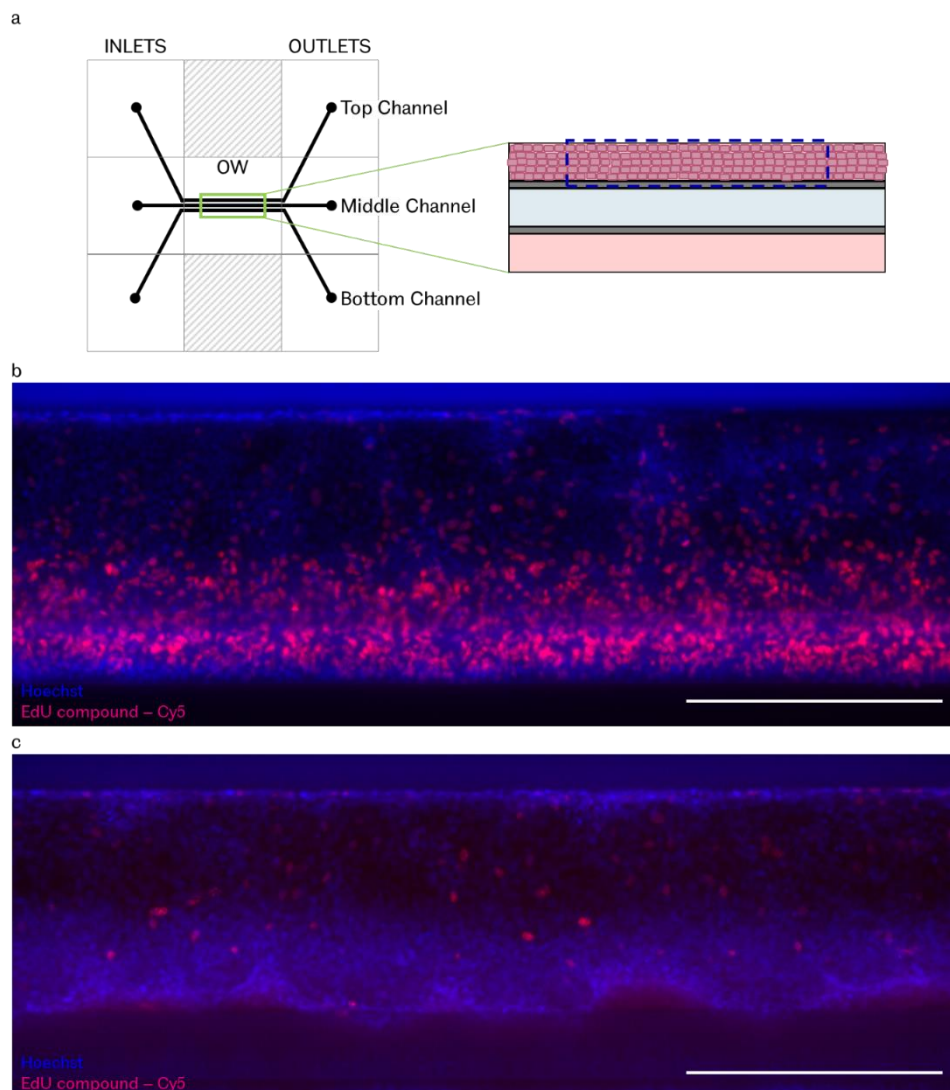


Figure A. 9 | EdU signal in DLD-1 WT tubules at early and late stage in 3-lane OrganoPlate®.

Example of fluorescent images following an EdU assay on DLD-1 WT tubule. **a.** 3-lane OrganoPlate® design. Samples were imaged through the Observation Window (OW – green box). During image processing, images were cropped to keep only the top channel containing cells (dotted blue box). **b & c.** DLD-1 WT tubule at Day4 (**b**) and Day10 (**c**). Sum projection of Z-stacks images acquired with a MolDev confocal microscope 20x objective after EdU assay. Hoechst was used as nuclear counterstain and EdU was conjugated to a Cy5 secondary antibody, represented in red here. Scale bars: 100µm. At Day4, many cells are proliferating while at Day10, in a relatively old tubule, very few still enter the cell cycle.

~ Number of nuclei per picture: We observed that the cell number in tubules at Day4 of culture was homogenous in MAGI knockout clones and DLD-1 WT. At Day10, the cell number seemed slightly more varied among samples (**Figure A. 10b**). As this assay was carried out on two independent plates, we can only carefully interpret the tendency between early and late stage tubules. Our preliminary data suggests that MAGI-3 KO might negatively affect cell number between Day4 and Day10. The MAGI1/MAGI3 double KO clone B5+6 2 follows that trend as well.

~ EdU-Cy5 intensity per nucleus: Samples were incubated for 4hrs with the EdU compound during which time the modified thymine analogue was incorporated in the newly synthesised DNA at each division. Since mammalian cells are believed to divide approximately every 24hrs (381), our incubation time only allowed maximum one division per cell. For all the cells that divided and went back to G1 phase, the intensity of the EdU-Cy5 signal should be identical. Regarding cells that were undergoing division at the time of fixation, the EdU-Cy5 signal detected should be somewhat dimer depending on which phase they were in. Normalising the total EdU-Cy5 intensity per picture to the number of nuclei gives an average intensity per cell which reflects the proportion of dividing cells per sample. At Day4, even though DLD-1 WT show very similar cell number in both replicates (**Figure A. 10a**), the EdU-Cy5 signal is quite different (2-fold), leading to a high standard deviation (**Figure A. 10d**). If considering DLD-1 WT mean \pm S.E.M., all mean values from the other cell lines fit within that range, except for MAGI-3 KO clones. MAGI-1 KO clones, G1 8 and G2 14, show similar EdU signal as DLD-1 WT. G5+6 28, MAGI-3 single KO clone, on the other hand is at the lower end of the WT range. Both MAGI1/MAGI3 double knockout clones, A5+6 7 and B5+6 2, seem to show slightly elevated EdU signal compared to WT and this difference is magnified when compared to MAGI-3 single KO. Between Day4 and Day10, we observed an overall dramatic decrease of the proportion of proliferating cells across all cell lines (**Figure A. 10f**), indicating a growth arrest between early and late stages tubules. However, when looking more closely to the Day10 EdU quantification, we notice a tendency of MAGI-3 and the MAGI1/MAGI3 double KO clone

B5+6 2 to have a higher proportion of proliferating cells compared to WT or MAGI-1 knockout (Figure A. 10e).

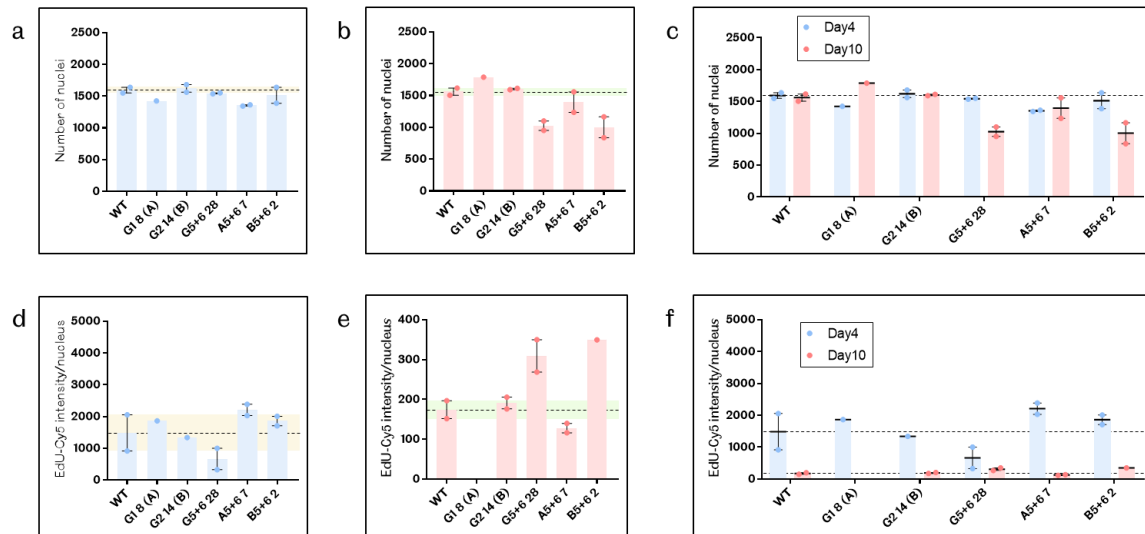


Figure A. 10 | Growth arrest of cells in OrganoPlate® between Day4 and Day10.

DLD-1 WT and derived CRISPR knockout cell lines were seeded in triplicates in two 3-lane OrganoPlate® six days apart. An EdU assay was performed on both plates simultaneously, on Day4 and Day10 respectively (n=1). Data are represented in a bar graph with each dot corresponding to each replicate. Some of the pictures had very dim Hoechst staining (nuclear counterstain) impairing the quantification. These values were excluded leading to a single value (or no values at all for G1 8 (A) Day10) for some samples. Means are indicated by the height of the bar and error bars correspond to the standard error to the mean (\pm S.E.M.). The mean (dotted lines) \pm S.E.M. (yellow and green coloured bands) of DLD-1 WT are indicated as point of comparison. **a, b & c**, Number of nuclei per picture on Day4 (**a**), Day10 (**b**) or both combined (**c**). The cell number in the tubules is quite homogenous at early stage (Day4). Small variations between samples can be observed at a later stage (Day10). **d, e & f**, EdU signal intensity normalised by the number of nuclei per picture on Day4 (**d**), Day10 (**e**) or both combined (**f**). Although the cell number in the tubule does not change much between early and late stage, the number of proliferating cells dramatically drops.

Taken together, our preliminary results appear to show that all cell lines have a very similar number of cells in the tubules at Day4. Even though, tubules are fully-formed at Day4, cells still heavily undergo proliferation. Surprisingly, the cell number, at least for DLD-1 WT, was very similar at a later stage on Day10. At this point, the proportion of proliferating cells is very low throughout all cell lines considered. Since the cell number remains mostly unchanged, tubules must be keeping a perfect balance between cell proliferation and cell death.

Second, we asked whether MAGIs were affecting cell viability in tubules. MAGI-1, MAGI-3 and MAGI1/MAGI3 CRISPR knockout clones were cultured alongside DLD-1 WT cells in the OrganoPlate® for seven days. A WST-8 assay was performed (See detailed protocol in Section 0). The absorbance measured was directly proportional to the number of live cells present in the tubules. Data are shown in **Figure A. 11b**. No major difference was observed between DLD-

1 WT and any of the cell lines. Our preliminary data show that the overall cell number in tubules, resulting from a balance between cell proliferation and cell death, after seven days of culture is similar in DLD-1 WT and in MAGI knockouts, corroborating our EdU results at Day4 and Day10.

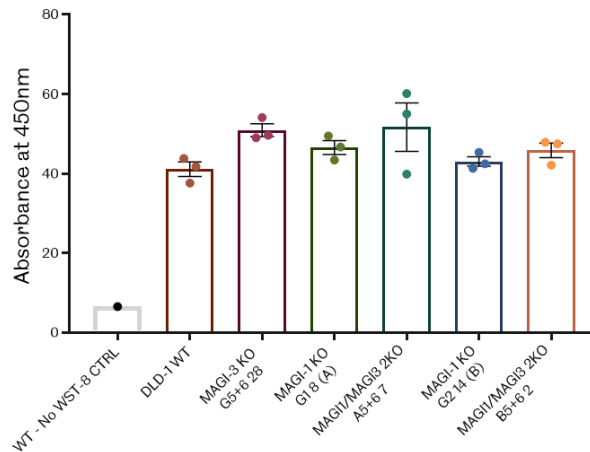


Figure A. 11 | MAGI knockouts do not affect cell viability.

DLD-1 WT and derived cell lines were seeded in triplicates in a 3-lane OrganoPlate®. A WST-8 assay was performed on Day7 (n=1). One extra DLD-1 WT chip was used as a negative control without WST-8. Absorbance was measured at 450nm and normalised to the cell-free control (blank). Data are represented in a bar graph with each dot corresponding to each replicate. Means are indicated by the height of the bar ±S.E.M. No major difference was observed.

To summarise, we found that the cell number in tubules from DLD-1 WT and MAGI knockouts is similar from Day4 until Day10.

II. The loss of barrier integrity in B5+6 2 clone correlates with defect in Occludin

Epithelial tissues are characterised by their ability to form a selective barrier between their apical and basal sides. Cells are sealed to one another by tight junctions that restrict the paracellular passage of molecules. Here, we found that at least one of our MAGI1/MAGI3 double knockout clone had lost this paramount barrier function (**Figure 3.20**). However, ZO-1 staining was intact in this clone (**Figure A. 14**). We therefore asked if other proteins essential for assembly of the tight junctions or maintenance of the barrier function was affected by MAGI knockouts. We focused on (1) Occludin which is known to play a critical role in both aforementioned functions (85,382-386) and (2) E-cadherin which is a major component of adherence junctions and is believed to regulate signalling towards the assembly of other junctions such as TJs (387). Moreover, E-cadherin is also a known epithelial marker as loss of E-cadherin for N-cadherin is a sign of epithelial to mesenchymal transition (EMT) (388,389).

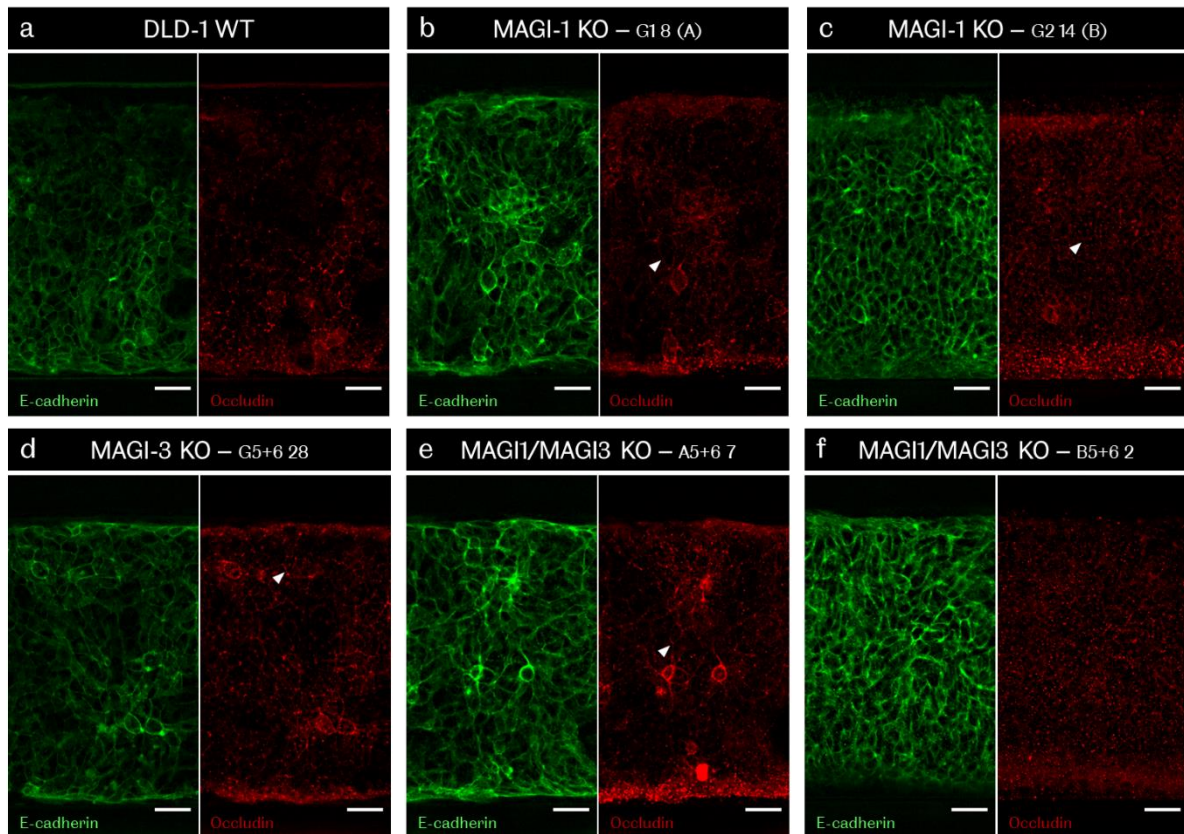


Figure A. 12 | E-cadherin and Occludin staining in DLD-1 tubules in the 3-lane OrganoPlate®.

Day4 DLD-1 tubules were stained with an anti-E-cadherin (Green) and an anti-Occludin (Red) antibody (n=1). Z-stacks were acquired using a confocal microscope, with a 20x objective. Scale bars: 50µm. A single slice is shown: apical view of the bottom cell layer of the tubules. E-cadherin staining is localised at the plasma membrane. The white arrows indicate Occludin at the cell-cell junctions. B5+6 2 clone does not seem to express Occludin.

In light of these paramount functions of both Occludin and E-cadherin in epithelial tissues, we stained Day4 tubules to verify their expression and localisation. Z-stacks were taken using a confocal microscope with a 20x objective. All images were acquired and processed identically. A single slice corresponding to the apical view of the bottom cell layer (**Figure A. 13c**) is shown in **Figure A. 12**.

~ Occludin: Overall, the antibody presented a very punctuated signal. Most cell lines presented an Occludin staining properly localised at the cell-cell junctions (**white arrows**). However, B5+6 2 displayed a very noisy punctuated signal with no particular enrichment at the membrane, suggesting a potential loss of Occludin in this MAGI1/MAGI3 double knockout clone. That could explain B5+6 2 behaviour in the BI assay and its loss of barrier function (**Figure 3.20**).

E-cadherin: All cell lines considered presented an E-cadherin signal properly localised at the cell membrane. These results are contradicting Zaric and collaborators results who found defect in E-cadherin upon MAGI-1 transient knockdown (252).

Taken together, our results show that MAGI1/MAGI3 double knockout clone, B5+6 2, has an impaired barrier function and it correlates with a lack of Occludin at the cell-cell contacts. MAGI knockouts does not appear to affect E-cadherin nor ZO-1 localisation.

III. MAGI knockout does not appear to disturb F-actin cytoskeleton

MAGI-1 knockdown in SW480 cells was reported to disturb actin stress fibres formation (252). Actin cytoskeleton plays a major role in YAP mechanosensing and regulation, in several cases, independently of the core Hippo cascade. For example, YAP translocation from nucleus to cytoplasm has been shown to be triggered in single cells by a reduction of the available adhesive surface (180,188). The cell density trigger encompasses two components: (1) formation of tight junctions and proper polarisation of cells and (2) reduction of the space available to each cell. We therefore asked whether MAGIs knockouts were affecting the actin cytoskeleton in 3D cultures.

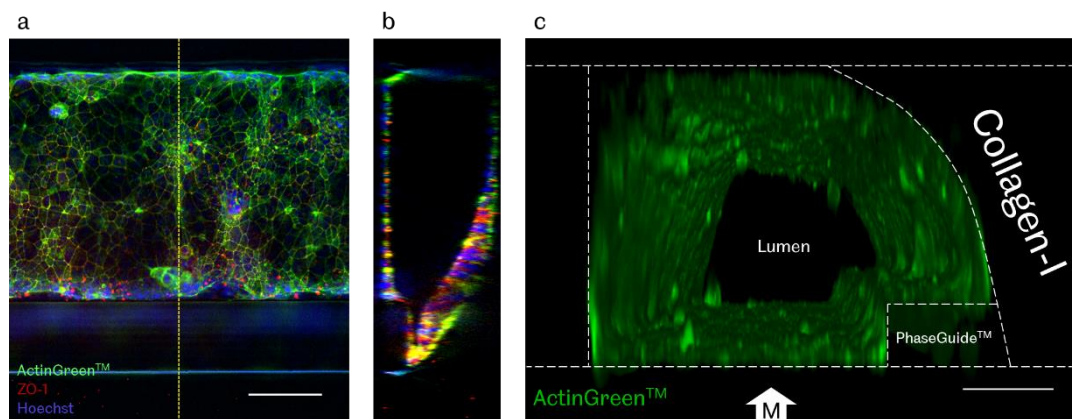


Figure A. 13 | Immunostaining of a DLD-1 WT tubule.

Day4 DLD-1 tubule stained with Hoechst (nuclear counterstain, Blue), ActinGreen™ (Green) and anti-ZO-1 (Red) antibodies. Images acquired with a confocal microscope, 20x objective. Scale bar: 50µm. **a**, Single slice of a Z-stack corresponding to the bottom layer of cells. **b**, Cross section of the tubule from the Z-stack along the yellow dotted line. **c**, 3D reconstruction of a tubule showing ActinGreen™ staining. The positions of the lumen, PhaseGuide™ and ECM are indicated. The microscope acquires images from below the plate (indicated by the white arrow and the M).

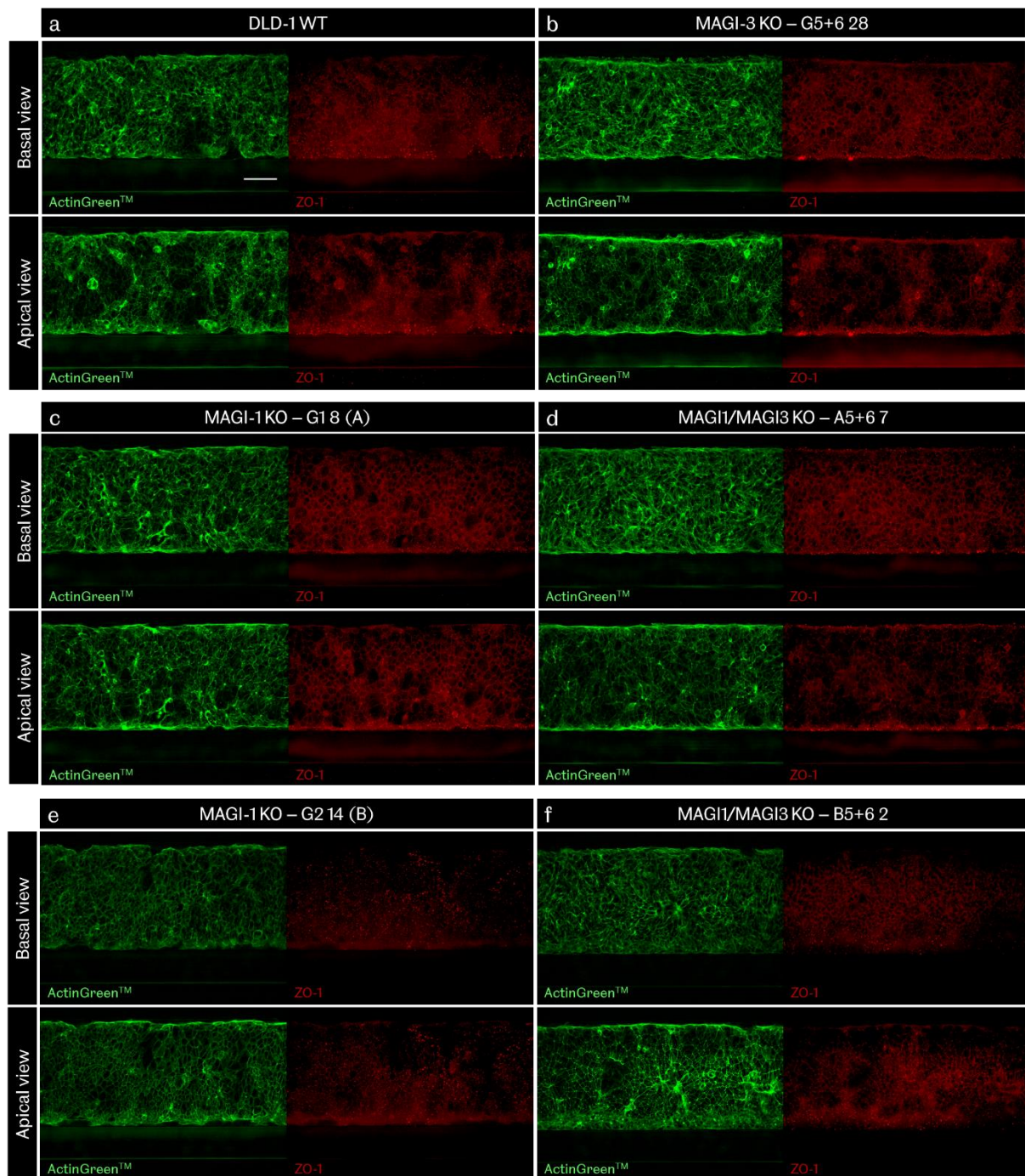


Figure A. 14 | DLD-1 tubules in the OrganoPlate® show proper F-actin and ZO-1 polarisation.

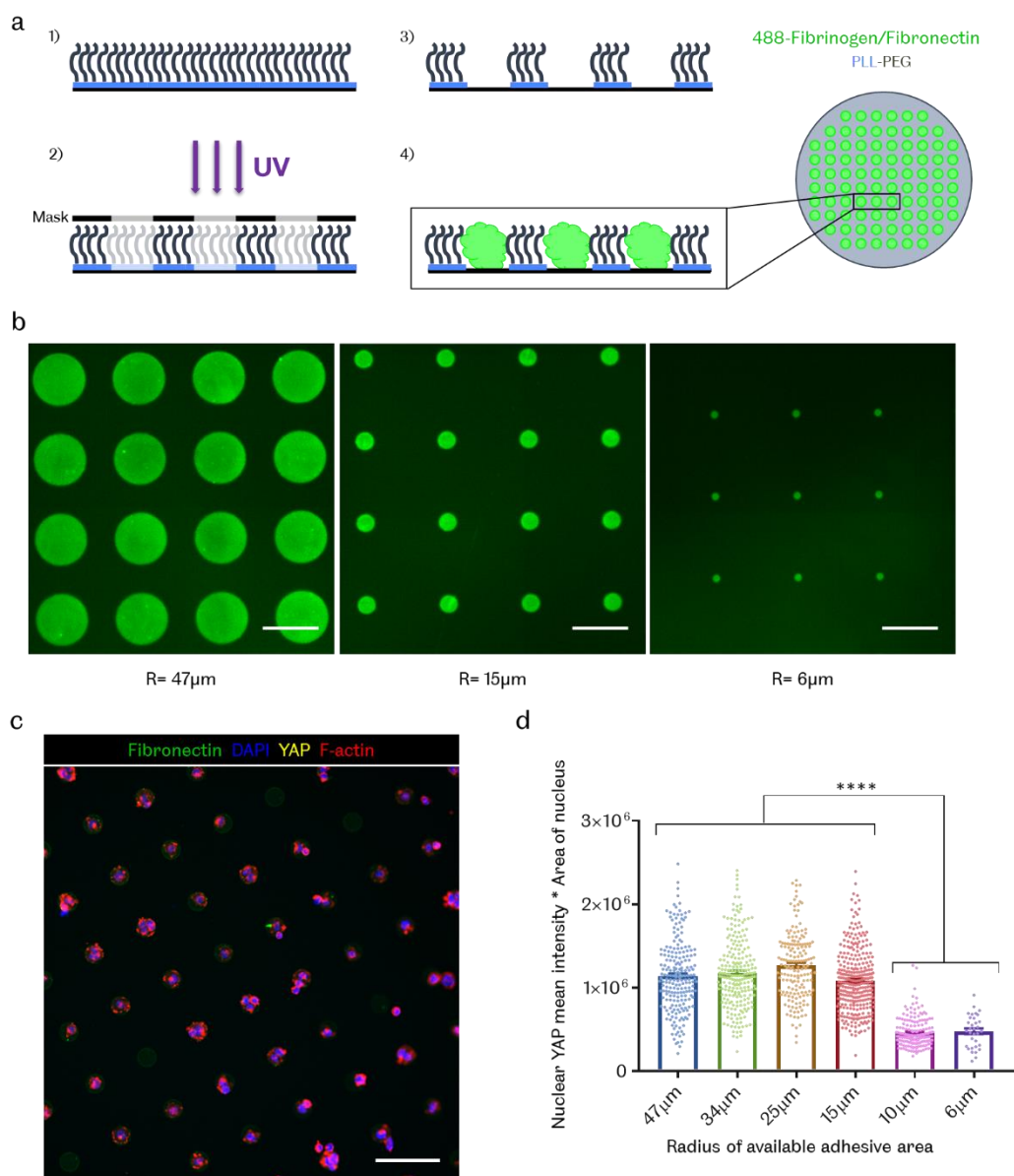
Day4 DLD-1 tubules were stained with the ready probe ActinGreen™ (Green) and an anti-ZO-1 antibody (Red) (n=1). Z-stacks were acquired using a confocal microscope, with a 20x objective. Hoechst: nuclear counterstain (blue). Scale bar: 50µm. Two slices are shown: apical and basal views of the bottom cell layer of the tubules (**Figure A. 13**). F-actin stress fibres are observed in the basal view while the apical view shows the circumferential actin belt and ZO-1 staining limited to the junctions. **a**, DLD-1 WT cells. **b**, G5+6 28, MAGI-3 knockout clone. **c**, G1 8 (A), MAGI-1 knockout clone. **d**, A5+6 7, MAGI1/MAGI3 double knockout clone. **e**, G2 14 (B), MAGI-1 knockout clone. **f**, B5+6 2, MAGI1/MAGI3 double knockout clone.

We looked at the actin cytoskeleton's integrity. DLD-1 WT cells, MAGI-1 KO, MAGI-3 and MAGI1/MAGI3 knockout clones were seeded in a 3-lane OrganoPlate[®]. After four day of culture under bilateral flow, tubules were subjected to anti-ZO-1 and ActinGreen[™] immunostaining. Z-stacks images were acquired with a confocal microscope through the glass bottom of the OrganoPlate[®] (**Figure A. 13**). **Figure A. 14** recapitulates the apical and basal view of the bottom cell layer. All images were acquired and processed identically. On the basal side of each cell line, we observed actin stress fibres while on the apical side, facing the lumen, was the expected circumferential actin belt (66). ZO-1 staining was localised at the cell-cell junctions in the apical view, coinciding with the F-actin, and the staining was noisier on the basal view. Some samples, such as G2 14 (B) displayed quite faint ZO-1 staining altogether. To summarise, unlike Zaric and collaborators, we did not observe a defect in actin stress fibres upon MAGI knockout (252).

ANNEX 5: Spatial confinement of single cells induces cytoplasmic YAP past a certain threshold

This part was performed in the lab of Dr. Matthieu Piel at Institut Curie, Paris, France.

YAP nucleocytoplasmic shuttling is cell-density dependent, yet, single cells restricted to a small adhesive area, less than $300\mu\text{m}^2$, were shown to display cytoplasmic YAP (180,188). It was suggested that micropatterns restrict single cell spreading to a degree comparable to high cell density condition.



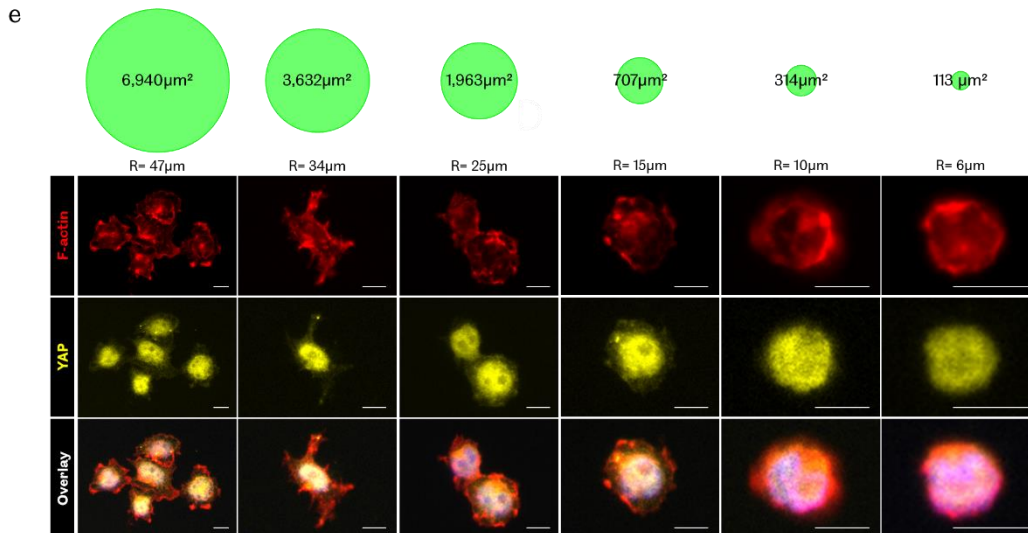


Figure A. 15 | Effects of 2D spatial confinement on YAP subcellular localisation in HEK293 cells.

a. Micropatterning on glass: 1) A glass coverslip is passivated with a layer of Polyethylene glycol (PEG) grafted onto Poly-L-Lysine (PLL) chains, 2) The glass coverslip is illuminated with deep UV through a quartz mask which represent the negative of the desired micropatterns. 3) The PLL-PEG has been removed in the illuminated areas. 4) The glass coverslip is then incubated with a solution of 488-fibrinogen/fibronectin to cover the free areas (desired micropatterns). This technique was used to produce fibronectin-coated islands of various sizes: Radius=47, 34, 25, 15, 10 and 6 μm . **b.** Example of 488-fibronectin-coated islands of R=47, 15 and 6 μm (from left to right) observed with an epifluorescence microscope. Scale bars: 100 μm . **c.** Full microscope field of HEK293 cells seeded onto the R=15 μm 488-fibronectin islands and stained with an anti-YAP/TAZ antibody (Yellow) and 594-Phalloidin. DAPI: nuclear counterstain. Scale bars: 100 μm . **d.** HEK293 cells were subjected to immunostaining with DAPI, anti-YAP/TAZ antibody (Yellow) and 594-Phalloidin. Cells were observed with an epifluorescence microscope. Quantification of the nuclear YAP was performed using DAPI to create a mask in Fiji. The mean YAP nuclear value for each cell was then multiplied by the nucleus area. Values for each micropattern area were collected from n cells: n= 213 (47 μm), n= 230 (34 μm), n= 173 (25 μm), n= 315 (15 μm), n= 170 (10 μm), n= 33 (6 μm). The graph shows the quantification of nuclear YAP with respect to the available adhesive area. Each value is represented by a dot, the bars represent mean values \pm S.E.M., n=1. A Brown-Forsythe one-way ANOVA was performed ($F(5,914.161)=142.46$, $p<0.0001$) followed by Games-Howell's multi comparisons test. Nuclear YAP in the two smaller patterns was significantly lower than in the four bigger ones (****, $p<0.0001$). **e.** Zoom in on a single pattern per condition. On the bigger islands, R=47 μm to R=15 μm , cells are able to spread and YAP is clearly enriched in the nucleus. On the R=10 μm and R=6 μm islands, cells' size and spreading are restricted by the available adhesive area (fibronectin). The cell shape is rounder and YAP appears to be evenly distributed between the cytoplasm and the nucleus. Scale bars: 10 μm .

Here, we used fibronectin-coated circular micropatterns with areas ranging across the established threshold of 300 μm^2 . The method to achieve micropatterns is described in **Figure A. 15a**. We tested six conditions: Radius=47, 34, 25, 15, 10 and 6 μm (**Figure A. 15**). HEK293 cells were seeded onto the patterns for 24hrs before being subjected to immunostaining with an anti-YAP/TAZ antibody and 594-Phalloidin. On the islands of radius between 47 μm to 15 μm , cells are able to spread out and YAP was localised predominantly in the nucleus. However, for

smaller patterns (R=10 and 6 μ m), cell size was reduced and their shape appeared rounder as they were restricted by the small adhesive area available. In these two conditions, YAP appeared evenly distributed between nucleus and cytoplasm. Quantification of the mean fluorescence intensity of nuclear YAP multiplied by the area of the nucleus showed a significant decrease of nuclear YAP for the R=10 and 6 μ m conditions compared to the four bigger islands (Games Howell multiple comparison's test, $p < 0.0001$). The islands with a 10 μ m radius correspond to 314 μ m². We therefore found a threshold comparable to that of the literature (180,188).

ANNEX 6: Is MAGI-1 stabilising PTPN14?

Over all the pulldowns performed, we noticed that the exogenous PTPN14 protein levels were increasing along with MAGI-1 overexpression. The pattern varied depending on which mMAGI-1 sub-construct was co-expressed. For example, the overexpression of MAGI-1 WW domains together with PTPN14 WT appeared to enhance PTPN14 protein levels. This effect was obliterated upon mutation of PTPN14 PPxY motifs (**Figure 4.3**, input lanes). This effect could be occurring at the mRNA or at the protein level. We hypothesised that MAGI-1 interaction with PTPN14 was stabilising the latter protein. Interestingly, two E3 ligase complexes are reported in the literature to target PTPN14 for proteasomal degradation: CRL2_{LRR1}, that acts at low density (74) and WWP1, a NEDD4-like E3 ligase (206) (**Figure A. 16a & b**).

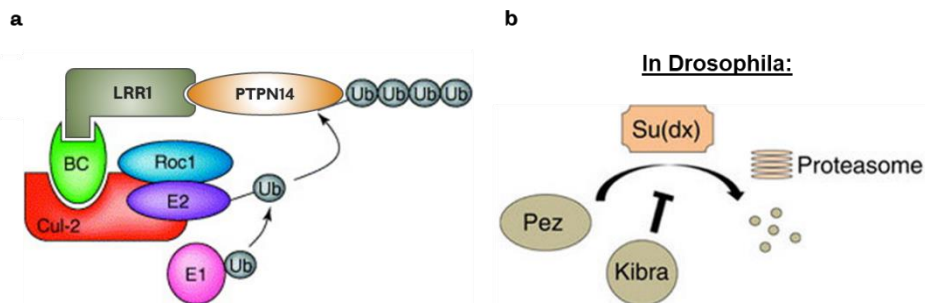


Figure A. 16 | PTPN14 is targeted for degradation by two E3 ubiquitin ligases.

a. The E3 ligase complex CRL2_{LRR1} is driving PTPN14 ubiquitination and subsequent degradation in sparse cells. CRL2 is composed of multiple subunits: the scaffolding protein Cullin2 (Cul-2), Roc1 which recruits the ubiquitin-conjugating enzyme 2 (E2), two adaptor proteins Elongin B and Elongin C (BC) and a substrate-recognising adaptor LRR1. Figure adapted from (390). **b.** In *Drosophila*, Su(dx) targets Pez, PTPN14's homologue, for degradation which can be rescued by Kibra. This mechanism relies of WW-PPxY binding between Kibra and Pez. Figure adapted from (206).

I. CRL2_{LRR1} complex

The experiments conducted in this thesis that led to the observation that overexpression of MAGI-1 increased PTPN14 protein levels were conducted at high cell density. In these conditions, according to the paper, CRL2_{LRR1} should no longer be able to target PTPN14 for degradation, due to the adaptor protein LRR1 being itself degraded at high density (74). Moreover, overexpression of MAGI-1 at low density failed to induce cytoplasmic retention unlike overexpression of PTPN14 (**Figure 3.4**). It is therefore probable that MAGI-1 does not antagonise CRL2_{LRR1} over PTPN14 degradation as MAGI-1 overexpression did not phenocopy that of PTPN14.

II. WWP1 E3 ubiquitin ligase

In *Drosophila*, PTPN14 homologue, Pez, was reported to interact with and be targeted for degradation by Suppressor of Deltex (Su(dx)), a member of the NEDD4 (neural precursor cell-expressed developmentally downregulated gene 4) E3 ligase family. Wang et al. showed that Pez can be rescued from Su(dx)-mediated degradation via interaction with Kibra, another upstream regulator of the Hippo pathway, in a PPxY-WW manner. In mammalian systems, this mechanism is partly conserved with the proteins' homologues (**Figure A. 17**). However, in the mammalian system, Kibra (WWC1) could not rescue PTPN14 from WWP1-mediated degradation (206). It opens the possibility for another WW-domain containing protein to fulfil the role of rescuing PTPN14 from WWP1-mediated degradation in mammalian cells. We hypothesised that MAGI-1 could be the protein stabilising PTPN14.

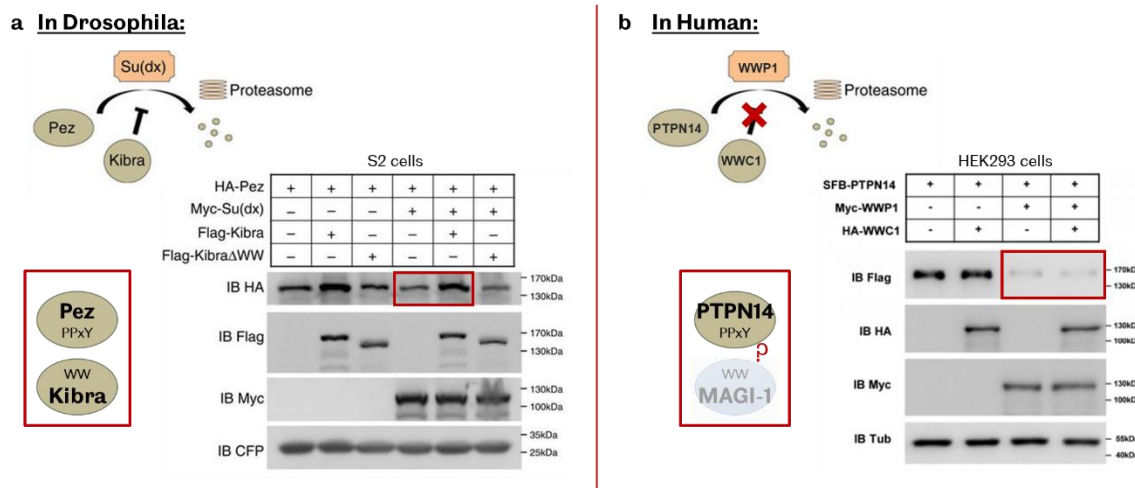


Figure A. 17 | MAGI-1 could be the protein rescuing PTPN14 from WWP1-mediated degradation in human.

a. In *Drosophila*, Pez is targeted for proteasomal degradation by the E3 ligase Su(dx). Kibra can rescue Pez from Su(dx)-mediated degradation via its WW domain interaction with Pez PY motifs. Adapted from Figure 5a and 5d of (206). **b.** In Human, the mechanism is partially conserved with the proteins' homologues. Indeed, PTPN14 is subjected to WWP1-mediated degradation. However, WWC1 is not able to rescue PTPN14, leaving this role open for another potential WW-containing interactor's of PTPN14 such as MAGI-1. Adapted from Figure 5a and Supplementary Figure 8g of (206).

The NEDD4 E3 ligases family comprises nine members, such as WWP1, Smurf2 and NEDD4-2, and has a specific domain structure displayed in **Figure A. 18**. In particular, WWP1 possesses a C2 domain, known to mediate membrane localisation (391), four WW domains with which it binds to its substrates, such as PTPN14, and an HECT domain containing the catalytic cysteine, C890, allowing ubiquitination (**Figure A. 18**). The catalytic cysteine located in the HECT domain is essential to mediate proteasomal degradation of the substrate as Wang and co-workers reported that Su(dx)C917A failed to trigger Pez degradation (206).

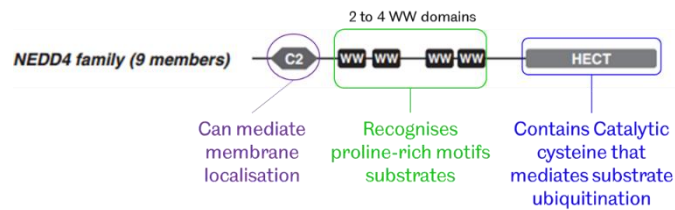


Figure A. 18 | Modular structure of the NEDD4 family of E3 ubiquitin ligases.

All nine members of the NEDD4 family present the same modular structure with a C2 domain followed by 2 to 4 WW domains and a C-terminal HECT domain. C2: thought to be involved in calcium-dependent phospholipid binding (392), HECT: Homologous to the E6-AP Carboxyl Terminus. Adapted from Figure 1 of (393).

Interestingly, several studies report autoinhibitory mechanism of the NEDD4 family members (**Figure A. 19**) (394-396). They suggested that a similar mechanism could potentially occur with other members of the NEDD4 family.

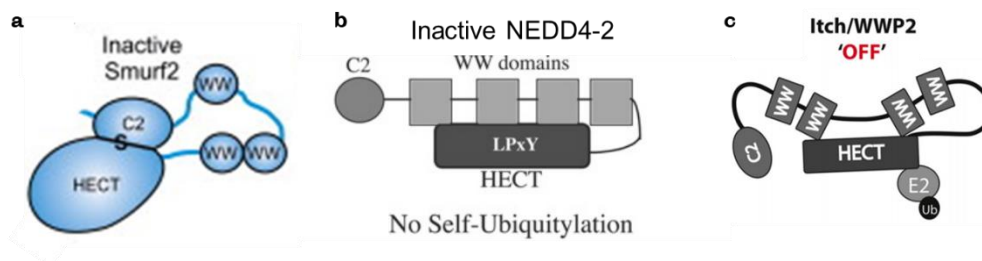


Figure A. 19 | Autoinhibition mechanisms of E3 ligases of the NEDD4 family.

a. Smurf2 is in an inactive state through a disulfide bond forming intramolecularly between its C2 and HECT domains. Adapted from Figure 6 of (394). **b.** NEDD4-2 possesses a LPxY motif within its HECT domain that interacts weakly with its own WW domains and thereby autoinhibits its activity. Adapted from Figure 9a of (395). **c.** Itch and WWP2, other members of the NEDD4 E3 ligase family, are in an 'OFF' conformation through an intramolecular interaction between their WW domain region and their HECT domain, preventing the docking of the E2 and subsequent transthiolation. Adapted from Figure 11 of (396).

We found, when mapping the interaction between MAGI-1 and PTPN14, that the WW1 domain was interacting with while the WW2 domain was “stabilising” PTPN14 (**Figure 4.1c**). This suggests that MAGI-1 does not need to bind to PTPN14 in order to potentially stabilise it. Interestingly, WWP1 E3 ligase possesses two LPxY motifs in its HECT domain, one of which (LPPY) is only a few amino acids downstream of the catalytic cysteine (C890). Building on the information found in the literature, MAGI-1’s WW domains could potentially bind WWP1 on this particular site and transiently inactivate it (**Figure A. 20**). By creating steric hindrance around the catalytic cysteine of the E3 ligase, MAGI-1 could be interfering with the E3-E2 transthiolation, transiently inhibiting WWP1 and preventing PTPN14 degradation. This mechanism would have to be investigated and the model validated. In addition, it would be interesting to assess whether PTPN14 stabilisation by MAGI-1 is dependent on upstream signals

and cellular context. Indeed, Nishimura et al. discovered a tyrosine phosphorylation site (Tyr373) within MAGI-1 WW2 domain (234). Although the kinase involved remains unknown, Ptpnz phosphatase was later identified to dephosphorylate that particular residue (360). The phosphorylation status of this tyrosine residue within MAGI-1 WW2 domain is believed to affect its interactions and could thereby modulate its ability to rescue PTPN14 from degradation.

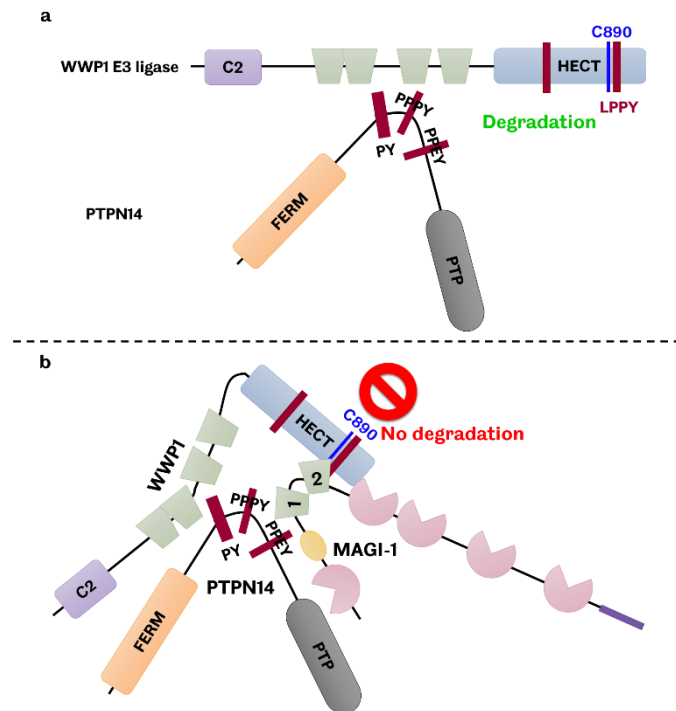


Figure A. 20 | Potential rescue mechanism of PTPN14's WWP1-mediated degradation by MAGI-1.

a. WWP1 is active. PTPN14 PY and PPxY motifs bind to WWP1's WW domains and the C890 mediates subsequent ubiquitination and degradation. **b.** WWP1 is potentially inhibited by MAGI-1. PTPN14 PPxY motifs interact with both WWP1 and MAGI-1. The interaction between MAGI-1 and PTPN14 being mediated via WW1 only, the second WW domain is free to bind to the C-terminal LPxY of WWP1, thereby shielding PTPN14 from the catalytic cysteine. In that speculated configuration, MAGI-1 is preventing PTPN14's WWP1-mediated degradation.

Unfortunately, due to time restriction, this model could not be validated nor investigated further.

ANNEX 7: Optimisation of pulldown experiments for MAGI1/LATS interaction

Chronologically, MAGI-1's interaction with the LATS kinases was the first to be addressed. We wanted to investigate whether there was a physical interaction between the afore mentioned proteins on top of the close proximity reported by a large scale proximity-dependent biotinylation study of the Hippo pathway (221). The only MAGI-1 construct available on Addgene was the mouse Flag-mMAGI-1B (280), endogenous isoform to brain and heart tissues (233). To begin the study, we performed a Myc-trap[®] pulldown of Flag-mMAGI-1B with Myc-LATS1/2, with the co-IP buffer commonly used in the laboratory: HEPES lysis buffer, 1% Triton X-100, supplemented with protease cocktail inhibitor. That first attempt was only successful in precipitating low amount of Myc-LATS1 or Myc-LATS2 and Flag-mMAGI-1B was barely detected in the pulldown complexes (**Figure A. 21a**). To address the issue of low efficiency, the second attempt was carried out using more Myc-trap[®] beads. This measure improved the quantity of Myc-tagged proteins pulled-down compared to the INPUT fractions. However, Flag-mMAGI-1B could not be detected in the pulldown lanes (**Figure A. 21b**). Couzens et al. reported that MAGI-1 was found in close proximity of the LATS kinases using a Bio-ID assay (221). This did not necessarily entail that the proteins interact but rather that they were close enough to allow biotinylation. Other possibilities would be that the interaction is transient, therefore not represented using this co-IP technique, or rather weak and requires different and milder buffer conditions. To address this point, we decided to compare the results obtained with HEPES buffer, to two other solutions commonly used in co-immunoprecipitation experiments (**Figure A. 21c**). For this optimisation phase, we focused on only one of the LATS kinases: LATS2. Increasing the pH of the buffer from 7.5 to 8.0 and switching from Triton X-100 to NP-40, a milder non-ionic detergent, resulted in Flag-mMAGI1B being successfully pulled-down along with Myc-LATS2 (**Figure A. 21d**). The interaction between MAGI-1 and LATS most likely required gentler buffer conditions to be detected. The strongest interaction was found using the NETN lysis buffer, containing EDTA rather than glycerol, and was therefore chosen to continue the study. We performed a Myc-trap[®] pulldown experiment of MAGI-1 with either Myc-LATS1 or Myc-LATS2. MAGI-1 was present in both protein complexes confirming interactions with LATS1/2 (**Figure A. 21e**).

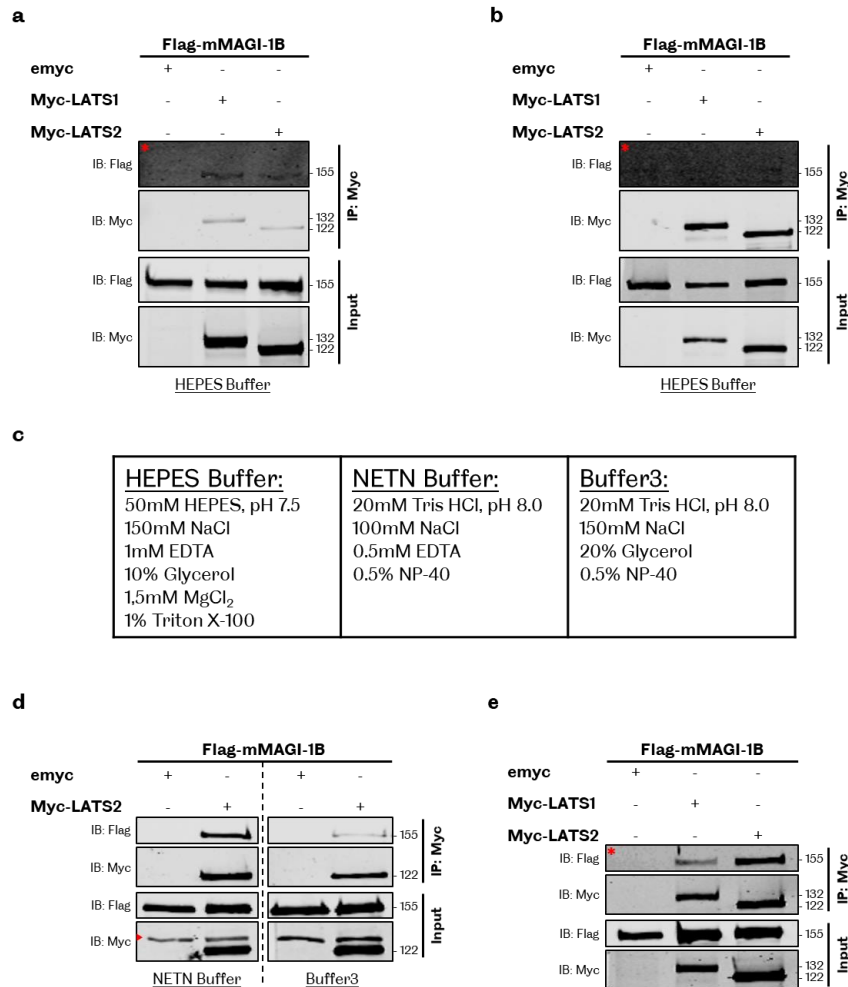


Figure A. 21 | MAGI-1 interacts with both LATS1 and LATS2 kinases.

The indicated plasmids were transfected into HEK293 cells. Cell lysates were subjected to immunoprecipitation (IP) and western blotting (IB) as indicated. Empty vectors (eMyc) were used as control. Protein expression levels are confirmed in the input fractions (1.5% of total cell lysates). Theoretical molecular weights are indicated in kDa on the right side of the western blots. *: increased brightness and contrast compared to the corresponding input fraction. The buffer used for the lysis and pulldown is indicated below each panel. **a**, First, co-immunoprecipitation experiment attempted of Flag-mMAGI-1B with Myc-LATS1 or Myc-LATS2 using Myc-trap[®] resin. MAGI-1 is very faintly detected in both LATS kinases pulldown complexes. **b**, Second, co-immunoprecipitation experiment attempted of Flag-mMAGI-1B with Myc-LATS1 or Myc-LATS2 using Myc-trap[®] resin. Even when increasing the image brightness and contrast, MAGI-1 is not detected in any of the pulldown complexes. **c**, Table containing the composition of the three lysis buffers tested during the optimisation of the MAGI1/LATS pulldowns. **d**, Co-immunoprecipitation experiments of Flag-mMAGI-1B with Myc-LATS2 using Myc-trap[®] resin and performed in parallel with two different buffers. MAGI-1 is clearly detected in the pulldown complex of LATS2 with both buffers (n=2). The NETN buffer conditions seem to favour the strongest interaction and is therefore chosen for the following steps. The red arrow points out an unspecific band of the Myc antibody. **e**, Co-immunoprecipitation experiment of Flag-mMAGI-1B with either Myc-LATS1 or Myc-LATS2 using Myc-trap[®] resin (n=1). MAGI-1 interacts with both LATS kinases and seems to have a stronger affinity for LATS2. NETN buffer.

References

1. Carter, S. B. (1968) Tissue homeostasis and the biological basis of cancer. *Nature* **220**, 970-974
2. Stoker, M. G., and Rubin, H. (1967) Density dependent inhibition of cell growth in culture. *Nature* **215**, 171-172
3. Puliafito, A., Hufnagel, L., Neveu, P., Streichan, S., Sigal, A., Fygenson, D. K., and Shraiman, B. I. (2012) Collective and single cell behavior in epithelial contact inhibition. *Proceedings of the National Academy of Sciences of the United States of America* **109**, 739-744
4. Eisenhoffer, G. T., Loftus, P. D., Yoshigi, M., Otsuna, H., Chien, C. B., Morcos, P. A., and Rosenblatt, J. (2012) Crowding induces live cell extrusion to maintain homeostatic cell numbers in epithelia. *Nature* **484**, 546-549
5. Marinari, E., Mehonic, A., Curran, S., Gale, J., Duke, T., and Baum, B. (2012) Live-cell delamination counterbalances epithelial growth to limit tissue overcrowding. *Nature* **484**, 542-545
6. Justice, R. W., Zilian, O., Woods, D. F., Noll, M., and Bryant, P. J. (1995) The drosophila tumor-suppressor gene Warts encodes a homolog of human myotonic-dystrophy kinase and is required for the control of cell-shape and proliferation *Genes & Development* **9**, 534-546
7. Xu, T. A., Wang, W. Y., Zhang, S., Stewart, R. A., and Yu, W. (1995) Identifying tumor suppressors in genetic mosaic - The drosophila Lats gene encodes a putative protein-kinase. *Development* **121**, 1053-1063
8. Zhao, B., Wei, X., Li, W., Udan, R. S., Yang, Q., Kim, J., Xie, J., Ikenoue, T., Yu, J., Li, L., Zheng, P., Ye, K., Chinnaiyan, A., Halder, G., Lai, Z. C., and Guan, K. L. (2007) Inactivation of YAP oncoprotein by the Hippo pathway is involved in cell contact inhibition and tissue growth control. *Genes & Development* **21**, 2747-2761
9. Harvey, K. F., Pflieger, C. M., and Hariharan, I. K. (2003) The Drosophila Mst ortholog, hippo, restricts growth and cell proliferation and promotes apoptosis. *Cell* **114**, 457-467
10. Jia, J., Zhang, W., Wang, B., Trinko, R., and Jiang, J. (2003) The Drosophila Ste20 family kinase dMST functions as a tumor suppressor by restricting cell proliferation and promoting apoptosis. *Genes & Development* **17**, 2514-2519
11. Pantalacci, S., Tapon, N., and Leopold, P. (2003) The Salvador partner Hippo promotes apoptosis and cell-cycle exit in Drosophila. *Nature Cell Biology* **5**, 921-927
12. Udan, R. S., Kango-Singh, M., Nolo, R., Tao, C., and Halder, G. (2003) Hippo promotes proliferation arrest and apoptosis in the Salvador/Warts pathway. *Nature Cell Biology* **5**, 914-920
13. Wu, S., Huang, J., Dong, J., and Pan, D. (2003) Hippo encodes a Ste-20 family protein kinase that restricts cell proliferation and promotes apoptosis in conjunction with salvador and warts. *Cell* **114**, 445-456
14. Kango-Singh, M., Nolo, R., Tao, C., Verstreken, P., Hiesinger, P. R., Bellen, H. J., and Halder, G. (2002) Shar-pei mediates cell proliferation arrest during imaginal disc growth in Drosophila. *Development* **129**, 5719-5730
15. Tapon, N., Harvey, K. F., Bell, D. W., Wahrer, D. C., Schiripo, T. A., Haber, D., and Hariharan, I. K. (2002) salvador Promotes both cell cycle exit and apoptosis in Drosophila and is mutated in human cancer cell lines. *Cell* **110**, 467-478
16. Lai, Z. C., Wei, X., Shimizu, T., Ramos, E., Rohrbaugh, M., Nikolaidis, N., Ho, L. L., and Li, Y. (2005) Control of cell proliferation and apoptosis by mob as tumor suppressor, mats. *Cell* **120**, 675-685
17. Huang, J. B., Wu, S., Barrera, J., Matthews, K., and Pan, D. J. (2005) The Hippo signaling pathway coordinately regulates cell proliferation and apoptosis by inactivating Yorkie, the Drosophila homolog of YAP. *Cell* **122**, 421-434
18. Wu, S., Liu, Y., Zheng, Y. G., Dong, J. X., and Pan, D. J. (2008) The TEAD/TEF family protein scalloped mediates transcriptional output of the hippo growth-regulatory pathway. *Developmental Cell* **14**, 388-398

19. Zhang, L., Ren, F. F., Zhang, Q., Chen, Y. B., Wang, B., and Jiang, J. (2008) The TEAD/TEF family of transcription factor scalloped mediates hippo signaling in organ size control. *Developmental Cell* **14**, 377-387
20. Dong, J. X., Feldmann, G., Huang, J. B., Wu, S., Zhang, N. L., Comerford, S. A., Gayyed, M. F., Anders, R. A., Maitra, A., and Pan, D. J. (2007) Elucidation of a universal size-control mechanism in Drosophila and mammals. *Cell* **130**, 1120-1133
21. Varelas, X. (2014) The Hippo pathway effectors TAZ and YAP in development, homeostasis and disease. *Development* **141**, 1614-1626
22. Pan, D. (2010) The hippo signaling pathway in development and cancer. *Developmental Cell* **19**, 491-505
23. Chan, E. H., Nousiainen, M., Chalamalasetty, R. B., Schafer, A., Nigg, E. A., and Sillje, H. H. W. (2005) The Ste20-like kinase Mst2 activates the human large tumor suppressor kinase Lats1. *Oncogene* **24**, 2076-2086
24. Callus, B. A., Verhagen, A. M., and Vaux, D. L. (2006) Association of mammalian sterile twenty kinases, Mst1 and Mst2, with hSalvador via C-terminal coiled-coil domains, leads to its stabilization and phosphorylation. *FEBS Journal* **273**, 4264-4276
25. Praskova, M., Xia, F., and Avruch, J. (2008) MOBKL1A/MOBKL1B phosphorylation by MST1 and MST2 inhibits cell proliferation. *Current Biology* **18**, 311-321
26. Hergovich, A., Schmitz, D., and Hemmings, B. A. (2006) The human tumour suppressor LATS1 is activated by human MOB1 at the membrane. *Biochemical and Biophysical Research Communications* **345**, 50-58
27. Yin, F., Yu, J. Z., Zheng, Y. G., Chen, Q., Zhang, N. L., and Pan, D. J. (2013) Spatial Organization of Hippo Signaling at the Plasma Membrane Mediated by the Tumor Suppressor Merlin/NF2. *Cell* **154**, 1342-1355
28. Avruch, J., Praskova, M., Ortiz-Vega, S., Liu, M. R., and Zhang, X. F. (2006) Nore1 and RASSF1 regulation of cell proliferation and of the MST1/2 kinases. in *Regulators and Effectors of Small Gtpases: Ras Family* (Balch, W. E., Der, C. J., and Hall, A. eds.), Elsevier Academic Press Inc, San Diego. pp 290-310
29. Sudol, M. (1994) Yes-associated protein (YAP65) is a proline-rich phosphoprotein that binds to the SH3 domain of the yes protooncogene product. *Oncogene* **9**, 2145-2152
30. Kanai, F., Marignani, P. A., Sarbassova, D., Yagi, R., Hall, R. A., Donowitz, M., Hisaminato, A., Fujiwara, T., Ito, Y., Cantley, L. C., and Yaffe, M. B. (2000) TAZ: a novel transcriptional co-activator regulated by interactions with 14-3-3 and PDZ domain proteins. *EMBO Journal* **19**, 6778-6791
31. Hao, Y. W., Chun, A., Cheung, K., Rashidi, B., and Yang, X. L. (2008) Tumor suppressor LATS1 is a negative regulator of oncogene YAP. *Journal of Biological Chemistry* **283**, 5496-5509
32. Vassilev, A., Kaneko, K. J., Shu, H. J., Zhao, Y. M., and DePamphilis, M. L. (2001) TEAD/TEF transcription factors utilize the activation domain of YAP65, a Src/Yes-associated protein localized in the cytoplasm. *Genes & Development* **15**, 1229-1241
33. Basu, S., Totty, N. F., Irwin, M. S., Sudol, M., and Downward, J. (2003) Akt phosphorylates the Yes-associated protein, YAP, to induce interaction with 14-3-3 and attenuation of p73-mediated apoptosis. *Molecular Cell* **11**, 11-23
34. Ota, M., and Sasaki, H. (2008) Mammalian Tead proteins regulate cell proliferation and contact inhibition as transcriptional mediators of Hippo signaling. *Development* **135**, 4059-4069
35. Zhao, B., Ye, X., Yu, J. D., Li, L., Li, W. Q., Li, S. M., Yu, J. J., Lin, J. D., Wang, C. Y., Chinnaiyan, A. M., Lai, Z. C., and Guan, K. L. (2008) TEAD mediates YAP-dependent gene induction and growth control. *Genes & Development* **22**, 1962-1971
36. Chen, L. M., Loh, P. G., and Song, H. W. (2010) Structural and functional insights into the TEAD-YAP complex in the Hippo signaling pathway. *Protein & Cell* **1**, 1073-1083
37. Camargo, F. D., Gokhale, S., Johnnidis, J. B., Fu, D., Bell, G. W., Jaenisch, R., and Brummelkamp, T. R. (2007) YAP1 increases organ size and expands undifferentiated progenitor cells. *Current Biology* **17**, 2054-2060

38. Chan, S. W., Lim, C. J., Loo, L. S., Chong, Y. F., Huang, C., and Hong, W. (2009) TEADs mediate nuclear retention of TAZ to promote oncogenic transformation. *Journal of Biological Chemistry* **284**, 14347-14358
39. Zhang, J., Ji, J. Y., Yu, M., Overholtzer, M., Smolen, G. A., Wang, R., Brugge, J. S., Dyson, N. J., and Haber, D. A. (2009) YAP-dependent induction of amphiregulin identifies a non-cell-autonomous component of the Hippo pathway. *Nature Cell Biology* **11**, 1444-1450
40. Zhao, B., Lei, Q. Y., and Guan, K. L. (2008) The Hippo-YAP pathway: new connections between regulation of organ size and cancer. *Current Opinion in Cell Biology* **20**, 638-646
41. Zhou, Y., Huang, T., Cheng, A. S. L., Yu, J., Kang, W., and To, K. F. (2016) The TEAD Family and Its Oncogenic Role in Promoting Tumorigenesis. *International Journal of Molecular Sciences* **17**
42. Zhou, Y., Huang, T., Zhang, J., Wong, C. C., Zhang, B., Dong, Y., Wu, F., Tong, J. H. M., Wu, W. K. K., Cheng, A. S. L., Yu, J., Kang, W., and To, K. F. (2017) TEAD1/4 exerts oncogenic role and is negatively regulated by miR-4269 in gastric tumorigenesis. *Oncogene* **36**, 6518-6530
43. Chen, L., Chan, S. W., Zhang, X., Walsh, M., Lim, C. J., Hong, W., and Song, H. (2010) Structural basis of YAP recognition by TEAD4 in the hippo pathway. *Genes & Development* **24**, 290-300
44. Chen, Y. A., Lu, C. Y., Cheng, T. Y., Pan, S. H., Chen, H. F., and Chang, N. S. (2019) WW Domain-Containing Proteins YAP and TAZ in the Hippo Pathway as Key Regulators in Stemness Maintenance, Tissue Homeostasis, and Tumorigenesis. *Frontiers in Oncology* **9**
45. Creative Commons.
46. Strano, S., Munarriz, E., Rossi, M., Castagnoli, L., Shaul, Y., Sacchi, A., Oren, M., Sudol, M., Cesareni, G., and Blandino, G. (2001) Physical interaction with Yes-associated protein enhances p73 transcriptional activity. *Journal of Biological Chemistry* **276**, 15164-15173
47. Vitolo, M. I., Anglin, I. E., Mahoney, W. M., Jr., Renoud, K. J., Gartenhaus, R. B., Bachman, K. E., and Passaniti, A. (2007) The RUNX2 transcription factor cooperates with the YES-associated protein, YAP65, to promote cell transformation. *Cancer Biology & Therapy* **6**, 856-863
48. Hong, J. H., Hwang, E. S., McManus, M. T., Amsterdam, A., Tian, Y., Kalmukova, R., Mueller, E., Benjamin, T., Spiegelman, B. M., Sharp, P. A., Hopkins, N., and Yaffe, M. B. (2005) TAZ, a transcriptional modulator of mesenchymal stem cell differentiation. *Science* **309**, 1074-1078
49. Strano, S., Monti, O., Pediconi, N., Baccarini, A., Fontemaggi, G., Lapi, E., Mantovani, F., Damalas, A., Citro, G., Sacchi, A., Del Sal, G., Levrero, M., and Blandino, G. (2005) The transcriptional coactivator Yes-associated protein drives p73 gene-target specificity in response to DNA damage. *Molecular Cell* **18**, 447-459
50. Varelas, X., Sakuma, R., Samavarchi-Tehrani, P., Peerani, R., Rao, B. M., Dembowy, J., Yaffe, M. B., Zandstra, P. W., and Wrana, J. L. (2008) TAZ controls Smad nucleocytoplasmic shuttling and regulates human embryonic stem-cell self-renewal. *Nature Cell Biology* **10**, 837-848
51. Alarcon, C., Zaromytidou, A. I., Xi, Q., Gao, S., Yu, J., Fujisawa, S., Barlas, A., Miller, A. N., Manova-Todorova, K., Macias, M. J., Sapkota, G., Pan, D., and Massague, J. (2009) Nuclear CDKs drive Smad transcriptional activation and turnover in BMP and TGF-beta pathways. *Cell* **139**, 757-769
52. Komuro, A., Saeki, M., and Kato, S. (1999) Association of two nuclear proteins, Npw38 and NpwBP, via the interaction between the WW domain and a novel proline-rich motif containing glycine and arginine. *Journal of Biological Chemistry* **274**, 36513-36519
53. Kay, B. K., Williamson, M. P., and Sudol, M. (2000) The importance of being proline: the interaction of proline-rich motifs in signaling proteins with their cognate domains. *FASEB Journal* **14**, 231-241
54. Chen, H. I., Einbond, A., Kwak, S. J., Linn, H., Koepf, E., Peterson, S., Kelly, J. W., and Sudol, M. (1997) Characterization of the WW domain of human yes-associated protein and its polyproline-containing ligands. *Journal of Biological Chemistry* **272**, 17070-17077

55. Ingham, R. J., Colwill, K., Howard, C., Dettwiler, S., Lim, C. S. H., Yu, J., Hersi, K., Raaijmakers, J., Gish, G., Mbamalu, G., Taylor, L., Yeung, B., Vassilovski, G., Amin, M., Chen, F., Matskova, L., Winberg, G., Ernberg, I., Linding, R., O'Donnell, P., Starostine, A., Keller, W., Metalnikov, P., Stark, C., and Pawson, T. (2005) WW domains provide a platform for the assembly of multiprotein networks. *Molecular and Cellular Biology* **25**, 7092-7106
56. Tapia, V. E., Nicolaescu, E., McDonald, C. B., Musi, V., Oka, T., Inayoshi, Y., Satteson, A. C., Mazack, V., Humbert, J., Gaffney, C. J., Beullens, M., Schwartz, C. E., Landgraf, C., Volkmer, R., Pastore, A., Farooq, A., Bollen, M., and Sudol, M. (2010) Y65C missense mutation in the WW domain of the Golabi-Ito-Hall syndrome protein PQBP1 affects its binding activity and deregulates pre-mRNA splicing. *Journal of Biological Chemistry* **285**, 19391-19401
57. Zhang, J. M., Smolen, G. A., and Haber, D. A. (2008) Negative regulation of YAP by LATS1 underscores evolutionary conservation of the Drosophila Hippo pathway. *Cancer Research* **68**, 2789-2794
58. Matallanas, D., Romano, D., Yee, K., Meissl, K., Kucerova, L., Piazzolla, D., Baccharini, M., Vass, J. K., Kolch, W., and O'Neill, E. (2007) RASSF1A elicits apoptosis through an MST2 pathway directing proapoptotic transcription by the p73 tumor suppressor protein. *Molecular Cell* **27**, 962-975
59. Oka, T., Mazack, V., and Sudol, M. (2008) Mst2 and lats kinases regulate apoptotic function of Yes kinase-associated protein (YAP). *Journal of Biological Chemistry* **283**, 27534-27546
60. Yu, F. X., Zhao, B., Panupinthu, N., Jewell, J. L., Lian, I., Wang, L. H., Zhao, J. G., Yuan, H. X., Tumaneng, K., Li, H. R., Fu, X. D., Mills, G. B., and Guan, K. L. (2012) Regulation of the Hippo-YAP Pathway by G-Protein-Coupled Receptor Signaling. *Cell* **150**, 780-791
61. Azzolin, L., Panciera, T., Soligo, S., Enzo, E., Bicciato, S., Dupont, S., Bresolin, S., Frasson, C., Basso, G., Guzzardo, V., Fassina, A., Cordenonsi, M., and Piccolo, S. (2014) YAP/TAZ Incorporation in the beta-Catenin Destruction Complex Orchestrates the Wnt Response. *Cell* **158**, 157-170
62. Fulford, A., Tapon, N., and Ribeiro, P. S. (2018) Upstairs, downstairs: spatial regulation of Hippo signalling. *Current Opinion in Cell Biology* **51**, 22-32
63. Zhao, B., Li, L., Tumaneng, K., Wang, C. Y., and Guan, K. L. (2010) A coordinated phosphorylation by Lats and CK1 regulates YAP stability through SCF beta-TRCP. *Genes & Development* **24**, 72-85
64. Liu, C. Y., Zha, Z. Y., Zhou, X., Zhang, H., Huang, W., Zhao, D., Li, T. T., Chan, S. W., Lim, C. J., Hong, W. J., Zhao, S. M., Xiong, Y., Lei, Q. Y., and Guan, K. L. (2010) The Hippo Tumor Pathway Promotes TAZ Degradation by Phosphorylating a Phosphodegron and Recruiting the SCF beta-TrCP E3 Ligase. *Journal of Biological Chemistry* **285**, 37159-37169
65. Oka, T., Remue, E., Meerschaert, K., Vanloo, B., Boucherie, C., Gfeller, D., Bader, G. D., Sidhu, S. S., Vandekerckhove, J., Gettemans, J., and Sudol, M. (2010) Functional complexes between YAP2 and ZO-2 are PDZ domain-dependent, and regulate YAP2 nuclear localization and signalling. *Biochemical Journal* **432**, 461-472
66. Furukawa, K. T., Yamashita, K., Sakurai, N., and Ohno, S. (2017) The Epithelial Circumferential Actin Belt Regulates YAP/TAZ through Nucleocytoplasmic Shuttling of Merlin. *Cell Reports* **20**, 1435-1447
67. Kofler, M., Speight, P., Little, D., Di Ciano-Oliveira, C., Szaszi, K., and Kapus, A. (2018) Mediated nuclear import and export of TAZ and the underlying molecular requirements. *Nature Communications* **9**, 4966
68. Silvis, M. R., Kreger, B. T., Lien, W. H., Klezovitch, O., Rudakova, G. M., Camargo, F. D., Lantz, D. M., Seykora, J. T., and Vasioukhin, V. (2011) alpha-catenin is a tumor suppressor that controls cell accumulation by regulating the localization and activity of the transcriptional coactivator Yap1. *Science Signaling* **4**, ra33
69. Liu, O. X., Lin, L. B., Chew, T., Motegi, F., and Low, B. C. (2018) ZO-2 induces cytoplasmic retention of YAP by promoting a LATS1-ZO-2-YAP complex at tight junctions. *BioRxiv*
70. Schlegelmilch, K., Mohseni, M., Kirak, O., Pruszek, J., Rodriguez, J. R., Zhou, D. W., Kreger, B. T., Vasioukhin, V., Avruch, J., Brummelkamp, T. R., and Camargo, F. D. (2011) Yap1 Acts Downstream of alpha-Catenin to Control Epidermal Proliferation. *Cell* **144**, 782-795

71. Huang, J. M., Nagatomo, I., Suzuki, E., Mizuno, T., Kumagai, T., Berezov, A., Zhang, H., Karlan, B., Greene, M. I., and Wang, Q. (2013) YAP modifies cancer cell sensitivity to EGFR and survivin inhibitors and is negatively regulated by the non-receptor type protein tyrosine phosphatase 14. *Oncogene* **32**, 2220-2229
72. Liu, X., Yang, N., Figel, S. A., Wilson, K. E., Morrison, C. D., Gelman, I. H., and Zhang, J. (2013) PTPN14 interacts with and negatively regulates the oncogenic function of YAP. *Oncogene* **32**, 1266-1273
73. Michaloglou, C., Lehmann, W., Martin, T., Delaunay, C., Hueber, A., Barys, L., Niu, H. L., Billy, E., Wartmann, M., Ito, M., Wilson, C. J., Digan, M. E., Bauer, A., Voshol, H., Christofori, G., Sellers, W. R., Hofmann, F., and Schmelzle, T. (2013) The Tyrosine Phosphatase PTPN14 Is a Negative Regulator of YAP Activity. *Plos One* **8**, 9
74. Wang, W. Q., Huang, J., Wang, X., Yuan, J. S., Li, X., Feng, L., Park, J. I., and Chen, J. J. (2012) PTPN14 is required for the density-dependent control of YAP1. *Genes & Development* **26**, 1959-1971
75. Wilson, K. E., Li, Y. W., Yang, N., Shen, H., Orillion, A. R., and Zhang, J. M. (2014) PTPN14 Forms a Complex with Kibra and LATS1 Proteins and Negatively Regulates the YAP Oncogenic Function. *Journal of Biological Chemistry* **289**, 23693-23700
76. Zhao, B., Li, L., Lu, Q., Wang, L. H., Liu, C.-Y., Lei, Q., and Guan, K.-L. (2011) Angiomotin is a novel Hippo pathway component that inhibits YAP oncoprotein. *Genes & Development* **25**, 51-63
77. Chan, S. W., Lim, C. J., Chong, Y. F., Pobbati, A. V., Huang, C. X., and Hong, W. J. (2011) Hippo Pathway-independent Restriction of TAZ and YAP by Angiomotin. *Journal of Biological Chemistry* **286**, 7018-7026
78. Chan, S. W., Lim, C. J., Guo, F. S., Tan, I., Leung, T., and Hong, W. J. (2013) Actin-binding and Cell Proliferation Activities of Angiomotin Family Members Are Regulated by Hippo Pathway-mediated Phosphorylation. *Journal of Biological Chemistry* **288**, 37296-37307
79. Cox, C. M., Mandell, E. K., Stewart, L., Lu, R., Johnson, D. L., McCarter, S. D., Tavares, A., Runyan, R., Ghosh, S., and Wilson, J. M. (2015) Endosomal regulation of contact inhibition through the AMOT:YAP pathway. *Molecular Biology of the Cell* **26**, 2673-2684
80. Nishioka, N., Inoue, K., Adachi, K., Kiyonari, H., Ota, M., Ralston, A., Yabuta, N., Hirahara, S., Stephenson, R. O., Ogonuki, N., Makita, R., Kurihara, H., Morin-Kensicki, E. M., Nojima, H., Rossant, J., Nakao, K., Niwa, H., and Sasaki, H. (2009) The Hippo Signaling Pathway Components Lats and Yap Pattern Tead4 Activity to Distinguish Mouse Trophoblast from Inner Cell Mass. *Developmental Cell* **16**, 398-410
81. Plouffe, S. W., Lin, K. C., Moore, J. L., 3rd, Tan, F. E., Ma, S., Ye, Z., Qiu, Y., Ren, B., and Guan, K. L. (2018) The Hippo pathway effector proteins YAP and TAZ have both distinct and overlapping functions in the cell. *Journal of Biological Chemistry* **293**, 11230-11240
82. Fanning, A. S., Jameson, B. J., Jesaitis, L. A., and Anderson, J. M. (1998) The tight junction protein ZO-1 establishes a link between the transmembrane protein occludin and the actin cytoskeleton. *Journal of Biological Chemistry* **273**, 29745-29753
83. Itoh, M., Furuse, M., Morita, K., Kubota, K., Saitou, M., and Tsukita, S. (1999) Direct binding of three tight junction-associated MAGUKs, ZO-1, ZO-2, and ZO-3, with the COOH termini of claudins. *Journal of Cell Biology* **147**, 1351-1363
84. Roh, M. H., Liu, C. J., Laurinec, S., and Margolis, B. (2002) The carboxyl terminus of zona occludens-3 binds and recruits a mammalian homologue of discs lost to tight junctions. *Journal of Biological Chemistry* **277**, 27501-27509
85. Balda, M. S., Whitney, J. A., Flores, C., Gonzalez, S., Cereijido, M., and Matter, K. (1996) Functional dissociation of paracellular permeability and transepithelial electrical resistance and disruption of the apical-basolateral intramembrane diffusion barrier by expression of a mutant tight junction membrane protein. *Journal of Cell Biology* **134**, 1031-1049
86. Fanning, A. S., and Anderson, J. M. (1996) Protein-protein interactions: PDZ domain networks. *Current Biology* **6**, 1385-1388

87. Tsukita, S., Yamazaki, Y., Katsuno, T., and Tamura, A. (2008) Tight junction-based epithelial microenvironment and cell proliferation. *Oncogene* **27**, 6930-6938
88. McCarthy, K. M., Skare, I. B., Stankewich, M. C., Furuse, M., Tsukita, S., Rogers, R. A., Lynch, R. D., and Schneeberger, E. E. (1996) Occludin is a functional component of the tight junction. *Journal of Cell Science* **109**, 2287-2298
89. Ikenouchi, J., Umeda, K., Tsukita, S., and Furuse, M. (2007) Requirement of ZO-1 for the formation of belt-like adherens junctions during epithelial cell polarization. *Journal of Cell Biology* **176**, 779-786
90. Aberle, H., Butz, S., Stappert, J., Weissig, H., Kemler, R., and Hoschuetzky, H. (1994) Assembly of the cadherin-catenin complex in vitro with recombinant proteins. *Journal of Cell Science* **107**, 3655-3663
91. Nelson, W. J., and Nusse, R. (2004) Convergence of Wnt, beta-catenin, and cadherin pathways. *Science* **303**, 1483-1487
92. Takai, Y., Ikeda, W., Ogita, H., and Rikitake, Y. (2008) The immunoglobulin-like cell adhesion molecule nectin and its associated protein afadin. *Annual Review of Cell & Developmental Biology* **24**, 309-342
93. Bhat, A. A., Uppada, S., Achkar, I. W., Hashem, S., Yadav, S. K., Shanmugakonar, M., Al-Naemi, H. A., Haris, M., and Uddin, S. (2018) Tight Junction Proteins and Signaling Pathways in Cancer and Inflammation: A Functional Crosstalk. *Frontiers in Physiology* **9**, 1942
94. Perrais, M., Chen, X., Perez-Moreno, M., and Gumbiner, B. M. (2007) E-cadherin homophilic ligation inhibits cell growth and epidermal growth factor receptor signaling independently of other cell interactions. *Molecular Biology of the Cell* **18**, 2013-2025
95. Varelas, X., Samavarchi-Tehrani, P., Narimatsu, M., Weiss, A., Cockburn, K., Larsen, B. G., Rossant, J., and Wrana, J. L. (2010) The Crumbs Complex Couples Cell Density Sensing to Hippo-Dependent Control of the TGF-beta-SMAD Pathway. *Developmental Cell* **19**, 831-844
96. Hirate, Y., Hirahara, S., Inoue, K., Suzuki, A., Alarcon, V. B., Akimoto, K., Hirai, T., Hara, T., Adachi, M., Chida, K., Ohno, S., Marikawa, Y., Nakao, K., Shimono, A., and Sasaki, H. (2013) Polarity-Dependent Distribution of Angiomotin Localizes Hippo Signaling in Preimplantation Embryos. *Current Biology* **23**, 1181-1194
97. Kim, N. G., Koh, E., Chen, X., and Gumbiner, B. M. (2011) E-cadherin mediates contact inhibition of proliferation through Hippo signaling-pathway components. *Proceedings of the National Academy of Sciences of the United States of America* **108**, 11930-11935
98. Benham-Pyle, B. W., Pruitt, B. L., and Nelson, W. J. (2015) Cell adhesion. Mechanical strain induces E-cadherin-dependent Yap1 and beta-catenin activation to drive cell cycle entry. *Science* **348**, 1024-1027
99. Gumbiner, B., Stevenson, B., and Grimaldi, A. (1988) The role of the cell adhesion molecule uvomorulin in the formation and maintenance of the epithelial junctional complex. *Journal of Cell Biology* **107**, 1575-1587
100. Nejsum, L. N., and Nelson, W. J. (2009) Epithelial cell surface polarity: the early steps. *Frontiers in Biosciences* **14**, 1088-1098
101. Tinkle, C. L., Lechler, T., Pasolli, H. A., and Fuchs, E. (2004) Conditional targeting of E-cadherin in skin: insights into hyperproliferative and degenerative responses. *Proceedings of the National Academy of Sciences of the United States of America* **101**, 552-557
102. Tunggal, J. A., Helfrich, I., Schmitz, A., Schwarz, H., Gunzel, D., Fromm, M., Kemler, R., Krieg, T., and Niessen, C. M. (2005) E-cadherin is essential for in vivo epidermal barrier function by regulating tight junctions. *EMBO Journal* **24**, 1146-1156
103. Ozawa, M., and Kobayashi, W. (2014) Cadherin Cytoplasmic Domains Inhibit the Cell Surface Localization of Endogenous E-Cadherin, Blocking Desmosome and Tight Junction Formation and Inducing Cell Dissociation. *PLoS One* **9**
104. Dimarco Hewitt, P. (2015) *Regulation of Cell Adhesion by the FERM Proteins, PTPN14 and Merlin*. PhD, The Texas Medical Center

105. Wadham, C., Gamble, J. R., Vadas, M. A., and Khew-Goodall, Y. (2003) The protein tyrosine phosphatase pez is a major phosphatase of adherens junctions and dephosphorylates beta-catenin. *Molecular Biology of the Cell* **14**, 2520-2529
106. Hamaratoglu, F., Willecke, M., Kango-Singh, M., Nolo, R., Hyun, E., Tao, C. Y., Jafar-Nejad, H., and Halder, G. (2006) The tumour-suppressor genes NF2/Merlin and Expanded act through Hippo signalling to regulate cell proliferation and apoptosis. *Nature Cell Biology* **8**, 27-U29
107. Genevet, A., Wehr, M. C., Brain, R., Thompson, B. J., and Tapon, N. (2010) Kibra is a regulator of the Salvador/Warts/Hippo signaling network. *Developmental Cell* **18**, 300-308
108. Yu, J., Zheng, Y., Dong, J., Klusza, S., Deng, W. M., and Pan, D. (2010) Kibra functions as a tumor suppressor protein that regulates Hippo signaling in conjunction with Merlin and Expanded. *Developmental Cell* **18**, 288-299
109. Xiao, L., Chen, Y., Ji, M., and Dong, J. (2011) KIBRA regulates Hippo signaling activity via interactions with large tumor suppressor kinases. *Journal of Biological Chemistry* **286**, 7788-7796
110. Lallemand, D., Curto, M., Saotome, I., Giovannini, M., and McClatchey, A. I. (2003) NF2 deficiency promotes tumorigenesis and metastasis by destabilizing adherens junctions. *Genes & Development* **17**, 1090-1100
111. Gladden, A. B., Hebert, A. M., Schneeberger, E. E., and McClatchey, A. I. (2010) The NF2 tumor suppressor, Merlin, regulates epidermal development through the establishment of a junctional polarity complex. *Developmental Cell* **19**, 727-739
112. Scoles, D. R. (2008) The merlin interacting proteins reveal multiple targets for NF2 therapy. *Biochimica Biophysica Acta-Reviews on Cancer* **1785**, 32-54
113. Tikoo, A., Varga, M., Ramesh, V., Gusella, J., and Maruta, H. (1994) An anti-Ras function of neurofibromatosis type 2 gene product (NF2/Merlin). *Journal of Biological Chemistry* **269**, 23387-23390
114. Lutchman, M., and Rouleau, G. A. (1995) The neurofibromatosis type 2 gene product, schwannomin, suppresses growth of NIH 3T3 cells. *Cancer Research* **55**, 2270-2274
115. Harvey, K., and Tapon, N. (2007) The Salvador-Warts-Hippo pathway - an emerging tumour-suppressor network. *Nature Reviews Cancer* **7**, 182-191
116. Halder, G., and Johnson, R. L. (2011) Hippo signaling: growth control and beyond. *Development* **138**, 9-22
117. Li, Y. J., Zhou, H., Li, F. Z., Chan, S. W., Lin, Z. J., Wei, Z. Y., Yang, Z., Guo, F. S., Lim, C. J., Xing, W. C., Shen, Y. Q., Hong, W. J., Long, J. F., and Zhang, M. J. (2015) Angiomotin binding-induced activation of Merlin/NF2 in the Hippo pathway. *Cell Research* **25**, 801-817
118. Li, W., Cooper, J., Zhou, L., Yang, C. Y., Erdjument-Bromage, H., Zagzag, D., Snuderl, M., Ladanyi, M., Hanemann, C. O., Zhou, P. B., Karajannis, M. A., and Giancotti, F. G. (2014) Merlin/NF2 Loss-Driven Tumorigenesis Linked to CRL4(DCAF1)-Mediated Inhibition of the Hippo Pathway Kinases Lats1 and 2 in the Nucleus. *Cancer Cell* **26**, 48-60
119. Hikasa, H., Sekido, Y., and Suzuki, A. (2016) Merlin/NF2-Lin28B-let-7 Is a Tumor-Suppressive Pathway that Is Cell-Density Dependent and Hippo Independent. *Cell Reports* **14**, 2950-2961
120. Kressel, M., and Schmucker, B. (2019) Nucleocytoplasmic transfer of the NF2 tumor suppressor protein merlin is regulated by exon 2 and a CRM1-dependent nuclear export signal in exon 15. *Human Molecular Genetics* **11**, 2269-2278
121. Wells, C. D., Fawcett, J. P., Traweger, A., Yamanaka, Y., Goudreault, M., Elder, K., Kulkarni, S., Gish, G., Virag, C., Lim, C., Colwill, K., Starostine, A., Metalnikov, P., and Pawson, T. (2006) A Rich1/Amot complex regulates the Cdc42 GTPase and apical-polarity proteins in epithelial cells. *Cell* **125**, 535-548
122. Nishimura, M., Kakizaki, M., Ono, Y., Morimoto, K., Takeuchi, M., Inoue, Y., Imai, T., and Takai, Y. (2002) JEAP, a novel component of tight junctions in exocrine cells. *Journal of Biological Chemistry* **277**, 5583-5587

123. Ernkvist, M., Birot, O., Sinha, I., Veitonmaki, N., Nystrom, S., Aase, K., and Holmgren, L. (2008) Differential roles of p80- and p130-angiomotin in the switch between migration and stabilization of endothelial cells. *Biochimica et Biophysica Acta-Molecular Cell Research* **1783**, 429-437
124. Sugihara-Mizuno, Y., Adachi, M., Kobayashi, Y., Hamazaki, Y., Nishimura, M., Imai, T., Furuse, M., and Tsukita, S. (2007) Molecular characterization of angiomotin/JEAP family proteins: interaction with MUPP1/Patj and their endogenous properties. *Genes Cells* **12**, 473-486
125. Ernkvist, M., Aase, K., Ukomadu, C., Wohlschlegel, J., Blackman, R., Veitonmaki, N., Bratt, A., Dutta, A., and Holmgren, L. (2006) p130-Angiomotin associates to actin and controls endothelial cell shape. *FEBS Journal* **273**, 2000-2011
126. Dai, X. M., She, P. L., Chi, F. T., Feng, Y., Liu, H., Jin, D. Q., Zhao, Y. Q., Guo, X. C., Jiang, D. D., Guan, K. L., Zhong, T. P., and Zhao, B. (2013) Phosphorylation of Angiomotin by Lats1/2 Kinases Inhibits F-actin Binding, Cell Migration, and Angiogenesis. *Journal of Biological Chemistry* **288**, 34041-34051
127. Zheng, Y., Vertuani, S., Nystrom, S., Audebert, S., Meijer, I., Tegnebratt, T., Borg, J. P., Uhlen, P., Majumdar, A., and Holmgren, L. (2009) Angiomotin-like protein 1 controls endothelial polarity and junction stability during sprouting angiogenesis. *Circulation Research* **105**, 260-270
128. Gagne, V., Moreau, J., Plourde, M., Lapointe, M., Lord, M., Gagnon, E., and Fernandes, M. J. (2009) Human angiomotin-like 1 associates with an angiomotin protein complex through its coiled-coil domain and induces the remodeling of the actin cytoskeleton. *Cell Motility and the Cytoskeleton* **66**, 754-768
129. Yi, C. L., Shen, Z. W., Stemmer-Rachamimov, A., Dawany, N., Troutman, S., Showe, L. C., Liu, Q., Shimono, A., Sudol, M., Holmgren, L., Stanger, B. Z., and Kissil, J. L. (2013) The p130 Isoform of Angiomotin Is Required for Yap-Mediated Hepatic Epithelial Cell Proliferation and Tumorigenesis. *Science Signaling* **6**, 12
130. Lv, M., Chen, L., Qin, T., Zhang, X., Liu, P., and Yang, J. (2015) Angiomotin promotes breast cancer cell proliferation and invasion. *Oncology Reports* **33**, 1938-1946
131. Lv, M., Li, S., Luo, C., Zhang, X., Shen, Y., Sui, Y. X., Wang, F., Wang, X., Yang, J., and Liu, P. (2016) Angiomotin promotes renal epithelial and carcinoma cell proliferation by retaining the nuclear YAP. *Oncotarget* **7**, 12393-12403
132. Ortiz, A., Zeng, H., and Lin, S. H. (2014) Angiomotin regulates the Hippo pathway to increase prostate cancer cell growth. *Cancer Research* **74**, 1
133. Yi, C., Shen, Z., Stemmer-Rachamimov, A., Dawany, N., Troutman, S., Showe, L. C., Liu, Q., Shimono, A., Sudol, M., Holmgren, L., Stanger, B. Z., and Kissil, J. L. (2013) The p130 isoform of angiomotin is required for Yap-mediated hepatic epithelial cell proliferation and tumorigenesis. *Science Signaling* **6**, ra77
134. Artinian, N., Cloninger, C., Holmes, B., Benavides-Serrato, A., Bashir, T., and Gera, J. (2015) Phosphorylation of the Hippo Pathway Component AMOTL2 by the mTORC2 Kinase Promotes YAP Signaling, Resulting in Enhanced Glioblastoma Growth and Invasiveness. *Journal of Biological Chemistry* **290**, 19387-19401
135. Hsu, Y. L., Hung, J. Y., Chou, S. H., Huang, M. S., Tsai, M. J., Lin, Y. S., Chiang, S. Y., Ho, Y. W., Wu, C. Y., and Kuo, P. L. (2015) Angiomotin decreases lung cancer progression by sequestering oncogenic YAP/TAZ and decreasing Cyr61 expression. *Oncogene* **34**, 4056-4068
136. Wang, Y., Justilien, V., Brennan, K. I., Jamieson, L., Murray, N. R., and Fields, A. P. (2017) PKC δ regulates nuclear YAP1 localization and ovarian cancer tumorigenesis. *Oncogene* **36**, 534-545
137. Oka, T., Schmitt, A. P., and Sudol, M. (2012) Opposing roles of angiomotin-like-1 and zona occludens-2 on proapoptotic function of YAP. *Oncogene* **31**, 128-134
138. Wang, W. Q., Huang, J., and Chen, J. J. (2011) Angiomotin-like Proteins Associate with and Negatively Regulate YAP1. *Journal of Biological Chemistry* **286**, 4364-4370
139. Sowa, M. E., Bennett, E. J., Gygi, S. P., and Harper, J. W. (2009) Defining the Human Deubiquitinating Enzyme Interaction Landscape. *Cell* **138**, 389-403

140. Paramasivam, M., Sarkeshik, A., Yates, J. R., III, Fernandes, M. J. G., and McCollum, D. (2011) Angiomotin family proteins are novel activators of the LATS2 kinase tumor suppressor. *Molecular Biology of the Cell* **22**, 3725-3733
141. Mana-Capelli, S., and McCollum, D. (2018) Angiomotins stimulate LATS kinase autophosphorylation and act as scaffolds that promote Hippo signaling. *Journal of Biological Chemistry* **293**, 18230-18241
142. Adler, J. J., Johnson, D. E., Heller, B. L., Bringman, L. R., Ranahan, W. P., Conwell, M. D., Sun, Y., Hudmon, A., and Wells, C. D. (2013) Serum deprivation inhibits the transcriptional co-activator YAP and cell growth via phosphorylation of the 130-kDa isoform of Angiomotin by the LATS1/2 protein kinases. *Proceedings of the National Academy of Sciences of the United States of America* **110**, 17368-17373
143. Adler, J. J., Heller, B. L., Bringman, L. R., Ranahan, W. P., Cocklin, R. R., Goebel, M. G., Oh, M., Lim, H. S., Ingham, R. J., and Wells, C. D. (2013) Amot130 Adapts Atrophin-1 Interacting Protein 4 to Inhibit Yes-associated Protein Signaling and Cell Growth. *Journal of Biological Chemistry* **288**, 15181-15193
144. Mana-Capelli, S., Paramasivam, M., Dutta, S., and McCollum, D. (2014) Angiomotins link F-actin architecture to Hippo pathway signaling. *Molecular Biology of the Cell* **25**, 2
145. Moleirinho, S., Hoxha, S., Mandati, V., Curtale, G., Troutman, S., Ehmer, U., and Kissil, J. L. (2017) Regulation of localization and function of the transcriptional co-activator YAP by angiomotin. *Elife* **6**
146. Yi, C., Troutman, S., Kissil, J. L., Shimono, A., Giovannini, M., Shen, Z., Liu, Q., Showe, L. C., Stanger, B. Z., Holmgren, L., Stemmer-Rachamimov, A., Sudol, M., and Dawany, N. (2013) Expression analysis of YAP and Angiomotin target genes. ArrayExpress Archive
147. Ragni, C. V., Diguët, N., Le Garrec, J. F., Novotova, M., Resende, T. P., Pop, S., Charon, N., Guillemot, L., Kitasato, L., Badouel, C., Dufour, A., Olivo-Marin, J. C., Trouve, A., McNeill, H., and Meilhac, S. M. (2017) Amotl1 mediates sequestration of the Hippo effector Yap1 downstream of Fat4 to restrict heart growth. *Nature Communication* **8**, 14582
148. Chen, Q., Zhang, N. L., Xie, R., Wang, W., Cai, J., Choi, K. S., David, K. K., Huang, B., Yabuta, N., Nojima, H., Anders, R. A., and Pan, D. J. (2015) Homeostatic control of Hippo signaling activity revealed by an endogenous activating mutation in YAP. *Genes & Development* **29**, 1285-1297
149. Dai, X. M., Liu, H., Shen, S. Y., Guo, X. C., Yan, H., Ji, X. Y., Li, L., Huang, J., Feng, X. H., and Zhao, B. (2015) YAP activates the Hippo pathway in a negative feedback loop. *Cell Research* **25**, 1175-1178
150. Moroishi, T., Park, H. W., Qin, B. D., Chen, Q., Meng, Z. P., Plouffe, S. W., Taniguchi, K., Yu, F. X., Karin, M., Pan, D. J., and Guan, K. L. (2015) A YAP/TAZ-induced feedback mechanism regulates Hippo pathway homeostasis. *Genes & Development* **29**, 1271-1284
151. Gonzalez-Mariscal, L., Ponce, A., Alarcon, L., and Jaramillo, B. E. (2006) The tight junction protein ZO-2 has several functional nuclear export signals. *Experimental Cell Research* **312**, 3323-3335
152. Jaramillo, B. E., Ponce, A., Moreno, J., Betanzos, A., Huerta, M., Lopez-Bayghen, E., and Gonzalez-Mariscal, L. (2004) Characterization of the tight junction protein ZO-2 localized at the nucleus of epithelial cells. *Experimental Cell Research* **297**, 247-258
153. Islas, S., Vega, J., Ponce, L., and Gonzalez-Mariscal, L. (2002) Nuclear localization of the tight junction protein ZO-2 in epithelial cells. *Experimental Cell Research* **274**, 138-148
154. Tapia, R., Huerta, M., Islas, S., Avila-Flores, A., Lopez-Bayghen, E., Weiske, J., Huber, O., and Gonzalez-Mariscal, L. (2009) Zona occludens-2 inhibits cyclin D1 expression and cell proliferation and exhibits changes in localization along the cell cycle. *Molecular Biology of the Cell* **20**, 1102-1117
155. Quiros, M., Alarcon, L., Ponce, A., Giannakouros, T., and Gonzalez-Mariscal, L. (2013) The intracellular fate of zonula occludens 2 is regulated by the phosphorylation of SR repeats and the phosphorylation/O-GlcNAcylation of S257. *Molecular Biology of the Cell* **24**, 2528-2543

156. Chamorro, D., Alarcon, L., Ponce, A., Tapia, R., Gonzalez-Aguilar, H., Robles-Flores, M., Mejia-Castillo, T., Segovia, J., Bandala, Y., Juaristi, E., and Gonzalez-Mariscal, L. (2009) Phosphorylation of zona occludens-2 by protein kinase C epsilon regulates its nuclear exportation. *Molecular Biology of the Cell* **20**, 4120-4129
157. Assemat, E., Bazellieres, E., Pallesi-Pocachard, E., Le Bivic, A., and Massey-Harroche, D. (2008) Polarity complex proteins. *Biochimica et Biophysica Acta-Biomembranes* **1778**, 614-630
158. Rodriguez-Boulan, E., and Macara, I. G. (2014) Organization and execution of the epithelial polarity programme. *Nature Reviews Molecular Cell Biology* **15**, 225-242
159. Cordenonsi, M., Zanconato, F., Azzolin, L., Forcato, M., Rosato, A., Frasson, C., Inui, M., Montagner, M., Parenti, A. R., Poletti, A., Daidone, M. G., Dupont, S., Basso, G., Bicciato, S., and Piccolo, S. (2011) The Hippo Transducer TAZ Confers Cancer Stem Cell-Related Traits on Breast Cancer Cells. *Cell* **147**, 759-772
160. Mohseni, M., Sun, J. L., Lau, A., Curtis, S., Goldsmith, J., Fox, V. L., Wei, C. J., Frazier, M., Samson, O., Wong, K. K., Kim, C., and Camargo, F. D. (2014) A genetic screen identifies an LKB1-MARK signalling axis controlling the Hippo-YAP pathway. *Nature Cell Biology* **16**, 108-+
161. Elsum, I. A., Yates, L. L., Pearson, H. B., Pheesse, T. J., Long, F., O'Donoghue, R., Ernst, M., Cullinane, C., and Humbert, P. O. (2014) Scrib heterozygosity predisposes to lung cancer and cooperates with KRas hyperactivation to accelerate lung cancer progression in vivo. *Oncogene* **33**, 5523-5533
162. Martin-Belmonte, F., and Perez-Moreno, M. (2011) Epithelial cell polarity, stem cells and cancer. *Nature Reviews Cancer* **12**, 23-38
163. Pearson, H. B., Perez-Mancera, P. A., Dow, L. E., Ryan, A., Tennstedt, P., Bogani, D., Elsum, I., Greenfield, A., Tuveson, D. A., Simon, R., and Humbert, P. O. (2011) SCRIB expression is deregulated in human prostate cancer, and its deficiency in mice promotes prostate neoplasia. *Journal of Clinical Investigation* **121**, 4257-4267
164. Zhan, L., Rosenberg, A., Bergami, K. C., Yu, M., Xuan, Z., Jaffe, A. B., Allred, C., and Muthuswamy, S. K. (2008) Deregulation of scribble promotes mammary tumorigenesis and reveals a role for cell polarity in carcinoma. *Cell* **135**, 865-878
165. Lemmers, C., Michel, D., Lane-Guermonprez, L., Delgrossi, M. H., Medina, E., Arsanto, J. P., and Le Bivic, A. (2004) CRB3 binds directly to Par6 and regulates the morphogenesis of the tight junctions in mammalian epithelial cells. *Molecular Biology of the Cell* **15**, 1324-1333
166. Fogg, V. C., Liu, C. J., and Margolis, B. (2005) Multiple regions of Crumbs3 are required for tight junction formation in MCF10A cells. *Journal of Cell Science* **118**, 2859-2869
167. Makarova, O., Roh, M. H., Liu, C. J., Laurinec, S., and Margolis, B. (2003) Mammalian Crumbs3 is a small transmembrane protein linked to protein associated with Lin-7 (Pals1). *Gene* **302**, 21-29
168. Roh, M. H., Makarova, O., Liu, C. J., Shin, K., Lee, S., Laurinec, S., Goyal, M., Wiggins, R., and Margolis, B. (2002) The Maguk protein, Pals1, functions as an adapter, linking mammalian homologues of Crumbs and Discs Lost. *Journal of Cell Biology* **157**, 161-172
169. Mao, X. N., Li, P. P., Wang, Y. C., Liang, Z. Y., Liu, J., Li, J., Jiang, Y. N., Bao, G., Li, L., Zhu, B. F., Ren, Y., Zhao, X. H., Zhang, J. M., Liu, Y., Yang, J., and Liu, P. J. (2017) CRB3 regulates contact inhibition by activating the Hippo pathway in mammary epithelial cells. *Cell Death & Disease* **8**, 13
170. Suzuki, A., and Ohno, S. (2006) The PAR-aPKC system: lessons in polarity. *Journal of Cell Science* **119**, 979-987
171. Lv, X. B., Liu, C. Y., Wang, Z., Sun, Y. P., Xiong, Y., Lei, Q. Y., and Guan, K. L. (2015) PARD3 induces TAZ activation and cell growth by promoting LATS1 and PP1 interaction. *EMBO Reports* **16**, 975-985
172. Zhang, P., Wang, S. T., Wang, S., Qiao, J., Zhang, L., Zhang, Z., and Chen, Z. J. (2016) Dual function of partitioning-defective 3 in the regulation of YAP phosphorylation and activation. *Cell Discovery* **2**, 17
173. Vogel, V., and Sheetz, M. (2006) Local force and geometry sensing regulate cell functions. *Nature Reviews Molecular Cell Biology* **7**, 265-275

174. Parsons, J. T., Horwitz, A. R., and Schwartz, M. A. (2010) Cell adhesion: integrating cytoskeletal dynamics and cellular tension. *Nature Reviews Molecular Cell Biology* **11**, 633-643
175. Janmey, P. A., and Miller, R. T. (2011) Mechanisms of mechanical signaling in development and disease. *Journal of Cell Science* **124**, 9-18
176. Discher, D. E., Mooney, D. J., and Zandstra, P. W. (2009) Growth Factors, Matrices, and Forces Combine and Control Stem Cells. *Science* **324**, 1673-1677
177. Jaalouk, D. E., and Lammerding, J. (2009) Mechanotransduction gone awry. *Nature Reviews Molecular Cell Biology* **10**, 63-73
178. Mammoto, A., and Ingber, D. E. (2009) Cytoskeletal control of growth and cell fate switching. *Current Opinion in Cell Biology* **21**, 864-870
179. Wozniak, M. A., and Chen, C. S. (2009) Mechanotransduction in development: a growing role for contractility. *Nature Reviews Molecular Cell Biology* **10**, 34-43
180. Dupont, S., Morsut, L., Aragona, M., Enzo, E., Giulitti, S., Cordenonsi, M., Zanconato, F., Le Digabel, J., Forcato, M., Bicciato, S., Elvassore, N., and Piccolo, S. (2011) Role of YAP/TAZ in mechanotransduction. *Nature* **474**, 179-U212
181. Wrighton, K. H. (2011) Mechanotransduction: YAP and TAZ feel the force. *Nature reviews. Molecular cell biology* **12**, 404
182. Gaspar, P., and Tapon, N. (2014) Sensing the local environment: actin architecture and Hippo signalling. *Current Opinion in Cell Biology* **31**, 74-83
183. Matsui, Y., and Lai, Z. C. (2013) Mutual regulation between Hippo signaling and actin cytoskeleton. *Protein Cell* **4**, 904-910
184. Murrell, M., Oakes, P. W., Lenz, M., and Gardel, M. L. (2015) Forcing cells into shape: the mechanics of actomyosin contractility. *Nature Reviews Molecular Cell Biology* **16**, 486-498
185. Meng, Z., Moroishi, T., Mottier-Pavie, V., Plouffe, S. W., Hansen, C. G., Hong, A. W., Park, H. W., Mo, J. S., Lu, W., Lu, S., Flores, F., Yu, F. X., Halder, G., and Guan, K. L. (2015) MAP4K family kinases act in parallel to MST1/2 to activate LATS1/2 in the Hippo pathway. *Nature Communications* **6**, 8357
186. Wada, K., Itoga, K., Okano, T., Yonemura, S., and Sasaki, H. (2011) Hippo pathway regulation by cell morphology and stress fibers. *Development* **138**, 3907-3914
187. Zhao, B., Li, L., Wang, L., Wang, C. Y., Yu, J. D., and Guan, K. L. (2012) Cell detachment activates the Hippo pathway via cytoskeleton reorganization to induce anoikis. *Genes & Development* **26**, 54-68
188. Aragona, M., Panciera, T., Manfrin, A., Giulitti, S., Michielin, F., Elvassore, N., Dupont, S., and Piccolo, S. (2013) A Mechanical Checkpoint Controls Multicellular Growth through YAP/TAZ Regulation by Actin-Processing Factors. *Cell* **154**, 1047-1059
189. Piccolo, S., Dupont, S., and Cordenonsi, M. (2014) The biology of YAP/TAZ: Hippo signaling and beyond. *Physiological Reviews* **94**, 1287-1312
190. Zhou, D. W., Conrad, C., Xia, F., Park, J. S., Payer, B., Yin, Y., Lauwers, G. Y., Thasler, W., Lee, J. T., Avruch, J., and Bardeesy, N. (2009) Mst1 and Mst2 Maintain Hepatocyte Quiescence and Suppress Hepatocellular Carcinoma Development through Inactivation of the Yap1 Oncogene. *Cancer Cell* **16**, 425-438
191. Panciera, T., Azzolin, L., Cordenonsi, M., and Piccolo, S. (2017) Mechanobiology of YAP and TAZ in physiology and disease. *Nature Reviews Molecular Cell Biology* **18**, 758-770
192. Calvo, F., Ege, N., Grande-Garcia, A., Hooper, S., Jenkins, R. P., Chaudhry, S. I., Harrington, K., Williamson, P., Moeendarbary, E., Charras, G., and Sahai, E. (2013) Mechanotransduction and YAP-dependent matrix remodelling is required for the generation and maintenance of cancer-associated fibroblasts. *Nature Cell Biology* **15**, 637-646

193. Totaro, A., Castellan, M., Battilana, G., Zanconato, F., Azzolin, L., Giulitti, S., Cordenonsi, M., and Piccolo, S. (2017) YAP/TAZ link cell mechanics to Notch signalling to control epidermal stem cell fate. *Nature Communications* **8**, 15206
194. Musah, S., Wrighton, P. J., Zaltsman, Y., Zhong, X., Zorn, S., Parlato, M. B., Hsiao, C., Palecek, S. P., Chang, Q., Murphy, W. L., and Kiessling, L. L. (2014) Substratum-induced differentiation of human pluripotent stem cells reveals the coactivator YAP is a potent regulator of neuronal specification. *Proceedings of the National Academy of Sciences of the United States of America* **111**, 13805-13810
195. Sun, Y., Yong, K. M., Villa-Diaz, L. G., Zhang, X., Chen, W., Philson, R., Weng, S., Xu, H., Krebsbach, P. H., and Fu, J. (2014) Hippo/YAP-mediated rigidity-dependent motor neuron differentiation of human pluripotent stem cells. *Nature Materials* **13**, 599-604
196. Bertero, T., Cottrill, K. A., Lu, Y., Haeger, C. M., Dieffenbach, P., Annis, S., Hale, A., Bhat, B., Kaimal, V., Zhang, Y., Y., Graham, B. B., Kumar, R., Sagggar, R., Wallace, W. D., Ross, D. J., Black, S. M., Fratz, S., Fineman, J. R., Vargas, S. O., Haley, K. J., Waxman, A. B., Chau, B. N., Fredenburgh, L. E., and Chan, S. Y. (2015) Matrix Remodeling Promotes Pulmonary Hypertension through Feedback Mechanoactivation of the YAP/TAZ-miR-130/301 Circuit. *Cell Reports* **13**, 1016-1032
197. Bertero, T., Oldham, W. M., Cottrill, K. A., Pisano, S., Vanderpool, R. R., Yu, Q., Zhao, J., Tai, Y., Tang, Y., Zhang, Y., Y., Rehman, S., Sugahara, M., Qi, Z., Gorcsan, J., 3rd, Vargas, S. O., Sagggar, R., Wallace, W. D., Ross, D. J., Haley, K. J., Waxman, A. B., Parikh, V. N., De Marco, T., Hsue, P. Y., Morris, A., Simon, M. A., Norris, K. A., Gaggioli, C., Loscalzo, J., Fessel, J., and Chan, S. Y. (2016) Vascular stiffness mechanoactivates YAP/TAZ-dependent glutaminolysis to drive pulmonary hypertension. *Journal of Clinical Investigation* **126**, 3313-3335
198. Mannaerts, I., Leite, S. B., Verhulst, S., Claerhout, S., Eysackers, N., Thoen, L. F., Hoorens, A., Reynaert, H., Halder, G., and van Grunsven, L. A. (2015) The Hippo pathway effector YAP controls mouse hepatic stellate cell activation. *Journal of Hepatology* **63**, 679-688
199. Caliani, S. R., Perepelyuk, M., Cosgrove, B. D., Tsai, S. J., Lee, G. Y., Mauck, R. L., Wells, R. G., and Burdick, J. A. (2016) Stiffening hydrogels for investigating the dynamics of hepatic stellate cell mechanotransduction during myofibroblast activation. *Scientific Reports* **6**, 21387
200. Wang, K. C., Yeh, Y. T., Nguyen, P., Limqueco, E., Lopez, J., Thorossian, S., Guan, K. L., Li, Y. J., and Chien, S. (2016) Flow-dependent YAP/TAZ activities regulate endothelial phenotypes and atherosclerosis. *Proceedings of the National Academy of Sciences of the United States of America* **113**, 11525-11530
201. Wang, L., Luo, J. Y., Li, B., Tian, X. Y., Chen, L. J., Huang, Y., Liu, J., Deng, D., Lau, C. W., Wan, S., Ai, D., Mak, K. K., Tong, K. K., Kwan, K. M., Wang, N., Chiu, J. J., and Zhu, Y. (2016) Integrin-YAP/TAZ-JNK cascade mediates atheroprotective effect of unidirectional shear flow. *Nature* **540**, 579-582
202. Nakajima, H., Yamamoto, K., Agarwala, S., Terai, K., Fukui, H., Fukuhara, S., Ando, K., Miyazaki, T., Yokota, Y., Schmelzer, E., Belting, H. G., Affolter, M., Lecaudey, V., and Mochizuki, N. (2017) Flow-Dependent Endothelial YAP Regulation Contributes to Vessel Maintenance. *Developmental Cell* **40**, 523-536.e526
203. Zhong, W., Zhang, W., Wang, S., and Qin, J. (2013) Regulation of fibrochondrogenesis of mesenchymal stem cells in an integrated microfluidic platform embedded with biomimetic nanofibrous scaffolds. *PLoS One* **8**, e61283
204. Kim, K. M., Choi, Y. J., Hwang, J. H., Kim, A. R., Cho, H. J., Hwang, E. S., Park, J. Y., Lee, S. H., and Hong, J. H. (2014) Shear stress induced by an interstitial level of slow flow increases the osteogenic differentiation of mesenchymal stem cells through TAZ activation. *PLoS One* **9**, e92427
205. He, M. J., Zhou, Z., Shah, A. A., Hong, Y., Chen, Q. M., and Wan, Y. (2016) New insights into posttranslational modifications of Hippo pathway in carcinogenesis and therapeutics. *Cell Division* **11**, 10
206. Wang, C., Zhang, W. X., Yin, M. X., Hu, L. X., Li, P. X., Xu, J. J., Huang, H. L., Wang, S. M., Lu, Y., Wu, W. Q., Ho, M. S., Li, L., Zhao, Y., and Zhang, L. (2015) Suppressor of Deltex mediates Pez degradation and modulates Drosophila midgut homeostasis. *Nature Communications* **6**, 10

207. Bae, S. J., Kim, M., Kim, S. H., Kwon, Y. E., Lee, J. H., Kim, J., Chung, C. H., Lee, W. J., and Seol, J. H. (2015) NEDD4 controls intestinal stem cell homeostasis by regulating the Hippo signalling pathway. *Nature Communications* **6**, 15
208. Wang, J., Peng, Q. S., Lin, Q., Childress, C., Carey, D., and Yang, W. N. (2010) Calcium Activates Nedd4 E3 Ubiquitin Ligases by Releasing the C2 Domain-mediated Auto-inhibition. *Journal of Biological Chemistry* **285**, 12279-12288
209. Liu, J., Wan, L. X., Liu, P. D., Inuzuka, H., Liu, J. K., Wang, Z. W., and Wei, W. Y. (2014) SCF beta-TRCP-mediated degradation of NEDD4 inhibits tumorigenesis through modulating the PTEN/Akt signaling pathway. *Oncotarget* **5**, 1026-1036
210. Overholtzer, M., Zhang, J., Smolen, G. A., Muir, B., Li, W., Sgroi, D. C., Deng, C. X., Brugge, J. S., and Haber, D. A. (2006) Transforming properties of YAP, a candidate oncogene on the chromosome 11q22 amplicon. *Proceedings of the National Academy of Sciences of the United States of America* **103**, 12405-12410
211. Lei, Q. Y., Zhang, H., Zhao, B., Zha, Z. Y., Bai, F., Pei, X. H., Zhao, S., Xiong, Y., and Guan, K. L. (2008) TAZ promotes cell proliferation and epithelial-mesenchymal transition and is inhibited by the hippo pathway. *Molecular and Cellular Biology* **28**, 2426-2436
212. Oka, T., and Sudol, M. (2009) Nuclear localization and pro-apoptotic signaling of YAP2 require intact PDZ-binding motif. *Genes to Cells* **14**, 607-615
213. Takahashi, K., and Yamanaka, S. (2006) Induction of pluripotent stem cells from mouse embryonic and adult fibroblast cultures by defined factors. *Cell* **126**, 663-676
214. Mo, J. S., Park, H. W., and Guan, K. L. (2014) The Hippo signaling pathway in stem cell biology and cancer. *EMBO Reports* **15**, 642-656
215. Xu, M. Z., Yao, T. J., Lee, N. P. Y., Ng, I. O. L., Chan, Y. T., Zender, L., Lowe, S. W., Poon, R. T. P., and Luk, J. M. (2009) Yes-Associated Protein Is an Independent Prognostic Marker in Hepatocellular Carcinoma. *Cancer* **115**, 4576-4585
216. Harvey, K. F., Zhang, X. M., and Thomas, D. M. (2013) The Hippo pathway and human cancer. *Nature Reviews Cancer* **13**, 246-257
217. Steinhardt, A. A., Gayyed, M. F., Klein, A. P., Dong, J. X., Maitra, A., Pan, D., Montgomery, E. A., and Anders, R. A. (2008) Expression of Yes-associated protein in common solid tumors. *Human Pathology* **39**, 1582-1589
218. Ma, Y. L., Yang, Y. Z., Wang, F., Wei, Q., and Qin, H. L. (2015) Hippo-YAP signaling pathway: A new paradigm for cancer therapy. *International Journal of Cancer* **137**, 2275-2286
219. Sudol, M., Shields, D. C., and Farooq, A. (2012) Structures of YAP protein domains reveal promising targets for development of new cancer drugs. *Seminars in Cell & Developmental Biology* **23**, 827-833
220. Zhang, J. M., Yang, P. L., and Gray, N. S. (2009) Targeting cancer with small molecule kinase inhibitors. *Nature Reviews Cancer* **9**, 28-39
221. Couzens, A. L., Knight, J. D. R., Kean, M. J., Teo, G., Weiss, A., Dunham, W. H., Lin, Z. Y., Bagshaw, R. D., Sicheri, F., Pawson, T., Wrana, J. L., Choi, H., and Gingras, A. C. (2013) Protein Interaction Network of the Mammalian Hippo Pathway Reveals Mechanisms of Kinase-Phosphatase Interactions. *Science Signaling* **6**, 12
222. Huttlin, E. L., Ting, L., Bruckner, R. J., Gebreab, F., Gygi, M. P., Szpyt, J., Tam, S., Zarraga, G., Colby, G., Baltier, K., Dong, R., Guarani, V., Vaites, L. P., Ordureau, A., Rad, R., Erickson, B. K., Wuhr, M., Chick, J., Zhai, B., Kolippakkam, D., Mintseris, J., Obar, R. A., Harris, T., Artavanis-Tsakonas, S., Sowa, M. E., De Camilli, P., Paulo, J. A., Harper, J. W., and Gygi, S. P. (2015) The BioPlex Network: A Systematic Exploration of the Human Interactome. *Cell* **162**, 425-440
223. Patrie, K. M. (2005) Identification and characterization of a novel tight junction-associated family of proteins that interacts with a WW domain of MAGI-1. *Biochimica Et Biophysica Acta-Molecular Cell Research* **1745**, 131-144

224. Bratt, A., Birot, O., Sinha, I., Veitonmaki, N., Aase, K., Ernkvist, M., and Holmgren, L. (2005) Angiomotin regulates endothelial cell-cell junctions and cell motility. *Journal of Biological Chemistry* **280**, 34859-34869
225. Dobrosotskaya, I., Guy, R. K., and James, G. L. (1997) MAGI-1, a membrane-associated guanylate kinase with a unique arrangement of protein-protein interaction domains. *Journal of Biological Chemistry* **272**, 31589-31597
226. Hirao, K., Hata, Y., Ide, N., Takeuchi, M., Irie, M., Yao, I., Deguchi, M., Toyoda, A., Sudhof, T. C., and Takai, Y. (1998) A novel multiple PDZ domain-containing molecule interacting with N-methyl-D-aspartate receptors and neuronal cell adhesion proteins. *Journal of Biological Chemistry* **273**, 21105-21110
227. Wu, X., Hepner, K., Castelino-Prabhu, S., Do, D., Kaye, M. B., Yuan, X. J., Wood, J., Ross, C., Sawyers, C. L., and Whang, Y. E. (2000) Evidence for regulation of the PTEN tumor suppressor by a membrane-localized multi-PDZ domain containing scaffold protein MAGI-2. in *Proceedings of the National Academy of Sciences of the United States of America*. pp 4233-4238
228. Javier, R. T., and Rice, A. P. (2011) Emerging theme: cellular PDZ proteins as common targets of pathogenic viruses. *Journal of Virology* **85**, 11544-11556
229. Sudol, M. (1998) From Src Homology domains to other signaling modules: proposal of the 'protein recognition code'. *Oncogene* **17**, 1469-1474
230. Kim, E., Naisbitt, S., Hsueh, Y. P., Rao, A., Rothschild, A., Craig, A. M., and Sheng, M. (1997) GKAP, a novel synaptic protein that interacts with the guanylate kinase-like domain of the PSD-95/SAP90 family of channel clustering molecules. *Journal of Cell Biology* **136**, 669-678
231. Takeuchi, M., Hata, Y., Hirao, K., Toyoda, A., Irie, M., and Takai, Y. (1997) SAPAPs - A family of PSD-95/SAP90-associated proteins localized at postsynaptic density. *Journal of Biological Chemistry* **272**, 11943-11951
232. Zhu, J., Shang, Y., Xia, C., Wang, W., Wen, W., and Zhang, M. (2011) Guanylate kinase domains of the MAGUK family scaffold proteins as specific phospho-protein-binding modules. *EMBO Journal* **30**, 4986-4997
233. Laura, R. P., Ross, S., Koeppen, H., and Lasky, L. A. (2002) MAGI-1: A widely expressed, alternatively spliced tight junction protein. *Experimental Cell Research* **275**, 155-170
234. Nishimura, W., Iizuka, T., Hirabayashi, S., Tanaka, N., and Hata, Y. (2000) Localization of BAI-associated protein1/membrane-associated guanylate kinase-1 at adherens junctions in normal rat kidney cells: Polarized targeting mediated by the carboxyl-terminal PDZ domains. *Journal of Cellular Physiology* **185**, 358-365
235. Hirabayashi, S., Tajima, M., Yao, I., Nishimura, W., Mori, H., and Hata, Y. (2003) JAM4, a junctional cell adhesion molecule interacting with a tight junction protein, MAGI-1. *Molecular Cell Biology* **23**, 4267-4282
236. Patrie, K. M., Drescher, A. J., Welihinda, A., Mundel, P., and Margolis, B. (2002) Interaction of two actin-binding proteins, synaptopodin and alpha-actinin-4, with the tight junction protein MAGI-1. *Journal of Biological Chemistry* **277**, 30183-30190
237. Dobrosotskaya, I. Y., and James, G. L. (2000) MAGI-1 interacts with beta-catenin and is associated with cell-cell adhesion structures. *Biochemical and Biophysical Research Communications* **270**, 903-909
238. Nakai, K., and Horton, P. (1999) PSORT: a program for detecting sorting signals in proteins and predicting their subcellular localization. *Trends in Biochemical Sciences* **24**, 34-35
239. Robbins, J., Dilworth, S. M., Laskey, R. A., and Dingwall, C. (1991) Two independent basic domains in nucleoplasmin nuclear targeting sequence: Identification of a class of bipartite nuclear targeting sequence. *Cell* **64**, 615-623
240. Kranjec, C., and Banks, L. (2011) A systematic analysis of human papillomavirus (HPV) E6 PDZ substrates identifies MAGI-1 as a major target of HPV type 16 (HPV-16) and HPV-18 whose loss accompanies disruption of tight junctions. *Journal of Virology* **85**, 1757-1764
241. Hirao, K., Hata, Y., Yao, I., Deguchi, M., Kawabe, H., Mizoguchi, A., and Takai, Y. (2000) Three isoforms of synaptic scaffolding molecule and their characterization. Multimerization between the isoforms and their interaction

- with N-methyl-D-aspartate receptors and SAP90/PSD-95-associated protein. *Journal of Biological Chemistry* **275**, 2966-2972
242. Adamsky, K., Arnold, K., Sabanay, H., and Peles, E. (2003) Junctional protein MAGI-3 interacts with receptor tyrosine phosphatase beta (RTP beta) and tyrosine-phosphorylated proteins. *Journal of Cell Science* **116**, 1279-1289
243. Ide, N., Hata, Y., Nishioka, H., Hirao, K., Yao, I., Deguchi, M., Mizoguchi, A., Nishimori, H., Tokino, T., Nakamura, Y., and Takai, Y. (1999) Localization of membrane-associated guanylate kinase (MAGI)-1/BAI-associated protein (BAP) 1 at tight junctions of epithelial cells. *Oncogene* **18**, 7810-7815
244. Harris, B. Z., and Lim, W. A. (2001) Mechanism and role of PDZ domains in signaling complex assembly. *Journal of Cell Science* **114**, 3219-3231
245. Zaessinger, S., Zhou, Y. X., Bray, S. J., Tapon, N., and Djiane, A. (2015) Drosophila MAGI interacts with RASSF8 to regulate E-Cadherinbased adherens junctions in the developing eye. *Development* **142**, 1102-1112
246. Padash Barmchi, M., Samarasekera, G., Gilbert, M., Auld, V. J., and Zhang, B. (2016) Magi Is Associated with the Par Complex and Functions Antagonistically with Bazooka to Regulate the Apical Polarity Complex. *PLoS One* **11**, e0153259
247. Stetak, A., and Hajnal, A. (2011) The C. elegans MAGI-1 protein is a novel component of cell junctions that is required for junctional compartmentalization. *Developmental Biology* **350**, 24-31
248. Lynch, A. M., Grana, T., Cox-Paulson, E., Couthier, A., Cameron, M., Chin-Sang, I., Pettitt, J., and Hardin, J. (2012) A genome-wide functional screen shows MAGI-1 is an L1CAM-dependent stabilizer of apical junctions in C. elegans. *Current Biology* **22**, 1891-1899
249. Kawajiri, A., Itoh, N., Fukata, M., Nakagawa, M., Yamaga, M., Iwamatsu, A., and Kaibuchi, K. (2000) Identification of a novel beta-catenin-interacting protein. *Biochemical and Biophysical Research Communications* **273**, 712-717
250. Gujral, T. S., Karp, E. S., Chan, M., Chang, B. H., and MacBeath, G. (2013) Family-wide Investigation of PDZ Domain-Mediated Protein-Protein Interactions Implicates beta-Catenin in Maintaining the Integrity of Tight Junctions. *Chemistry & Biology* **20**, 816-827
251. Ma, Q., Yang, Y., Feng, D., Zheng, S., Meng, R., Fa, P., Zhao, C., Liu, H., Song, R., Tao, T., Yang, L., Dai, J., Wang, S., Jiang, W. G., and He, J. (2015) MAGI3 negatively regulates Wnt/ β -catenin signaling and suppresses malignant phenotypes of glioma cells. *Oncotarget* **6**, 35851-35865
252. Zaric, J., Joseph, J. M., Tercier, S., Sengstag, T., Ponsonnet, L., Delorenzi, M., and Ruegg, C. (2012) Identification of MAGI1 as a tumor-suppressor protein induced by cyclooxygenase-2 inhibitors in colorectal cancer cells. *Oncogene* **31**, 48-59
253. Kotelevets, L., van Hengel, J., Bruyneel, E., Mareel, M., van Roy, F., and Chastre, E. (2004) Implication of the MAGI-1b/PTEN signalosome in stabilization of adherens junctions and suppression of invasiveness. *FASEB Journal* **18**
254. Withanage, K., Nakagawa, K., Ikeda, M., Kurihara, H., Kudo, T., Yang, Z. Y., Sakane, A., Sasaki, T., and Hata, Y. (2012) Expression of RASSF6 in kidney and the implication of RASSF6 and the Hippo pathway in the sorbitol-induced apoptosis in renal proximal tubular epithelial cells. *Journal of Biochemistry* **152**, 111-119
255. Ikeda, M., Kawata, A., Nishikawa, M., Tateishi, Y., Yamaguchi, M., Nakagawa, K., Hirabayashi, S., Bao, Y. J., Hidaka, S., Hirata, Y., and Hata, Y. (2009) Hippo Pathway-Dependent and -Independent Roles of RASSF6. *Science Signaling* **2**, 11
256. Gregorc, U., Ivanova, S., Thomas, M., Guccione, E., Glaunsinger, B., Javier, R., Turk, V., Banks, L., and Turk, B. (2007) Cleavage of MAGI-1, a tight junction PDZ protein, by caspases is an important step for cell-cell detachment in apoptosis. *Apoptosis* **12**, 343-354
257. Ivanova, S., Repnik, U., Banks, L., Turk, V., and Turk, B. (2007) Cellular localization of MAGI-1 caspase cleavage products and their role in apoptosis. *Biological Chemistry* **388**, 1195-1198

258. Javier, R. T. (1994) Adenovirus type 9 E4 open reading frame 1 encodes a transforming protein required for the production of mammary tumors in rats. *Journal of Virology* **68**, 3917-3924
259. Thomas, D. L., Shin, S., Jiang, B. H., Vogel, H., Ross, M. A., Kaplitt, M., Shenk, T. E., and Javier, R. T. (1999) Early region 1 transforming functions are dispensable for mammary tumorigenesis by human adenovirus type 9. *Journal of Virology* **73**, 3071-3079
260. Fields, B. N., Knipe, D. M., and Howley, P. M. (1996) *Fields virology*, Lippincott-Raven Publishers, Philadelphia
261. Glaunsinger, B. A., Lee, S. S., Thomas, M., Banks, L., and Javier, R. (2000) Interactions of the PDZ-protein MAGI-1 with adenovirus E4-ORF1 and high-risk papillomavirus E6 oncoproteins. *Oncogene* **19**, 5270-5280
262. Thomas, M., Glaunsinger, B., Pim, D., Javier, R., and Banks, L. (2001) HPV E6 and MAGUK protein interactions: determination of the molecular basis for specific protein recognition and degradation. *Oncogene* **20**, 5431-5439
263. Kranjec, C., Massimi, P., and Banks, L. (2014) Restoration of MAGI-1 Expression in Human Papillomavirus-Positive Tumor Cells Induces Cell Growth Arrest and Apoptosis. *Journal of Virology* **88**, 7155-7169
264. Thomas, M., Laura, R., Hepner, K., Guccione, E., Sawyers, C., Lasky, L., and Banks, L. (2002) Oncogenic human papillomavirus E6 proteins target the MAGI-2 and MAGI-3 proteins for degradation. *Oncogene* **21**, 5088-5096
265. Khanzada, Z. (2018) *Role Of Magi Proteins In Invasiveness Of Human Colorectal Cancer Cells*. Doctor of Medicine, Cardiff University
266. Noren, E., Mellander, M. R., Almer, S., and Soderman, J. (2018) Genetic Variation and Gene Expression Levels of Tight Junction Genes Indicates Relationships Between PTEN as well as MAGI1 and Microscopic Colitis. *Digestive Diseases and Sciences* **63**, 105-112
267. Noren, E., Almer, S., and Soderman, J. (2017) Genetic variation and expression levels of tight junction genes identifies association between MAGI3 and inflammatory bowel disease. *BMC Gastroenterology* **17**, 68
268. McGovern, D. P., Taylor, K. D., Landers, C., Derkowski, C., Dutridge, D., Dubinsky, M., Ippoliti, A., Vasiliauskas, E., Mei, L., Mengesha, E., King, L., Pressman, S., Targan, S. R., and Rotter, J. I. (2009) MAGI2 genetic variation and inflammatory bowel disease. *Inflammatory Bowel Diseases* **15**, 75-83
269. Wolters, V. M., Xu, W., Zhao, X., Walters, T. D., Griffiths, A. M., Silverberg, M. S., and Muis, A. M. (2011) Replication of genetic variation in the MYO9B gene in Crohn's disease. *Human Immunology* **72**, 592-597
270. Wapenaar, M. C., Monsuur, A. J., van Bodegraven, A. A., Weersma, R. K., Bevova, M. R., Linskens, R. K., Howdle, P., Holmes, G., Mulder, C. J., Dijkstra, G., van Heel, D. A., and Wijmenga, C. (2008) Associations with tight junction genes PARD3 and MAGI2 in Dutch patients point to a common barrier defect for coeliac disease and ulcerative colitis. *Gut* **57**, 463-467
271. Jia, X., Zhai, T., Wang, B., Zhang, J., and Zhang, F. (2018) The MAGI2 gene polymorphism rs2160322 is associated with Graves' disease but not with Hashimoto's thyroiditis. *Journal of Endocrinological Investigation*
272. Meddings, J. B., Jarand, J., Urbanski, S. J., Hardin, J., and Gall, D. G. (1999) Increased gastrointestinal permeability is an early lesion in the spontaneously diabetic BB rat. *American Journal of Physiology-Gastrointestinal and Liver Physiology* **276**, G951-957
273. Groschwitz, K. R., and Hogan, S. P. (2009) Intestinal barrier function: molecular regulation and disease pathogenesis. *Journal of Allergy and Clinical Immunology* **124**, 3-20; quiz 21-22
274. Matsuda, S., and Kitagishi, Y. (2013) MAGI Scaffolding Molecules Involved in Cancer Cell Signaling | OMICS International. *Journal of Carcinogenesis & Mutagenesis* **4**, 1
275. Chastre, E., Abdessamad, M., Kruglov, A., Bruyneel, E., Bracke, M., Di Gioia, Y., Beckerle, M. C., van Roy, F., and Kotelevets, L. (2009) TRIP6, a novel molecular partner of the MAGI-1 scaffolding molecule, promotes invasiveness. *FASEB Journal* **23**, 916-928

276. Georgescu, M. M., Kirsch, K. H., Akagi, T., Shishido, T., and Hanafusa, H. (1999) The tumor-suppressor activity of PTEN is regulated by its carboxyl-terminal region. *Proceedings of the National Academy of Sciences of the United States of America* **96**, 10182-10187
277. Subauste, M. C., Nalbant, P., Adamson, E. D., and Hahn, K. M. (2005) Vinculin controls PTEN protein level by maintaining the interaction of the adherens junction protein beta-catenin with the scaffolding protein MAGI-2. *Journal of Biological Chemistry* **280**, 5676-5681
278. Tolkacheva, T., Boddapati, M., Sanfiz, A., Tsuchida, K., Kimmelman, A. C., and Chan, A. M. (2001) Regulation of PTEN binding to MAGI-2 by two putative phosphorylation sites at threonine 382 and 383. *Cancer Research* **61**, 4985-4989
279. Hu, Y., Li, Z., Guo, L., Wang, L., Zhang, L., Cai, X., Zhao, H., and Zha, X. (2007) MAGI-2 Inhibits cell migration and proliferation via PTEN in human hepatocarcinoma cells. *Archives of Biochemistry and Biophysics* **467**, 1-9
280. Vazquez, F., Grossman, S. R., Takahashi, Y., Rokas, M. V., Nakamura, N., and Sellers, W. R. (2001) Phosphorylation of the PTEN tail acts as an inhibitory switch by preventing its recruitment into a protein complex. *Journal of Biological Chemistry* **276**, 48627-48630
281. Torres, J., and Pulido, R. (2001) The tumor suppressor PTEN is phosphorylated by the protein kinase CK2 at its C terminus. Implications for PTEN stability to proteasome-mediated degradation. *Journal of Biological Chemistry* **276**, 993-998
282. Gao, Y., and Wang, H. Y. (2006) Casein kinase 2 is activated and essential for Wnt/beta-catenin signaling. *Journal of Biological Chemistry* **281**, 18394-18400
283. Wu, Y., Dowbenko, D., Spencer, S., Laura, R., Lee, J., Gu, Q., and Lasky, L. A. (2000) Interaction of the tumor suppressor PTEN/MMAC with a PDZ domain of MAGI3, a novel membrane-associated guanylate kinase. *Journal of Biological Chemistry* **275**, 21477-21485
284. Ma, Q., Zhang, Y., Meng, R., Xie, K. M., Xiong, Y., Lin, S., He, Z. L., Tao, T., Yang, Y., Zhao, J. Z., and He, J. Q. (2015) MAGI3 Suppresses Glioma Cell Proliferation via Upregulation of PTEN Expression. *Biomedical and Environmental Sciences* **28**, 502-509
285. Eberhart, C. E., Coffey, R. J., Radhika, A., Giardiello, F. M., Ferrenbach, S., and DuBois, R. N. (1994) Up-regulation of cyclooxygenase 2 gene expression in human colorectal adenomas and adenocarcinomas. *Gastroenterology* **107**, 1183-1188
286. Gupta, R. A., and Dubois, R. N. (2001) Colorectal cancer prevention and treatment by inhibition of cyclooxygenase-2. *Nature Reviews Cancer* **1**, 11-21
287. Marnett, L. J., and DuBois, R. N. (2002) COX-2: a target for colon cancer prevention. *Annual Review of Pharmacology and Toxicology* **42**, 55-80
288. Fodde, R., and Brabletz, T. (2007) Wnt/beta-catenin signaling in cancer stemness and malignant behavior. *Current Opinion in Cell Biology* **19**, 150-158
289. Lee, S. J., Ritter, S. L., Zhang, H., Shim, H., Hall, R. A., and Yun, C. C. (2011) MAGI-3 competes with NHERF-2 to negatively regulate LPA2 receptor signaling in colon cancer cells. *Gastroenterology* **140**, 924-934
290. Goetzl, E. J., Dolezalova, H., Kong, Y., Hu, Y. L., Jaffe, R. B., Kalli, K. R., and Conover, C. A. (1999) Distinctive expression and functions of the type 4 endothelial differentiation gene-encoded G protein-coupled receptor for lysophosphatidic acid in ovarian cancer. *Cancer Research* **59**, 5370-5375
291. Yun, C. C., Sun, H., Wang, D., Rusovici, R., Castleberry, A., Hall, R. A., and Shim, H. (2005) LPA2 receptor mediates mitogenic signals in human colon cancer cells. *American Journal of Physiology. Cell Physiology*. **289**, C2-11
292. Kitayama, J., Shida, D., Sako, A., Ishikawa, M., Hama, K., Aoki, J., Arai, H., and Nagawa, H. (2004) Over-expression of lysophosphatidic acid receptor-2 in human invasive ductal carcinoma. *Breast Cancer Research* **6**, R640-646

293. Rusovici, R., Ghaleb, A., Shim, H., Yang, V. W., and Chris Yun, C. (2007) Lysophosphatidic acid prevents apoptosis of Caco-2 colon cancer cells via activation of mitogen-activated protein kinase and phosphorylation of Bad. *Biochimica et Biophysica Acta-General Subject* **1770**, 1194-1203
294. Oh, Y. S., Jo, N. W., Choi, J. W., Kim, H. S., Seo, S. W., Kang, K. O., Hwang, J. I., Heo, K., Kim, S. H., Kim, Y. H., Kim, I. H., Kim, J. H., Banno, Y., Ryu, S. H., and Suh, P. G. (2004) NHERF2 specifically interacts with LPA2 receptor and defines the specificity and efficiency of receptor-mediated phospholipase C- β 3 activation. *Molecular Cell Biology* **24**, 5069-5079
295. Zhang, H., Wang, D., Sun, H., Hall, R. A., and Yun, C. C. (2007) MAGI-3 regulates LPA-induced activation of Erk and RhoA. *Cell Signaling* **19**, 261-268
296. Yamada, T., Ohoka, Y., Kogo, M., and Inagaki, S. (2005) Physical and functional interactions of the lysophosphatidic acid receptors with PDZ domain-containing Rho guanine nucleotide exchange factors (RhoGEFs). *Journal of Biological Chemistry* **280**, 19358-19363
297. Creighton, C. J., Li, X., Landis, M., Dixon, J. M., Neumeister, V. M., Sjolund, A., Rimm, D. L., Wong, H., Rodriguez, A., Herschkowitz, J. I., Fan, C., Zhang, X., He, X., Pavlick, A., Gutierrez, M. C., Renshaw, L., Larionov, A. A., Faratian, D., Hilsenbeck, S. G., Perou, C. M., Lewis, M. T., Rosen, J. M., and Chang, J. C. (2009) Residual breast cancers after conventional therapy display mesenchymal as well as tumor-initiating features. *Proceedings of the National Academy of Sciences of the United States of America* **106**, 13820-13825
298. Cerami, E., Gao, J., Dogrusoz, U., Gross, B. E., Sumer, S. O., Aksoy, B. A., Jacobsen, A., Byrne, C. J., Heuer, M. L., Larsson, E., Antipin, Y., Reva, B., Goldberg, A. P., Sander, C., and Schultz, N. (2012) The cBio cancer genomics portal: an open platform for exploring multidimensional cancer genomics data. *Cancer Discovery* **2**, 401-404
299. Gao, J., Aksoy, B. A., Dogrusoz, U., Dresdner, G., Gross, B., Sumer, S. O., Sun, Y., Jacobsen, A., Sinha, R., Larsson, E., Cerami, E., Sander, C., and Schultz, N. (2013) Integrative analysis of complex cancer genomics and clinical profiles using the cBioPortal. *Science Signaling* **6**, pl1
300. Banerji, S., Cibulskis, K., Rangel-Escareno, C., Brown, K. K., Carter, S. L., Frederick, A. M., Lawrence, M. S., Sivachenko, A. Y., Sougnez, C., Zou, L., Cortes, M. L., Fernandez-Lopez, J. C., Peng, S., Ardlie, K. G., Auclair, D., Bautista-Pina, V., Duke, F., Francis, J., Jung, J., Maffuz-Aziz, A., Onofrio, R. C., Parkin, M., Pho, N. H., Quintana-Jurado, V., Ramos, A. H., Rebollar-Vega, R., Rodriguez-Cuevas, S., Romero-Cordoba, S. L., Schumacher, S. E., Stransky, N., Thompson, K. M., Uribe-Figueroa, L., Baselga, J., Beroukhi, R., Polyak, K., Sgroi, D. C., Richardson, A. L., Jimenez-Sanchez, G., Lander, E. S., Gabriel, S. B., Garraway, L. A., Golub, T. R., Melendez-Zajgla, J., Toker, A., Getz, G., Hidalgo-Miranda, A., and Meyerson, M. (2012) Sequence analysis of mutations and translocations across breast cancer subtypes. *Nature* **486**, 405-409
301. Ni, T. K., and Kuperwasser, C. (2016) Premature polyadenylation of MAGI3 produces a dominantly-acting oncogene in human breast cancer. *Elife* **5**
302. Kolawole, A. O., Sharma, P., Yan, R., Lewis, K. J. E., Xu, Z. G., Hostetler, H. A., and Excoffon, K. (2012) The PDZ1 and PDZ3 Domains of MAGI-1 Regulate the Eight-Exon Isoform of the Coxsackievirus and Adenovirus Receptor. *Journal of Virology* **86**, 9244-9254
303. Ran, F. A., Hsu, P. D., Wright, J., Agarwala, V., Scott, D. A., and Zhang, F. (2013) Genome engineering using the CRISPR-Cas9 system. *Nature Protocols* **8**, 2281-2308
304. Graham, F. L., Smiley, J., Russell, W. C., and Nairn, R. (1977) Characteristics of a human cell line transformed by DNA from human adenovirus type 5. *Journal of General Virology* **36**, 59-74
305. Graham, F. L., Harrison, T., and Williams, J. (1978) Defective transforming capacity of adenovirus type 5 host-range mutants. *Virology* **86**, 10-21
306. Fogh, J., Wright, W. C., and Loveless, J. D. (1977) Absence of HeLa cell contamination in 169 cell lines derived from human tumors. *Journal of the National Cancer Institute* **58**, 209-214
307. Tibbetts, L. M., Chu, M. Y., Hager, J. C., Dexter, D. L., and Calabresi, P. (1977) Chemotherapy of cell-line-derived human colon carcinomas in mice immunosuppressed with antithymocyte serum. *Cancer* **40**, 2651-2659
308. Dexter, D. L., Barbosa, J. A., and Calabresi, P. (1979) N,N-Dimethylformamide-induced Alteration of Cell Culture

Characteristics and Loss of Tumorigenicity in Cultured
Human Colon Carcinoma Cells. *Cancer Research* **39**, 1020-1025

309. Ishino, Y., Shinagawa, H., Makino, K., Amemura, M., and Nakata, A. (1987) Nucleotide sequence of the *iap* gene, responsible for alkaline phosphatase isozyme conversion in *Escherichia coli*, and identification of the gene product. *Journal of Bacteriology* **169**, 5429-5433
310. Mojica, F. J., Diez-Villasenor, C., Soria, E., and Juez, G. (2000) Biological significance of a family of regularly spaced repeats in the genomes of Archaea, Bacteria and mitochondria. *Molecular Microbiology* **36**, 244-246
311. Jansen, R., Embden, J. D., Gastra, W., and Schouls, L. M. (2002) Identification of genes that are associated with DNA repeats in prokaryotes. *Molecular Microbiology* **43**, 1565-1575
312. Haeussler, M., Schonig, K., Eckert, H., Eschstruth, A., Mianne, J., Renaud, J. B., Schneider-Maunoury, S., Shkumatava, A., Teboul, L., Kent, J., Joly, J. S., and Concordet, J. P. (2016) Evaluation of off-target and on-target scoring algorithms and integration into the guide RNA selection tool CRISPOR. *Genome Biology* **17**, 148
313. Ogino, S., Gully, M. L., den Dunnen, J. T., and Wilson, R. B. (2007) Standard Mutation Nomenclature in Molecular Diagnostics : Practical and Educational Challenges. *Journal of Molecular Diagnostics* **9**, 1-6
314. Trietsch, S. J., Naumovska, E., Kurek, D., Setyawati, M. C., Vormann, M. K., Wilschut, K. J., Lanz, H. L., Nicolas, A., Ng, C. P., Joore, J., Kustermann, S., Roth, A., Hankemeier, T., Moisan, A., and Vulto, P. (2017) Membrane-free culture and real-time barrier integrity assessment of perfused intestinal epithelium tubes. *Nature Communications* **8**, 262
315. Kolb, H. C., Finn, M. G., and Sharpless, K. B. (2001) Click Chemistry: Diverse Chemical Function from a Few Good Reactions. *Angewandte Chemie International Edition England* **40**, 2004-2021
316. Salic, A., and Mitchison, T. J. (2008) A chemical method for fast and sensitive detection of DNA synthesis in vivo. *Proceedings of the National Academy of Sciences of the United States of America* **105**, 2415-2420
317. Rostovtsev, V. V., Green, L. G., Fokin, V. V., and Sharpless, K. B. (2002) A stepwise Huisgen cycloaddition process: copper(I)-catalyzed regioselective "ligation" of azides and terminal alkynes. *Angewandte Chemie International Edition England* **41**, 2596-2599
318. Zhang, X., and Zhang, Y. (2013) Applications of azide-based bioorthogonal click chemistry in glycobiology. *Molecules* **18**, 7145-7159
319. Zhu, C., Li, L., and Zhao, B. (2015) The regulation and function of YAP transcription co-activator. *Acta Biochimica Et Biophysica Sinica* **47**, 16-28
320. Stolfi, C., Fina, D., Caruso, R., Caprioli, F., Sarra, M., Fantini, M. C., Rizzo, A., Pallone, F., and Monteleone, G. (2008) Cyclooxygenase-2-dependent and -independent inhibition of proliferation of colon cancer cells by 5-aminosalicylic acid. *Biochemical Pharmacology* **75**, 668-676
321. Dexter, D. L., Spremulli, E. N., Fligel, Z., Barbosa, J. A., Vogel, R., VanVoorhees, A., and Calabresi, P. (1981) Heterogeneity of cancer cells from a single human colon carcinoma. *American Journal of Medicine* **71**, 949-956
322. Hammad, M. M., Dunn, H. A., and Ferguson, S. S. G. (2016) MAGI Proteins Regulate the Trafficking and Signaling of Corticotropin-Releasing Factor Receptor 1 via a Compensatory Mechanism. *Journal of Molecular Signaling* **11**
323. Gee, H. Y., Kim, Y. W., Jo, M. J., Namkung, W., Kim, J. Y., Park, H. W., Kim, K. S., Kim, H., Baba, A., Yang, J., Kim, E., Kim, K. H., and Lee, M. G. (2009) Synaptic scaffolding molecule binds to and regulates vasoactive intestinal polypeptide type-1 receptor in epithelial cells. *Gastroenterology* **137**, 607-617, 617.e601-604
324. Vermeulen, S. J., Chen, T. R., Speleman, F., Nollet, F., Van Roy, F. M., and Mareel, M. M. (1998) Did the four human cancer cell lines DLD-1, HCT-15, HCT-8, and HRT-18 originate from one and the same patient? *Cancer Genetics and Cytogenetics* **107**, 76-79

325. Oh, H., and Irvine, K. D. (2008) In vivo regulation of Yorkie phosphorylation and localization. *Development* **135**, 1081-1088
326. Ma, T. Y. (1997) Intestinal epithelial barrier dysfunction in Crohn's disease. *Proceedings of the Society for Experimental Biology and Medicine* **214**, 318-327
327. Wevers, N. R., Kasi, D. G., Gray, T., Wilschut, K. J., Smith, B., van Vught, R., Shimizu, F., Sano, Y., Kanda, T., Marsh, G., Trietsch, S. J., Vulto, P., Lanz, H. L., and Obermeier, B. (2018) A perfused human blood-brain barrier on-a-chip for high-throughput assessment of barrier function and antibody transport. *Fluids Barriers CNS* **15**, 23
328. Callus, B. A., Finch-Edmondson, M. L., Fletcher, S., and Wilton, S. D. (2019) YAPping about and not forgetting TAZ. *FEBS Letters* **593**, 253-276
329. Zhang, H., Liu, C. Y., Zha, Z. Y., Zhao, B., Yao, J., Zhao, S., Xiong, Y., Lei, Q. Y., and Guan, K. L. (2009) TEAD transcription factors mediate the function of TAZ in cell growth and epithelial-mesenchymal transition. *Journal of Biological Chemistry* **284**, 13355-13362
330. Hahn, C., and Schwartz, M. A. (2009) Mechanotransduction in vascular physiology and atherogenesis. *Nature Reviews Molecular Cell Biology* **10**, 53-62
331. Sabine, A., Bovay, E., Demir, C. S., Kimura, W., Jaquet, M., Agalarov, Y., Zangger, N., Scallan, J. P., Graber, W., Gulpinar, E., Kwak, B. R., Makinen, T., Martinez-Corral, I., Ortega, S., Delorenzi, M., Kiefer, F., Davis, M. J., Djonov, V., Miura, N., and Petrova, T. V. (2015) FOXC2 and fluid shear stress stabilize postnatal lymphatic vasculature. *Journal of Clinical Investigation* **125**, 3861-3877
332. Rausch, V., Bostrom, J. R., Park, J., Bravo, I. R., Feng, Y., Hay, D. C., Link, B. A., and Hansen, C. G. (2019) The Hippo Pathway Regulates Caveolae Expression and Mediates Flow Response via Caveolae. *Current Biology* **29**, 242-255.e246
333. Stevenson, B. R., and Keon, B. H. (1998) The tight junction: morphology to molecules. *Annual Review of Cell and Developmental Biology* **14**, 89-109
334. Ekobom, A., Helmick, C., Zack, M., and Adami, H. O. (1990) Ulcerative colitis and colorectal cancer. A population-based study. *New England Journal of Medicine* **323**, 1228-1233
335. Mattar, M. C., Lough, D., Pishvaian, M. J., and Charabaty, A. (2011) Current management of inflammatory bowel disease and colorectal cancer. *Gastrointestinal Cancer Research* **4**, 53-61
336. Keller, D. S., Windsor, A., Cohen, R., and Chand, M. (2019) Colorectal cancer in inflammatory bowel disease: review of the evidence. *Techniques in Coloproctology* **23**, 3-13
337. Saunders, P. T., and Ho, M. W. (1976) On the increase in complexity in evolution. *Journal of Theoretical Biology* **63**, 375-384
338. Sebe-Pedros, A., Zheng, Y., Ruiz-Trillo, I., and Pan, D. (2012) Premetazoan origin of the hippo signaling pathway. *Cell Reports* **1**, 13-20
339. Weng, G., Bhalla, U. S., and Iyengar, R. (1999) Complexity in biological signaling systems. *Science* **284**, 92-96
340. Salah, Z., and Aqeilan, R. I. (2011) WW domain interactions regulate the Hippo tumor suppressor pathway. *Cell Death and Disease* **2**, e172
341. Sudol, M. (2010) Newcomers to the WW Domain-Mediated Network of the Hippo Tumor Suppressor Pathway. *Genes & cancer* **1**, 1115-1118
342. Salah, Z., Alian, A., and Aqeilan, R. I. (2012) WW domain-containing proteins: retrospectives and the future. *Frontiers in Bioscience (Landmark Ed)* **17**, 331-348
343. Roux, K. J., Kim, D. I., Raida, M., and Burke, B. (2012) A promiscuous biotin ligase fusion protein identifies proximal and interacting proteins in mammalian cells. *Journal of Cell Biology* **196**, 801-810

344. Boldt, K., van Reeuwijk, J., Lu, Q., Koutroumpas, K., Nguyen, T. M., Texier, Y., van Beersum, S. E., Horn, N., Willer, J. R., Mans, D. A., Dougherty, G., Lamers, I. J., Coene, K. L., Arts, H. H., Betts, M. J., Beyer, T., Bolat, E., Gloeckner, C. J., Haidari, K., Hetterschijt, L., Iaconis, D., Jenkins, D., Klose, F., Knapp, B., Latour, B., Letteboer, S. J., Marcelis, C. L., Mitic, D., Morleo, M., Oud, M. M., Riemersma, M., Rix, S., Terhal, P. A., Toedt, G., van Dam, T. J., de Vrieze, E., Wissinger, Y., Wu, K. M., Apic, G., Beales, P. L., Blacque, O. E., Gibson, T. J., Huynen, M. A., Katsanis, N., Kremer, H., Omran, H., van Wijk, E., Wolfrum, U., Kepes, F., Davis, E. E., Franco, B., Giles, R. H., Ueffing, M., Russell, R. B., and Roepman, R. (2016) An organelle-specific protein landscape identifies novel diseases and molecular mechanisms. *Nature Communications* **7**, 11491
345. Huttlin, E. L., Bruckner, R. J., Paulo, J. A., Cannon, J. R., Ting, L., Baltier, K., Colby, G., Gebreab, F., Gygi, M. P., Parzen, H., Szpyt, J., Tam, S., Zarraga, G., Pontano-Vaites, L., Swarup, S., White, A. E., Schweppe, D. K., Rad, R., Erickson, B. K., Obar, R. A., Guruharsha, K. G., Li, K., Artavanis-Tsakonas, S., Gygi, S. P., and Harper, J. W. (2017) Architecture of the human interactome defines protein communities and disease networks. *Nature* **545**, 505-509
346. Cho, K. O., Hunt, C. A., and Kennedy, M. B. (1992) The rat brain postsynaptic density fraction contains a homolog of the *Drosophila* discs-large tumor suppressor protein. *Neuron* **9**, 929-942
347. Woods, D. F., and Bryant, P. J. (1993) ZO-1, DlgA and PSD-95/SAP90: homologous proteins in tight, septate and synaptic cell junctions. *Mechanisms of Development* **44**, 85-89
348. Kim, E., Niethammer, M., Rothschild, A., Jan, Y. N., and Sheng, M. (1995) Clustering of Shaker-type K⁺ channels by interaction with a family of membrane-associated guanylate kinases. *Nature* **378**, 85-88
349. Chishti, A. H., Kim, A. C., Marfatia, S. M., Lutchnan, M., Hanspal, M., Jindal, H., Liu, S. C., Low, P. S., Rouleau, G. A., Mohandas, N., Chasis, J. A., Conboy, J. G., Gascard, P., Takakuwa, Y., Huang, S. C., Benz, E. J., Jr., Bretscher, A., Fehon, R. G., Gusella, J. F., Ramesh, V., Solomon, F., Marchesi, V. T., Tsukita, S., Hoover, K. B., and et al. (1998) The FERM domain: a unique module involved in the linkage of cytoplasmic proteins to the membrane. *Trends in Biochemical Sciences* **23**, 281-282
350. Xu, X. Z., Choudhury, A., Li, X., and Montell, C. (1998) Coordination of an array of signaling proteins through homo- and heteromeric interactions between PDZ domains and target proteins. *Journal of Cell Biology* **142**, 545-555
351. Lin, D., Edwards, A. S., Fawcett, J. P., Mbamalu, G., Scott, J. D., and Pawson, T. (2000) A mammalian PAR-3-PAR-6 complex implicated in Cdc42/Rac1 and aPKC signalling and cell polarity. *Nature Cell Biology* **2**, 540-547
352. Marfatia, S. M., Byron, O., Campbell, G., Liu, S. C., and Chishti, A. H. (2000) Human homologue of the *Drosophila* discs large tumor suppressor protein forms an oligomer in solution. Identification of the self-association site. *Journal of Biological Chemistry* **275**, 13759-13770
353. Salah, Z., Cohen, S., Itzhaki, E., and Aqeilan, R. I. (2013) NEDD4 E3 ligase inhibits the activity of the Hippo pathway by targeting LATS1 for degradation. *Cell Cycle* **12**, 3817-3823
354. Schuchardt, B. J., Mikles, D. C., Hoang, L. M., Bhat, V., McDonald, C. B., Sudol, M., and Farooq, A. (2014) Ligand binding to WW tandem domains of YAP2 transcriptional regulator is under negative cooperativity. *FEBS Journal* **281**, 5532-5551
355. Hirate, Y., and Sasaki, H. (2014) The role of angiomin phosphorylation in the Hippo pathway during preimplantation mouse development. *Tissue Barriers* **2**, e28127
356. Li, X., Tran, K. M., Aziz, K. E., Sorokin, A. V., Chen, J., and Wang, W. (2016) Defining the Protein-Protein Interaction Network of the Human Protein Tyrosine Phosphatase Family. *Molecular and Cellular Proteomics* **15**, 3030-3044
357. Sudol, M., and Harvey, K. F. (2010) Modularity in the Hippo signaling pathway. *Trends in Biochemical Sciences* **35**, 627-633
358. Li, Y. W., Guo, J., Shen, H., Li, J., Yang, N., Frangou, C., Wilson, K. E., Zhang, Y. L., Mussell, A. L., Sudol, M., Farooq, A., Qu, J., and Zhang, J. M. (2016) Phosphorylation of Tyr188 in the WW domain of YAP1 plays an essential role in YAP1-induced cellular transformation. *Cell Cycle* **15**, 2497-2505

359. Reuven, N., Shanzer, M., and Shaul, Y. (2015) Tyrosine phosphorylation of WW proteins. *Experimental Biology and Medicine* **240**, 375-382
360. Fujikawa, A., Fukada, M., Makioka, Y., Suzuki, R., Chow, J. P. H., Matsumoto, M., and Noda, M. (2011) Consensus Substrate Sequence for Protein-tyrosine Phosphatase Receptor Type Z. *Journal of Biological Chemistry* **286**, 37137-37146
361. Lee, H. J., and Zheng, J. J. (2010) PDZ domains and their binding partners: structure, specificity, and modification. *Cell Communication and Signaling* **8**, 8
362. Hui, S., and Bader, G. D. (2010) Proteome scanning to predict PDZ domain interactions using support vector machines. *BMC Bioinformatics* **11**, 507
363. Wang, W., Li, X., Huang, J., Feng, L., Dolinta, K. G., and Chen, J. (2014) Defining the protein-protein interaction network of the human hippo pathway. *Molecular and Cellular Proteomics* **13**, 119-131
364. Yoshihama, Y., Sasaki, K., Horikoshi, Y., Suzuki, A., Ohtsuka, T., Hakuno, F., Takahashi, S., Ohno, S., and Chida, K. (2011) KIBRA suppresses apical exocytosis through inhibition of aPKC kinase activity in epithelial cells. *Current Biology* **21**, 705-711
365. Zhang, L., Yang, S., Wennmann, D. O., Chen, Y., Kremerskothen, J., and Dong, J. (2014) KIBRA: In the brain and beyond. *Cell Signaling* **26**, 1392-1399
366. Alessi, D. R., Caudwell, F. B., Andjelkovic, M., Hemmings, B. A., and Cohen, P. (1996) Molecular basis for the substrate specificity of protein kinase B; comparison with MAPKAP kinase-1 and p70 S6 kinase. *FEBS Letters* **399**, 333-338
367. Datta, S. R., Dudek, H., Tao, X., Masters, S., Fu, H., Gotoh, Y., and Greenberg, M. E. (1997) Akt phosphorylation of BAD couples survival signals to the cell-intrinsic death machinery. *Cell* **91**, 231-241
368. Obata, T., Yaffe, M. B., Leparo, G. G., Piro, E. T., Maegawa, H., Kashiwagi, A., Kikkawa, R., and Cantley, L. C. (2000) Peptide and protein library screening defines optimal substrate motifs for AKT/PKB. *Journal of Biological Chemistry* **275**, 36108-36115
369. Wang, C., An, J., Zhang, P., Xu, C., Gao, K., Wu, D., Wang, D., Yu, H., Liu, J. O., and Yu, L. (2012) The Nedd4-like ubiquitin E3 ligases target angiotensin II to ubiquitin-dependent degradation. *Biochemical Journal* **444**, 279-289
370. Wennmann, D. O., Schmitz, J., Wehr, M. C., Krahn, M. P., Koschmal, N., Gromnitsa, S., Schulze, U., Weide, T., Chekuri, A., Skryabin, B. V., Gerke, V., Pavenstadt, H., Duning, K., and Kremerskothen, J. (2014) Evolutionary and molecular facts link the WWC protein family to Hippo signaling. *Molecular Biology and Evolution* **31**, 1710-1723
371. Lin, Z., Yang, Z., Xie, R., Ji, Z., Guan, K., and Zhang, M. (2019) Decoding WW Domain Tandem-mediated Target Recognitions in Tissue Growth and Cell Polarity.
372. Hergovich, A., Bichsel, S. J., and Hemmings, B. A. (2005) Human NDR Kinases Are Rapidly Activated by MOB Proteins through Recruitment to the Plasma Membrane and Phosphorylation. *Molecular Cell Biology* **25**, 8259-8272
373. Kondo, T., and Hayashi, S. (2015) Mechanisms of cell height changes that mediate epithelial invagination. *Development, Growth & Differentiation* **57**, 313-323
374. Melani, M., Simpson, K. J., Brugge, J. S., and Montell, D. (2008) Regulation of cell adhesion and collective cell migration by hindsight and its human homolog RREB1. *Current Biology* **18**, 532-537
375. Hannezo, E., Prost, J., and Joanny, J. F. (2014) Theory of epithelial sheet morphology in three dimensions. *Proceedings of the National Academy of Sciences of the United States of America* **111**, 27-32
376. Yoshida, M., Zhao, L., Grigoryan, G., Shim, H., He, P., and Yun, C. C. (2016) Deletion of Na⁺/H⁺ exchanger regulatory factor 2 represses colon cancer progress by suppression of Stat3 and CD24. *American Journal of Physiology. Gastrointestinal and Liver Physiology* **310**, G586-598

377. Mohler, P. J., Kreda, S. M., Boucher, R. C., Sudol, M., Stutts, M. J., and Milgram, S. L. (1999) Yes-associated protein 65 localizes p62(c-Yes) to the apical compartment of airway epithelia by association with EBP50. *Journal of Cell Biology* **147**, 879-890
378. Enzo, E., Santinon, G., Pocaterra, A., Aragona, M., Bresolin, S., Forcato, M., Grifoni, D., Pession, A., Zanconato, F., Guzzo, G., Bicciato, S., and Dupont, S. (2015) Aerobic glycolysis tunes YAP/TAZ transcriptional activity. *EMBO Journal* **34**, 1349-1370
379. Xie, S., Shen, B., Zhang, C., Huang, X., and Zhang, Y. (2014) sgRNAs9: a software package for designing CRISPR sgRNA and evaluating potential off-target cleavage sites. *PLoS One* **9**, e100448
380. Dunn, H. A., and Ferguson, S. S. (2015) PDZ Protein Regulation of G Protein-Coupled Receptor Trafficking and Signaling Pathways. *Molecular Pharmacology* **88**, 624-639
381. Cooper, G. M. (2000) The Eukaryotic Cell Cycle. in *The Cell: A Molecular Approach. 2nd Edition.*, Sinauer Associates. pp
382. Feldman, G. J., Mullin, J. M., and Ryan, M. P. (2005) Occludin: structure, function and regulation. *Advanced Drug Delivery Reviews* **57**, 883-917
383. Chelakkot, C., Ghim, J., and Ryu, S. H. (2018) Mechanisms regulating intestinal barrier integrity and its pathological implications. *Experimental and Molecular Medicine* **50**, 103
384. Kevil, C. G., Okayama, N., Trocha, S. D., Kalogeris, T. J., Coe, L. L., Specian, R. D., Davis, C. P., and Alexander, J. S. (1998) Expression of zonula occludens and adherens junctional proteins in human venous and arterial endothelial cells: role of occludin in endothelial solute barriers. *Microcirculation* **5**, 197-210
385. Balda, M. S., Flores-Maldonado, C., Cerejido, M., and Matter, K. (2000) Multiple domains of occludin are involved in the regulation of paracellular permeability. *Journal of Cellular Biochemistry* **78**, 85-96
386. Chen, Y., Merzdorf, C., Paul, D. L., and Goodenough, D. A. (1997) COOH terminus of occludin is required for tight junction barrier function in early *Xenopus* embryos. *Journal of Cell Biology* **138**, 891-899
387. van Roy, F., and Berx, G. (2008) The cell-cell adhesion molecule E-cadherin. *Cellular and Molecular Life Sciences* **65**, 3756-3788
388. Hazan, R. B., Qiao, R., Keren, R., Badano, I., and Suyama, K. (2004) Cadherin switch in tumor progression. *Gastroenteropancreatic Neuroendocrine Tumor Disease: Molecular and Cell Biological Aspects* **1014**, 155-163
389. Wheelock, M. J., Shintani, Y., Maeda, M., Fukumoto, Y., and Johnson, K. R. (2008) Cadherin switching. *Journal of Cell Science* **121**, 727-735
390. Kile, B. T., Schulman, B. A., Alexander, W. S., Nicola, N. A., Martin, H. M. E., and Hilton, D. J. (2002) The SOCS box: a tale of destruction and degradation. *Trends in Biochemical Sciences* **27**, 235-241
391. Corbin, J. A., Evans, J. H., Landgraf, K. E., and Falke, J. J. (2007) Mechanism of Specific Membrane Targeting by C2 Domains: Localized Pools of Target Lipids Enhance Ca²⁺ Affinity. *Biochemistry* **46**, 4322-4336
392. Davletov, B. A., and Sudhof, T. C. (1993) A single C2 domain from synaptotagmin I is sufficient for high affinity Ca²⁺/phospholipid binding. *Journal of Biological Chemistry* **268**, 26386-26390
393. Scheffner, M., and Kumar, S. (2014) Mammalian HECT ubiquitin-protein ligases: biological and pathophysiological aspects. *Biochimica et Biophysica Acta-Molecular Cell Research* **1843**, 61-74
394. Wiesner, S., Ogunjimi, A. A., Wang, H. R., Rotin, D., Sicheri, F., Wrana, J. L., and Forman-Kay, J. D. (2007) Autoinhibition of the HECT-type ubiquitin ligase Smurf2 through its C2 domain. *Cell* **130**, 651-662
395. Bruce, M. C., Kanelis, V., Fouladkou, F., Debonneville, A., Staub, O., and Rotin, D. (2008) Regulation of Nedd4-2 self-ubiquitination and stability by a PY motif located within its HECT-domain. *Biochemical Journal* **415**, 155-163

396. Riling, C., Kamadurai, H., Kumar, S., O'Leary, C. E., Wu, K. P., Manion, E. E., Ying, M., Schulman, B. A., and Oliver, P. M. (2015) Itch WW Domains Inhibit Its E3 Ubiquitin Ligase Activity by Blocking E2-E3 Ligase Trans-thiolation. *Journal of Biological Chemistry* **290**, 23875-23887